



HAL
open science

Study of a planar lighting device

Yida Wen

► **To cite this version:**

Yida Wen. Study of a planar lighting device. Optics [physics.optics]. Université Paris Sud - Paris XI, 2015. English. NNT: 2015PA112181 . tel-03270750

HAL Id: tel-03270750

<https://theses.hal.science/tel-03270750>

Submitted on 25 Jun 2021

HAL is a multi-disciplinary open access archive for the deposit and dissemination of scientific research documents, whether they are published or not. The documents may come from teaching and research institutions in France or abroad, or from public or private research centers.

L'archive ouverte pluridisciplinaire **HAL**, est destinée au dépôt et à la diffusion de documents scientifiques de niveau recherche, publiés ou non, émanant des établissements d'enseignement et de recherche français ou étrangers, des laboratoires publics ou privés.

UNIVERSITÉ PARIS-SUD

ÉCOLE DOCTORALE 422 :
SCIENCES ET TECHNOLOGIES DE L'INFORMATION DES TÉLÉCOMMUNICATIONS
ET DES SYSTÈMES

Laboratoire : Institut d'Électronique Fondamentale

THÈSE DE DOCTORAT

PHYSIQUE

par

Yida WEN

**Etude d'un système d'éclairage surfacique à
géométrie planaire**

Study of a planar lighting device

Date de soutenance : 23/09/2015

Composition du jury :

Président du jury :	Pascal BESNARD	Professeur (ENSSAT)
Directrice de thèse :	Béatrice DAGENS	Directrice de recherche CNRS (IEF)
Rapporteurs :	Olivier GAUTHIER-LAFAYE	Chargé de recherche CNRS (LAAS-CNRS)
	Jean-Claude WEEBER	Professeur (Université de Bourgogne)
Examineurs :	David BARAT	Docteur-Ingénieur (PSA Peugeot Citroën)
	Pascal BESNARD	Professeur (ENSSAT)
	Whilk-Marcelino GONÇALVES	Docteur-Ingénieur (PSA Peugeot Citroën)



PSA PEUGEOT CITROËN 

Thèse préparée à

Institut d'Électronique Fondamentale

Bâtiment 220, Campus Scientifique d'Orsay,
91405 Orsay, France

PSA Peugeot Citroën

Centre technique de Vélizy, route de Gisy,
78140 Vélizy-Villacoublay, France

ACKNOWLEDGEMENTS

There are too many people who have encouraged and supported me during my 3-year research work as the first PhD student supported by the *PSA Peugeot Citroën - Université Paris-Sud Optoelectronics and plasmonics research chair* since 2012. Meanwhile, this thesis could never be realized without the doctorant grant CIFRE-2011/1610 approved by the French *Association Nationale de la Recherche et de la Technologie*.

First and foremost, I would like to express my grateful thanks to my research advisor, Béatrice Dagens, for her kindness, patience and excellent guidance through the years. Her dedication and professionalism have always motivated me to work harder and more autonomously. I would like to specially thank my administrative supervisor, David Barat, for his warm-hearted welcome in PSA and indispensable energy in coordinating all of participants within this interdisciplinary research project.

I would like to thank Olivier Gauthier-Lafaye and Jean-Claude Weeber for their helpful and insightful advice to my manuscripts of thesis. I also want to thank Pascal Besnard and Whilk-Marcelino Gonçalves for the examination of my manuscripts.

I am thankful to the scientific director of PSA, Sylvain Allano, and managers and experts within the service of DSTF/SIEP, Jean-Yves Marteau, Bernard Bavoux and Laetitia Pradéré, for their absolute trust and limitless assistance.

Without the discussion and collaboration with all of my colleagues at the IEF, my progress in research could not have occurred. Especially, I thank Philippe Gogol for the ellipsometry measurement and experimental data fitting. I want to express my special thanks to Jean-René Coudevylle, for his hand-in-hand teaching in cleanroom fabrication. I would like to thank all of the CIMPHONIE members, Hervé Bertin, Benjamin Leroy and Giovanni Magno for their assistance and insight in fabrication and simulation. I want to say MERCI to Michael Fevrier, Matthias Grangier, Qiran Li, Navy Yam and Robert Mégy for their help and suggestions during these years.

I have enjoyed the extracurricular life with all my friends in France. I will never forget the happy hours in the bars and restaurants with my dear buddies David Le Bourdais and Georg Kurji and their girlfriends. I will never forget the exciting football match in Gif-sur-Yvette every Sunday morning playing with my dear teammates: Yuan, Nan, Hezhi, Siqi, Jihua...

Finally, I would like to thank my parents for their support and encouragement, and also thank my dear Violaine for love and consideration.

ABSTRACT	1
CHAPTER I: GENERAL INTRODUCTION TO RESEARCH BACKGROUND AND OBJECTIVE	5
I.1 Photonics in the automotive industry	5
<i>I.1.1 Brief history of automotive lighting and signalling systems</i>	6
<i>I.1.2 Evolution of advanced driver assistance systems</i>	7
I.2 Research background	9
<i>I.2.1 Targeted embedded holographic signalling system</i>	9
<i>I.2.2 Restitution principle of predetermined 3D holographic image</i>	11
<i>I.2.3 Problematical analysis of existed holographic system</i>	12
I.3 Objective and planning of research	13
<i>I.3.1 Panorama of targeted holographic illumination system</i>	14
<i>I.3.2 1st subsystem: visible PICs</i>	15
<i>I.3.3 2nd subsystem: controllable nano-emitters</i>	16
<i>I.3.4 3rd subsystem: organic amplifier</i>	18
I.4 Conclusion	18
CHAPTER II: INTRODUCTION TO THE Si₃N₄ WAVEGUIDES PLATFORM	19
II.1 Context of silicon photonics	19
II.2 PICs for visible applications	21
<i>II.2.1 Bottleneck of the development of visible PICs</i>	22
<i>II.2.2 History of 1D Si₃N₄ slab waveguides</i>	23
<i>II.2.3 Structured 2D Si₃N₄ waveguides: pioneer results for multimode waveguides</i>	28
II.3 The state-of-the-art Si₃N₄ waveguides operating at visible wavelengths	34
II.4 Conclusion	36
CHAPTER III: DESIGN AND SIMULATION OF Si₃N₄ WAVEGUIDES	39
III.1 Numerical simulation-assisted design	39
<i>III.1.1 Modeling of guided modes: methods and structures</i>	40
<i>III.1.2 Measurement of refractive index</i>	45

III.1.3	<i>The effective index and confinement coefficient of TE modes</i>	48
III.1.4	<i>Conclusion</i>	67
III.2	Visible PICs based on Si₃N₄ /SiO₂ platform	67
III.2.1	<i>Review of 1 × N light beam splitters</i>	68
III.2.2	<i>Design and simulation of beam splitting devices</i>	77
III.2.3	<i>Design and evaluation of bent waveguides</i>	90
III.2.4	<i>Evaluation of lemniscate-like and S-Function bent waveguides</i>	101
III.2.5	<i>Conclusion</i>	109
III.3	Conclusion	110
CHAPTER IV: FABRICATION AND CHARACTERIZATION of Si₃N₄		
WAVEGUIDES		
IV.1	Cleanroom fabrication process	111
IV.1.1	<i>Deposition of materials</i>	112
IV.1.2	<i>Electron beam lithography</i>	114
IV.1.3	<i>Reactive ionic etching</i>	123
IV.1.4	<i>Cut and cleavage of the samples</i>	129
IV.1.5	<i>Conclusion</i>	132
IV.2	Characterization of fabricated waveguides	132
IV.2.1	<i>Characterization platform</i>	132
IV.2.2	<i>Transmission measurement of the straight waveguides</i>	136
IV.2.3	<i>Discussion, conclusion and perspectives of fabrication</i>	142
IV.3	Conclusion	144
CHAPTER V: COUPLING BETWEEN MNP CHAIN AND Si₃N₄		
WAVEGUIDE		
V.1	Basic knowledge and state of the art	145
V.1.1	<i>Surface plasmonic modes in a metallic nanoparticle (MNP) chain</i>	145
V.1.2	<i>Coupling between plasmonic waveguides and 2D dielectric waveguides</i>	152
V.1.3	<i>Applications based on hybrid dielectric/MNP chain waveguides</i>	153
V.2	Modelling of MNP chain integrated on a Si₃N₄ waveguide	159
V.2.1	<i>Punctual dipole model</i>	159
V.2.2	<i>Optical properties of the metals</i>	161

<i>V.2.3 Computed single MNP resonance</i>	163
<i>V.2.4 FDTD simulation</i>	167
V.3 Conclusion	172
CONCLUSION AND PERSPECTIVES	173
ANNEXE I: Effective index method for 1D dielectric waveguide	177
<u>RÉSUMÉ EN LANGUE FRANÇAISE</u>	181
REFERENCE	209

ABSTRACT

Industry analysts usually divide the existed automotive photonic systems in four application domains depending on its integration in a car [COCHA15]: interiors, exterior, powertrain and the advanced driver assistance system (ADAS). To our knowledge, the pioneer advanced automotive photonic application can date back to the year of 2000. In order to increase the data stream's transmission and exchanging rate, the media oriented system transport (MOST) based on optical fibers have been developed and then widely used to form a ring-like data stream network of communications between each multimedia component. Since 2008, with the development of the semiconductor industrials, the light-emitting diode (LED) lighting source and display screens have been widely used in the automotive domain due to its outstanding compactness, high efficiency and reliable stability. Most of existing automotive photonic applications aim at improving driver and passenger's experience with the human-machine interface (HMI) and multimedia entertainment.

Henceforth the advanced photonics and optoelectronics embedded system will pay more attention to the security of driving. Differently to the traditional lighting and signalling usage, these new photonic and optoelectronic devices bring new-fashion functionalities into the passenger cars, such as optical-frequency sensing, light beam carried communication, high-density illumination and holographic displaying. Actually, PSA Peugeot Citroën has developed a 3D holographic imaging prototype for a security-related application [FR2949725 (A1)]. The objective of this system is to generate at least one predetermined 3D image(s) in the free space behind the car in the risky or dangerous situation, where another car follows and then approaches too close from behind. This 3D image composed of several warning symbols, aims at reminding driver in the following car to slow down and to keep a security distance. The prototype of this holographic imaging system includes a series of optical mirrors and lenses. It thus occupies a lot of space (i.e: the length is up to 80 cm), and there is no enough space to integrate all the optical components in the car body. In this context, we are looking for a technical solution to make this optical system much more compact.

In parallel with the development of the automotive photonics, physicists and engineers have also made revolutionary progress in the theoretical and experimental research of nanotechnologies and nanophotonics for last few decades. For instance, the photonic integrated circuits (PICs) have been deeply investigated and applied in the telecommunication

domain, notably due to the fabrication process and facilities' compatibility with the mature complementary metal oxide semiconductor (CMOS) Pilot-line. Consequently, a series of novel optoelectronic devices are designed to realize optical wave's routing, switching, emitting and detecting. And besides, the huge progress in terms of patterning and miniaturization due to the development of nanotechnology, is giving access today to planar visible wavelength single-mode waveguide fabrication. Integrated circuits developed for near-infrared (NIR) telecom applications can be thus now transposed to visible domain applications. Meanwhile, surface plasmon excitation in hybrid dielectric and metallic structures is also appeared as an attractive topic due to its specific sub-wavelength light concentration characteristics within an interesting visible and NIR wavelength range. The development of nano-photonics and plasmonics opens thus the way to new high-density photonic integrated devices.

Inspired by both the industrial need for PSA's auto-embedded optoelectronic application and the academic research of IEF in the domain of nanophotonics and plasmonics, since 2011, a close collaboration between PSA and IEF has been built for the research and development of automotive photonic and plasmonic integrated devices and systems. This manuscript is presented as a memorandum of the 1st CIFRE¹ PhD research work benefited from this collaboration framework. The main objective of this work consists of the study and development of an ultra-compact, coherent and uniform holographic illumination system. The manuscript is divided into 3 main parts:

In the 1st part, the evolution of the automotive photonic applications and devices will be systematically reviewed in order to introduce with more evidence our research background and objective. We will put great emphasis on how the application of nanotechnologies and nanophotonics would disruptively improve the compactness of the mentioned holographic illumination system. The basic design of the targeted PIC will be briefly presented, including notably optical waveguide arrays and integrated plasmonic nanoantennas. This part is presented in Chapter I. The 2nd part is dedicated to the research work on Si₃N₄ waveguide-based PICs, and on the theoretical and experimental study of several specific elementary building blocks: Si₃N₄ based straight and bent waveguides and 1 × N uniform beam splitters, for operation at 633 nm. This part occupies the largest space in the manuscript and is composed of the Chapters II, III and IV. In the 3rd part, we will present the evaluation of plasmonic nanoantennas integration on Si₃N₄ waveguides, for 633 nm working wavelength. The coupling effects from the photonic modes in the dielectric waveguide to the plasmonic

¹ CIFRE: Abbreviation for the French industry academic program: "les Conventions Industrielles de Formation par la Recherche".

modes in an Au or Ag nanoparticle chain deposited on top of the Si_3N_4 rectangular waveguide are studied, including coupling and resonance efficiency. This part will be presented in Chapter V. The manuscript is then achieved with a conclusion of the whole research work during 3-year PhD study, as well as its perspectives.

CHAPTER I: GENERAL INTRODUCTION TO RESEARCH

BACKGROUND AND OBJECTIVE

Photonics in automotive is the main context of this work. After a review of the progressive implementation of photonics in automotive, we will introduce in a general way the background of our research project, which aims at developing an integrated photonic and plasmonic device for a compact automotive holographic system. We will thus present and explain the purpose and the content of this work by showing a comprehensive description of the targeted system, the innovative points and potential challenges attached to the research project.

I.1 PHOTONICS IN THE AUTOMOTIVE INDUSTRY

As one of the most traditional industries, automotive covers multidisciplinary modern science and engineering. Photonic technologies have been first embedded into automotive vehicles through its lighting and signalling functions with the first headlamp introduced in 1880. Since then, many developments have been done on exterior lighting with projectors composed of light sources (Halogen, Xenon, LED and laser) and mirrors, and also on different illumination sources and devices for the cockpit. To give an idea, global market of exterior lighting was 12 b€ in 2013. Nowadays, research and developments on advanced driver assistance systems (ADAS) are increasing as, for example, embedded light detection and ranging (LIDAR) system for forward collision warning [SAMMA00]. Meanwhile, aesthetic should also be taken into account during the design of the different systems and photonics could have a clear contribution.

However, there is actually not so much space for the car manufacturers and their suppliers to integrate all the different systems and functions in the vehicle. As an example for lighting, free space optics and bulky traditional optical components make integration of new systems tricky. In this context, nanophotonic technologies may have more and more opportunities to participate in design, functions and fabrication of future cars. For example, flexible organic light-emitting diode (OLED) displays [AKEDO06], laser projector, photonic sensors, smart windows and light fidelity (Li-Fi) based intra-/inter-vehicle communication [CAILE12] are presently investigated in automotive. Therefore, we must point out that photonics will not only

play a vital role in the current automotive research and development domain, but also will bring a technological revolution to the three main priorities of automotive innovation which are attractiveness, clean technologies and autonomous and connected vehicle [BARAT].

I.1.1 Brief history of automotive lighting and signalling systems

As one of the most representative lighting systems, lamps have been applied and integrated into automotive vehicles for the purpose of illuminate the roadway for the driver and increase the conspicuity of vehicle in order to be observed by the other drivers and pedestrians. The first affordable civil vehicle, the Ford Model T, came out about 100 years ago and has used carbide lamp for headlamps and kerosene lamp for tail lamp. The famous halogen sealed beam headlamp was then introduced and dominated the vehicle headlamp markets for several decades. In the USA, since the first joint IES and SAE² specification relating to optical performances of headlamps in 1918, the authority had formulated strict road safety laws and vehicle manufacture industrial standards to regularize the design and use of the lamps along with the home-use car's popularization and the new lamp technology's development.

In Europe, the first High-intensity discharge (HID) headlamps were introduced on production vehicles in 1991 [NEUMA94]. Comparing to the classic sealed beam headlamp, the HID lamp such as the Xenon lamp has obviously advantages in the commercial vehicle market, such as longer lifetime, greater durability and enhanced light-source performances (increased lumens, beam-pattern intensity, color temperature) [MOORE98]. Along with the development of LED technologies, more and more car manufacturers have chosen this new lighting source as the turning or stop signals and daytime running headlights since the beginning of 21st century. The LED lamps have long service lifetime, good vibration resistance, natural high energy-efficiency, compactness and fast response time. Recently, the high brightness LED-matrix headlamp (i.e.: blue LED with phosphor to generate white emission) systems have also been demonstrated in the luxury-car and sport car market for the purpose of its brighter, more homogeneous and more precise illumination of the apex of a bend, especially at night. In the future, the laser high beam based super white headlamp may also be equipped in the production cars since there are already some pioneers launched into the passenger car's market, as Audi R8 and BMW i8. The history of the headlamp's evolution is presented in Figure I.1.

² IES: Illuminating Engineering Society; SAE: Society of Automotive Engineers.

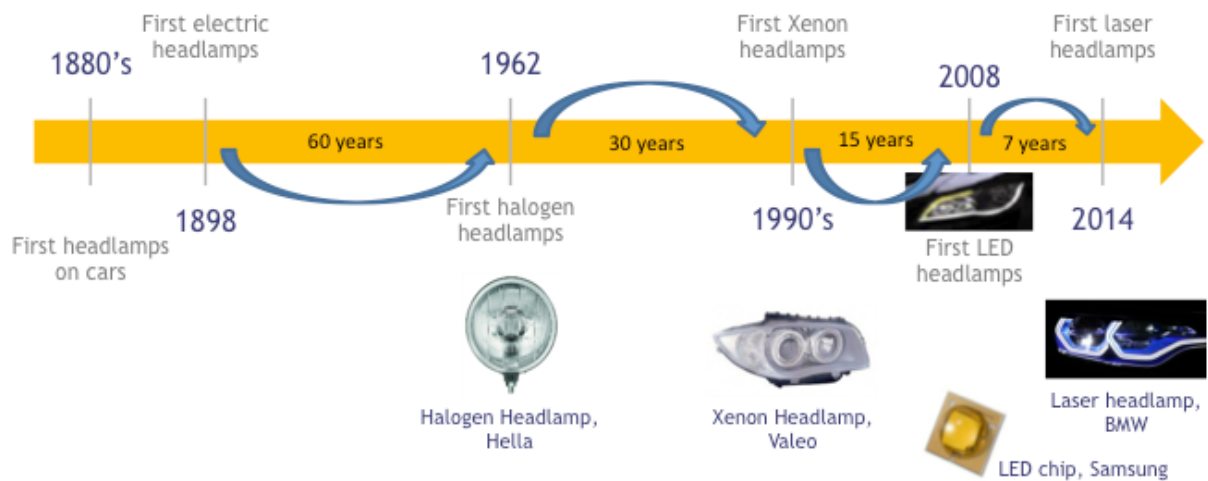


Figure I.1: Evolution history of automotive headlamps (taken from [COCHA15]).

Therefore, the automotive lighting system could be regarded as a key factor of vehicle's outward appearances and functional components to attract potential customers among the brutal competition of market.

I.1.2 Evolution of advanced driver assistance systems

According to a report from French analyst firm Tematys [COCHA15], the advanced driver assistance systems (ADAS) have been estimated to occupy about $\frac{1}{4}$ of automotive photonic market in 2018 and to keep fastest growth rate in the next few years comparing to the other embedded photonic applications including all of the interior and exterior lighting devices. The statistic diagram of the estimated automotive photonics market revenue in ADAS from 2013 to 2015 is presented in Figure I.2. Based on their analysis, this high growth of ADAS segment in the global vehicle supplier market could be driven by both automotive industry's dynamic market evolution and new customers' increasing demands of connectivity, security and ecology. As a result, there would be a huge opportunity for automotive photonic technologies in a vast range of engineering domains.

For the purpose of making progress in driver's amenity and car's security design, vehicle embedded vision systems become multifunctional to assist car driver. Generally speaking, there are mainly two kinds of vision systems, one for monitoring the exterior environment or health state of the driver and the other for displaying vehicle and travel information. Several

cameras are already integrated at different position of vehicle, such as reversing camera, 360° surrounding cameras or front camera to detect obstacles. Usually visible cameras are helpful to observe easily the blind spots from driver’s point of view, in order to make reversing easier in avoiding collision with the obstacles or pedestrians, or to call attention to keep a safety distance from the other vehicles [XU00, US6115651(A), US6175300(B1)]. Infrared cameras are also used for a specific usage, like night vision and animal or pedestrian detection [US5001558(A), OMALL10]. On the other hand, there are also some TFT screens installed besides the dashboard to display vehicle’s information, GPS-guiding map or even Multimedia Entertainment Systems (MES) interface. For some business or luxury class models, each passenger has his own interactive display screen. Nowadays, the Head-Up Display (HUD) technology has been generalized to medium and upper class vehicles. The HUD system uses an additional semi-transparent mirror or the windshield as an interface to project navigation information in the field of view of the driver at a distance around 2 m. At last, future of HUD systems would be “augmented reality systems”. These systems would project navigation information at a distance around 20 m avoiding accommodation and convergence problems of the driver. The challenge is then to make a compact system, which can be integrated in a cockpit.

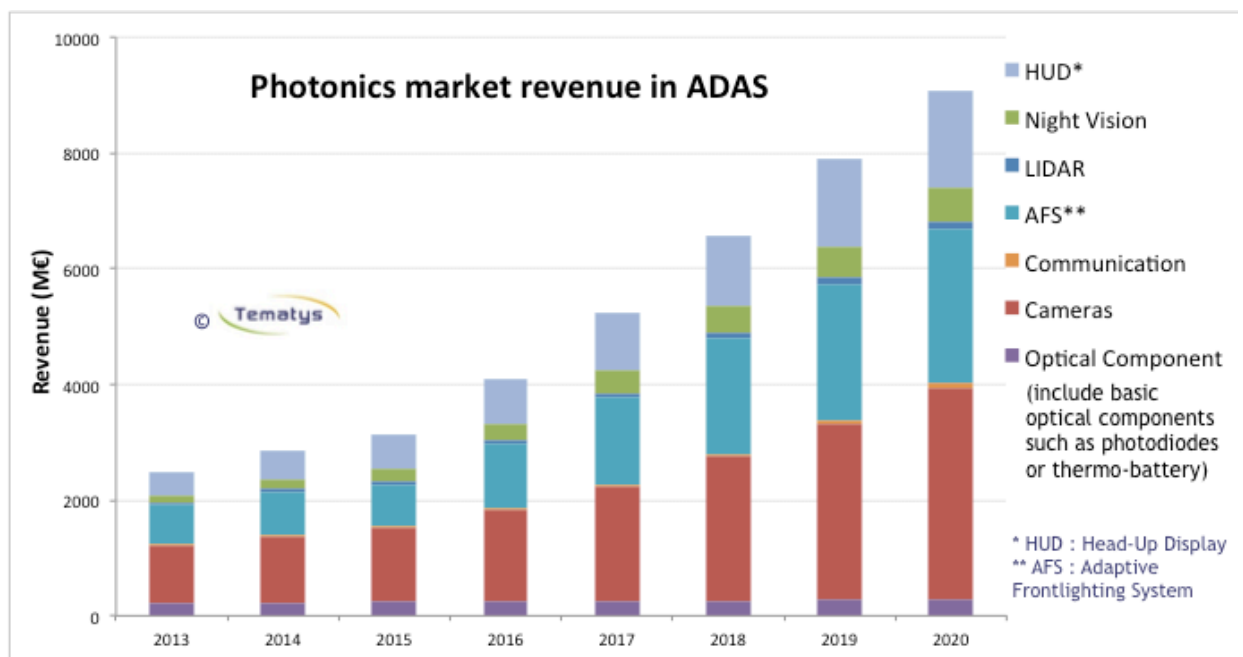


Figure I.2: Estimated photonics market revenue in ADAS by technology from 2013 to 2020 (taken from [COCHA15]).

I.2 RESEARCH BACKGROUND

Since we have already reviewed the mainstream applications of photonics in the automotive market, we will start with an introduction to the research background, which is related to our embedded innovative holographic signalling project based on the collaboration between the scientific division of PSA Peugeot Citroën and photonic department of Institut d'Electronique Fondamentale, a laboratory of Université Paris-Sud.

I.2.1 Targeted embedded holographic signalling system

Our research project is based on a rear-signalling device patented by PSA Peugeot Citroën [FR2949725(A1)]. This system has a holographic image generating unit, independent of lighting and signalling functions, which creates at least 2 registered holographic images visible by observer(s) located at exterior of vehicle (i.e.: driver in a following vehicle). To simplify the explanation of the operation principle of such a device, we consider here one of the device's uses when it shows a possible danger to the following car's driver in a conventional forward moving process. We suppose that the holographic image is always scattered in the upward direction, and there are at least 2 different recorded images, which could be scattered in two different angles. The schematic diagram is presented in Figure I.3.

In the first case shown in Figure I.3.(a), once the following car's driver keeps a safety distance, the driver's field of view has not enter into the effective zone of reconstructed holographic image due to its limited diffusion angle, which has been fixed during the holographic plate's record. Therefore, driver in the following car could not observe the holographic warning image. Once the following car moves closer and reaches the safety distance (see Figure I.3.(b)), driver's field of view intersects diffusion cone of the holographic image and a holographic image between the two vehicles can be seen by the driver. At last, when the following car comes closer to the leading one, the driver will observe a different image generated in a different diffusion cone (see Figure I.3.(c)). Holographic plate is composed of two different transmission holograms which are diffraction gratings containing whole information of recorded objects (i.e. "!" and "STOP" logo images).

To go further, PSA has also published another patent [FR2995269 (A1)], in which there is a sensor used to detect inter-vehicle distance and, in a dangerous case, the warning system can be turned on and a 3D holographic imaging system will emit a series of warning symbols.

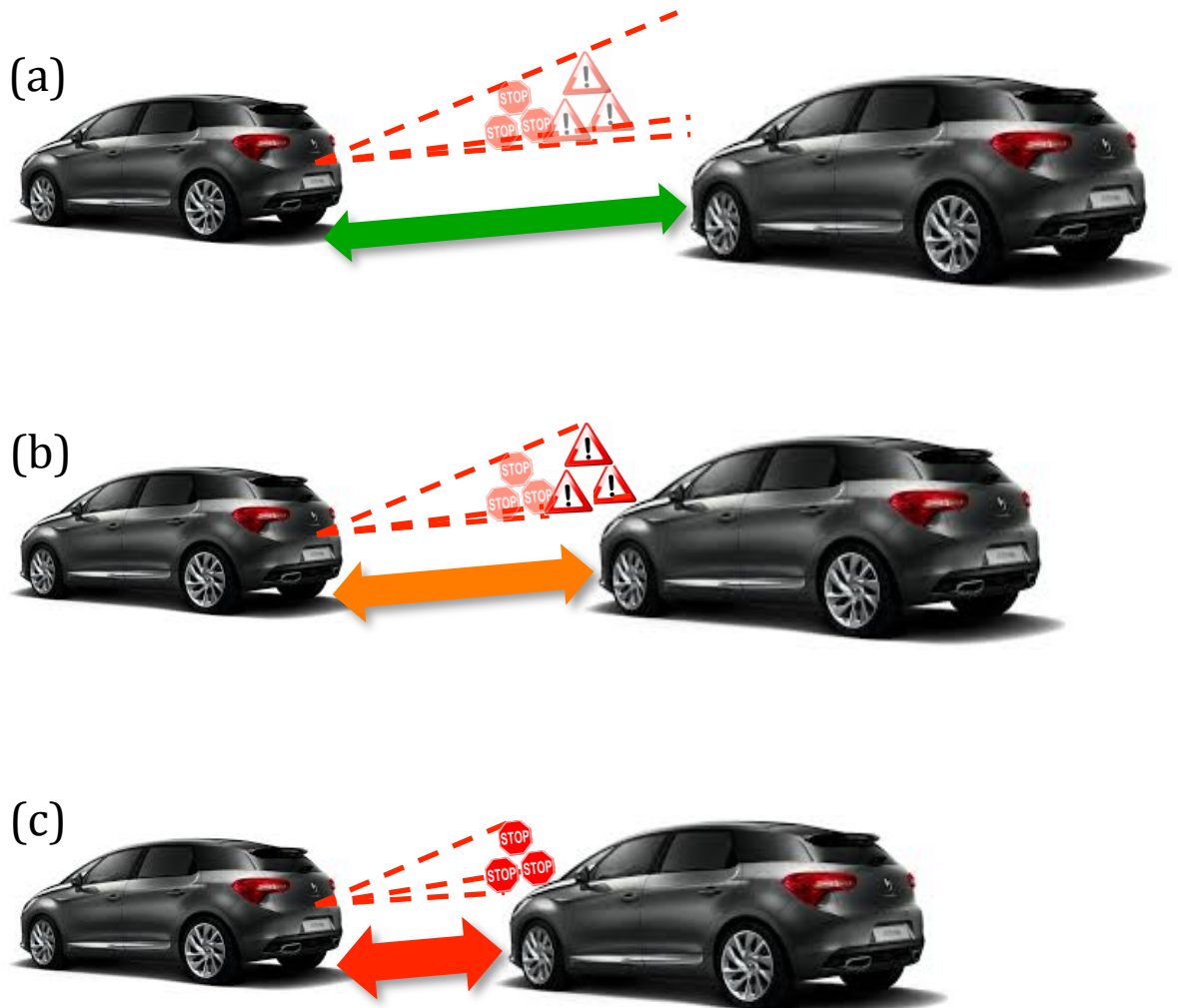


Figure I.3: Schematic diagram showing the principle of the PSA Peugeot Citroen rear signalling device: (a). Safety mode: when the safety distance is respected, there is no holographic image observed; (b). Warning mode: when the distance is reduced close to the safety distance, the first holographic warning pictogram is activated and observed; (c). Danger mode: when the distance continues to decrease far inferior to the safety distance, the second holographic image including a serial of “STOP” pictograms is observed.

I.2.2 Restitution principle of predetermined 3D holographic image

The holographic image reconstruction mentioned in the signalling device is the same as a conventional transmission hologram [BENTO69]. The principle is shown schematically in Figure I.4. A light beam S illuminates pattern-contained holographic plate H. This pattern is a diffraction grating with fringes placed horizontally (in the width of the holographic plate) and contains all the information of the real object (position, form...).

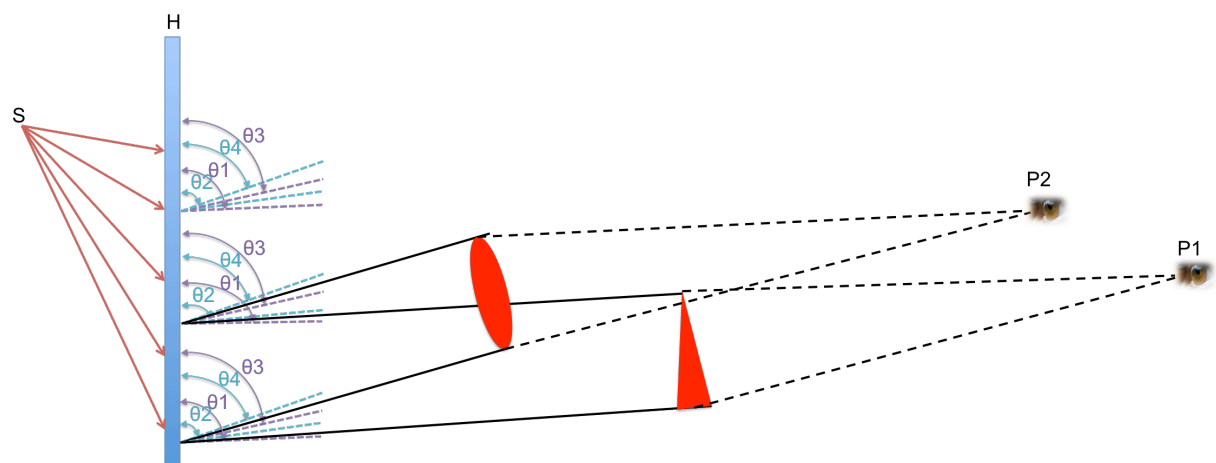


Figure I.4: Schematic illustration of transmission hologram principle for generating two different images as a function of observer's angular position. S: reconstructing coherent light beam; H: hologram plate; P1/P2: observer position.

In order to have two different holographic images visible in two different diffusion cones with the same restitution beam, the patterns have to be fixed during recording by realizing interferences between the reference beam and the two object beams. The two objects beams come from reference beam passing through the two objects, which are placed at two different places and angles from the holographic plate.

To be able to reconstruct correctly holographic images, the light beam S has to be identical to the reference beam used during holographic recording process. Caution should be taken if the restitution beam isn't monochromatic. Due to the dispersion effect when passing through diffraction grating, the diffracted beam could be split into several sub-orders and finally leads to a blurring effect for the observer of holographic image. In our case, the restitution beam S has to be monochromatic at 633 nm, uniform for all the holographic plate and with an angle of 56° to the normal of the holographic plate.

I.2.3 Problematical analysis of existed holographic system

We firstly present in Figure I.5 a schematic illustration of the existed holographic system consisting of a 633 nm laser source, a series of cylindrical lens, a holographic optical element and the pre-fabricated holographic plate [FR2949725(A1)]. This first restitution system is bulky because it requires a large inner space close to 1 m to expand initial light beam from the laser source and also generating the uniform and coherent restitution beam.

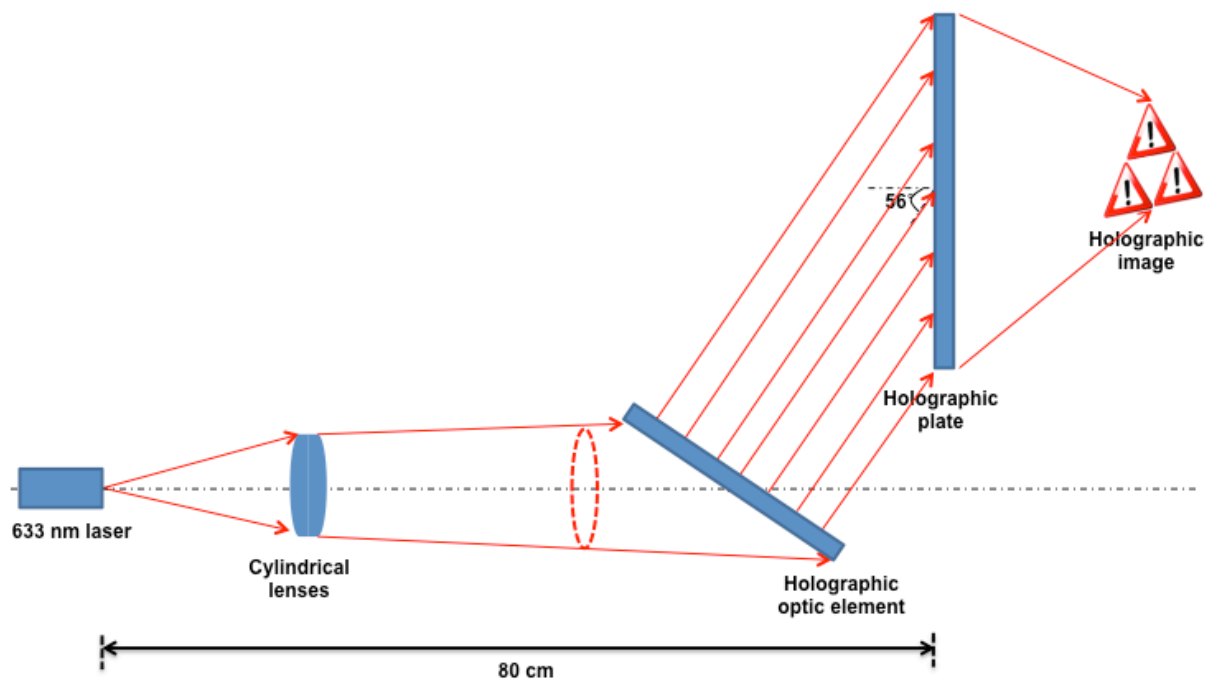


Figure I.5: Schematic illustration of the existed conventional optical holographic imaging system.

Furthermore, as the visibility of the different holograms is dependent on the size of the holographic plate (i.e.: 40 cm × 60 cm) and as the observer will be far from the holographic plate, the decrease of the volume of the whole system has to be done by decreasing the volume of the holographic reconstruction system, which generates the targeted beam. In this situation, we are willing to find a solution in order to compress the expanding optical path in the free space and even replacing the conventional optical components, such as mirrors and lenses.

In this context, *Gonçalves and al.* patented a technical design to compact the system in [FR3005011]. These solutions propose to replace the straightforward optical path between the cylindrical lens system and the holographic optical element (shown in Figure I.5) by a multi-stage folded light path. This light path can be achieved by two solutions. As shown in Figure

I.6.FIG1, the first solution is to set in space a series of total reflection mirrors, in order to fold the straight optical path in a short distance.

The second solution is shown in Figure I.6.FIG2. The idea is to add a parabolic reflection mirror following the punctual light source in order to collimate the beam. Then, a series of beam splitters in a row is added with different reflection/transmission coefficients to deflect successively the incident parallel beam to the holographic plate.

In conclusion, the auto-embedded holographic reconstruction system can be realized by using the traditional optical component. These solutions are interesting and reduce the size of the initial system but we think that integrated photonic system could give a breakthrough by reducing more the size and allow mass production for this system in the future vehicles.

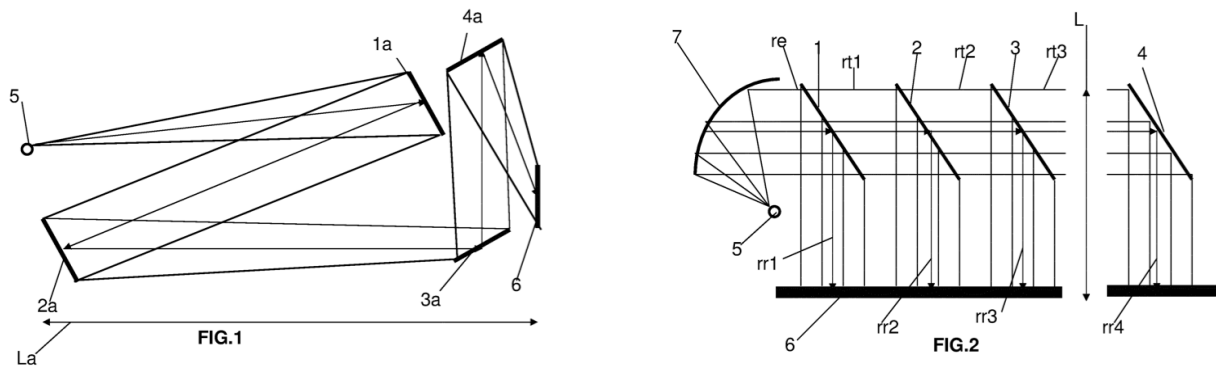


Figure I.6: Schematic illustration of the folded optical path design within a compact holographic illumination system. In FIG.1, 1a, 2a, 3a and 4a are total reflection mirrors; in FIG.2, 1, 2, 3 and 4 are ratio-tunable beam splitters and 7 is the parabolic reflection mirror; In both the figures, 5 and 6 are respectively the punctual coherent light source and holographic plate.

I.3 OBJECTIVE AND PLANNING OF RESEARCH

Inspired by the rapid development of the nanotechnologies and nano-optics, we are intended to look for an advanced solution to replace the previous restitution system within the framework of this collaboration research project between PSA and IEF.

I.3.1 Panorama of targeted holographic illumination system

Our ambitious research project of developing compact illumination system to reconstruct holographic image could be divided into 3 main subsystem's study. A schematic diagram of our targeted global system is presented in Figure I.7. By the way, the mentioned prototype of such a holographic signalling system has recorded the holographic patterns consisting of two different images with an incident angle of 56° by using 632.8 nm laser, and the necessary power density for reconstructing illumination light beam should be around 16 W/m^2 by taking in account transmission coefficients of the holographic plate and rear windshield and photometric regulatory requirements of stop lamp.

The 1st subsystem (typically Figure I.7.(a)) concerns visible-wavelength photonic integrated circuits (PICs) aiming at distributing a monochromatic coherent light source into a large surface by using optimized couplers and waveguides to keep the same intensity. In each sub-waveguide branch, specific optical transverse mode(s) (i.e.: TE mode) have to propagate with the minimum losses on top of a buffered silicium or glass wafer. The distribution surface of all the optical waveguides will be several cm^2 and ideally will match the size of the holographic plate, which has an around square shape.

The 2nd subsystem (zoom on Figure I.7.(b)) should be involved in the re-emission of guided optical waves. Each emission unit should be able to control angle (or direction), intensity and phase of the emitted beam, and will be positioned on the waveguides in order to illuminate the hologram plate under the conditions defined above and then reconstruct the holographic images.

The 3rd subsystem (shown in Figure I.7.(c)) aims at compensating the optical losses due to the material absorption and scattering along the relatively long dielectric waveguides and reemission system.

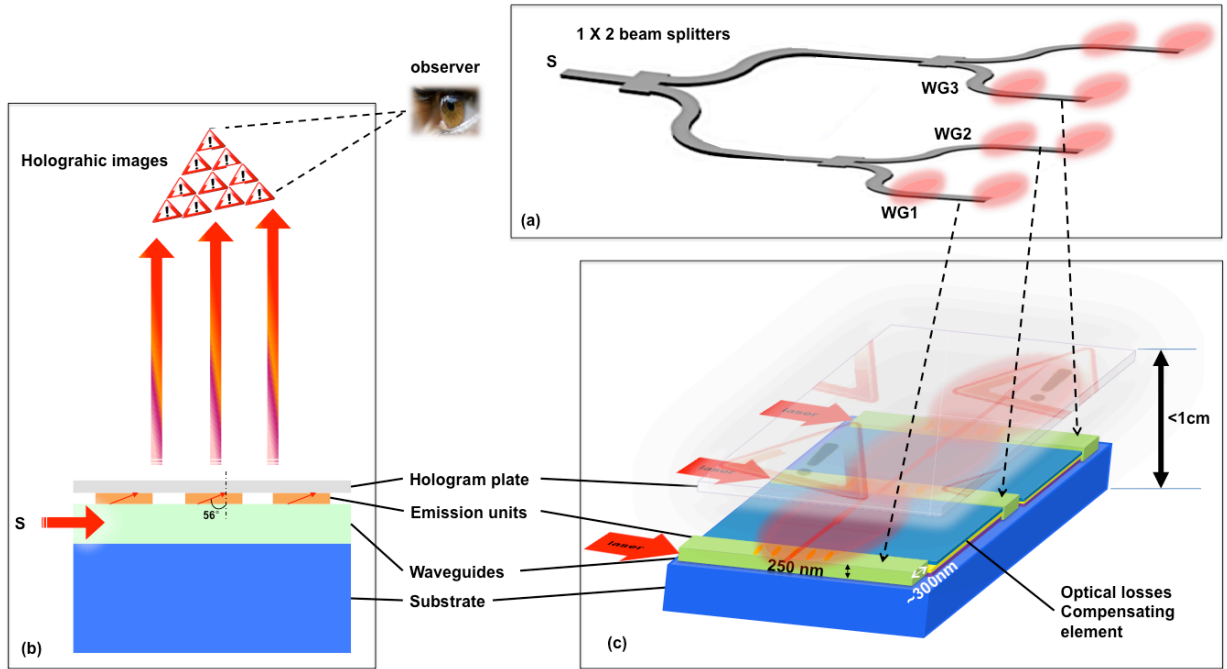


Figure I.7: (a). Schematic diagram of the 1×2 cascaded beam splitters and the re-emitters positioning on waveguides. (b). Schematic diagram of holographic image's reconstructing by our targeted surface illumination system. S is the initially used coherent 633 nm laser source. (c). PIC example overview for the surface illumination system, zoom on the nano-emitters section.

I.3.2 1st subsystem: *visible PICs*

To our knowledge, Si_3N_4 platform has a good compatibility and functionality of visible-wavelength PICs research and development due to its transparency, low material loss and nonlinearity within the whole visible band. Therefore our research interest of the 1st subsystem has concentrated on the Si_3N_4 waveguides to design and fabricate a uniform beam splitting PIC device shown as follows:

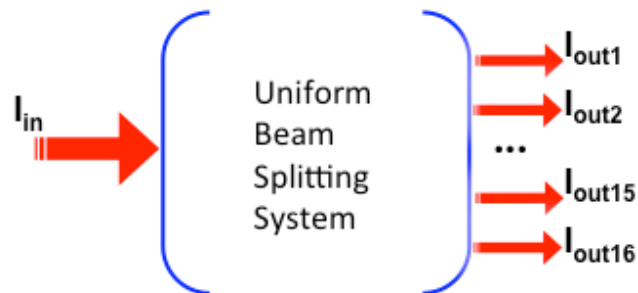


Figure I.8: Schematic diagram of the expected visible light beam splitting system operating at 633 nm.

The (single) input light source is supposed to be a 633 nm laser beam. We are intended to design a surface-geometry 1×16 beam splitter, which can be itself composed of several 1×2 or 1×4 splitters. At the end of each of the 16 outward waveguides, the split power should be identical. Meanwhile, the whole splitting system is expected as compact as possible.

Based on these requirements, the development work of this 1st sub-system has included several steps, presented within 3 chapters. After the state of the art presentation of Si_3N_4 platform and waveguides operating at visible wavelength in Chapter II, we will focus on the design and optimization of different Si_3N_4 passive devices, such as straight and bent waveguides, as well as optical splitters. This design work will be presented in Chapter III. Finally Chapter IV will be dedicated to the experimental part, including cleanroom fabrication and optical loss measurement of Si_3N_4 waveguides samples at visible wavelength.

1.3.3 2nd subsystem: *controllable nano-emitters*

The surface distributed emitters' array is used to illuminate the hologram plate in a coherent way. Since the human eye has normally a maximal theoretical resolution of 50 cycles per degree (a 350 μm line pair at 1 m) [RUSS06], we suppose once the interval of two neighboring emitters is inferior to a certain limit, from macroscopic viewpoint, the generated holographic images would be continuous and the blind points due to the spacing of emitters would not be detected by observer's eye. So the emitters' array should be basically of high density and uniform distribution. Since the optical power is split into 16 waveguides, there will be at least 16 emitters. We could easily control the lateral distribution of emitters by equally spaced waveguides, however caution must be taken for the arrangement of emitters in the main propagation direction along the waveguides. A schematic diagram of the guided optical beam's intensity variation after passing through an emitter array is presented in Figure I.9.

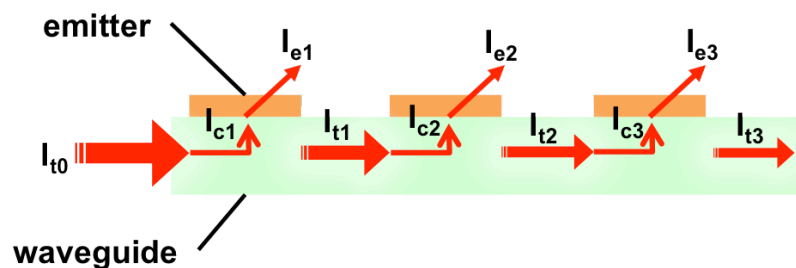


Figure I.9: Schematic diagram of emitters array arranged along the waveguide.

We define the input coherent light source's intensity as I_{t0} , and the coupled intensity, transmitted intensity and effectively illumination intensity affected by the i^{th} emitter as I_{ci} , I_{ti} and I_{ei} . The i^{th} emitter's coupling efficiency could be written as:

$$\eta_{ci} = I_{ci}/I_{t(i-1)} \quad (\text{I-1})$$

and its effective illumination efficiency could be written as:

$$\eta_{ei} = I_{ei}/I_{ci} \quad (\text{I-2})$$

and the transmission through the i^{th} emission unit is:

$$T_i = I_{ti}/I_{t(i-1)} \quad (\text{I-3})$$

The i^{th} emitter's effective illuminated intensity could thus be presented as:

$$I_{ei} = \eta_{ei}\eta_{ci}I_{t0} \prod_{j=1}^{i-1} T_j \quad (\text{I-4})$$

At the same time, the propagation attenuation passing through the i^{th} emitter is:

$$A_i = 1 - T_i - \eta_{ci} \quad (\text{I-5})$$

The optical losses could be due to material absorption, waveguide scattering and so on. As shown in (I-4), to keep each emitter's effective emission identical in intensity, in phase and with the same angle, all of its precedent emitters are involved. Limited by the unavoidable optical losses due to the materials for each emission unit, we need to design different parameters of each emitter to vary its coupling efficiency and emission efficiency. Meanwhile, the attenuation due to each emission unit should be optimized as small as possible in order to increase the number of the emitters.

Based on the experiences of our research of nanoparticle chain based plasmonics, we choose metallic optical nano-antenna as our 2nd subsystem's research target, instead of conventional Bragg grating based optical couplers. Indeed, it is possible to control the coupling efficiency, the emission efficiency and partially its directionality by slight design modifications of metallic nanoparticle chains. At first, we theoretically studied the optic-plasmonic coupling between the dielectric waveguides and the metallic nanoparticle (MNP) chain. At the same time we studied the emission properties of nanoparticle based optical antennas. Then we designed and simulated several plasmonic waveguide configurations consisting of Au or Ag made MNP chain and Si₃N₄ waveguides by using finite difference time domain (FDTD) numerical calculation method. From the transmission's viewpoint, we

analyzed the coupling efficiency as a function of the dimensions and materials of nanoparticles. A logical trend has been found to optimize the coupling efficiency. In the thesis, we will present in Chapter V the theoretical study concerning the MNP chain hybridized with the dielectric waveguides.

1.3.4 3rd subsystem: *organic amplifier*

In collaboration with our project partner in Wuhan National Lab for Optoelectronics, who is specialized in the domain of organic light emitting diode (OLED), the research work of optical amplifier made by organic materials has been launched at the same time. Since most of work has been independently carried on in China, no presentation of the progression and achievement of organic compensator's research would be included in this thesis.

1.4 CONCLUSION

In this chapter, we presented our research objectives of an auto-embedded holographic illumination system [WO2014106584(A1)]. We started with a brief review of photonic applications in the automotive domain, and then introduced the automotive industrial application background of our research target. We showed the typical PIC (photonic integrated circuit) scheme that we proposed in order to develop a compact solution for the holographic illumination system. The whole PIC includes the photonic circuit “backbone” (i.e. the array which splits the light into 16 waveguides), controllable emitters, and organic amplifiers. These different subsystems were then detailed, together with the manuscript outline and content presentation. Especially, within this very ambitious project, the achieved results, which will be presented here, include the visible light waveguide design, fabrication and test, the design of power splitters and of bent waveguides, as well as the evaluation of the metallic nano-antennas (nano-emitters) coupling with waveguides.

CHAPTER II: INTRODUCTION TO THE Si_3N_4 WAVEGUIDES PLATFORM

Since compact holographic illumination systems require visible-wavelength PICs, $\text{Si}_3\text{N}_4/\text{SiO}_2$ based platform has been considered as a good candidate for its transparency and low material loss and nonlinearity within the whole visible band. In this chapter, we will firstly review the evolution of the silicon nitride based integrated optics over the last four decades, especially some milestones in the progress of Si_3N_4 waveguide-related research. And then, we will target the performances of the Si_3N_4 2D waveguides used for planar integrated circuits in the visible wavelengths range. At the end, we will present the state-of-the-art research results in this domain.

II.1 CONTEXT OF SILICON PHOTONICS

The high-density Si-based integrated optics has been one of the hottest optoelectronic and microelectronic research topics in recent years, since the fabrication facilities of the silicon photonics platforms are compatible with the CMOS technology, which has reached highly mature, robust, accurate and reproducible industrialization. At the early stage of the development of the PICs, telecom industry piloted the research on silicon photonics using the infrastructure originally dedicated to microelectronic processing [BESTW99]. Thus so many novel high-quality PICs-made photonic devices operating at telecom wavelengths for the high-speed and wide-bandwidth data transmission system have been reported. The basic passive components of these integrated devices include low loss waveguides [BULLA99], fiber-chip couplers and power-splitters [LEE01], circulators [PINTU13], multiplexers [CHANG10], integrated optical Bragg gratings [MURPH01] and ring resonators [GONDA09, TIEN11]. However, some ring resonators have been used in other specific functional devices, such as optical filters [LITTL97, PRABH09], the others could also be hybridized with III-V materials (i.e.: GaAs, InP etc.) to realize active components, such as Raman amplifiers and lasers [DOYLE08, RONG08], hybrid III-V/silicon lasers [BOWER10, FANG12], photodiodes and photodetectors [CHEN09, DOYLE10, FARD14], and optoelectronic modulators [TANG12, WANG13]. Researchers from Glasgow showed a convincing general schematic of on-a-chip photonic circuits (see Figure II.1), which consists of a complete panel of Si-based integrated

components: low loss waveguides, fiber-guide couplers, beamsplitters, MMIs, photonic crystal optical non-linear devices, delay lines, Mach-Zehnder phase shifters, high-Q micro-ring cavities, and some other active components, such as Ge-on-Si single photon avalanche detectors, quantum confined Stark effect modulators, strain induced long wavelength emitters and photodetectors, semiconductor lasers and NIR LEDs.

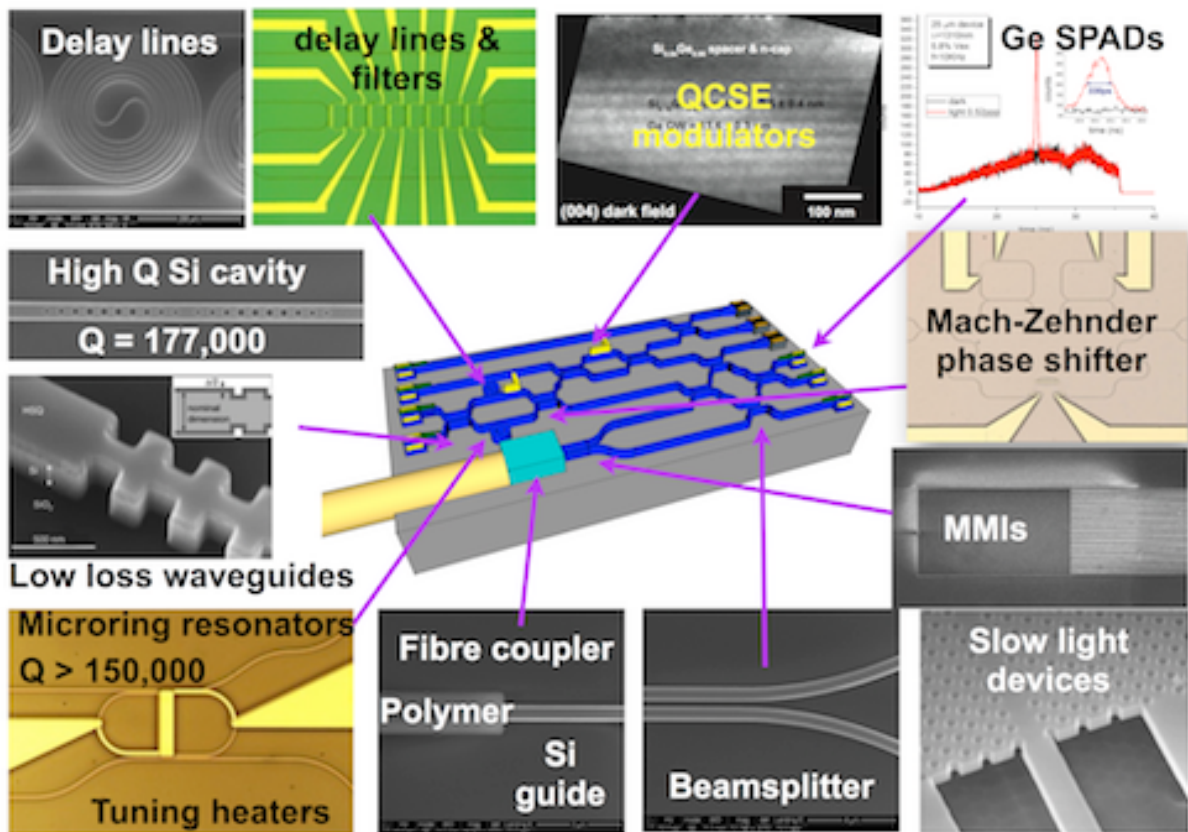


Figure II.1: General schematic of Si-based complete photonic circuits, taken from Prof. Douglas Paul’s webpage from The Semiconductor Device Group of University of Glasgow (taken from [PAUL]).

In general, the silica-based or silicon nitride-based PICs are used as passive devices to realize routing and switching functions, in which the guide core is mainly made of doped silica (p-Si or n-Si), silicon oxynitride (SiON) or silicon nitride (Si₃N₄) surrounded by a silicon dioxide (SiO₂) upper and lower cladding. On the other hand, the platform made of the III-V materials is well suited for the transceiver application, which consists of various active photonic integrated components, such as semiconductor lasers and photodetectors [HECK14].

We list below an overview table (see Table II-1), in which the goodness and weakness of different materials chosen to fabricate mainstream platform of PICs were summarized

qualitatively. As seen in Table II.1, none of the platforms made by single material can cover all the functionalities, except for the platforms made of hybrid silicon. Anyway, to be compatible with visible light operation, the main solution is based on ultra-low loss waveguides in silicon nitride based platform which helps enlarging the operation wavelength range cross the whole visible band, and down to the UV wavelengths [ROMER13, SUBRA13]. Many passive functions, which were developed for near-infrared PICs in silicon or III-V guiding structures, can be then transposed at visible light by using silicon nitride waveguides with adapted dimensions.

Table II-1: Qualitative overview³ of the main PIC platforms (data taken from [FANG2012]).

	III-V (i.e.: INP)	Silica	Silicon	Hybrid Silicon
Lasers	+++	NA	NA	+++
Photodetectors	+++	NA	++	+++
EO modulators	++	NA	+	++
Passive devices	+	+++	++	++
Wafer-level packaging	NA	+++	+++	+++
Electronic SoC and SiP integration	NA	+++	+++	+++

II.2 PICs FOR VISIBLE APPLICATIONS

Comparing to the huge quantity of academic publications and industrial products in the domain of silicon photonics for fiber-optics communication system (i.e.: operation wavelength within O-band or C-band) in the last decade, we have barely seen PICs-related research attaching equal importance to the visible range applications. In this part, we will review the research progress in the domain of visible-band integrated optics, especially the development of some types of passive devices, which have been used to guide the visible light in the on-chip PICs.

³ NA = not available; + = possible; ++ = good; +++ = best option; SoC = system on a chip; SiP = system in a package.

II.2.1 Bottleneck of the development of visible PICs

Firstly, at the beginning of the PICs development, the immature sub-micron level cleanroom techniques seemed to be an obvious bottleneck for the visible-band devices fabrication due to the limit of the conventional optical lithography resolution. On one hand, because the minimum feature size of the visible photonic integrated devices is smaller than the one of telecom devices. And besides, we need sometimes to limit the waveguide cross-section size for the single-mode or low-order modes in specific application. On the other hand, the resolution limit of the projection lithography system is determined by the Rayleigh's equation [KLEIN70]. The theoretical minimum resolvable feature, which is presented by the resolution R and the corresponding depth of focus (DOF), are given by the equations:

$$R = \frac{k_1 \times \lambda}{NA} \quad (\text{II-1})$$

$$DOF = \frac{k_2 \times \lambda}{NA^2} \quad (\text{II-2})$$

where λ is the lithographic exposure wavelength, NA is the numerical aperture of the optical system, and k_1 and k_2 are constants that depend on the specific resist material, process technology and image formation technique used. In order to fabricate a smaller component, we need a higher resolution of the lithography system, thus a shorter wavelength and a larger numerical aperture of the optical lens system. Generally speaking, the minimum feature size can be obtained with almost the same geometric dimension as the wavelength of exposure light [OKAZA91]. However the requested optical lens system needs a relatively large numerical aperture (typically $NA \approx 0.5$), so the DOF becomes very small, and the exposure process becomes sensitive to slight variations in the thickness and absolute position of the resist layer [ITO00]. That's why the lithography with state-of-the-art resolution enhancement technologies becomes the key factor of the visible PICs development.

The second reason could be due to mainstream PICs platform material's optical properties. Since not the entire core materials of Si-based PICs platforms could transmit visible light, i.e.: SOI waveguides and III-V doped waveguides, we don't have so many candidates of waveguide materials operating at a visible wavelength. Most people prefer silicon nitride to the other dielectrics, thanks to its transparency and considerably higher refractive index (typically $n=1.8-2.0$) than the popular cladding material SiO_2 (typically $n=1.4-1.5$) in the visible-band range (from 400 nm to 700 nm). However, the Rayleigh scattering in this sort of dielectric platform becomes more important for the visible light than

the IR light used for telecom devices because of the existence of impurity introduced by CVD process and fabrication defects. We suppose the average feature size of these impurities is much smaller than the light source wavelength in the PICs, so the Rayleigh scattering can be presented by the following expression:

$$\frac{I_{scat}}{I_0} = \frac{K}{\lambda^4} \quad (\text{II-3})$$

where K is a constant depends on the size and optical properties of the small impurities and the refractive index of the propagation medium, I_0 and I_{scat} the beam intensity of incident light and the scattered light, respectively [YOUNG81]. So the propagation losses due to small impurities scattering are much higher at a visible wavelength than the telecom wavelengths.

Thirdly, due to the heavy market demand of telecom terminal devices, the interest of researchers in the innovation of routing and switching PICs at visible wavelengths hasn't been extensively encouraged among the academics and industrials and more investments have been put into the R&D for on-a-chip PICs devices at telecom wavelengths (from 1.3 μm to 1.6 μm). In fact, as we explained in the first chapter, for the automotive industry, the visible light dominates the embedded lighting and vision system, especially the red part of the visible range for rear lighting and signaling functions. In this situation, our entire research project is focused on the integrated photonics operating at the wavelength of 633 nm. We will review in the following part several pioneers' original works in this domain, including materials choice, waveguide's design, fabrication and characterization.

II.2.2 History of 1D Si_3N_4 slab waveguides

As one of the most popular platforms of integrated optics for visible application, some suitable pairs of dielectric waveguide-buffer materials, such as silicon nitride core-silicon dioxide cladding have been deeply studied for a couple of years. The early research work on silicon nitride waveguides used for visible light propagation could date from 1977. *Stutius et al.* demonstrated a planar waveguide model with Si_3N_4 layer deposited on a SiO_2 buffer layer [STUTI77]. A classic prism coupler has been used to couple the red light into the Si_3N_4 layer (see Figure II.2) [HARRI70].

By the way, at that moment, a rutile (TiO_2) prism has been largely generalized as a relatively high efficient light coupler thanks to its high refractive index, large birefringence and high dispersion at visible wavelengths among natural crystals. Once a suitable incident

angle has been chosen, the light will penetrate into the core layer to realize inner total reflections propagation. The order of the transversal electromagnetic modes in the planar waveguide could be easily selected by choosing different incident angle, and different corner angle or refractive index of the rutile prism corresponding to specific wavelength of the incident light beam.

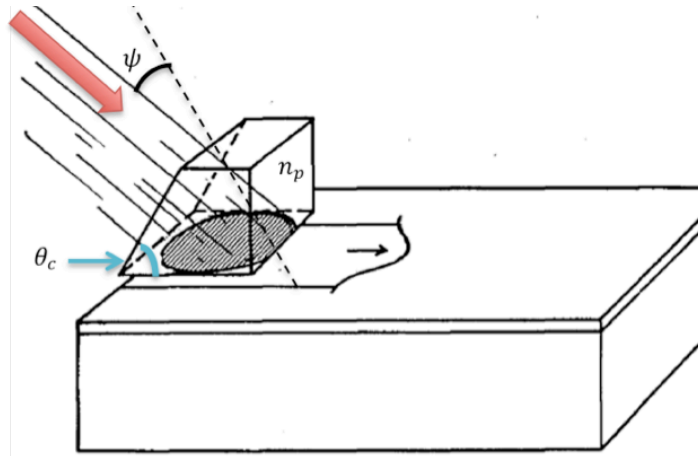


Figure II.2: Configuration employed to couple a collimated beam into a thin film through a tunneling layer between the prism and film (taken from [HARRI70]).

Three different chemical vapor deposition (CVD) techniques have been applied to deposit the Si_3N_4 film on a thermally grown SiO_2 buffer layer: Plasma-Enhanced CVD (PECVD), atmospheric pressure CVD and Low-Pressure CVD (LPCVD). But only the LPCVD sample has been characterized thanks to its excellent fabrication quality, while the two other samples contained minute cracks, which led to undesirable reflections or intolerable termination of the waveguide. These minute cracks were due to the residual stress in Si_3N_4 film, and *Irene et al.* have studied this issue by analyzing the Si_3N_4 film grown onto a (111) oriented Si wafer at the same time [IRENE77]. According to their report, the large tensile stress of Si_3N_4 films were composed of thermal and intrinsic stress components. The intrinsic stress was larger for room-temperature deposition; meanwhile, the thermal stress would increase with higher deposition temperatures. But once deposition temperatures increased, the intrinsic stress would decrease. Therefore, the total tensile stress was lower for higher film deposition temperatures, which permitted more movement on the surface and some relaxation of the stress. In fact, for a visible waveguide, a buffer SiO_2 layer should be always needed between the Si_3N_4 film and

the Si wafer, the tensile stress at the interface of Si₃N₄ and SiO₂ would depend on the thermally grown SiO₂ film's properties as well.

Due to the differences of deposition techniques, the measured refractive index of each Si₃N₄ film sample at 632.8 nm by ellipsometry is 2.1, a value between 1.95 to 2.0 and 2.01, respectively. The equivalent index n_{eq} of the propagated mode can be theoretically calculated by deducing the formula of propagation constant (β) as follows:

$$n_{eq} = \frac{\beta}{k_0} = n_p \sin(\arcsin\left(\frac{\sin\psi}{n_p}\right) + \theta_c) \quad (\text{II-4})$$

where k_0 is free-space wavenumber, n_p the prism index, θ_c the prism corner angle and ψ the incident angle measured from the prism normal (see Figure II.2). The comparison of the calculated and measured equivalent index of the fundamental and low-order TE and TM modes in such a Si₃N₄ planar waveguide has been presented in Figure II.3 to show the incident light's wavelength and waveguide's geometry dependence.

In this experimental set-up, TE₀, TM₀ and TE₁ modes correspond to the prism (corner angle = 30°) coupling angle of 35.3°, 43.8° and 8.75°, and the refractive index of the Si₃N₄ was assumed to vary from 2.03 to 2.055 when the light wavelength decreases from 632.8 nm to 470 nm [REIZM67]. As seen in Figure II.3, TE₀ and TM₀ modes with relatively high refractive indexes are more confined than the TE₁ mode with a lower equivalent index, which is rather close to the one of SiO₂. Meanwhile, the equivalent indexes of high-order modes have lightly stronger wavelength dependence. Furthermore, they compared also the optical losses for different transversal modes by measuring the net waveguide attenuation at 632.8 nm and calculating the radiation losses (see Table II-2).

As we can see from the Table II-2, due to the mode leakage into the SiO₂ layer, the optical losses for each mode have a remarkable increasing for the thinner buffer layer waveguide, in which the optical modes of higher order could not be guided. However, if the buffer layer is thick enough, so as to isolate guided light wave, Si₃N₄ should be a very good choice to fabricate a visible-band waveguide, even the performance for the propagation of the fundamental TE mode should be better.

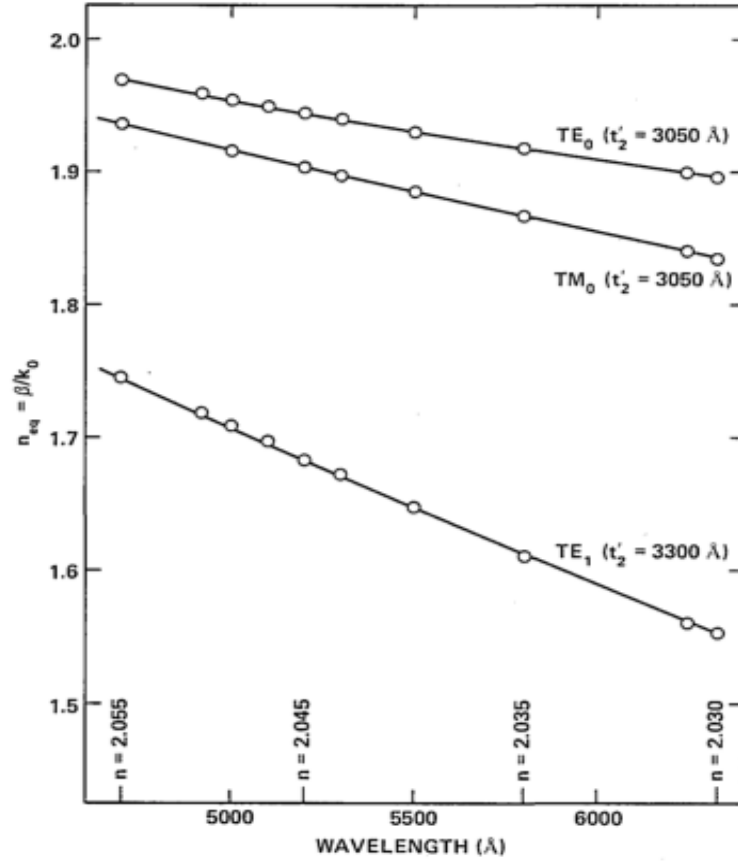


Figure II.3: Wavelength dependence of the measured (presented by circles) and calculated (presented by lines) propagation constants of some basic transversal EM modes in the Si_3N_4 waveguide of different thickness deposited onto a SiO_2 buffer layer of 816.5 nm (taken from [STUTI77]).

Table II-2: Optical properties of Si_3N_4 planar waveguide deposited by LPCVD and supported by thermally grown SiO_2 buffer layer of different thickness (data taken from [STUTI77]).

Mode	SiO ₂ buffer layer of 816.5 nm		SiO ₂ buffer layer of 400 nm	
	Calculated radiation losses	Measured net attenuation	Calculated radiation losses	Measured net attenuation
	α_{cal} (dB/cm)	α_{exp} (dB/cm)	α_{cal} (dB/cm)	α_{exp} (dB/cm)
TE ₀	≈0.0001	<0.1	2.7	3
TM ₀	≈0.0001	<0.1	7.8	6.3
TE ₁	4.2	6	380	NO
TM ₁	≈ 1700	NO ⁴	NA	NA

⁴ NO: Acronyms for *Not been Observed*.

Since the CVD techniques have also been developed very fast with the demand of high purity films, plasma-enhanced CVD (PECVD) technique was used to fabricate the Si_3N_4 film waveguide on a thermally oxidized Si substrate and became more and more expected and reliable. *Sriram et al.* presented their Si_3N_4 waveguide deposited by PECVD in 1983. A capacitively coupled glow discharge plasma in a reactant gas mixture of SiH_4 , NH_3 , and N_2 performed a deposit of a Si_3N_4 layer of 935 nm at relatively lower temperature of 200°C to 300°C , over $1\ \mu\text{m}$ thermally grown SiO_2 isolative layers on the Si substrate. Thanks to the low-substrate temperature, they succeeded to realize the Si_3N_4 planar waveguide on preprocessed silicon buffer layer without affecting the diffusion profiles that cause detector crosstalk or other device degradation [SRIRA83]. The same scattered light top-view method was applied to the optical loss measurement, just like the precedent experiment, which is based on the assumption that the observed scattered light intensity from the top of the waveguide came directly from the propagating light in the planar Si_3N_4 waveguide, and there should be a strict linear relation between these two variables of optical intensity. Using a set-up presented in Figure II.4, propagation losses in the Si_3N_4 waveguide have been measured to be as low as 1.14 dB/cm, which is comparable to the results obtained by *Stutius et al.*

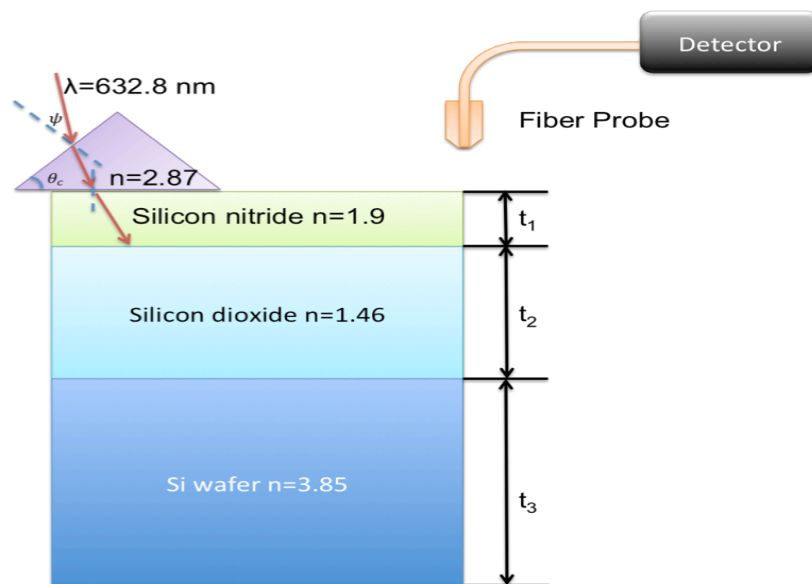


Figure II.4: Schematic of the rutil prism coupler and the planar Si_3N_4 waveguide structures. The waveguide attenuation has been measured by collecting the scattered light along the propagation path by a fiber probe placed several millimeters in front of the light beam. Si_3N_4 layer was deposited by PECVD with $t_1 = 935\ \text{nm}$, SiO_2 buffer layer was thermally grown with $t_2 = 1044\ \text{nm}$ and the substrate was a 5-cm diameter Si wafer (data taken from [SRIRA83]).

II.2.3 Structured 2D Si₃N₄ waveguides: pioneer results for multimode waveguides

The studies of the Si₃N₄ waveguides moved into the 2D area with the development of etching techniques. *Henry et al.* introduced a 2D structured Si₃N₄/SiO₂ waveguide on Si and lateral confinement of guided modes in the Si₃N₄ layer has been considered more attentively, especially for the TE modes [HENRY87]. In this work, wet etching with hot phosphoric acid at 174°C was used to form the mesa-like Si₃N₄ waveguide on top of the SiO₂ buffer layer, rather than a plasma etching technique. The general fabrication process is presented in Figure II.5.

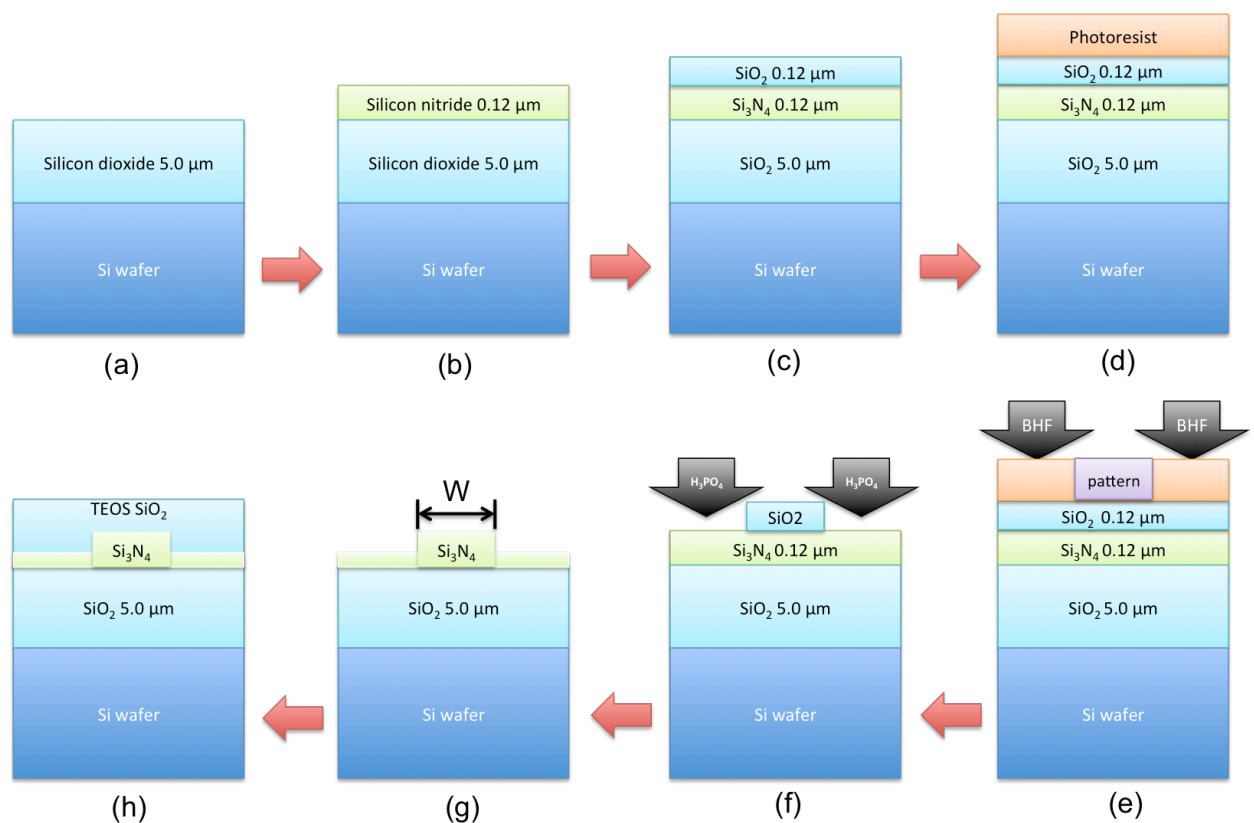


Figure II.5: Schematic of the mesa Si₃N₄ waveguide fabrication process made by *C.H. Henry et al.* (a). Realization of SiO₂ buffer layer by thermal oxidation (25 atm at 950°C); (b). Deposition of Si₃N₄ by CVD; (c). Deposition of a 120 nm thick film of SiO₂; (d). Photoresist coating and patterning; (e). Realization of SiO₂ mask (width lightly larger to the targeted width of mesa Si₃N₄ waveguide) by wet etching using (f). Wet etching of Si₃N₄ waveguide (rib form) with phosphoric acid (g). Since the chemical etching selectivity for SiO₂ and Si₃N₄ is different, the height of the etched Si₃N₄ film would be less than 120 nm, which means the shape guide was like a mesa, rather than a rib; (h). Bury of Si₃N₄ waveguide by deposition of an additional SiO₂ layer formed from tetra-ethyl-ortho-silicate (TEOS).

The efficiency of this mesa-like 2D waveguide structure could be estimated by the theoretically calculated transverse and lateral coupling losses due to the mismatch with the mode of laser source, as well as leakage losses into the SiO₂ film on the Si substrate (see Figure II.6).

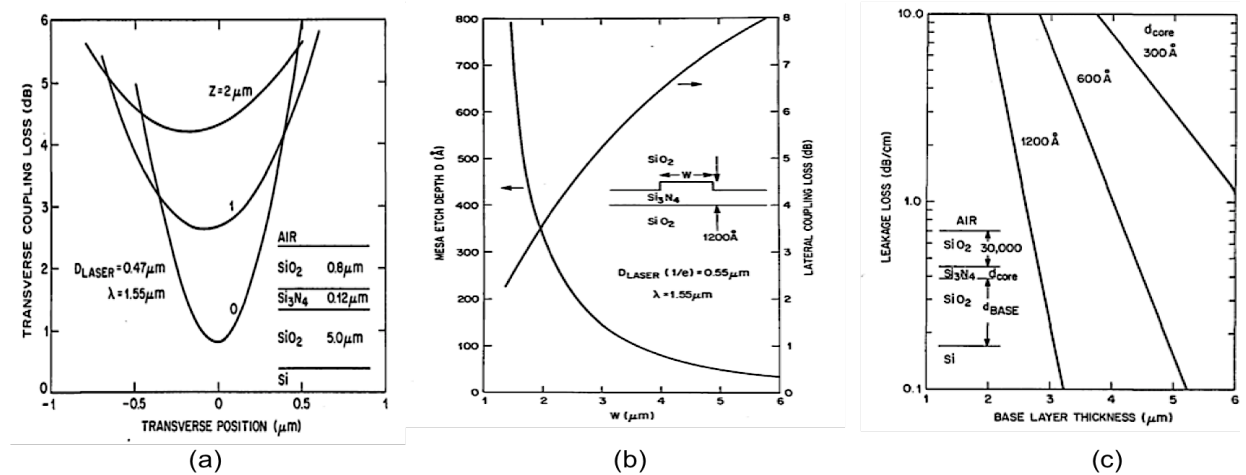


Figure II.6: (a). 1D calculation of theoretical transverse coupling losses vs vertical transverse position for several axial displacement Z , assuming that the CSBH⁵ laser used in the experiment has a tight Gaussian mode profile of 470 nm by 550 nm at 1/e of maximum power; (b). 2D calculation of theoretical mesa etch depth required for 75% confinement of optical power within the mesa and lateral butt coupling loss vs mesa width W ; (c). Theoretical leakage loss into the Si substrate vs base layer thickness (taken from [HENRY87]).

As seen in the above curves, the butt coupling loss could be less than 1 dB in a perfectly aligned position, but it would increase brutally, once there was a little axial displacement. Meanwhile, there was a considerable lateral coupling loss except for very narrow waveguides, however the sidewall roughness could not be negligible for the narrow waveguides. Moreover, a thicker buffer SiO₂ layer would avoid the mode leakage in the Si₃N₄ waveguide. Considering the upper SiO₂ cover, an equal thickness of both SiO₂ layers should be a good choice to keep the vertical symmetry of the guided modes.

On the other hand, they measured the IR transmission spectra by coupling light from a tungsten lamp into and out of the waveguide. By analyzing the IR transmission spectrum (see Figure II.7), an additional annealing process was proposed to eliminate the O-H absorption peak at 1400 nm and 1520 nm. Without annealing, the loss is about 1 dB/cm at 1550 nm and

⁵ CSBH laser: the channel substrate buried heterostructured laser.

much less at 1310 nm, while after annealing the loss decreases to less than 0.3 dB/cm in the whole telecom-wavelength range. Furthermore, the deposition technique of the SiO₂ buffer layer should also be optimized to obtain a smoother waveguide interfaces and a better waveguide sidewall roughness, aiming to decrease the influence of Rayleigh scattering. Thus the deposition technique of high-pressure steam oxidation of Si and the chemical mesa etching process were strongly recommended to realize 2D Si₃N₄ waveguide.

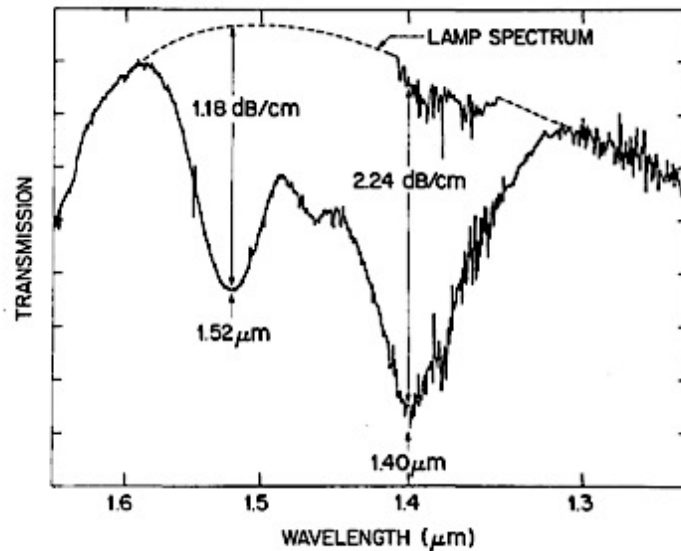


Figure II.7: Measured transmission spectra vs wavelength (taken from [HENRY1987]).

In 2004, *Daldosso et al.* reported their works of fabrication and optical characterization of thin 2D Si₃N₄ waveguides on Si substrate in visible and IR wavelength range [DALDO04a]. A CMOS pilot-line consisting of standard cleanroom processes of microelectronics industry has been applied to fabricated 2D Si₃N₄ waveguides of different profile shape, such as channel, rib and strip-loaded (see Figure II.8). They evaluated the geometry, sidewall and layer roughness by observing under SEM and AFM, as well as the optical propagation (at 632.8 nm and 780 nm) measurement by using the several different methods, such as cutback technique and scattered light top-view technique. The cutback technique uses waveguide- transmitted light intensity measurement and needs considerable amount of well-cleaved waveguide samples with different lengths. Moreover, each measurement needed reproducible and effective coupling conditions between source and Si₃N₄ waveguide, which relied on very smooth waveguide facets, and extremely precise nano-positioning stages. It is suitable for the well-cleaved short waveguides to do precise propagation attenuation measurement. Otherwise when

the channel top surface was irregularity-free space, according to the scattering theory, the decrease of the scattered light (supposing its intensity is directly proportional to the light intensity propagation in the waveguide) as a function of the position on the waveguide is representative of the attenuation of the optical mode propagating in the waveguide. In this situation, the top-view method, just described in the precedent part, will be more efficient and practical to measure the light attenuation in a long straight waveguide (up to several centimeters).

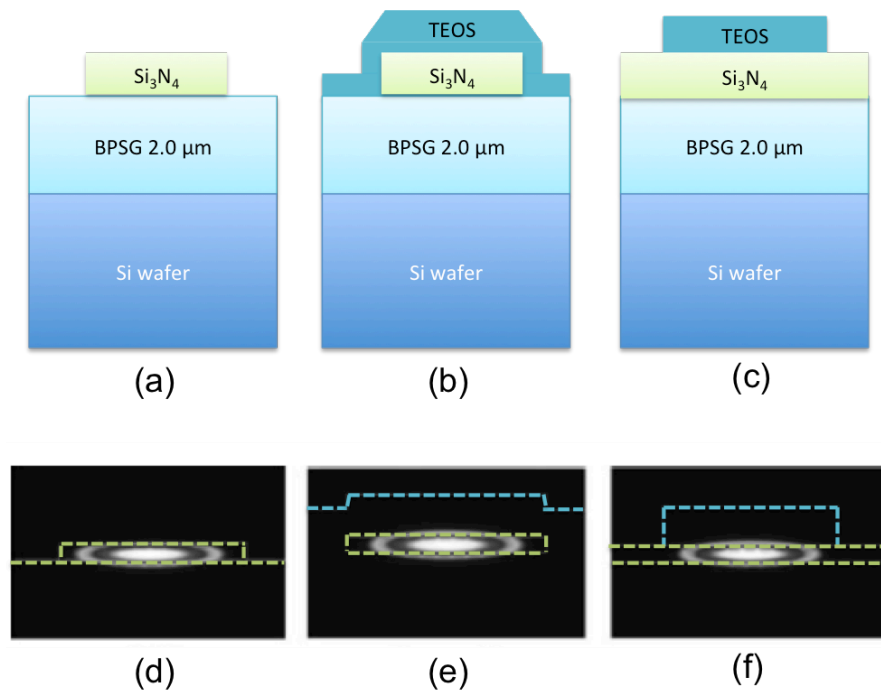


Figure II.8: (above). Schematic view of the rib (a), channel (b) and strip-loaded (c) 2D-rectangular waveguides deposited by LPCVD on Si substrate. The thickness of the Si₃N₄ core layer, the BPSG⁶ bottom cladding layer and the TEOS covering layer is 200 nm, 2 μm and 520 nm, respectively, and the Si₃N₄ etched width is 10 μm; (below). Simulated intensity profile of the fundamental guided mode TE₀ of rib (d), channel (e) and strip-loaded (f) Si₃N₄ waveguide, the filling factor/refractive effective index are 75%/1.723 for rib waveguide and 72%/1.755 for both channel and strip-loaded waveguide.

The measured optical losses at 780 nm of different types of 2D Si₃N₄ waveguides have been listed in Table II-3. As seen from the table, both of measurement methods confirmed a lower propagation loss coefficient of the channel-like waveguide among all the samples. Larger losses for rib waveguides should be due to the fact that the Si₃N₄ layer is exposed to air

⁶ BPSG: the boron phosphor silicate glass.

without an upper buffer layer, thus enhancing scattering losses caused by the roughness and defects on the top surface of the sample. Meanwhile, the different etching depth defined by different etching methods of the strip-load waveguides (oxide plasma etcher removed additionally 30 nm of Si₃N₄) led to different effective refractive index of the lateral cladding that would result in different optical modes confined within the Si₃N₄ waveguide. Obviously, the thinner one etched by oxide plasma had a better optical confinement, thus a lower propagation loss coefficient.

Table II-3: Measured propagation loss coefficient (at 780 nm) of different types of Si₃N₄ waveguides: the oxide plasma etcher attacked both Si₃N₄ and SiO₂. The etch rates for SiO₂ and Si₃N₄ were 390 and 250 nm/min, respectively; the nitride dedicated plasma etcher was better able to detect the Si₃N₄-SiO₂ interface with etching rate of 50 nm/min for the Si₃N₄ layer; the BHF was a 7:1 buffered HF solution that attacked very slowly the Si₃N₄ layer and stopped exactly at the Si₃N₄ - SiO₂ interface (data taken from [DALDO04a]).

Wave-guide type	Etching technique	Cut-back method		Top-view method	
		Propagation loss coefficient (dB/cm)	Measurement Errors (dB/cm)	Propagation loss coefficient (dB/cm)	Measurement Errors (dB/cm)
Rib	Oxide plasma	2	±1	1.8	±0.2
Channel	Nitride plasma	0.2	±0.2	0.1	±0.05
	Oxide plasma	0.3	±0.2	0.2	±0.2
Strip-loaded	BHF	2.5	±0.6	NA	
	Oxide plasma	1.5	±0.2	1.4	±0.4

Since conventional optical lithography technique was used to transfer the prepared straight waveguide's patterns from the lithography mask to the photoresist, the etched Si₃N₄ waveguides had nearly the same width as the one of the mask's pattern. Due to the limit of the fabrication resolution of the photolithography mask mentioned in the part II.2.1, the width of waveguides could only reach down to 10 μm. Even though the thickness of the Si₃N₄ layer was around 200 nm, there were practically several high-order TE modes allowed in the relatively quite wide rectangular waveguides (see Figure II.9).

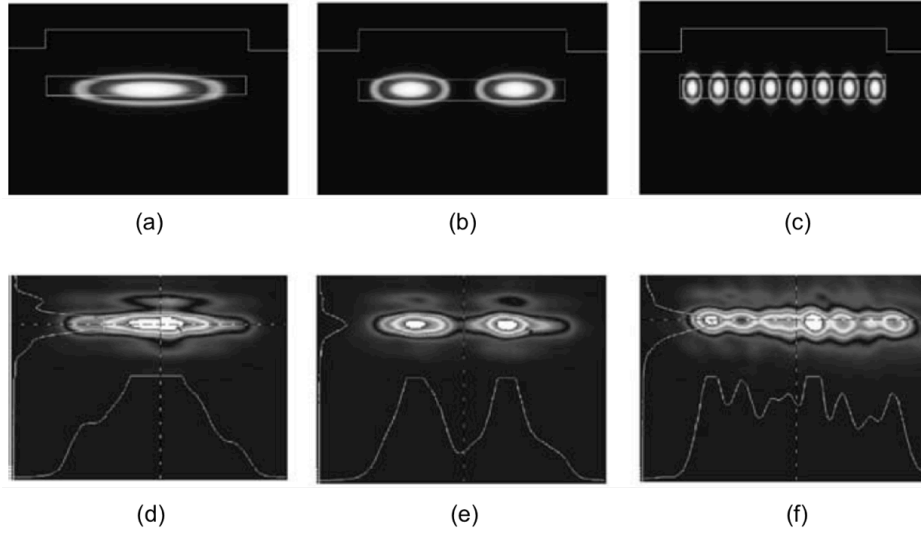


Figure II.9: (a) - (c): Simulated TE₀, TE₁ and TE₇ mode in the channel waveguide; (d) - (f): Beam analyzer measured intensity plot profiles corresponding to the above modes (taken from [DALDO04a]).

Their optical loss measurement setup was made of a He-Ne laser source (632.8 nm-5mW), a 40× objective and a TE/TM polarizer. Since the channel waveguides made by the silicon nitride dedicated plasma etching process presented the best optical propagation performance at a red-edge wavelength, a cutback measurement of the propagation loss coefficient in this channel waveguide was chosen (see Table II-4). As seen in the table, a better-confined mode resulted in a lower linear loss coefficient and the TM high-order modes had always more losses than the TE modes of the same order. The increase of propagation losses as a function of the mode order could be due to the increase scattering of light on the sidewalls of the channel. But once the width of the Si₃N₄ waveguides decreased to limit the existence of high-order modes, this defects scattering and sidewalls roughness would play a more important role in the light propagation in the 2D waveguides.

Table II-4: Propagation losses at 632.8 nm measured by cut-back technique as a function of guided mode and polarization of channel waveguides (data taken from [DALDO04a]).

1D mode	Propagation loss coefficient (dB/cm)	2D mode	Propagation loss coefficient (dB/cm)
TE ₀	0.2±0.2	TE ₁₀	0.8±0.2
TM ₀	0.3±0.2	TM ₁₀	1.2±0.2
TE ₁	0.2±0.2	TE ₁₄	1.0±0.2
TM ₁	0.3±0.2	TM ₁₄	1.3±0.2

II.3 THE STATE-OF-THE-ART Si_3N_4 WAVEGUIDES OPERATING AT VISIBLE

WAVELENGTHS

Up to now, we have reviewed the development of visible-wavelength silicon photonic integrated platform and 2D various Si_3N_4 waveguides buried or deposited on the SiO_2 layer, with dimensions only compatible with multimode behavior. The Si_3N_4 core - SiO_2 cladding pair should be the most compatible platform for the visible-wavelength light lossless propagation by optimizing the design of structured waveguide geometry and the fabrication process to obtain very low propagation loss coefficient with a dedicated characterization techniques. Especially with the development of the cleanroom facilities, including the limit pushing of the lithographic resolution, the increasing of the purity of the CVD deposition and the advancing of the plasma based etching technique, the Si_3N_4 based photonic integrated platform becomes a milestone of the generalization of Si based PICs from telecom applications to visible and very near infrared (VNIR), in which some particular features would be attractive for various domains, for example, the minimal photo damage to living cells, negligible water absorption and low fluorescence.

In 2008, *Gorin et al.* demonstrated low-loss high-index PECVD slab waveguides in the 470 nm–633 nm wavelength ranges. In this work, the precursor gas ratio of the PECVD has been optimized to reduce the absorption losses and rapid thermal annealing has been performed to eliminate as much as possible the sidewall roughness responsible for losses of the waveguides [GORIN08]. In 2013, *Romero-Gacia et al* presented their single mode photonic Si_3N_4 wire waveguide (with a width of 700 nm) with low propagation loss coefficient and low bend loss coefficient, which was fabricated within a CMOS pilot line and operated at 660 nm [ROMER13]. They compared two different claddings: one was made of water, and the other was classic SiO_2 . Both performed a tolerable TE_0 propagation loss coefficient. Recently, researchers from Ghent reported their low-loss PECVD silicon nitride photonic wire waveguides fabricated in a CMOS pilot line [SUBRA13]. They focused their research in the visible and very near infrared (VNIR), which correspond to the wavelength range from 500 nm to 950 nm. They deposited first 2–2.4 μm of silicon dioxide using a high-density plasma (HDP) CVD process, and two different thicknesses of Si_3N_4 layer were deposited using PECVD, one of 180 nm for 532 nm wavelength and one of 220 nm for 780 and 900 nm wavelengths. The inductive coupled plasma-reactive ion-etch (ICP-RIE) process was used to form the strip Si_3N_4 waveguides of 300 nm to 1 μm wide by etching the whole Si_3N_4 layer, and

an additional fluorine-based wet etcher etched a part of SiO_2 layer, following the 193 nm optical lithography. No annealing or thermal treatment was applied at the end of process, because there was no absorption band in the visible or VNIR wavelength range for Si_3N_4 . AFM and SEM have been used to evaluate the surface roughness and the cross-section dimensions of the fabricated samples. In fact, for such a sub-micron level integrated device, the conventional optical lithography technique seemed risky but efficient, especially for a long-length waveguide pattern. Some photos taken by SEM have shown the fabrication quality (see Figure II.10).

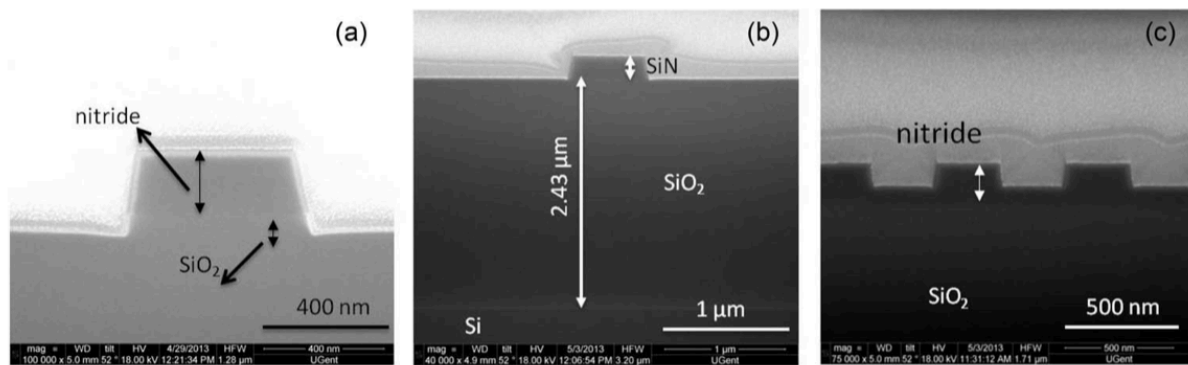


Figure II.10: SEM photos of Si_3N_4 waveguide cross-section prepared by focused ion beam: (a) Si_3N_4 waveguide, (b) complete cross-section including underlying SiO_2 and (c) grating coupler with 630 nm period and 140 nm etch depth (taken from [SUBRA13]).

Since the RIE based dry etching happened homogeneously in the vacuum chamber, the attack of Si_3N_4 would also accompany the consumption of the photoresist and the Si_3N_4 waveguide width would vary with the duration of etching process. That's why a trapeze-like cross-section has been observed rather than a common rectangular shape as seen in Figure II.10. Moreover, the cutback technique was also applied to evaluate the propagation loss of such fabricated waveguides in the visible and VNIR wavelength range. The variation of the waveguide loss as a function of waveguide width at several different wavelengths is presented in Figure II.11. Apparently, the waveguide losses should decrease brutally with the increasing of the width, because the scattering losses due to the roughness of the sidewall or defects become less important for relatively larger dimension waveguides. But the high-order modes would also appear in a wider waveguide. Comparing to the unclad Si_3N_4 waveguides, the clad waveguides with another upper SiO_2 film performed much better, because the 2D mode's profile and confinement in the waveguide strongly depend on the refractive index contrast and

on the geometrical symmetry. At the end of this chapter, we list some influenced work related to near-632.8 nm Si_3N_4 based waveguide and other on-a-chip passive PICs research, and we compare their performance by indicating the most representative light propagation index and the linear loss coefficient (see Table II-5). Overall, Si_3N_4 core paired with SiO_2 cladding should be a very reasonable photonic integrated platform for visible applications.

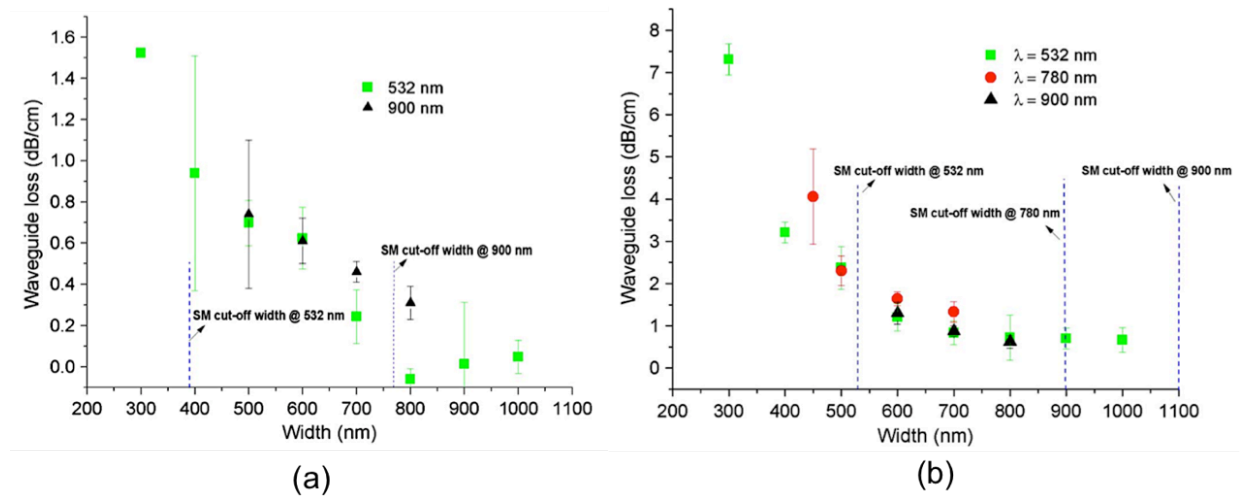


Figure II.11: Measured waveguide loss coefficients as a function of width of (a) clad Si_3N_4 waveguide at 532 nm and 900 nm; (b). Unclad Si_3N_4 waveguide at 532, 780, and 900 nm (taken from [SUBRA13]).

II.4 CONCLUSION

Whereas silicon and III-V platform have allowed monolithic or hybrid integration of photonics circuits, work has been done essentially driven by the telecom market, at near infrared wavelength. For visible light applications, the technological challenges imposed by material defaults and extremely reduced dimensions patterning are similar to those faced at the early age of telecom devices development. Nanotechnology and progress on dielectric material deposition permit only since recently to face these challenges. Promising single-mode Si_3N_4 waveguides have been demonstrated during these last 5 years, confirming the relevance of this technological platform for future visible wavelength PICs.

Table II-5: The state of the art of the Si₃N₄ waveguides operating at 632.8 nm.

Waveguides	Mode	Propagation loss coefficient	Reference
Si₃N₄ planar 1D waveguide		0.1 dB/cm	[STUTU77]
			[INUKA94]
			[BULLA99]
Si₃N₄ 2D multimode rectangular waveguide with SiO₂ cladding	TE ₀	0.3 dB/cm	[DEBRA91]
		1.1 dB/cm (HF-PECVD)	[GORI08]
		0.1 dB/cm (LF-PECVD)	
		0.6 dB/cm	[OHTAN92]
		0.2 dB/cm	[DALDO04a]
	TM ₀	0.3 dB/cm	
	TE ₁	0.2 dB/cm	
		TM ₁	0.3 dB/cm
Si₃N₄ wire waveguide	TE ₀ @ 660nm	0.71 dB/cm (Water cladding)	[ROMER13]
		0.51 dB/cm (SiO ₂ cladding)	

CHAPTER III: DESIGN AND SIMULATION OF Si_3N_4 WAVEGUIDES

In this chapter, we will present the theoretical study on the design of Si_3N_4 -based photonic integrated devices, which are required for the targeted automotive holographic system. Firstly, we will introduce the numerical simulation used to determine the cross-section dimensions of the mentioned Si_3N_4 rectangular waveguide for visible-wavelength propagation. Then, we will present designs of other integrated components based on the Si_3N_4 waveguide useful for the global device presented in Chapter I. This includes optical splitters and bent waveguides.

III.1 NUMERICAL SIMULATION-ASSISTED DESIGN

As described in a previous chapter, the photonic integrated devices for 633 nm-wavelength applications are based on a Si_3N_4 waveguide platform. The passive components within such a visible PIC include straight waveguides, bent waveguides and different types of optical couplers such as multi-branch optical splitters.

In the first phase of the visible PIC's development, we used different simulation methods to calculate the optical transverse modes of the Si_3N_4 rectangular waveguides in order to choose appropriate dimensions of waveguide, i.e dimensions allowing strongly confined TE fundamental mode propagation. More precisely the objective here is to obtain waveguides with the highest confinement fundamental TE mode in order to allow waveguide bending and to limit propagation losses induced by interface fabrication defaults. Single-mode operation is required for the good coupling with splitters and with nano-antennas. However at visible wavelength, we will see that the cross-section dimensions of the waveguide become very low. For this reason, we admit that slightly wider waveguides can be envisaged and first order modes with low confinement can be tolerated. Thus the dimensions must be chosen so that the waveguide is as wide as possible, but taking into account the optical confinement of possible higher order modes. We have thus evaluated different waveguide geometries by calculating fundamental and first order modes effective index and confinement. We will first present the different used methods, then the experimental determination of materials indexes for better calculation accuracy, and finally the mode calculations for three different claddings.

III.1.1 Modeling of guided modes: methods and structures

Sandwich-like layered structures such as dielectric slabs can be used to guide optical waves due to the vertical/transversal 1D confinement of the Electromagnetic (EM) modes in the higher refractive index layer, here the Si_3N_4 layer. By limiting also laterally the width of the Si_3N_4 film, the 2D confined waveguide becomes more efficient for the fundamental modes propagation of polarized light beam. Several methods can be used to calculate such 2D modes. Simple and fast approximate analytical approach consists in applying the effective index method (EIM), which is based on two successive effective index calculations (EIC) (see for example [YARIV06]).

a. 1D mode calculation: EIC and 1D confinement factor

We present the TE mode's mathematic derivation as an example of EIC 1D calculation in Annex I. The modeling of the 1D dielectric waveguide is schematically presented in Figure III.1.

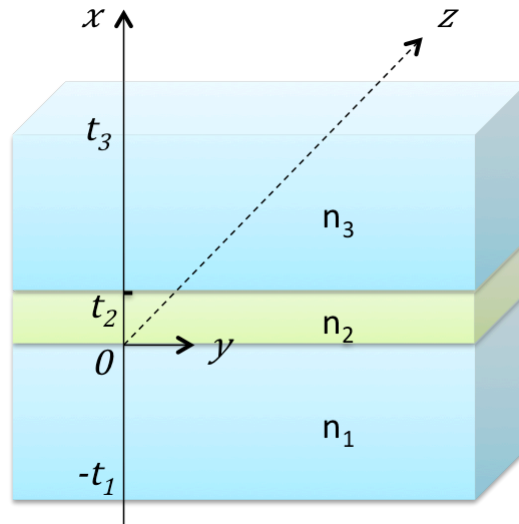


Figure III.1: Schematic diagram of the layered 1D dielectric waveguide structures.

Firstly, we can note the 1D index distribution as follows:

$$n(x) = \begin{cases} n_1, & -t_1 \leq x < 0 \\ n_2, & 0 \leq x \leq t_2 \\ n_3, & t_2 < x \leq t_3 \end{cases} \quad (\text{III-1})$$

As demonstrated in Annex I, the Eigenvalue equation of the TE mode can be presented as follows:

$$\tan(ht_2) = \frac{p + q}{h(1 - pq/h^2)} \quad (\text{III-2})$$

where h , p and q can be written as:

$$\begin{cases} p = \sqrt{\beta^2 - n_1^2 k_0^2} \\ h = \sqrt{n_2^2 k_0^2 - \beta^2} \\ q = \sqrt{\beta^2 - n_3^2 k_0^2} \end{cases} \quad (\text{III-3})$$

with $k_0 = \omega/c_0$ is the wave number in vacuum and β is the propagation constant for the guided TE mode. In fact, the difference between the TE and TM mode's calculation within the EIC is involved in the pair of index contrast coefficient: $\eta_1 = \eta_2 = 1$ for TE modes and $\eta_1 = (n_2/n_1)^2$ and $\eta_2 = (n_2/n_3)^2$ for the TM modes. Therefore we need to replace the p and q in the Eigenvalue equation shown in (III-2) for the TM modes:

$$\begin{cases} \bar{p} = \eta_1^2 p \\ \bar{q} = \eta_2^2 q \end{cases} \quad (\text{III-4})$$

Moreover, we defined the 1D coefficient of confinement as the ratio of the E_y 's intensity, which has been limited inside of the Si_3N_4 waveguide to the total intensity:

$$\eta_m(t_2) = \frac{\int_0^{t_2} E_m(x) dx}{\int_{-t_1}^{t_3} E_m(x) dx} \quad (\text{III-5})$$

where we suppose that t_2 is the only variable in the EIC and largely smaller than the cladding layer's thickness t_1 and t_3 , in order to match the real physical model of such a layered 1D dielectric waveguide. Physical interpretation is that a higher coefficient of confinement of concerned mode shows better guided wave propagation efficiency in avoiding the mode's leakage into the cladding or buffer layers.

b. 2D mode calculation: EIM and 2D confinement factor

We present here as an example the calculation principle of TE modes in such a rectangular 2D waveguide based on the 1D layered EIC algorithm. This 2D calculation is known as EIM (Effective Index Method). The modeling of the 2D rectangular dielectric waveguide is schematically presented in Figure III.2.

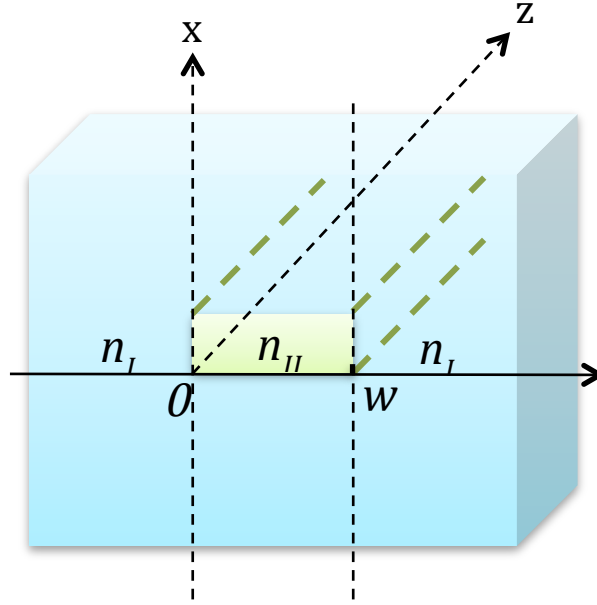


Figure III.2: Schematic diagram of the 2D rectangular dielectric waveguide structures.

Firstly, we can note the 2D effective index distribution as follows:

$$n_{eff}(y) = \begin{cases} n_I, & y \leq -\frac{w}{2} \\ n_{II}, & -\frac{w}{2} < y < \frac{w}{2} \\ n_I, & y \geq \frac{w}{2} \end{cases} \quad (\text{III-6})$$

where n_I should be equal to the refractive index of SiO_2 cladding, thus $n_1 = n_3 = n_I$; n_{II} is the calculated 1D effective index of TE modes, which has been presented in the above paragraphs.

Considering that for the 1st-step calculated TE modes, the E-field component should be always in the y-direction, we can write down the E_y component of this 2D waveguide structure by deducing the TM mode wave function in this 2nd-step, which is solution of the following eigenvalue equation which is similar to the 1D TE mode case deduced in Annex I:

$$\tan(hw) = \frac{h(\bar{p} + \bar{q})}{h^2 - \bar{p}\bar{q}} \quad (\text{III-7})$$

where \bar{p}, \bar{q} can be defined as follows:

$$\begin{cases} \bar{p} = \frac{n_{II}^2}{n_I^2} p \\ \bar{q} = \frac{n_{II}^2}{n_I^2} q \end{cases} \quad (\text{III-8})$$

Therefore we can describe this guided TE mode's propagation and find the 2D effective index by solving the Eigen equation. Since we evaluated the 1D confinement coefficient for the 1D layered waveguide structure, we can apply the same notion to define the confinement coefficient affected by the 2nd-step EIM calculation, which is as a function of the width of rectangular Si₃N₄ waveguide:

$$\eta_n(w) = \frac{\int_{-\frac{w}{2}}^{\frac{w}{2}} E_n(y) dy}{\int_{-\infty}^{\infty} E_n(y) dy} \quad (\text{III-9})$$

where n is the order of TM modes found in 2nd-step EIM calculated layered structure.

Caution should be taken when we calculate the TM modes of 2D rectangular waveguide. Since the TM modes have an orthogonal polarization state with the TE modes, the E-field of TM modes should have only x-direction component. In the 1st step of EIM calculation, we need to solve the TM mode's Eigenvalue equation to calculate the 1D effective index as a function of Si₃N₄ waveguide's thickness. However, in the 2nd step, for the purpose of seeking E_x component, we should apply the TE mode Eigen equation to calculate the 2D effective index for the TM modes.

By the way, we could separate the two orthogonal variables in the x-direction and in the y-direction in order to approximately calculate the 2D confinement coefficient for each 2D transverse modes of rectangular waveguide. The principle of the variable separation involved in the 2D confinement coefficient is presented in Figure III.3. For the simplest case, we consider a fundamental guided transverse mode with a round-like E field profile projected in xy plane. The optical propagative intensity should be confined in a rectangular zone of w × t₂, where w is the width of Si₃N₄ waveguide along y-direction and t₂ is the thickness of Si₃N₄ waveguide along x-direction. We could generalize the 2D confinement coefficient to high-order modes, in which the pattern of intensity profile would be no longer a round shape.

Therefore we can define 2D confinement coefficient of the rectangular Si₃N₄ waveguide:

$$\eta_{mn}(t_2, w) = \eta_m(t_2)\eta_n(w) \quad (\text{III-10})$$

where m is the order of concerned mode confined by the thickness of the waveguide calculated in 1st step and n is the order of concerned mode confined by the width of the waveguide calculated in 2nd step.

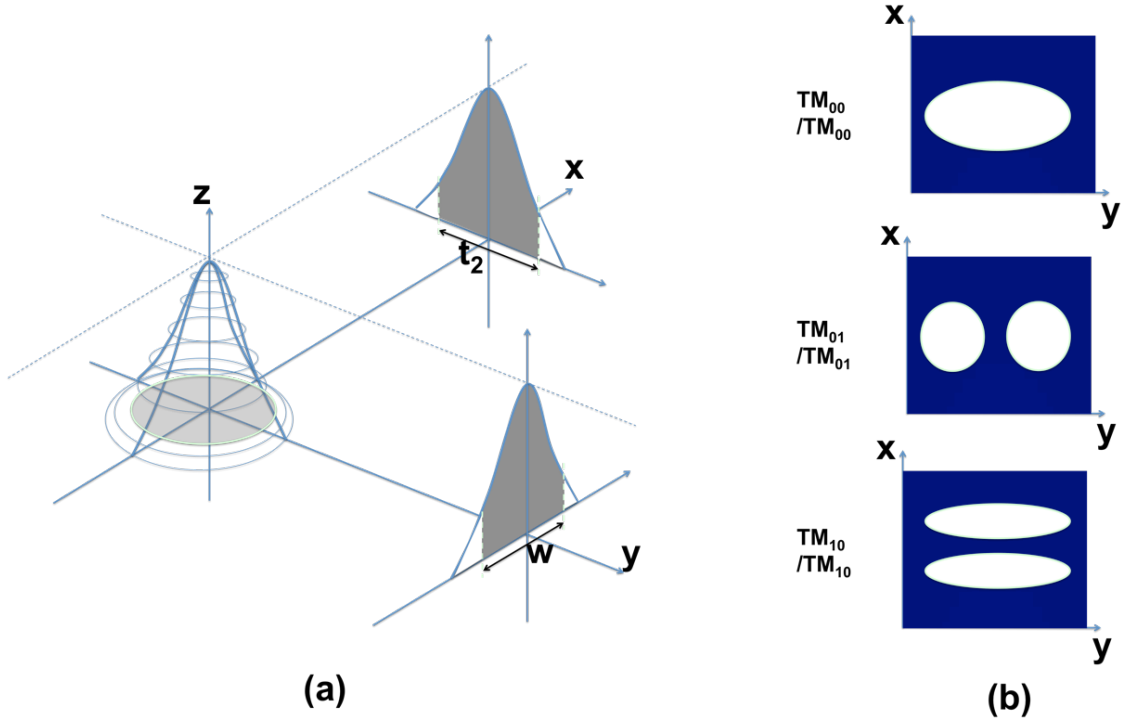


Figure III.3: Schematic diagram of transverse guided modes in a rectangular ($w \times t_2$) waveguide: (a). Fundamental mode distribution; (b). Intensity patterns of the fundamental (0-order) and 1st order 2D TE/TM modes.

c. Vectorial mode solver

These 1D and 2D analytical methods are efficient for most of the waveguide geometries and give in a short time effective indexes and confinement factors. However, as we will show it can be relevant to complete the study by vectorial calculations. This will be done with the mode solver of the software LUMERICAL FDTD Solution.

We must point out that as a vectorial computation method, the mode solver under the LUMERICAL simulation environment could be used to visualize directly the transverse mode's E-component, H-component and total intensity profile in each direction. Additionally mode solver provides at the same time the fraction of TE mode's E_y -polarization⁷. As we know, the pure TE mode's E-field has only non-zero component along the y direction (E_y) and H-field's non-zero component is along the z direction (H_z), or vice versa, a pure TM mode could be presented by its E_z or H_y modal field component. Since the LUMERICAL's mode solver applies a vectorial calculation algorithm, all of the modes found by the mode solver are

⁷ TE mode E_y -polarization fraction in Mode solver is defined as fraction of integral intensity of the y-direction E-field component over total intensity of all-direction E-fields.

not based on the hypothesis of pure TE or pure TM modes. However, the modal profile of each E_y and H_z or E_z and H_y are similar due to the orthogonality of propagative wave's electromagnetic field at the incident surface (yz plane). Therefore we can evaluate the relative dominance of TE or TM mode for each calculated transverse mode by using the E_y -polarization fraction.

d. Studied structures

The schematic of the modeled Si_3N_4 1D layered waveguide is presented in Figure III.4(a), as well as 2D rectangular waveguide in Figure III.4(b). In fact, for the completely buried Si_3N_4 waveguide, the thickness of the buffered layer is much larger than the one of waveguide layer in order to avoid the leakage of the guided modes into the Si wafer. The thickness of the SiO_2 buffer layer should be several micrometers, and the cross-section dimension of the Si_3N_4 rectangular should be around several hundred nanometers.

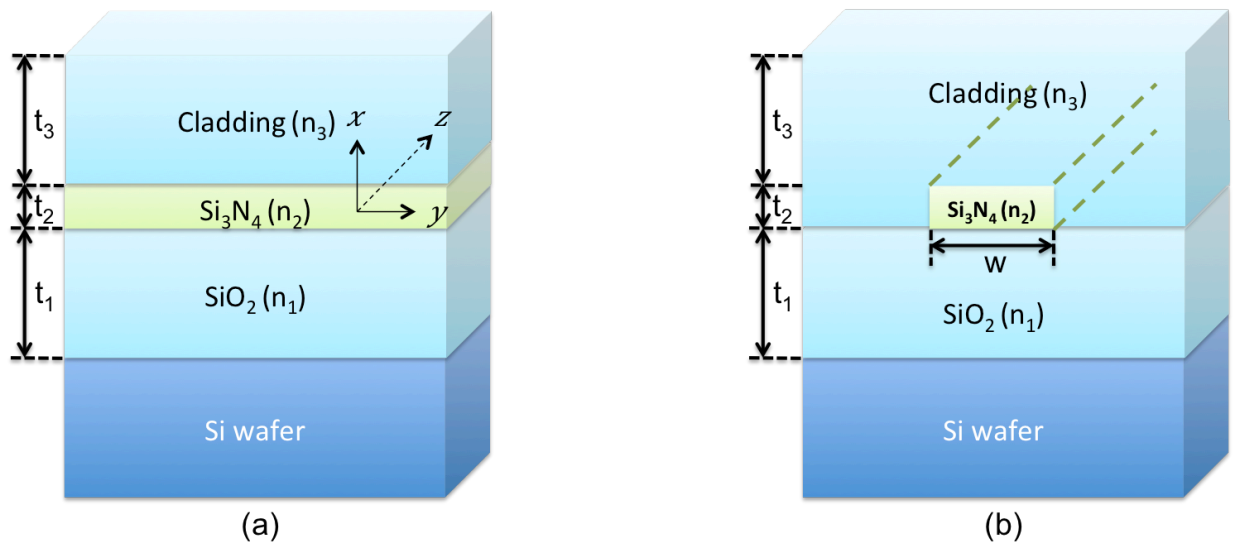


Figure III.4: Schematic of modeling structures: (a) 1D Si_3N_4 slab waveguide and (b) 2D Si_3N_4 ridge-like waveguide. t_1 , t_2 and t_3 are the thicknesses of lower SiO_2 buffered layer, Si_3N_4 waveguide layer and cladding layer, respectively; w is the width of the 2D rectangular waveguide along the y -direction.

III.1.2 Measurement of refractive index

The refractive indexes of deposited dielectric film are important optical constants to establish the waveguide design. We characterize 4-inch samples by the *J.A. WOOLLAM CO.* M2000-

UI® set-up [WOOLL07]. A conventional rotating compensator ellipsometry measurement set-up is illustrated in Figure III.5. The whole system is made of a quartz Tungsten halogen lighting source, a pair of fixed polarizer and analyzer, and continuously rotating compensators and detectors. In our measurement, there are 670 operation wavelengths that cover the whole visible and NIR range (from 245nm to 1690nm), so the detectors include a CCD array for the UV and visible wavelength range and a near infrared (NIR) photodetectors array.

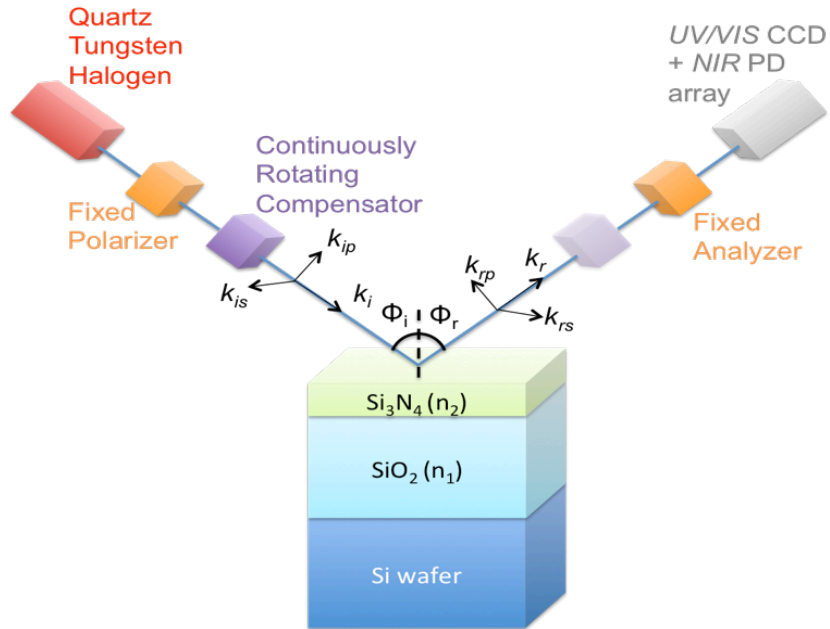


Figure III.5: Schematic diagram of our rotating compensator ellipsometric measurement setup.

Typically, the ellipsometric setup captures the change of polarization state of the light beam when it interacts with the layered dielectric structures. We could measure a multilayer sample's transmission at the same time and extract each layer's information separately during the data processing. Based on the Fresnel reflection equation for polarized light encountering boundaries in planar multilayer materials [AZZAM87], the theoretical spectral ellipsometry (SE) measurement result can be expressed as:

$$\rho = \frac{r_p}{r_s} = \tan(\Psi)e^{i\Delta} \quad (\text{III-11})$$

where ρ is the 2-layer induced complex reflectance ratio, r_p and r_s are the complex Fresnel reflection coefficients of the sample for p-plane and s-plane⁸ polarized light, Ψ is the deduced amplitude component and Δ is the phase difference, respectively.

Fitting the measured Ψ and Δ data involves supposing an analytic model of dielectric material's refractive index. Since both of our dielectric layers are transparent for the visible and NIR light, their refractive indices can be described by using the Cauchy or Sellmeier formula as follows:

$$n(\lambda) = A + \frac{B}{\lambda^2} + \frac{C}{\lambda^4} \quad (\text{III-12})$$

where A,B and C are coefficients corresponding mainly to refraction, absorption and dispersion of the transparent medium. The experimental SE fitting curves of complex reflectance ratio is presented in Figure III.6 and fitted results are shown in Table III-1.

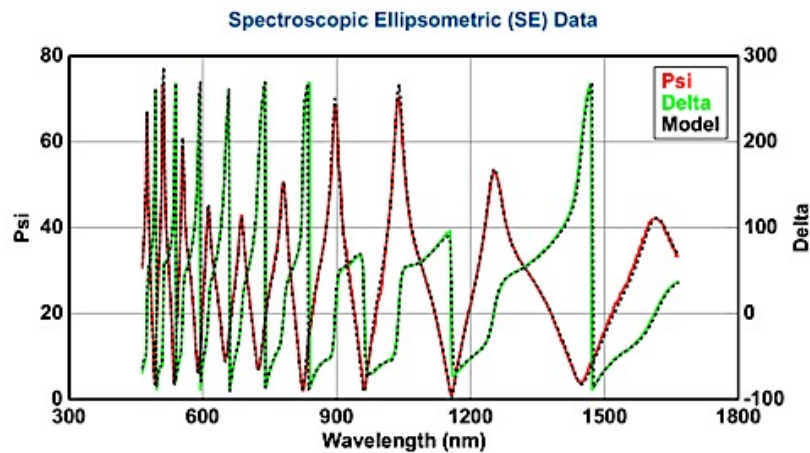


Figure III.6: RCE measurement of complex reflection ratio s for a 2-layers dielectric sample.

Table III-1: Cauchy model fitted experimental optical constants of Si₃N₄ – SiO₂ layered sample measured by rotating compensator ellipsometer.

SE Parameters	SiO ₂	Si ₃ N ₄
Thickness	2272.6 ± 10.2 nm	286.1 ± 0.7 nm
A	1.420 ± 0.0033	1.934 ± 0.0060
B	0.00949 ± 0.00055896	0.02958 ± 0.005032
C	-0.00091590 ± 0.00011479	-0.00211 ± 0.001016

⁸ p-plane: polarization direction parallel with the incident plane; s-plane: polarization direction perpendicular to the incident plane (contributed from the German word "senkrecht").

The refractive index curves as a function of wavelength for both dielectric materials are plotted in Figure III.7. As shown from the SE results, the experimental refractive indexes of our PECVD-made Si_3N_4 and SiO_2 layers at the targeted wavelength of 632.8 nm are $n_2 = 1.995$ and $n_1 = 1.438$ respectively, and the index contrast is about $\Delta n = 0.56$. We will keep these indexes in mind for our following waveguide design work. By the way, adjusting the PECVD operation parameters could vary the thickness of both layers, and we suppose the variation of thickness has not a remarkable influence on the refractive index.

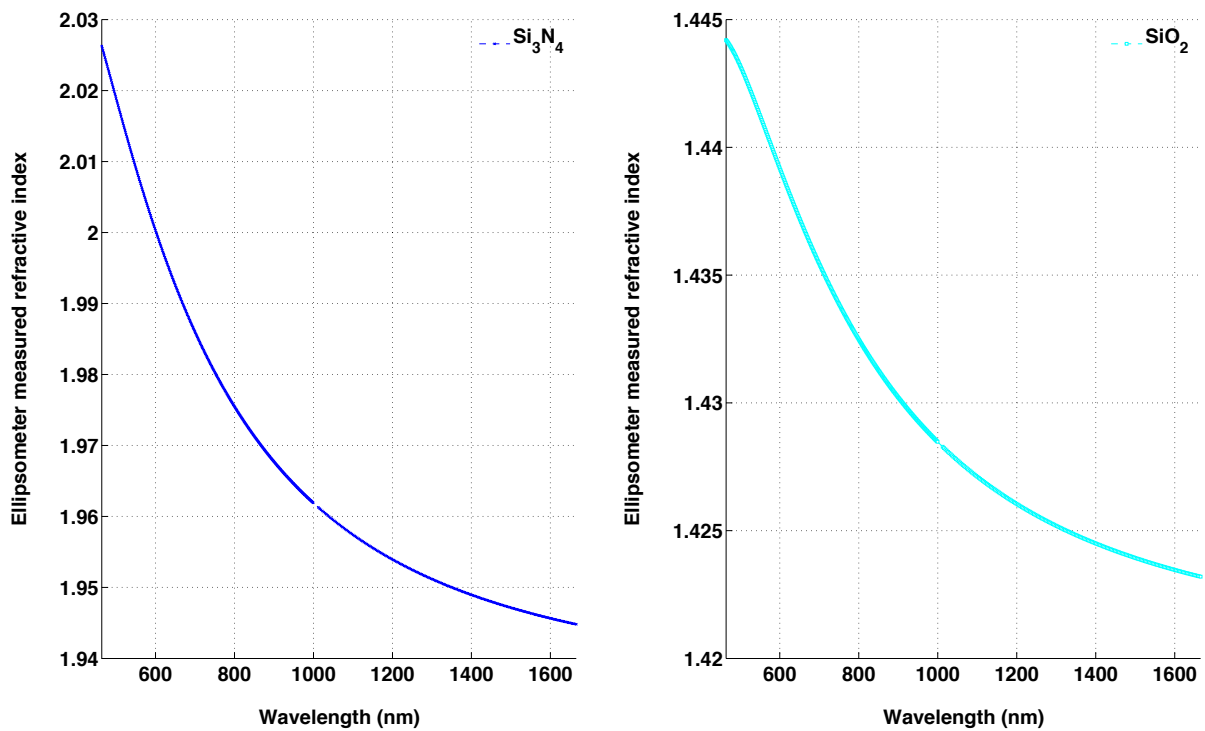


Figure III.7: Rotating compensator ellipsometer measured refractive index of PECVD deposited Si_3N_4 and SiO_2 films with thickness of 286.1 nm and 2272.6 nm, respectively.

III.1.3 The effective index and confinement coefficient of TE modes

Once we have reliable experimental refractive indexes of the different layers of our sample, we can study the optical transverse modes in the Si_3N_4 waveguide.

a. 1D mode calculation

We focus on mentioned layered structures illustrated schematically in Figure III.8. The first uncovered Si_3N_4 1D waveguide has its top surface totally exposed to the air; the second SiO_2 -

covered Si_3N_4 1D waveguide has a symmetric index distribution in the vertical direction; the last polymers-covered Si_3N_4 1D waveguide has a different upper cladding material with a bigger refractive index than the lower cladded SiO_2 layer (i.e.: PMMA, $n=1.489$).

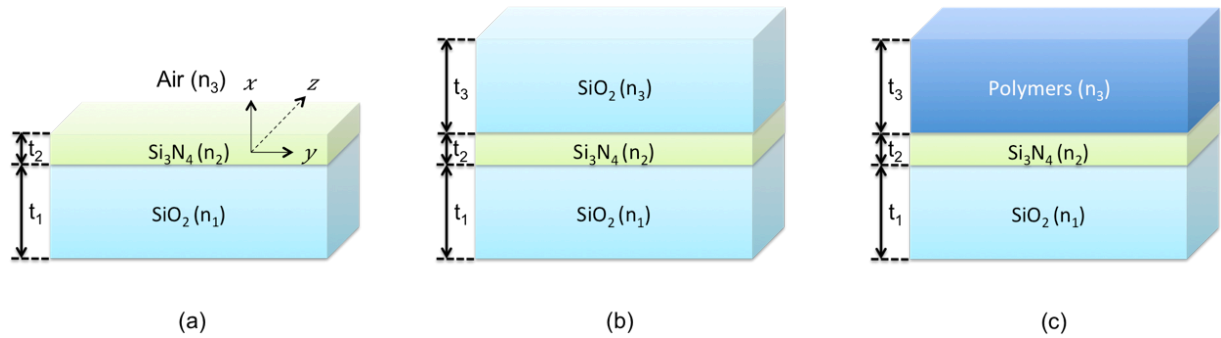


Figure III.8: Schematic diagrams of different 1D Si_3N_4 waveguide: (a). unclad waveguide ($n_3 = 1$); (b). symmetric SiO_2 cladded waveguide ($n_3 = n_1$); (c). asymmetric cladded waveguide ($n_2 > n_3 > n_1$).

In the first step, we used the EIC to study the TE mode in mentioned 1D waveguides. We can present the refractive index distribution along the vertical direction for the 1D confined waveguide structure in a Cartesian coordinates system shown in Figure III.8. We calculated the 1D effective index of the fundamental and 1st order TE/TM modes in each layered waveguide. The 1D EIC and coefficient of confinement are plotted in Figure III.9, Figure III.10 and Figure III.11, corresponding to the different 1D Si_3N_4 waveguides corresponding to Figure III.8.(a), (b) and (c), respectively.

a.1 Unclad waveguide

In the case of air cladding shown in Figure III.9, the confined modes should have a 1D effective index between the refractive indexes of bottom buffer layer ($n(\text{SiO}_2)=1.438$) and the propagation core layer ($n(\text{Si}_3\text{N}_4)=1.995$). As expected, there are cutoff values of 1D waveguide's thickness for the guided TE/TM modes. For the thickness slightly exceeding the cutoff, the fundamental mode's confinement is quite poor, lower than 20%. By increasing the thickness of the Si_3N_4 layer, the TE/TM modes become increasingly confined, and once it exceeds the first order mode cutoff condition, the TE_1 and TM_1 modes would come out immediately with a confinement coefficient higher than 50%. Finally their confinement coefficients tend to a limit value. The fundamental modes TE_0 and TM_0 would be close to 1 in a relatively thick 1D waveguide. In the viewpoint of mode's confinement, the TM modes

show a slight advantage comparing with the same-order TE modes, although the effective index of TM modes are obviously smaller than the one of the TE modes.

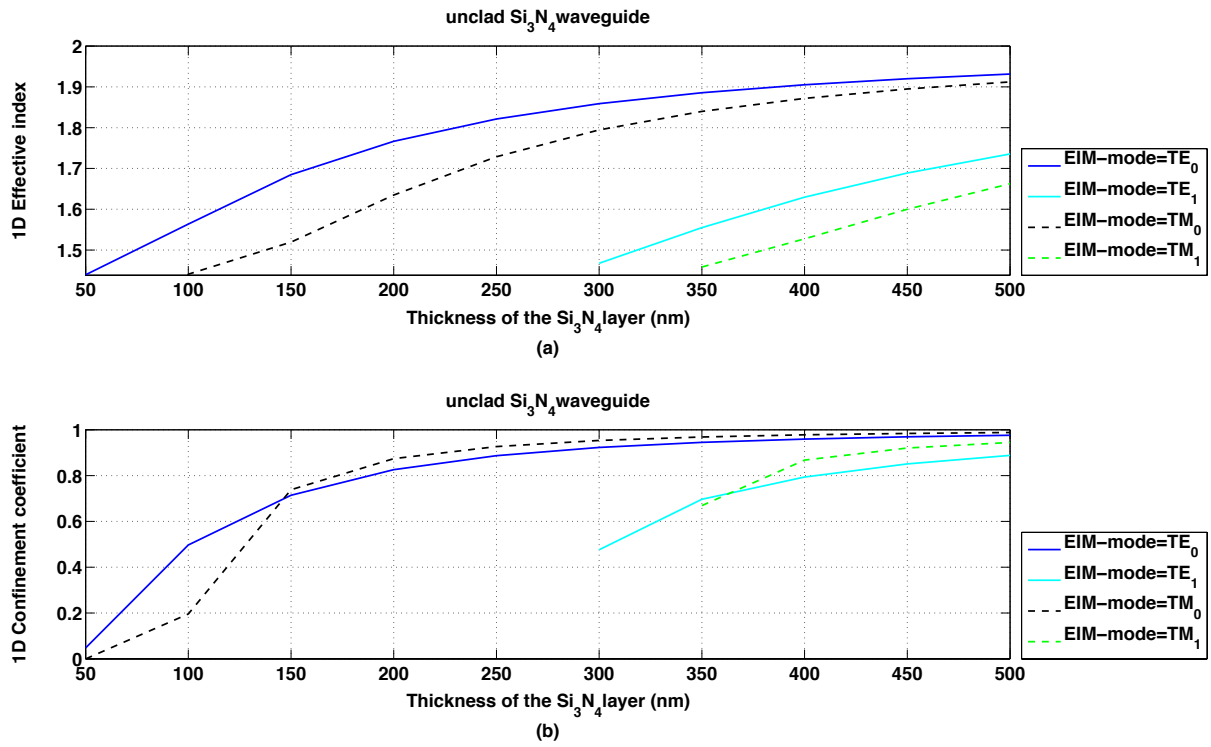


Figure III.9: Calculated 1D effective index of transverse modes at 633 nm in the unclad waveguide (see Figure III.8.(a)).

a.2 SiO₂ and PMMA cladded waveguide

We applied both the EIC and the FDTD solution software LUMERICAL to simulate the SiO₂ cladded 1D Si₃N₄ waveguide. We present simultaneously in Figure III.10 the effective index found by the mode solver attached to LUMERICAL. We employed the perfectly matched layer (PML) absorbing boundaries condition to both vertical sides of our simulated Si₃N₄ waveguide. In this case, the mode solver could consider the guiding core material only been limited in the x-direction and with an index contrast only at its top and bottom horizontal sides. In Figure III.10, the results of 1D effective index calculated by the mode solver of LUMERICAL correspond to the TE modes, in which the E-field has only a y-direction component. On the contrary, the EIC algorithm is based on scalar quantity computation. Therefore we can calculate rapidly the effective index and confinement coefficient as a

function of waveguide's dimension parameters under a basic hypothesis of pure TE or pure TM modes. As we can see, it shows a good agreement of results between both methods.

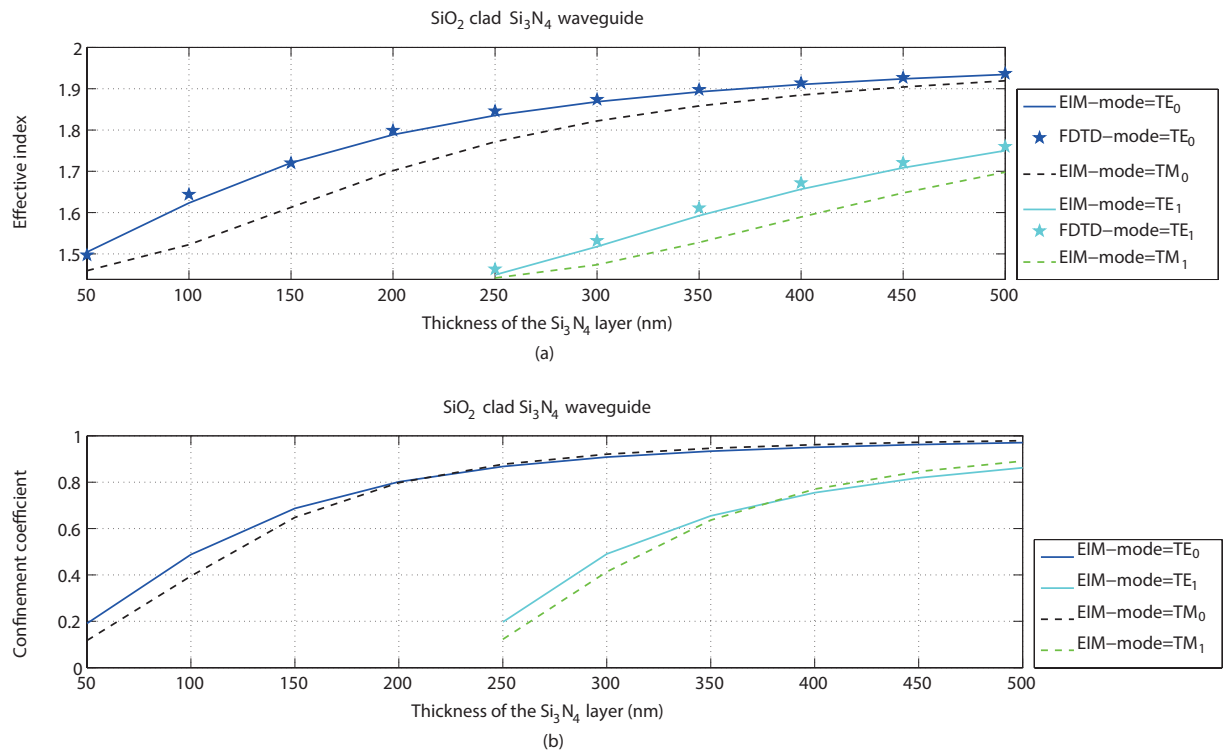


Figure III.10: Calculated 1D effective index of transverse modes at 633 nm in the SiO₂ clad symmetric waveguide (see Figure III.8.(b)).

As shown in Figure III.10 and Figure III.11, once we used a transparent and homogeneous dielectric or organic material to cover the top surface of the 1D Si₃N₄ waveguide, the transverse mode has a relatively higher effective index than the unclad case. The TM modes always have a smaller effective index than the TE modes, however they could be confined in the Si₃N₄ layer as well as the TE modes. Especially in the thick-waveguide case, there are slight differences of 1D confinement coefficient between both TE and TM modes. Due to this slight difference between the refraction index of SiO₂ ($n=1.44$) and PMMA ($n=1.49$), the SiO₂ clad waveguide has a smaller cutoff thickness for both TE and TM modes than PMMA clad waveguide. By the way, from the symmetric viewpoint of fundamental TE/TM mode, we prefer using the same silicon dioxide material as the bottom buffer layer to clad the top surface. The thickness of the SiO₂ clad Si₃N₄ waveguide should be chosen to lower to 250 nm for the purpose of keeping single-mode propagation condition. This limit of thickness could be enlarged with the increasing of cladding material's experimental refraction index.

Note that, near the cutoff thickness, both TE and TM modes would exist in the waveguide with a high confinement coefficient (i.e.: 85%).

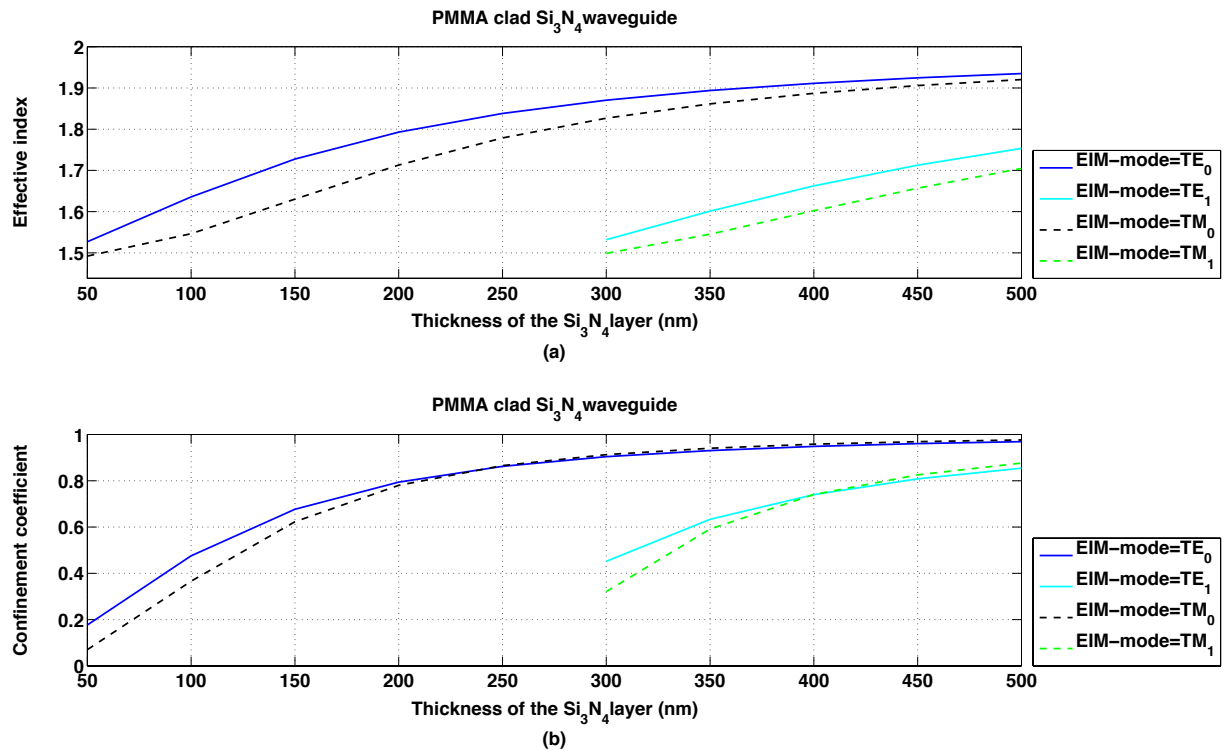


Figure III.11: Calculated 1D effective index of transverse modes at 633 nm in the PMMA clad waveguide (see Figure III.8.(c)).

b. 2D mode calculation

In order to study a rectangular Si_3N_4 waveguide, we are now considering the 2D waveguide structure shown in Figure III.4.(b). The origin of coordinates has been chosen in the middle point of the Si_3N_4 core-lower SiO_2 cladding, and the Cartesian coordinate system is the same as in the analysis of 1D EIC. The EIM calculated 2D effective indexes are plotted in Figure III.12, Figure III.14 and Figure III.16, corresponding to the different 1D Si_3N_4 waveguides shown in Figure III.8.(a), (b) and (c), respectively. We scanned the Si_3N_4 rectangular waveguide's width from 50 nm to 1000 nm with a step size of 50 nm. Meanwhile, the 2D confinement coefficient curves are plotted in Figure III.13, Figure III.15 and Figure III.17. In general, EIM provides us an efficient calculation method for a supposed pure TE modes and pure TM modes within a layered 1D or rectangular 2D dielectric waveguide. As shown in Figure III.4(b), we used the effective index method to calculate the transverse field

components E_y (or H_x) and H_y (or E_x) for the fundamental and the 1st order guided modes, in order to find the cut-off dimensions of rectangular dielectric waveguide for the purpose of single-mode application.

b.1 Unclad waveguide

Supposing the guided mode has always a 2D effective index inferior to the Si_3N_4 's refractive index but superior to the cladding material's highest refractive index, we find only one guided mode in the 100 nm-thick unclad waveguide, which is the fundamental TE mode TE_{00} . Similarly to the 1D effective index's characteristic, increasing the thickness from 100 nm to 150 nm could exceed the threshold thickness of 1D single-mode in the unclad waveguide. The first TM-like guided mode comes up when the width of 150 nm-thick waveguide is increased to 300 nm. However, once we slightly increase the thickness of waveguide to 200 nm, the TM_{00} mode could be excited at the same time of TE_{00} mode when the width of waveguide is going up to 300 nm. Moreover, we find always an intersection point between the width-dependent 2D effective index curves of TE_{00} and TM_{00} modes in this rectangular waveguide with a thickness larger than 200 nm. Before the intersection point, the TM_{00} mode would even have a slightly smaller cutoff width than the one of TE_{00} mode. Once the width continues to increase after the intersection point, the effective index of TE_{00} mode would rise faster than the TM_{00} mode with the increase of waveguide's width.

On the contrary, the guided TM modes in the unclad waveguide are confined strongly and even have a higher confinement coefficient than the TE modes of the same-order (see Figure III.13). Consequently for the purpose of TE mode's application, the unclad waveguide is not a good choice due to its tolerance of TM modes and weak index.

b.2 SiO_2 cladded waveguide

We studied the symmetric SiO_2 cladded waveguides by comparing the results obtained with two different calculations. Firstly, the EIM has been applied to scan a large range of rectangular dimensions for the calculation of 2D effective index of fundamental and 1st-order TE/TM modes and their confinement coefficient as well.

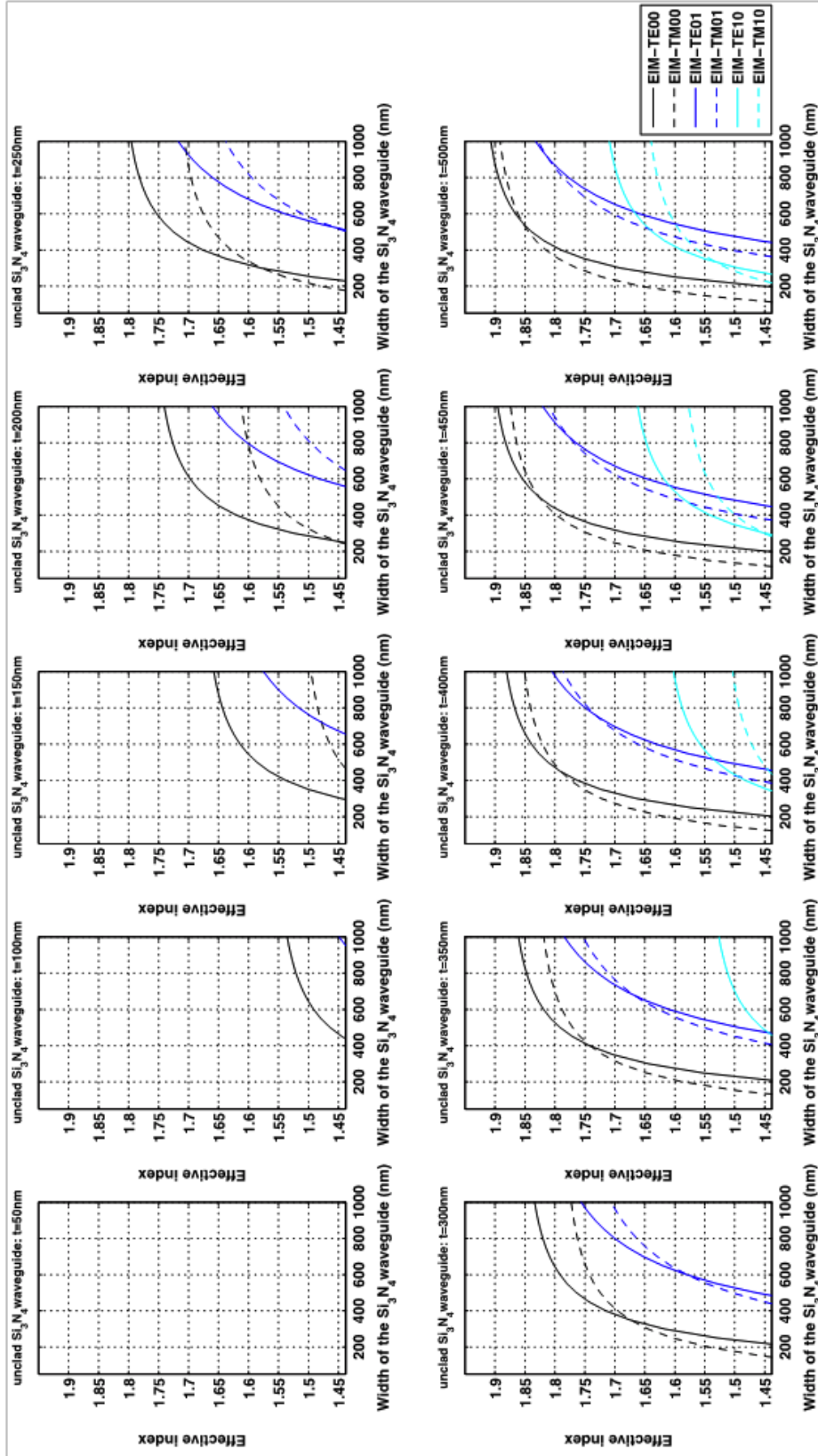


Figure III.12: Calculated 2D effective indexes of TE/TM modes at 633 nm in the unclad Si_3N_4 waveguide.

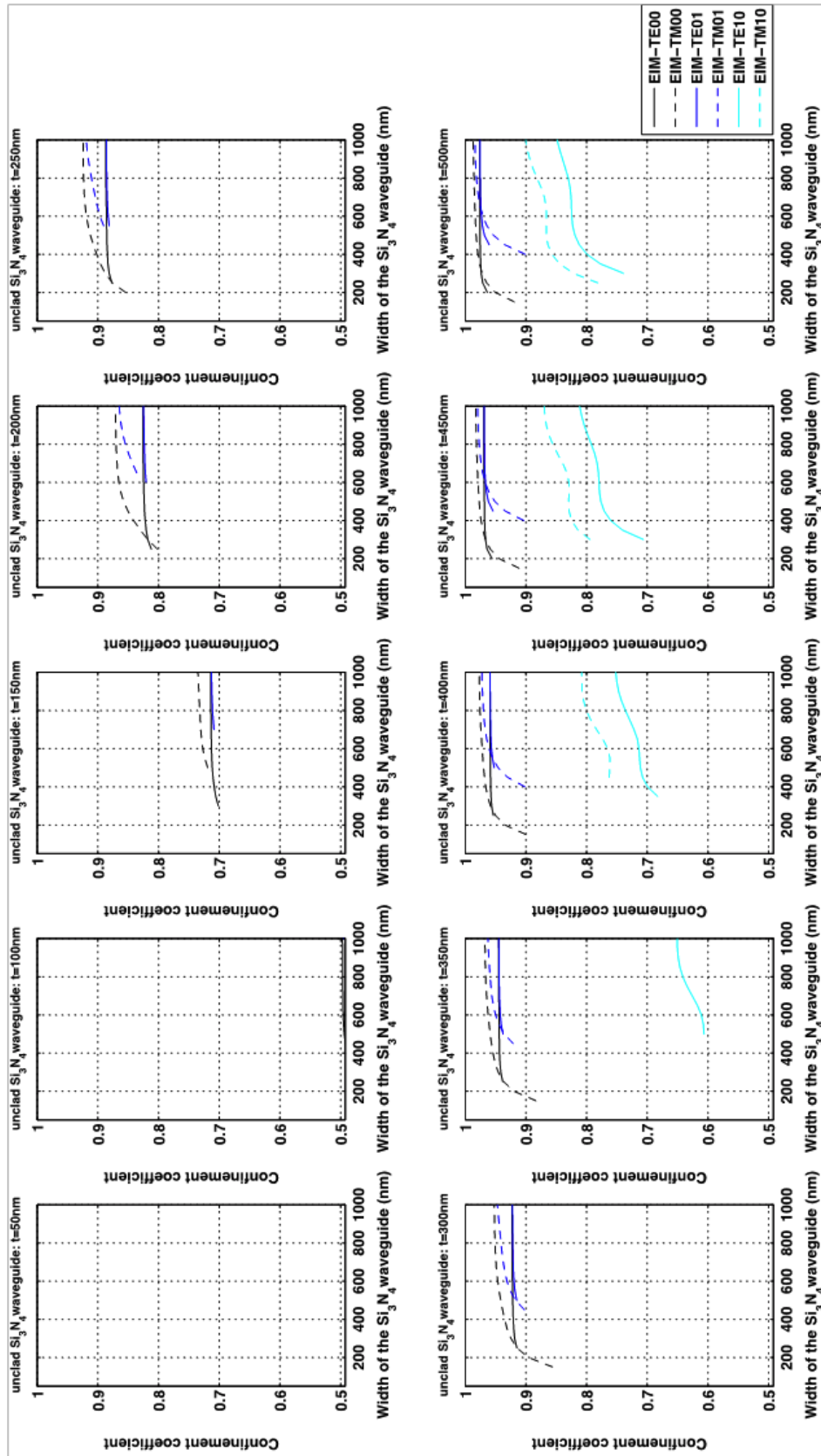


Figure III.13: Calculated 2D confinement coefficients at 633 nm of the unclad Si_3N_4 waveguide.

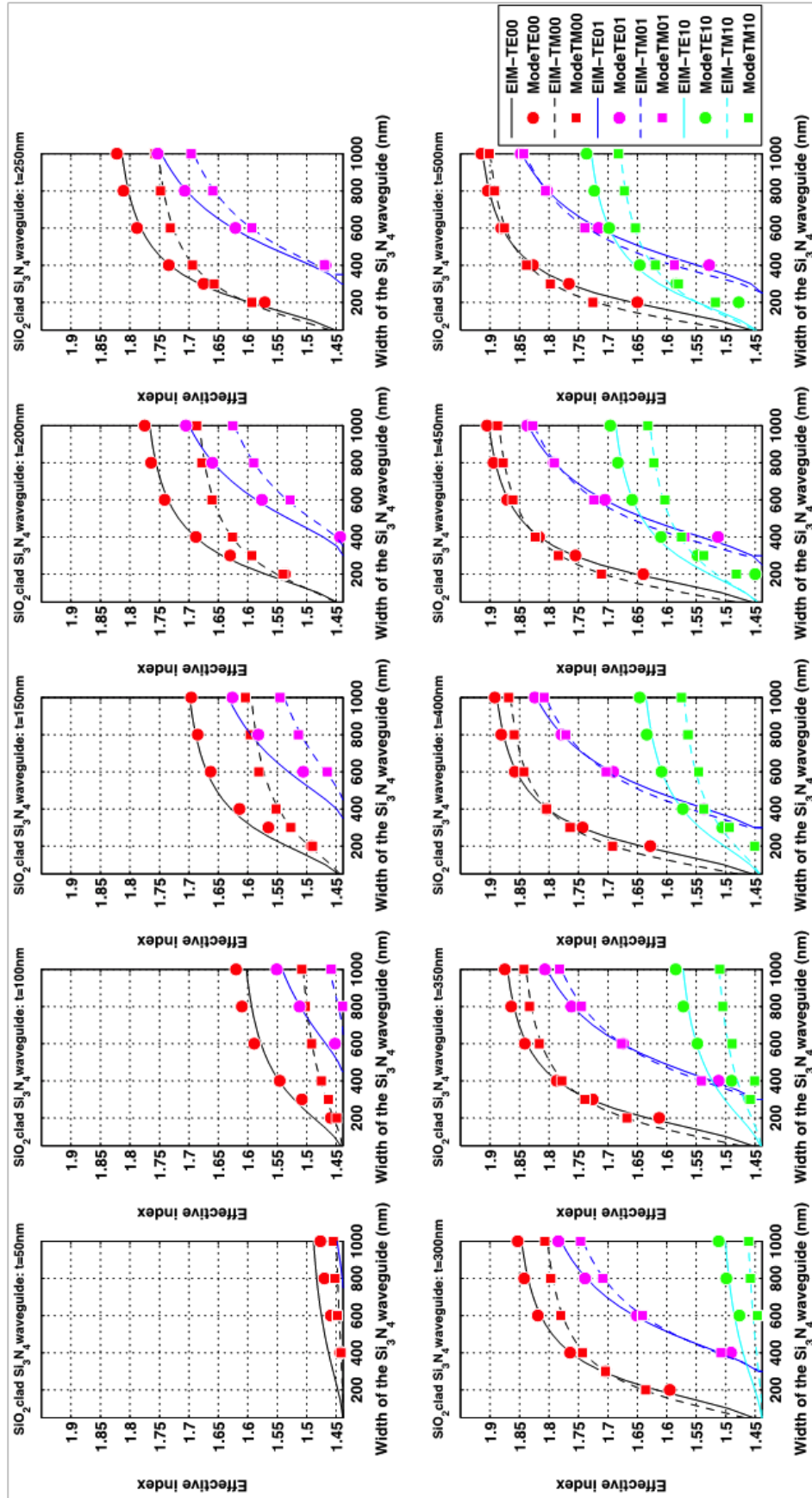


Figure III.14: Calculated 2D effective indexes of TE/TM modes at 633 nm in the SiO₂ cladded Si₃N₄ waveguide.

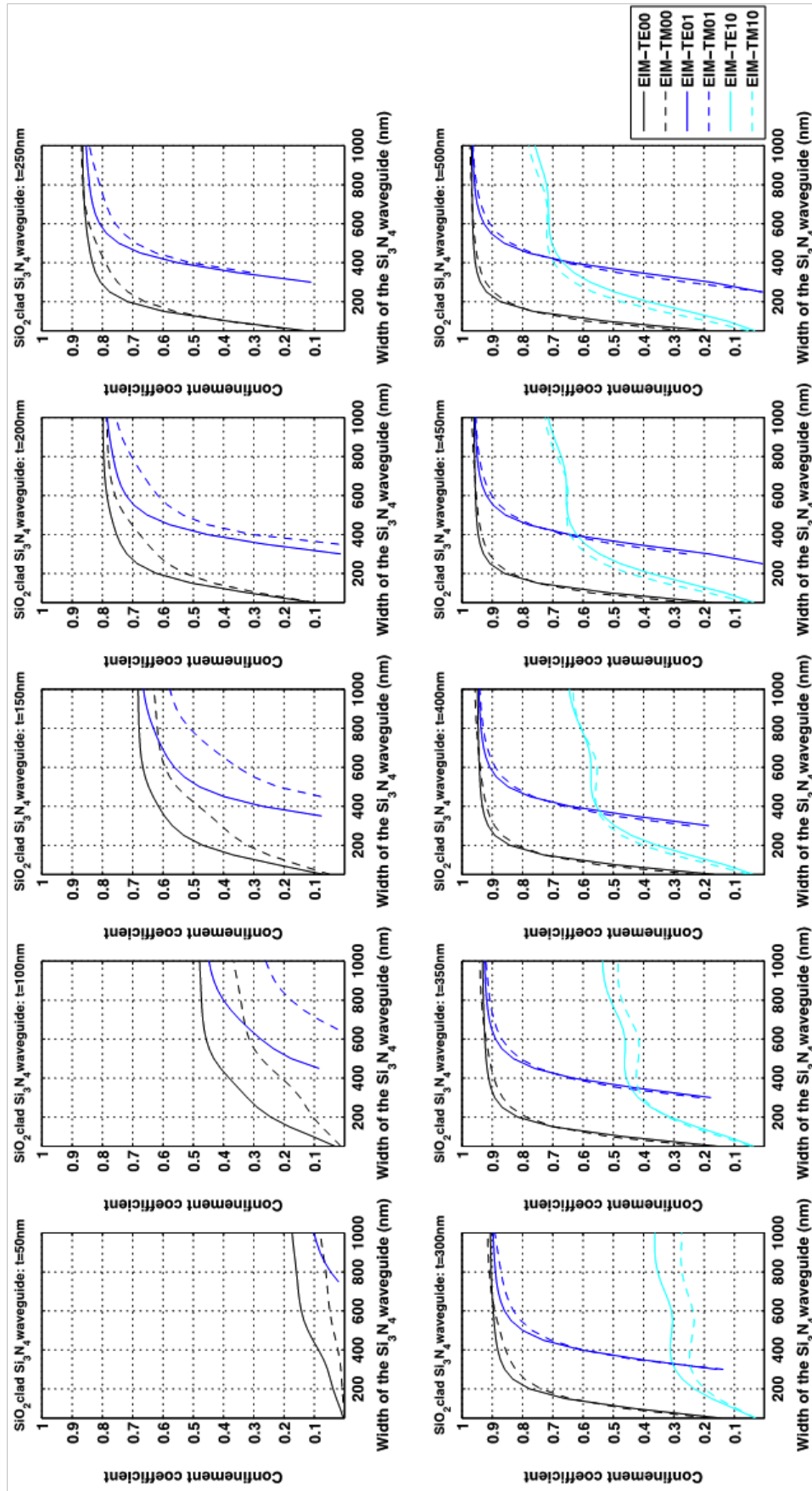


Figure III.15: Calculated 2D confinement coefficients at 633nm in the SiO_2 cladded Si_3N_4 waveguide.

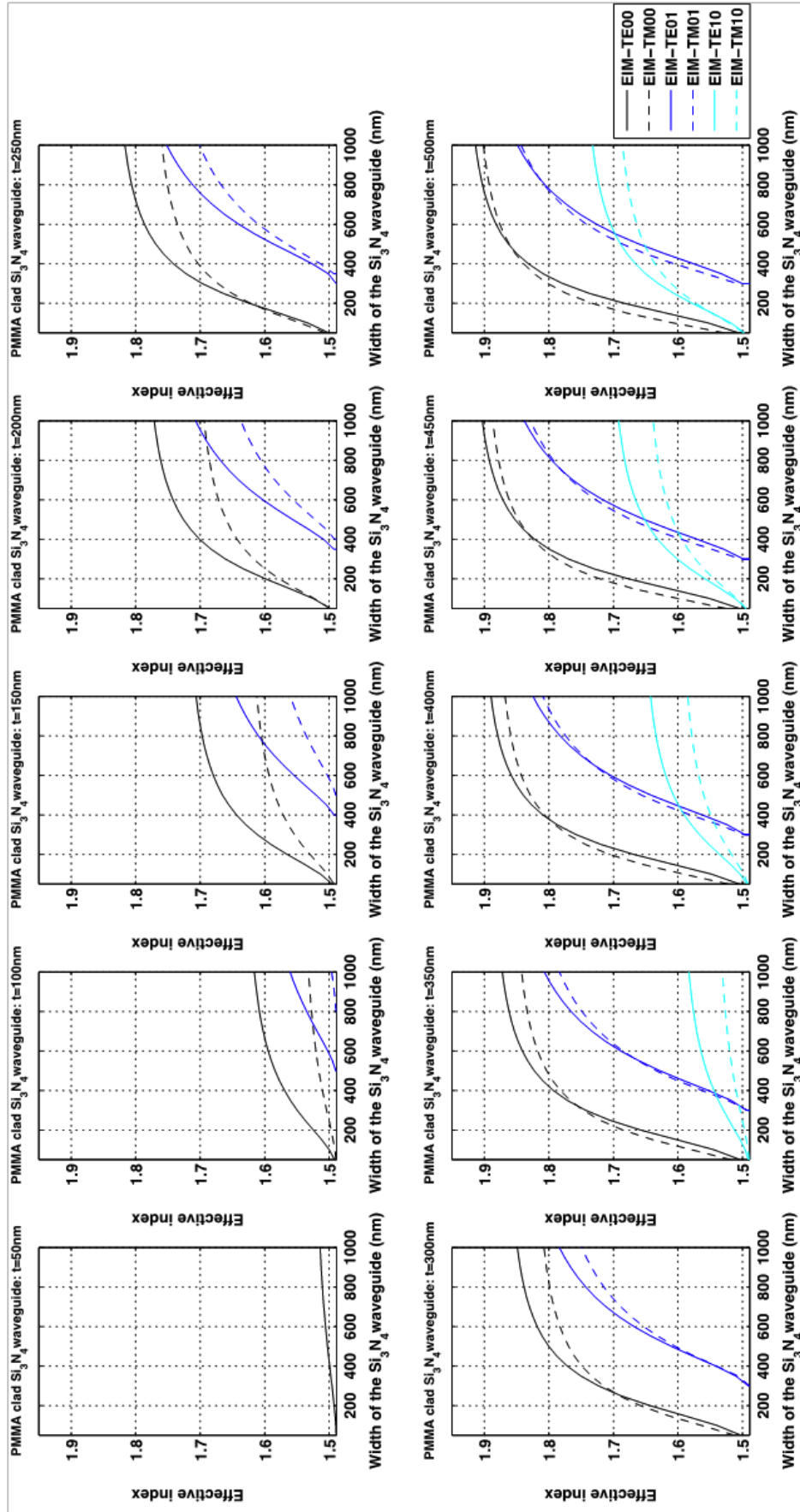


Figure III.16: Calculated 2D effective indexes of TE/TM modes at 633 nm in the PMMA clad Si₃N₄ waveguide.

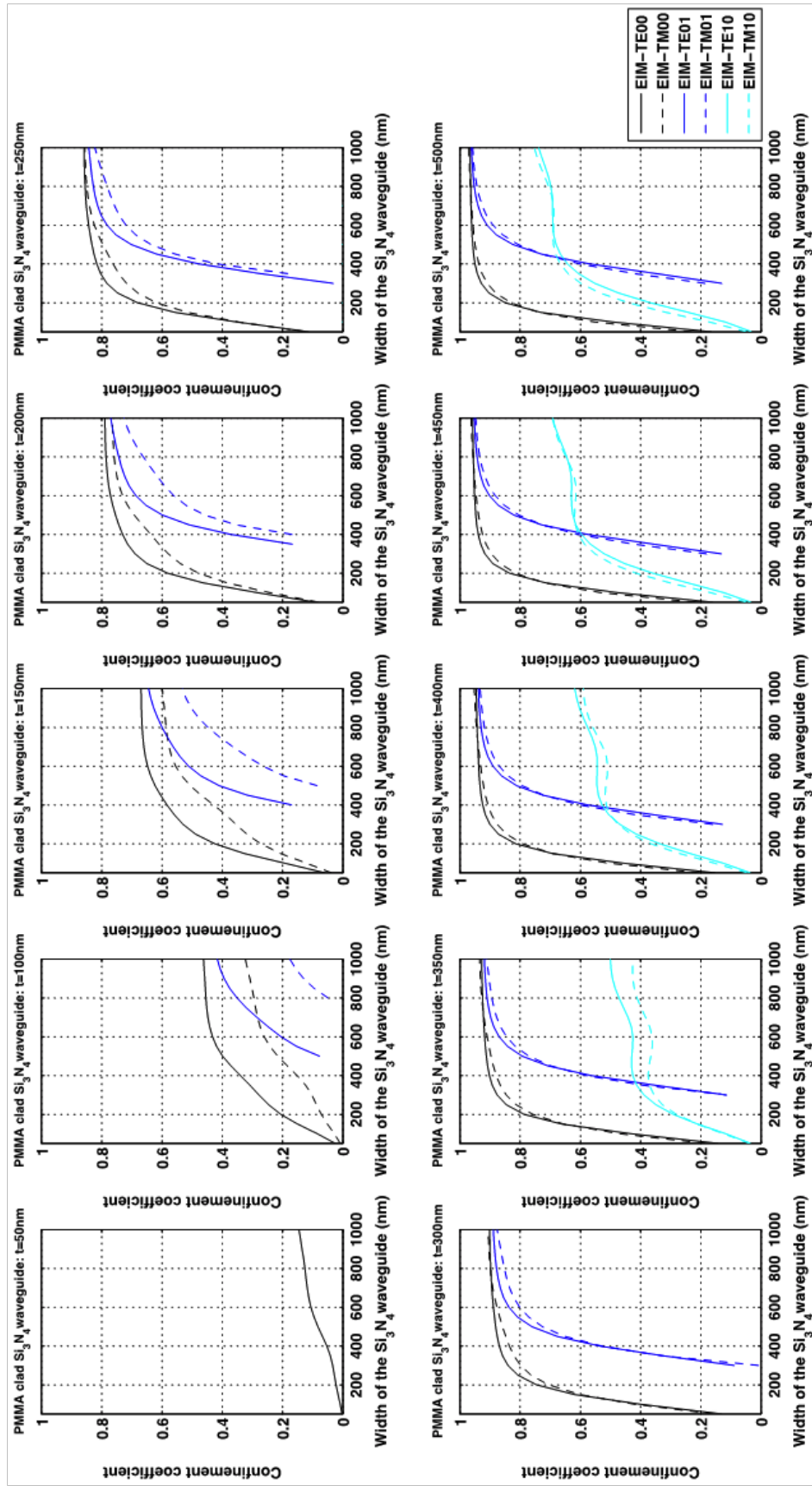


Figure III.17: Calculated 2D confinement coefficients at 633 nm in the PMMA clad Si_3N_4 waveguide.

Secondly, we used the LUMERICAL mode solver to calculate the guided modes in the thickness-varied Si_3N_4 waveguide with several selected widths, i.e.: 200 nm, 300 nm, 400 nm etc. As shown in Figure III.14, there is a good agreement of calculated 2D effective index curves between the EIM's scalar method and mode solver's vectorial method except for the relatively thin and narrow rectangular waveguides. In fact, due to the weak confinement of guided modes, the approximate calculation based on the EIM's scalar algorithm has probably a worse accuracy in the situation of such a small waveguide's dimensions. Considering the result of 2D confinement coefficient shown in Figure III.15, we found that the cut-off width of waveguide for the $\text{TE}_{01}/\text{TM}_{01}$ mode should be close to 300 nm. Comparing to the unclad waveguide's different cut-off width for the same-order TE and TM modes, the cladded waveguide has more similar cut-off widths for the TE_{mn} mode and TM_{mn} mode. However, the TE mode has generally a bigger 2D effective index than the TM mode, as well as its 2D confinement coefficient. The differences of 2D effective index between TE and TM mode becomes very important in a thinner and wider waveguide, but both TE and TM modes would be confined well without a big difference when the thickness of waveguide exceeds the 250 nm cut-off thickness. A comparison of mode solver calculated modes between $250 \text{ nm} \times 300 \text{ nm}$ and $500 \text{ nm} \times 300 \text{ nm}$ waveguides is presented in Table III-2. As shown in Table III-2.(I), LUMERICAL's mode solver has found only two guided modes with an effective index superior to the SiO_2 's refractive index in the SiO_2 cladded symmetric waveguide, in the case of the $250 \text{ nm} \times 300 \text{ nm}$ waveguide.

Table III-2: Mode solver calculated transverse modes at 633 nm in the SiO_2 cladded symmetric Si_3N_4 rectangular waveguide of different cross-section sizes.

No.	Mode1	Mode2	Mode3	Mode4	Mode5	Mode6
$t_2(\text{nm})/w(\text{nm})$	Effective index / TE mode E_y -polarization fraction (%)					
I. 250/300	1.675/99 (TE₀₀-like)	1.657/1 (TM₀₀-like)	N.A.	N.A.	N.A.	N.A.
II. 400/400	1.804/100 (TE ₀₀ -like)	1.573/0 (TM ₀₀ -like)	1.573/48 (TM₀₁-like/ TE₁₀-like)	1.539/52 (TE₁₀-like/ TM₀₁-like)	1.537/47 (TM ₁₀ -like/ TE ₀₁ -like)	1.487/52 (TE ₀₁ -like/ TM ₁₀ -like)
III. 500/300	1.798/0 (TM ₀₀ -like)	1.766/100 (TE ₀₀ -like)	1.584/96 (TE₁₀-like)	1.58/2 (TM₁₀-like)	1.465/2 (TM₀₁-like)	N.A.

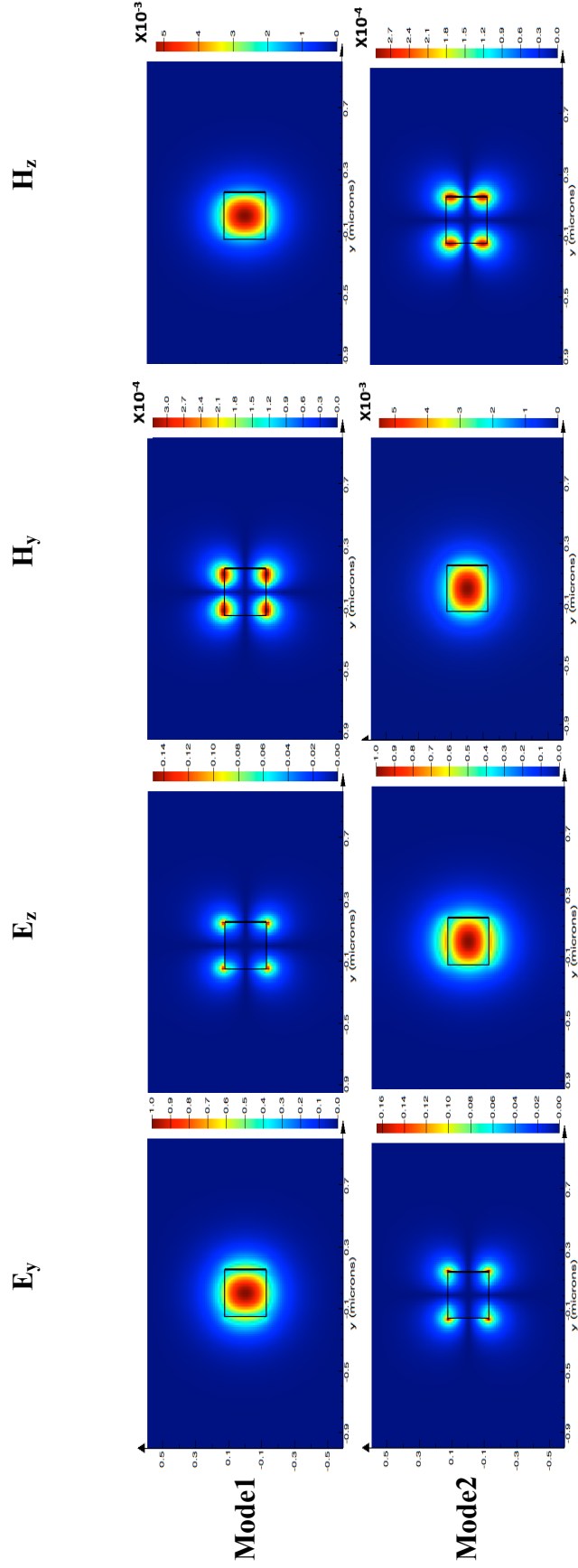


Figure III.18: The 1st and 2nd mode's E-/H-field components in a 250 nm × 300 nm waveguide.

We present in Figure III.18 the mode solver calculated y-direction and z-direction components of the electric and magnetic fields (E_y/E_z and H_y/H_z) corresponding to the transverse **Mode1** and **Mode2**. By the way, we used the same Cartesian coordinates system as shown in Figure III.8. As shown in Figure III.18 none of the y-direction or z-direction component of either E-field or H-field was null. The mode solver calculated **Mode1** and **Mode2** are thus hybridized by both of TE-like and TM-like transverse modes. However, **Mode1**'s E_z component's intensity profile is much weaker than the one of its E_y component. Meanwhile E_z component has a close-to-corner intensity distribution, which can't be strongly confined in the rectangular waveguide. But the round-like **Mode1**'s E_y has a higher confinement coefficient. From the viewpoint of the transverse modal field's profile, the **Mode1** could be totally regarded as TE mode. On the other hand, the **Mode2** is a quasi-TM mode. Therefore, we found that the effective index of the **Mode1** and **Mode2** calculated by mode solver coincide in Figure III.14 with the EIM calculated effective index curves of TE fundamental mode (TE_{00}) and TM fundamental mode (TM_{00}), respectively. At the same time, according to the EIM's 2D confinement coefficient calculation shown in Figure III.15, the TE_{00} modal field's confinement in the rectangular waveguide is higher than the TM_{00} mode. In fact, if we compare only the E-field intensity profile along y-direction and z-direction, we could have agreement with what EIM has predicted. Finally, in the $250 \text{ nm} \times 300 \text{ nm}$ waveguide, the **Mode1** with effective index of 1.675 is quasi-TE mode because 99% of E-field is distributed along y-direction. On the contrary, the **Mode2** is quasi-TM mode.

Hybridization effect in SiO_2 cladded waveguides

An interesting equal density TE/TM hybridization effect has been observed in some SiO_2 cladded waveguides, which have specifically square-like cross-section. For instance, for the dimensions of $400 \text{ nm} \times 400 \text{ nm}$ and $500 \text{ nm} \times 500 \text{ nm}$ shown in the curve of the 2D EIM-calculated effective index, TE_{01} mode and TE_{10} mode intersect with TM_{10} mode and TM_{01} mode, respectively. We investigate here the modal field distribution (including total E-field, E-field's y-direction and z-direction components and H-field's y-direction component) of the first and second non-fundamental modes (**Mode3** and **Mode4** in Table III-2) calculated by the mode solver for the SiO_2 cladded $400 \text{ nm} \times 400 \text{ nm}$ Si_3N_4 waveguide. The modal fields of the $400 \text{ nm} \times 400 \text{ nm}$ waveguide are presented in Figure III.19.

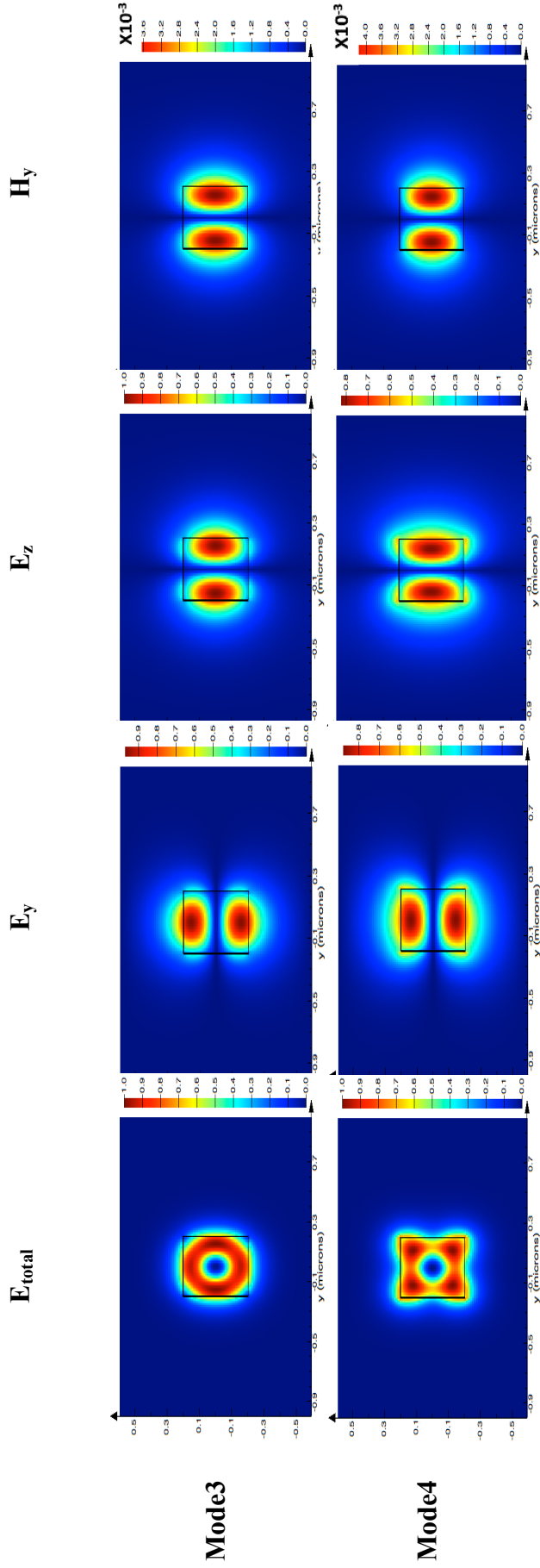


Figure III.19: The 3rd and 4th mode's E-/H-field components in a 400 nm × 400 nm waveguide.

As shown in Figure III.19, for the **Mode3**, the intensity of E_z is slightly stronger than the one of E_y . This difference could be also quantitatively presented by the mode solver calculated TE mode E_y -polarization fraction. Shown in Table III-2, the **Mode3** has a TE mode refraction of 48%, therefore the hybrid **Mode3** is slightly dominated by the TM-like mode. Similarly, the **Mode4** is slightly dominated by the TE-like mode. Moreover, the **Mode3**'s E_y and E_z intensity patterns are very similar but with a 90° rotated distribution: the E_y has two symmetric spots arranged in a column and the E_z 's two spots are in a row. In other words, the **Mode3** has a hybrid transverse mode of TE_{10} and TM_{01} . Similarly, the **Mode4** is also hybridized by TE_{10} and TM_{01} .

However, the **Mode3** has a larger effective index than the **Mode4**. Moreover, from the viewpoint of total E-field, it has a ring-like pattern and the **Mode4** has a square-like pattern. In fact, the TE_{10} -like field distributions of E_y and the TM_{01} -like field distributions of H_y (or E_z) are also different for the **Mode3** and **Mode4**. As shown in Figure III.19, E_y and E_z fields seem to be confined in the square waveguide in the **Mode3** more strongly than in the **Mode4**. Consequently, the total E-field in the **Mode3** should have a higher confinement coefficient than in the **Mode4**, as also suggested by the index effective index.

On the other hand, the **Mode5** and **Mode6** are similar to the **Mode3** and **Mode4** except the **Mode5** and **Mode6** are hybridized by different TE_{01} -like and TM_{10} -like modes. In one word, this symmetrically cladded dielectric waveguide with a cross-section close to square would excite at the same time several hybrid transverse modes, which have comparable quasi- TE_{01}/TM_{10} or quasi- TE_{10}/TM_{01} 's E_y -field/ H_y -field distribution but with different confinement coefficient. As the result, each hybrid mode has a different total E-field intensity pattern and a different 2D effective index.

For the purpose of compatibility with other integrated components, introducing these hybrid modes in our Si_3N_4 waveguide is not recommended. TE_{01} and TM_{01} -like modes could be easier split over from the bended Si_3N_4 waveguide.

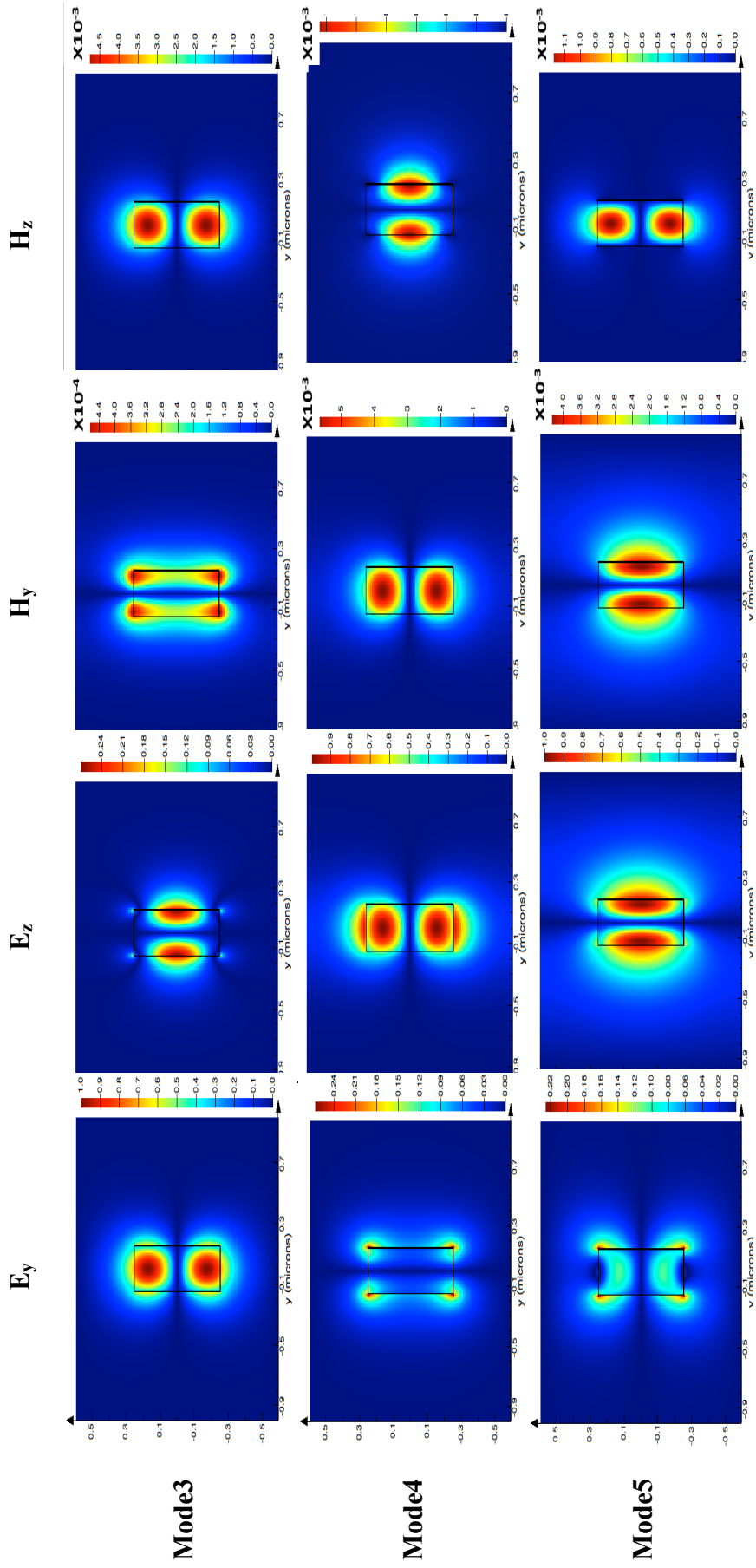


Figure III.20: The 3rd, 4th and 5th mode's E-/H-field components in a 500 nm × 300 nm waveguide.

We studied also the waveguide with a narrow but thick cross-section, for example $500 \text{ nm} \times 300 \text{ nm}$ from the model field's viewpoint. In that case high order modes can remain laterally monolobe. As shown in Table III-2, the first mode found by the mode solver is no longer the TE_{00} -like but the TM_{00} -like one due to the dimension's dominance of thickness over width. Moreover, it's easier to excite the $\text{TE}_{10}/\text{TM}_{10}$ mode rather than the $\text{TE}_{01}/\text{TM}_{01}$ mode in this waveguide. The E-field/H-field's y-direction and z-direction components of the first 3 non-fundamental transverse modes found by the mode solver are presented in Figure III.20. The **Mode3** is mainly dominated by the TE_{10} modes, but there is still a few TM_{01} -like mode showed in the E_y and H_z components. On the opposite, the **Mode4** and **Mode5** are dominated by the TM_{10} and TM_{01} modes, respectively. Meanwhile the TM_{10} mode has a bigger effective index and thus a higher confinement coefficient than the TM_{01} mode. However, for the TE single-mode application in the expected passive PIC, due to the presence of high-order TM modes, this cross-section of Si_3N_4 waveguide is not acceptable. By the way, it's also more difficult to fabricate a thick and narrow rectangular waveguide with a smooth and vertical sidewall.

b.3 PMMA cladded waveguides

The last study case corresponding to the Figure III.8.(c) is involved in the non-symmetric Si_3N_4 waveguide covered by the other suitable cladding material, for example PMMA. The EIM calculated 2D effective index and the confinement coefficient curves for a PMMA cladded Si_3N_4 waveguide are presented in Figure III.16 and Figure III.17, respectively.

As shown in Figure III.16, the PMMA cladded waveguide shows in general the same evolution tendency as the SiO_2 cladded waveguide. However, there are still two remarkable points to be pointed out. Firstly, due to the slight difference between the refractive index of SiO_2 and PMMA, there would be a different start value of effective index for each induced transverse mode and also a different cut-off width for the non-fundamental TE/TM modes. On the other hand, when the cross-section size becomes much larger than the single-mode limited size, the effective index would tend to a limit value, which is identical to the other cases. Finally, even without a vertical symmetry of 2D index-contrast comparing to the SiO_2 cladded waveguide, once the waveguide's cross-section goes close to a square, the $\text{TE}_{10}/\text{TM}_{01}$ and $\text{TE}_{01}/\text{TM}_{10}$ hybrid modes would be induced just like in the SiO_2 cladded case.

III.1.4 Conclusion

In this part, we presented our work on the design and simulation of rectangular Si_3N_4 waveguide, especially cladded in a homogeneous SiO_2 environment. The symmetric refractive index distribution around the rectangular waveguide allows excitation of strongly confined quasi- TE_{00} modes with a symmetric modal field distribution, which is very useful for our TE single-mode PIC. We have also evaluated first order mode waveguides, with the objective to use wider waveguides with anyway very low high order mode confinement. Reduced propagation losses are expected in that case, as well as easier technological fabrication. Such a way, several interesting hybrid modes have been observed when the cross-section of the simulated rectangular waveguide tends to be square-like. In general, more high order TE/TM modes would appear with a high confinement coefficient within a thicker or wider rectangular waveguide. Therefore, to keep the TE almost-monomode propagation in the expected PIC, we need to limit the thickness and width of waveguide around the multimode cut-off condition, avoiding too square configurations.

According to our EIM calculation, a first appropriate dimension should be around 250 nm \times 300 nm. This would be a reference value to guide our fabrication in cleanroom. By the way, as mentioned in the Chapter II, this tiny cross-section could be a big challenge for low-loss and longhaul light wave propagation.

III.2 VISIBLE PICs BASED ON $\text{Si}_3\text{N}_4/\text{SiO}_2$ PLATFORM

The objective of this sub-chapter is to evaluate the different optical components based on the SiO_2 cladded Si_3N_4 waveguide platform for the design of the complete 633 nm single-mode PIC as described in the Chapter I. The main elementary integrated devices are the $1 \times N$ optical splitters and the bent waveguides. In order to design these integrated passive devices, we have used analytical solution and optical 2D+z simulation software, Photon Design FIMMPROP®. At first, we will present our bibliographic research on the mainstream integrated optical splitters and compare their compatibilities with our expected uniform and coherent beam splitting system. Then we will focus on the evaluation and design of the multimode interference (MMI) coupler based $1 \times N$ splitter. Finally, we will introduce a bent waveguide's design inspired from the Lemniscate of Bernoulli.

III.2.1 Review of $1 \times N$ light beam splitters

a. Y-junctions splitter

A basic 1×2 Y-junctions optical-wavelength beam splitter has been largely studied as one of the most important and most compromising elements in the PICs. *Izutsu et al.* explained the working mechanism of single-mode optical-wavelength Y-junctions 1×2 splitter from the viewpoint of guided mode's field distribution [IZUTS81]. As shown in Figure III.21, we present schematically here a conventional single-mode Y-junctions 1×2 coupler and the guided TE modes field distribution, as well as the effective indexes variation along the propagation direction.

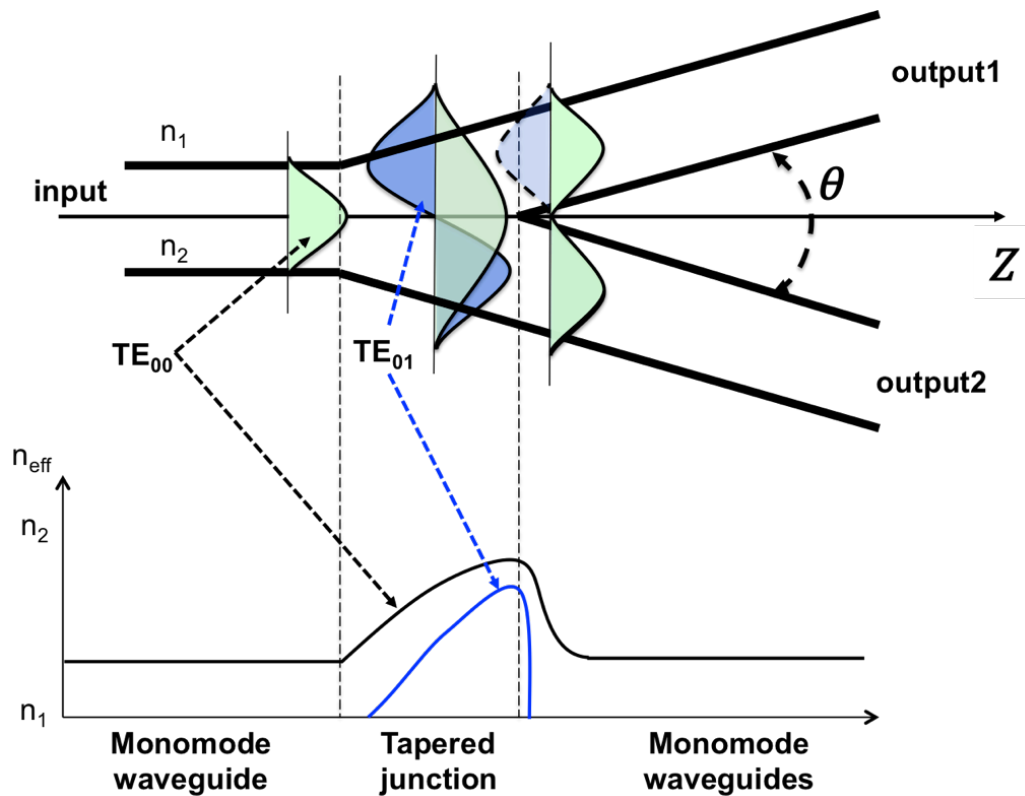


Figure III.21: Guided TE mode's field distribution and 2D effective index variation in a conventional single-mode Y-junction splitter with 1 straight-waveguide input and 2 inclined straight-waveguide outputs. n_1 and n_2 are the refractive indexes of the cladding and core materials, respectively, θ is the branching angle of Y-junctions.

In fact, the Y-junctions splitter is composed of the 1st input single-mode waveguide section, the 2nd tapered Y-junctions section and the 3rd output single-mode branching-waveguides section. In the beginning, the fundamental transverse mode is the only guided

mode with a good confinement coefficient in the input and output straight waveguide(s). Once the light wave goes into the Y-junctions section, with a growing waveguide's width, the guided fundamental mode's effective index would be increased and other higher order modes would come up as shown in Figure III.14. Generally, the tapered section-induced higher mode has a smaller effective index and confinement coefficient rather than the fundamental mode.

According to *Izutsu*, once the branching angle is small enough to permit application of the local normal modes theory, there should be only two types of mode, the even mode and the odd mode, which would exist in the tapered section. In the case of SiO₂ cladded Si₃N₄ rectangular waveguide, the fundamental mode TE₀₀ and the 1st-order mode TE₀₁ could be the analogy to the even mode and the odd mode in the local normal modes theory, respectively. At the starting point of this tapered section, both guided modes are propagating in the usual way. However, at the tapered section end connected with the branching section of the single-mode waveguides, only the fundamental mode is supported. The TE₀₁-like mode would be immediately converted into radiation mode at the starting point of the single-mode branching waveguides. This is due to the fact that the waveguide's width would become abruptly much narrower than the TE₀₁ mode's cut-off width. Considering the gradual change of the local normal modes, the important radiation loss at the junction should be always taken into account. In other words, for the purpose of single-mode optical power splitting with low loss, the branching angle should be very small to limit the transfer of power into high order mode, which could thus become radiation mode.

With the development of the planar lightwave circuits (PLC), these Y-junctions are widely used to realize more outputs optical power splitters in the communication-wavelength domain. *Takahashi et al.* reported design and fabrication of 1 × 128 Y-junction like symmetric Si-based power splitters with a measured average excess loss (EL) of 3.2 dB [TAKAH91]. *Hida et al.* fabricated a 1 × 32 silica-based splitters with a size of 6 × 24 mm² [HIDA98]. Some more compact 1 × 2^N branches optical power splitters with N-stage cascade Y-junctions came up during the past decade, such as polarization and wavelength independent 1 × 4 splitter [CHUNG06], 1 × 8 field matching splitter [GAMET04], silicon wire based 1 × 16 splitter on SOI [TAO08]. However, research on the Si₃N₄ waveguide based Y-junctions splitter in a visible light PIC is rare. The reason should be due to a considerable radiation loss in the tapered section induced by the weak index contrast between the core and cladding materials and relatively narrower waveguides for visible single-mode application.

b. Arrayed-waveguiding grating

Since we mentioned the popular usages of Y-junctions beam splitter in the telecommunication domain, we must point out here another important optical splitting device, the $N \times N$ arrayed-waveguide grating, which has been widely studied for the wavelength-division multiplexing (WDM) networks.

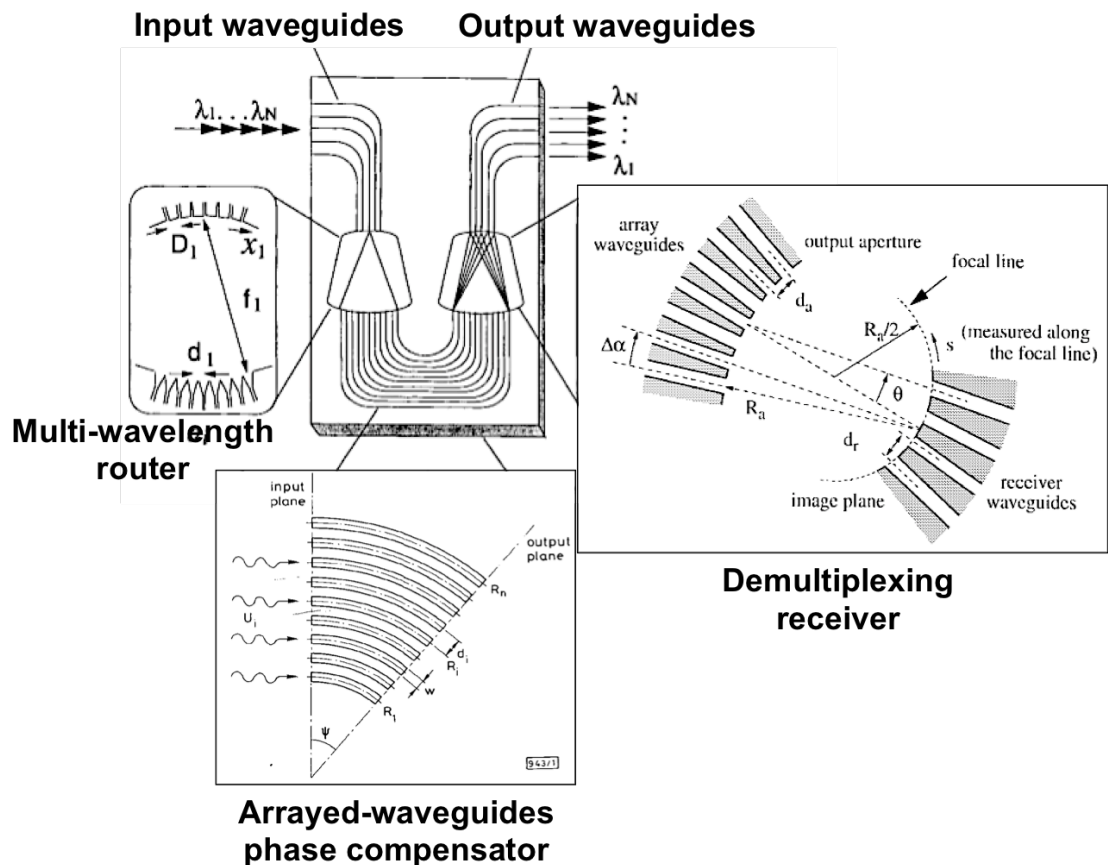


Figure III.22: Schematic configuration of conventional arrayed-waveguide grating multiplexer applied in a WDM system (reference [SMIT88], [SMIT96] and [OKAMO98]).

As shown in Figure III.22, there are 5 main elementary devices in the arrayed-waveguide grating multiplexer. The main interest of these structures is the wavelength selection and redistribution due to a wavelength dependent linear phase shift in each arrayed waveguide. More mathematical derivation could be found in [SMIT96, OKOMO98]. This function is not necessary in our case. However several efficient beam splitters have been designed for these PHASAR-like demultiplexers, which could be effectively used for single wavelength application as a multi waveguide splitter.

c. Multimode interference (MMI) coupler

Since 90', many of multimode interference (MMI) couplers have been widely reported to show their good performances for optical-wavelength beam's splitting. The main part of a conventional MMI device is a wide rectangular waveguide designed to support a large number of guided modes and then to excite the multimode interference effect. We present in Figure III.23 the schematic configuration of a conventional 1×2 MMI coupler based beam splitter, as well as the multi-TE mode field distribution and 2D effective indexes. For such a step-index rectangular MMI coupler, the EIM calculation results shown in Figure III.14 and Figure III.15 could be used to analysis the E-fields of guided transverse modes.

Generally, in a thin and wide MMI coupler (i.e.: $250 \text{ nm} \times 1 \text{ }\mu\text{m}$), the fundamental TE mode always has a larger 2D effective index than the other high order modes (see Figure III.14). However the TE_{01} mode could be confined in the Si_3N_4 waveguide as strongly as the TE_{00} (see Figure III.15). Once the width of the MMI coupler exceeds the cut-off condition, there would be some more TE high-order modes coming up. As shown in Figure III.23, we can simplify this planar device's schematic model from 3D to 2D because the thickness of each waveguide is fixed to a constant (i.e.: 250 nm). At the end of MMI coupler, we can find at some specific positions the input field's self-imaging pattern due to the interference. By adding a certain number of output waveguides, the uniform split light beams could be extracted from the MMI coupler. The design of conventional MMI coupler is thus involved in the self-imaging principle.

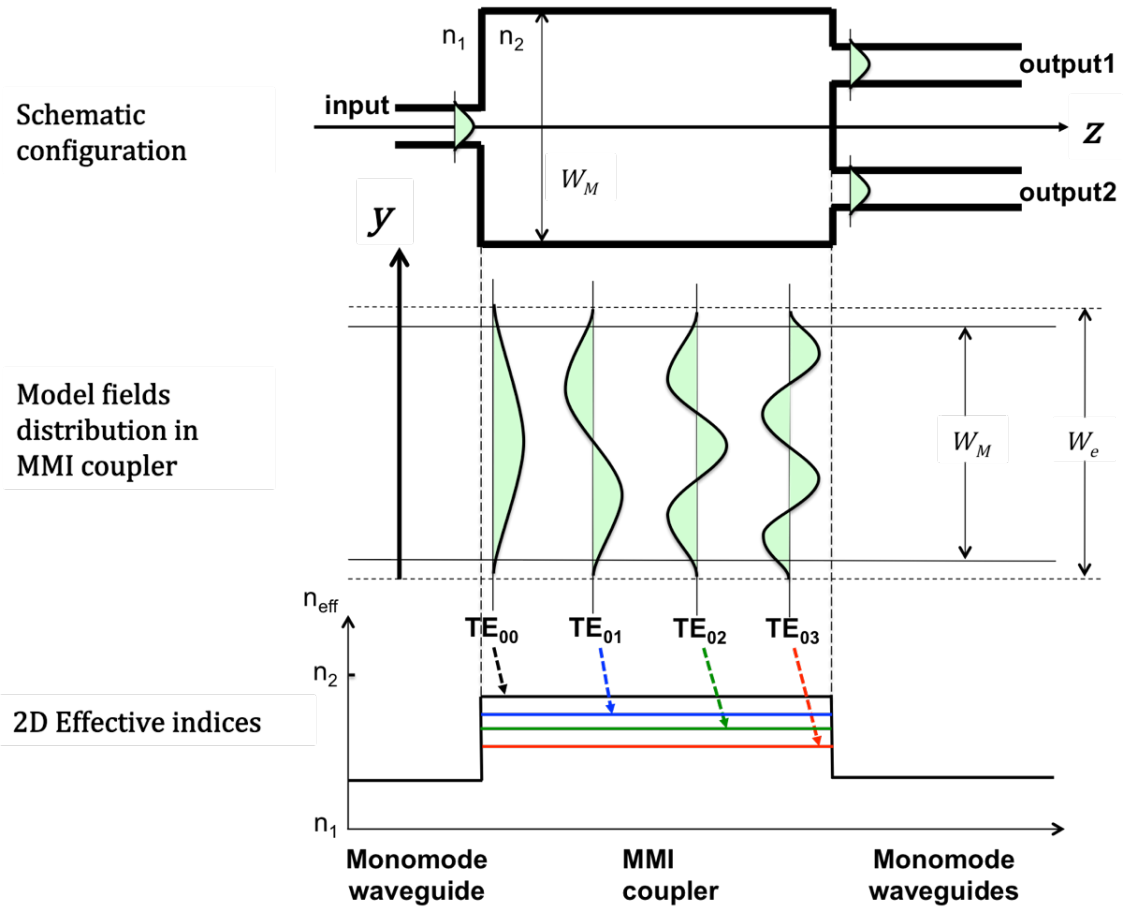


Figure III.23: Operation mechanism of a conventional 1×2 MMI coupler based beam splitter. W_M and W_e are the physical width and the effective width of the MMI coupler, respectively.

c.1 Principle of the self-imaging interference in a symmetric $1 \times N$ MMI coupler

Soldano et al. explained the conventional MMI coupler's operation mechanism from the aspect of input guided mode's self-imaging due to the strict interference [SOLDA95]. In fact, the self-imaging principle relies on the reproduction of input E-field profile in single or multiple images at periodic intervals along the propagation direction. According to the dispersion equation, the propagation constant for the m^{th} TE mode can be noted as:

$$\beta_m^2 = k_0^2 n_{eff1D}^2 - k_{ym}^2 \quad (\text{III-13})$$

with:

$$k_0 = \frac{2\pi}{\lambda_0} \quad (\text{III-14})$$

$$k_{ym} = \frac{(m+1)\pi}{W_{em}} \quad (\text{III-15})$$

where W_{em} is the effective width for the m^{th} TE mode's propagation in the W_M -wide MMI coupler. Theoretically W_{em} is slightly larger than W_M because of the presence of the *Goos-Hänchen* shift at the MMI coupler's lateral boundaries. However, in a high index-contrast waveguide, the guided mode's leakage into the cladding material is enough weak to eliminate the difference of penetration depths which depends on the order of TE modes. By the way, as we can see in Figure III.15, in a $1\mu\text{m}$ -waveguide, TE_{01} mode could also be strongly confined in the waveguide. Therefore, the m^{th} TE mode is supposed to be confined in the waveguide as well as the confinement for the TE_{00} . We could thus replace W_{em} by a constant W_e [ULRIC78]:

$$W_{em} \approx W_e = W_M + \frac{n_{SiO_2}^2 \lambda_0}{\pi n_{eff1D}^2} (n_{eff1D}^2 - n_{SiO_2}^2)^{-\frac{1}{2}} \quad (\text{III-16})$$

By substituting W_{em} in (III-15) and using the binomial expansion of (III-13) under the condition of $k_{ym} \ll k_0$ when $W_{em}/\lambda_0 \gg (m+1)/2$, we obtain the propagation constant for the m^{th} TE mode:

$$\beta_m \approx k_0 n_{eff1D} - \frac{(m+1)^2 \pi \lambda_0}{4 n_{eff1D} W_e^2} \quad (\text{III-17})$$

Meanwhile, we define the beat length between two lowest-order TE modes:

$$L_{2\pi} = \frac{2\pi}{\beta_0 - \beta_1} \quad (\text{III-18})$$

Therefore we obtain half beat length as a function of TE mode's effective width:

$$L_\pi = \frac{\pi}{\beta_0 - \beta_1} \approx \frac{4 n_{eff1D} W_e^2}{3 \lambda_0} \quad (\text{III-19})$$

There is a quadratic relation between the effective width and the beat length in a conventional MMI coupler. In general, for the $1 \times N$ MMI splitter, the position and the distance of the 1^{st} N -fold self-imaging patterns could be noted as follows:

$$P_N = \pm \frac{W_e}{2N}, \left(\pm \frac{3W_e}{2N}, \pm \frac{5W_e}{2N} \dots \right) \quad (\text{III-20})$$

$$L_N = (3/4N)L_\pi$$

As a result, there is a quadratic relation between the symmetric $1 \times N$ MMI coupler based beam splitter's width and length. Therefore for the conventional MMI couplers with the same number of outputs, increasing the spacing of the output waveguide results in increasing more the total length of MMI coupler. The beam splitter will occupy much more space in the horizontal (propagation) direction than in the vertical (lateral) direction.

c.2 MMI coupler based $1 \times N$ ($N \gg 2$) beam splitting applications

To our knowledge, the conventional MMI couplers have been used to fabricate the $1 \times N$ ($N \gg 2$) beam splitter by connecting directly N identical outward waveguides at the right hand side. Although the width of such a multi-output MMI coupler is quite large comparing with the input/output access waveguides, the growth of the MMI coupler's length could be relatively reduced with increasing number of outputs according to (III-20). We review here some representative applications of MMI coupler multi-output beam splitter.

Rasmussen et al. designed a 1×64 MMI power splitter with total dimensions of $42 \mu\text{m} \times 16 \mu\text{m}$ in SiO_2 used for fiber-optics communication systems [RASMU95]. They reported a minimum excess loss EL of 0.5 dB and nonuniformity NU of 1.7 dB at a wavelength of 1.55 μm . *Lai et al.* reported their silica-on-Si 1×8 MMI coupler with measured EL of 1.3 dB and a maximal unbalance of 0.5 dB during 1.3 – 1.6 μm [LAI97]. *Hosseini et al.* presented their work on design and fabrication of 1-by-12 MMI couplers with a size of 60 μm by 554 μm on a nano-membrane of silicon-on-insulator substrate with a width of waveguide varied from 0.5 μm to 3.5 μm operating at 1.55 μm [HOSSE10]. By the way, according to the report of *Hosseini*, both mathematic derivation and experimental characterization showed that EL and NU depend strongly on the width of the input access waveguide. Generally, a wider waveguide (i.e.: $W_{\text{WG}} > 2.0 \mu\text{m}$) had a much smaller excess loss and nonuniformity than the narrower waveguide (i.e.: $W_{\text{WG}} < 1.0 \mu\text{m}$).

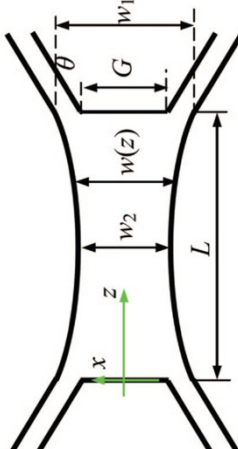
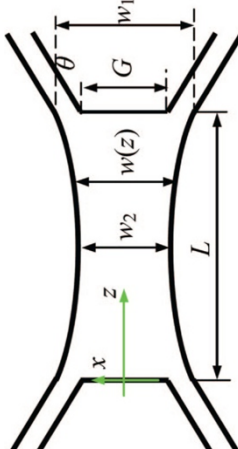
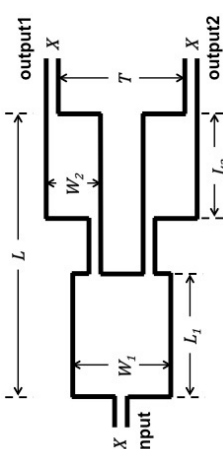
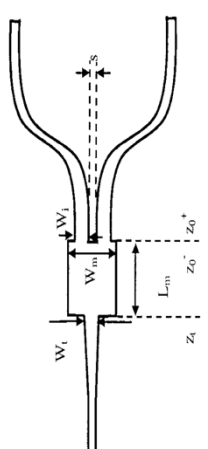
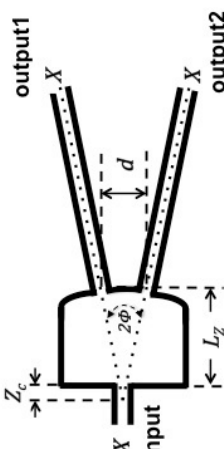
c.3 State-of-the-art 1×2 or 3dB beam splitters

We list in Table III-3 a comparison between several state-of-the-art 3dB optical power splitters. Typically these passive devices have been used for telecommunication wavelengths. They are thus usually based on SOI and InP/InGaAsP waveguide platform. The parabolically tapered MMI has a remarkably reduced length of the MMI coupler, but its non-uniformity between the two split beams became more and more considerable when the spacing between the outputs is increasing. The cascaded symmetric-asymmetric MMIs design overcame well the issue of non-uniformity comparing to the parabolic MMI coupler, but the splitting efficiency became worse. The Y-junctions based splitter is more suitable for the WDM application, in which the width of the waveguides is relatively bigger comparing to the TE/TM single-mode application. In fact, the conventional compact Y-junction splitters have more radiation leakage for narrower rib or rectangular waveguides, in which the index contrast is very low between cladding at core dielectric materials. The same effect has also been reported for the star-like splitter [CASSA03]. Therefore for our SiO_2 cladded Si_3N_4 rectangular single-

mode waveguide, the Y-junction and star-like splitters have not been considered as ideal candidates.

In a word, we prefer the MMI-based symmetric splitter design for purposes of obtaining better uniformity for the split light fields, as well as decreasing the complexity of fabrication comparing to the high-precision fabrication demand for the star-like couplers.

Table III-3: Comparison between different mainstream 1-to-2 way beam splitter design for PICs.

Type	References	Platform	Structure	Configure	Features
Parabolicall y-tapered 2-to-2 MMI coupler	[LEVY98]	InP-InGaAsP		$W_1/W_2 = 9.3 \mu\text{m}/5.6 \mu\text{m}$ $L_{\text{MMI}} = 66 \mu\text{m}$ $EL^9 < 0.5 \text{ dB}$	40% shorter than a conventional MMI coupler
	[DAI08]	SOI nanowire		$W_1/W_2 = 1.4 \mu\text{m}/1.0 \mu\text{m}$ $L_{\text{MMI}} = 4.7 \mu\text{m}$ $EL = 0.23 \text{ dB}$ & $NU^{10} = 0.75 \text{ dB}$	Suitable for arbitrary shape (variable W_2)
Cascaded 1-to-2 MMI beam splitter	[MASAN03]	InP-InGaAsP		$T = 12 \mu\text{m}$, $X = 2 \mu\text{m}$; $W_1 = 10.67 \mu\text{m}$; $W_2 = 5.33 \mu\text{m}$; $L = 526 \mu\text{m}$; Inherent loss = 0.29dB; $EL = 1.5 \text{ dB}$; $NL = 0.25 \text{ dB}$	50% shorter than a standard 1-to-2 MMI splitter; suitable for WDM application
Y branch with MMI section (Simulation)	[WANG02]	Silica-on-silicon		$W_m = 20 \mu\text{m}$; $W_t = 11.1 \mu\text{m}$; $s = 2 \mu\text{m}$; $W_i = 9.62 \mu\text{m}$; $L_M = 267.6 \mu\text{m}$; $T = 50 \mu\text{m}$; $EL = 0.11 \text{ dB}$	Excellent performance in wide wavelength range with less EL
Star-like ultracompact 1-to-2 way beam splitter	[KOSTE04]	SOI rib		$L_z = 5 \mu\text{m}$, $d = 1.05 \mu\text{m}$; $2\Phi = 8.6^\circ$; $X = 0.9 \mu\text{m}$; $EL = 0.144 \text{ dB}$	Relatively simply design which overcomes the limitation of rib waveguide's low confinement
	[RASIG10]				

⁹ EL: Excess loss of the global devices over straight waveguides, taper and bent waveguides.

¹⁰ NU: Nonuniformity defined by the dB ratio between the two-split outputs intensity.

III.2.2 Design and simulation of beam splitting devices

a. Modelling and simulation

We used commercial software Photon Design FIMMPROP to simulate the Elementary Devices. In fact, FIMMPROP's innovated EigenMode Expansion (EME) algorithm allowed us to model a complex 2D+z structure composed of different-width planar devices and obtained a considerable simulation accuracy of light propagation.

a.1 Simulation parameters

In order to evaluate the performance of our MMI coupler based beam splitter, we define two transmission-related features in our simulation as:

$$\text{excess loss (EL)} = -10 \log_{10} \left(\frac{\sum_{i=1}^N I_i}{I_{in}} \right) \quad (\text{III-21})$$

$$\text{non uniformity (NU)} = 10 \log_{10} \left(\frac{I_{max}}{I_{min}} \right) \quad (\text{III-22})$$

where I_i is the split beam's optical intensity from the i^{th} output waveguide, I_{min} and I_{max} are the minimal and maximal intensity among the split waveguides, respectively. I_{in} is the total optical intensity at the input of the device. Both of EL and NU are typically presented in dB. Normally, for the 1×2 symmetric beam splitter, the theoretical NU is close to zero. However, with the increasing of output waveguides' number, the NU would become important. On the other hand, the EL is always the critical feature of passive device's design.

a.2 Simulation methods

In the FIMMPROP simulation, we have chosen the FMM¹¹ (real) solver [GALLA03] to calculate the modes of each component. Since the whole planar waveguide system involves only RWG¹² dielectric devices, such as rectangular access waveguides, bent waveguides and MMI coupler based beam splitters, the FMM solver has been used to reduce the 2D problem of matching optical fields along just one vertical direction in order to accelerate the speed of simulation. Meanwhile, we can also take advantage of the symmetry of the devices to save calculation time, for example, we set the horizontal symmetry of TE-like modal fields in the input waveguides. However, in order to keep a complete mode list in the MMI coupler and the

¹¹ FMM solver: Film Mode Matching method using a fully or semi-fully vectorial algorithm to calculate slice-by-slice the planar waveguide's transverse electromagnetic modes.

¹² RWG: Rectangular-geometry Waveguide, including straight and bent access waveguides, MMI coupler based beam splitters etc.

taper section for the purpose of multimode interference, we eliminate this symmetric feature and then launch a full-vector calculation.

a.3 Modeling constants

The simulated MMI coupler based device consists of input straight waveguide, 1×2 conventional or tapered MMI coupler, output straight waveguides. Moreover, since we are interested in the TE single-mode (TE_{00}) application, as shown before, the thickness of the Si_3N_4 layer ($n_{Si_3N_4} = 2.0$) is fixed to 250 nm, therefore the RWG type of device is chosen to design planar structure. Both top and bottom SiO_2 cladding layers ($n_{SiO_2} = 1.45$) have thickness of 2 μm .

a.4 RWG parameters

We define the width of Si_3N_4 waveguide along y-direction for each RWG component and then calculate the transverse modes by the vectorial FMM solver. For the thin (i.e.: 250-400 nm) input/output Si_3N_4 waveguide, TE_{00} mode could be strongly confined, while the other high-order modes such as TE_{01} or TE_{10} have very low confinement coefficient or even are not excited. Therefore the maximal calculated mode's number (Maxmode) within the FMM solver has been chosen to relatively small, i.e.: Maxmode = 4. In the wider side of tapers (i.e.: 0.7-0.9 μm -wide), the Maxmode is set to 10, and the Maxmode is set to 20 and 30 for the 2 μm -wide and 4 μm -wide MMI coupler. In fact, the criteria of selecting an appropriate Maxmode in different RWG component are to allow all possible guided modes in the FMM calculation but also to avoid wasting time to seek physically meaningless low-index modes. However, on the output side of MMI coupler, we should probably double the Maxmode number due to the presence of anti-symmetric modes. For instance, the 2 symmetric-output waveguides RWG has a Maxmode of 8. Meanwhile, the FMM solver's mode profile resolution is fixed to ($n_x = 300$, $n_y = 300$) in the horizontal and vertical directions, respectively.

b. 1×2 MMI coupler based beam splitters

The optical intensity ($\lambda=633$ nm) patterns of simulated conventional 1×2 MMI coupler based beam splitter's are presented in Figure III.24. There are 3 elementary sections in this device. From left to right, the first is a single-mode input waveguide with a width of W_g ; the second is the conventional 1×2 symmetric MMI coupler, in which the width and the length are noted as W_m and L_m ; the third is a pair of symmetric 2-output waveguides with the same width of W_g . For the first and third section, the length of straight waveguides is noted as L_g . On the right-

hand side of the MMI coupler, the locations of the output waveguides are noted as $\pm P_g$ and symmetric about the horizontal middle line ($y = 0$). A pair of detecting ports is used to collect the transmitted optical signal from the output waveguide, so each port is aligned with corresponding output waveguide at the position of $\pm P_g$ and is wide enough (i.e.: $1 \mu\text{m}$) to maximize the received optical intensity.

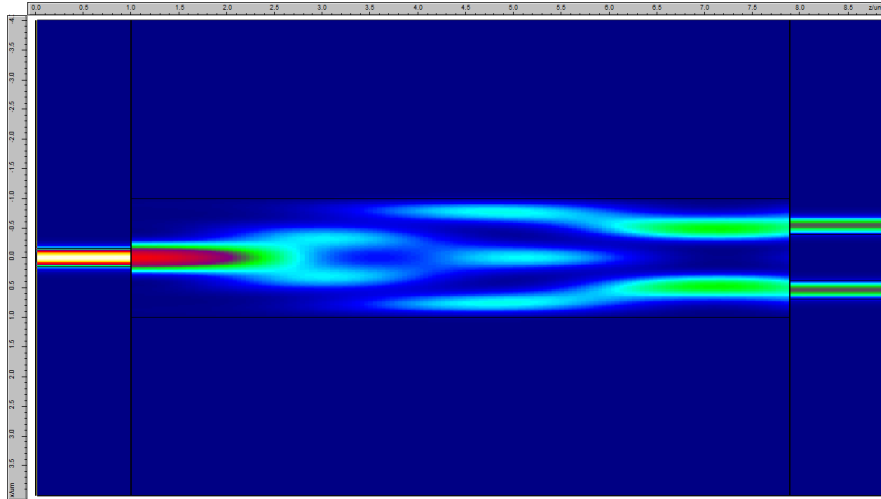


Figure III.24: Simulated light intensity patterns $I(y,z)$ in a conventional MMI 1×2 beam splitter.

A list of simulation parameters for the first conventional MMI 1×2 beam splitter is presented in Table III-4. W_e is the MMI coupler's effective width shown in (III-16). MMI coupler-related dimensions are calculated by referring to (III-20).

Table III-4: Simulation parameters and EL results of conventional 1×2 MMI beam splitter.

Parameters	W_g	W_m	W_e	L_m	P_g	EL
Values	$0.3 \mu\text{m}$	$2 \mu\text{m}$	$2.11 \mu\text{m}$	$6.51 \mu\text{m}$	$0.54 \mu\text{m}$	1.39 dB

b.1 Optimization of the MMI coupler's dimensions

Comparing with the state-of-the-art 1×2 beam splitters shown in Table III-3 the basic design based on a symmetric 1×2 MMI coupler's theoretical dimensions should be optimized in order to obtain a comparable EL value. According to the FMM solver's feature, once we fix the width of each RWG component, we don't need to recalculate each RWG section's transverse modes if we just change the length of device and redo the simulation. Therefore, we have firstly used FIMMPROP to scan the length of MMI coupler, in order to find the best

length with a minimal EL. Then we fix this optimized length and scan the position of 2 symmetric output waveguides. The EL characteristic curves as a function of L_m and P_g are presented in Figure III.25.

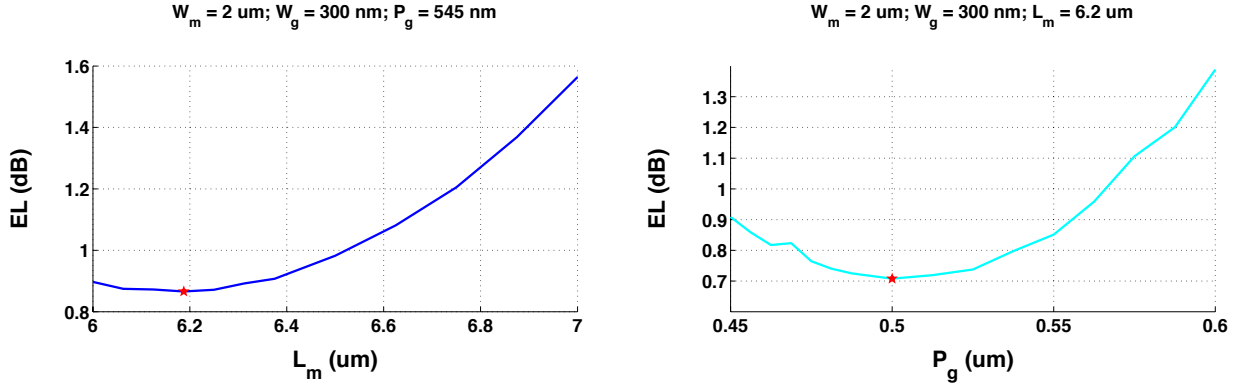


Figure III.25: EL characteristic curves as a function of L_m and P_g of basic 1×2 MMI beam splitter.

As shown in Figure III.25, the variation range of the L_m is from $6 \mu\text{m}$ to $7 \mu\text{m}$. The lowest EL could be obtained at $L_m = 6.2 \mu\text{m}$. The EL curve shows an exponential-like growth with the increasing of MMI's length. In fact, if we remove the *Goos-Hänchen* shift in the L_π calculation of (III-19), we should obtain a theoretical $L_m = 5.81 \mu\text{m}$. Therefore, the simulation found the minimal EL of 0.87 dB with an optimized length between the theoretical length with and without the *Goos-Hänchen* shift.

Meanwhile, we have scanned P_g from $0.45 \mu\text{m}$ to $0.6 \mu\text{m}$. The EL characteristic curve shows also dependence with the moving up of the output waveguides. The optimized position is situated at $0.5 \mu\text{m}$ from the middle line of MMI coupler, that means the *Goos-Hänchen* shift should thus not be considered in (III-20). These results also show that the *Goos-Hänchen* shift is a correction, which can be slightly excessive for low confinements. Finally, in the L_m and P_g optimized case, the EL can be close to 0.7 dB, which is reduced a half comparing with the mentioned non-optimized MMI coupler.

According to the [HOSSE10], the input/output waveguide's width should also be taken account into the MMI coupler's design. The width-dependent EL of the access waveguide in the optimized $2 \mu\text{m}$ -wide MMI coupler is presented in Figure III.26.

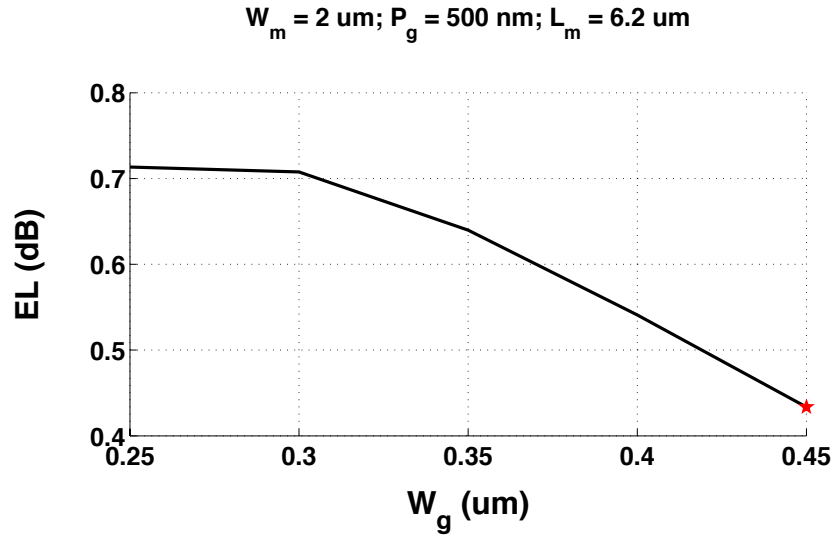


Figure III.26: EL characteristic curves as a function of W_g of optimized 1×2 MMI beam splitter.

As shown in Figure III.26, once the W_g exceeds $0.3 \text{ } \mu\text{m}$, the EL could decrease linearly with the W_g 's growth. However, as mentioned before, the width of the input and output waveguide should keep the single-mode propagation condition. As a result, we should fix the width of the access waveguides close or slightly superior to the cut-off width, i.e.: $300 - 400 \text{ nm}$. As shown in Figure III.15, for the case of $250 \text{ nm} \times 400 \text{ nm}$, the TE_{00} would be 85% confined in Si_3N_4 waveguide while the TE_{01} 's confinement coefficient is only 50%. Meanwhile, if the width of the access waveguide is increased from 300 nm to 400 nm , the EL would also go down from 0.7 dB to 0.5 dB .

b.2 Design of tapered 1×2 MMI coupler

In order to improve the MMI coupler's transmission, some taper-like transition components could be inserted between the input/out waveguides and the MMI coupler [MOERM97]. We have also designed some horn-like tapered MMI coupler and optimized the dimensions of these tapers in an optimized conventional 1×2 MMI beam splitter. The optical intensity ($\lambda=633 \text{ nm}$) patterns of simulated tapered 1×2 MMI coupler is presented in Figure III.27. We inserted a taper between the input waveguide and the left-hand side of MMI, and two tapers on the output side. The thinner side's and the wider side's width of such a taper are 0.7 and $0.4 \text{ } \mu\text{m}$, respectively. The other dimensions are listed in Table III-5.

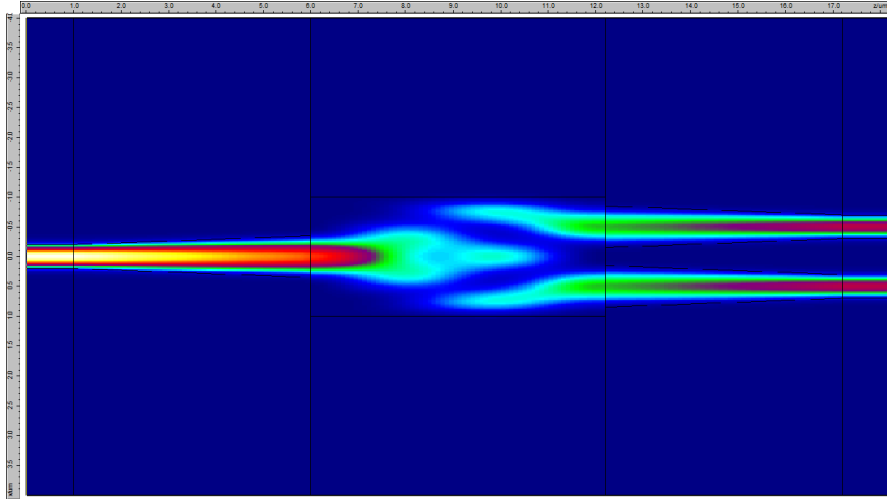


Figure III.27: Simulated light intensity patterns $I(y,z)$ in a tapered MMI 1×2 beam splitter.

Table III-5: Simulation parameters and EL results of optimized 1×2 MMI beam splitter.

Parameters	W_g	W_m	L_m	P_g	W_t	L_t	EL
Values	$0.4 \mu\text{m}$	$2 \mu\text{m}$	$6.2 \mu\text{m}$	$0.5 \mu\text{m}$	$0.7 \mu\text{m}$	$5 \mu\text{m}$	0.11 dB

Similarly to the optimization of MMI coupler, we scan at first the length of taper, and then fix an optimized length to scan the width. As shown in Figure III.28, the EL could be saturated as a function of the $0.7 \mu\text{m}$ -wide taper's length when the taper's length exceeds $6 \mu\text{m}$. At the threshold length i.e.: $L_t = 5 \mu\text{m}$, we scanned the width of the taper and obtained a lowest EL of 0.1 dB in the case of $W_t = 0.8 \mu\text{m}$. Comparing to the state-of-the-art 1×2 beam splitters shown in Table III-3 our design shows lower value of EL and more compact size.

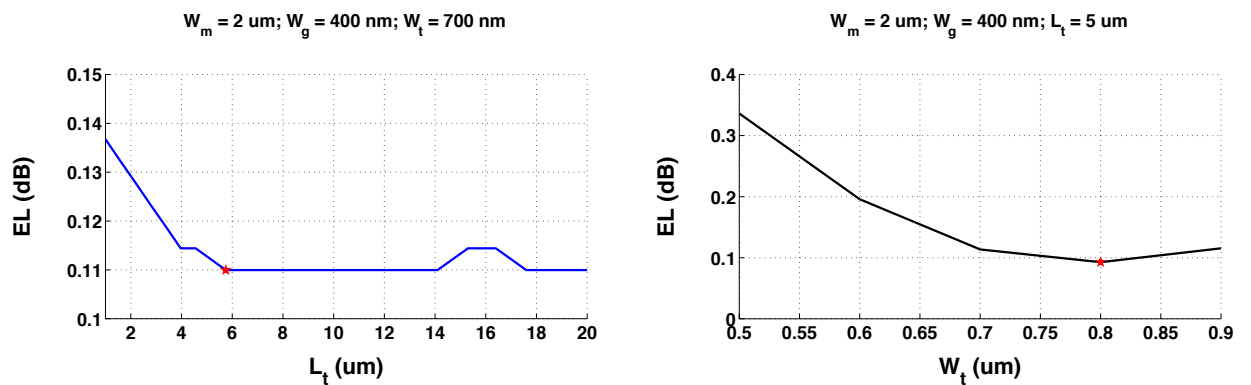


Figure III.28: EL characteristic curves as a function of L_t and W_t of tapered MMI beam splitter.

In conclusion, the optimized design of such a tapered MMI 1×2 beam splitter has a good performance for the purpose of low excess loss (down to 0.1 dB) propagation. At the same time, NU in these 1×2 beam splitters could be ignored since the whole device has a lateral symmetry. From the dimension point of view, each elementary 1×2 beam splitter could be compressed to $16.2 \mu\text{m} \times 2 \mu\text{m}$ including tapers. The minimal feature dimension in such an elementary beam splitter is the side-to-side spacing of $0.6 \mu\text{m}$ between the two outputs tapers on the right-hand side of the MMI coupler. By using the Electron Beam Lithographic (EBL) technique, fabrication of such a device should also be realized.

b.3 Design of parabolic 1 x 2 MMI coupler

We have also studied the parabolic tapered MMI coupler inspired from the work of *Levy et al.* [LEVY98, LEVY99, WEI01]. The structure of this compact 3 dB MMI coupler is illustrated in Figure III.29(b). Instead of a rectangular design, the width of the MMI coupler varied parabolically as a function of the horizontal distance z (supposing the left-hand side of the MMI is $z = 0$). Considering the *Goos-Hänchen* shift especially for the relatively thinner MMI coupler (i.e.: $W_m < 2 \mu\text{m}$), we can note the effective width of the parabolic MMI coupler as follows:

$$W_{em}(z) = W_l + (W_r - W_l) \left(\frac{z}{L_m} \right)^2 + W_{GH} \quad (\text{III-23})$$

with

$$W_{GH} = \frac{n_{SiO_2}^2 \lambda_0}{\pi n_{eff1D}^2} (n_{eff1D}^2 - n_{SiO_2}^2)^{-\frac{1}{2}} \quad (\text{III-24})$$

where W_l and W_r are the width of the MMI coupler on the left-hand side and on the right-hand side, respectively, and L_m is the length of the MMI coupler.

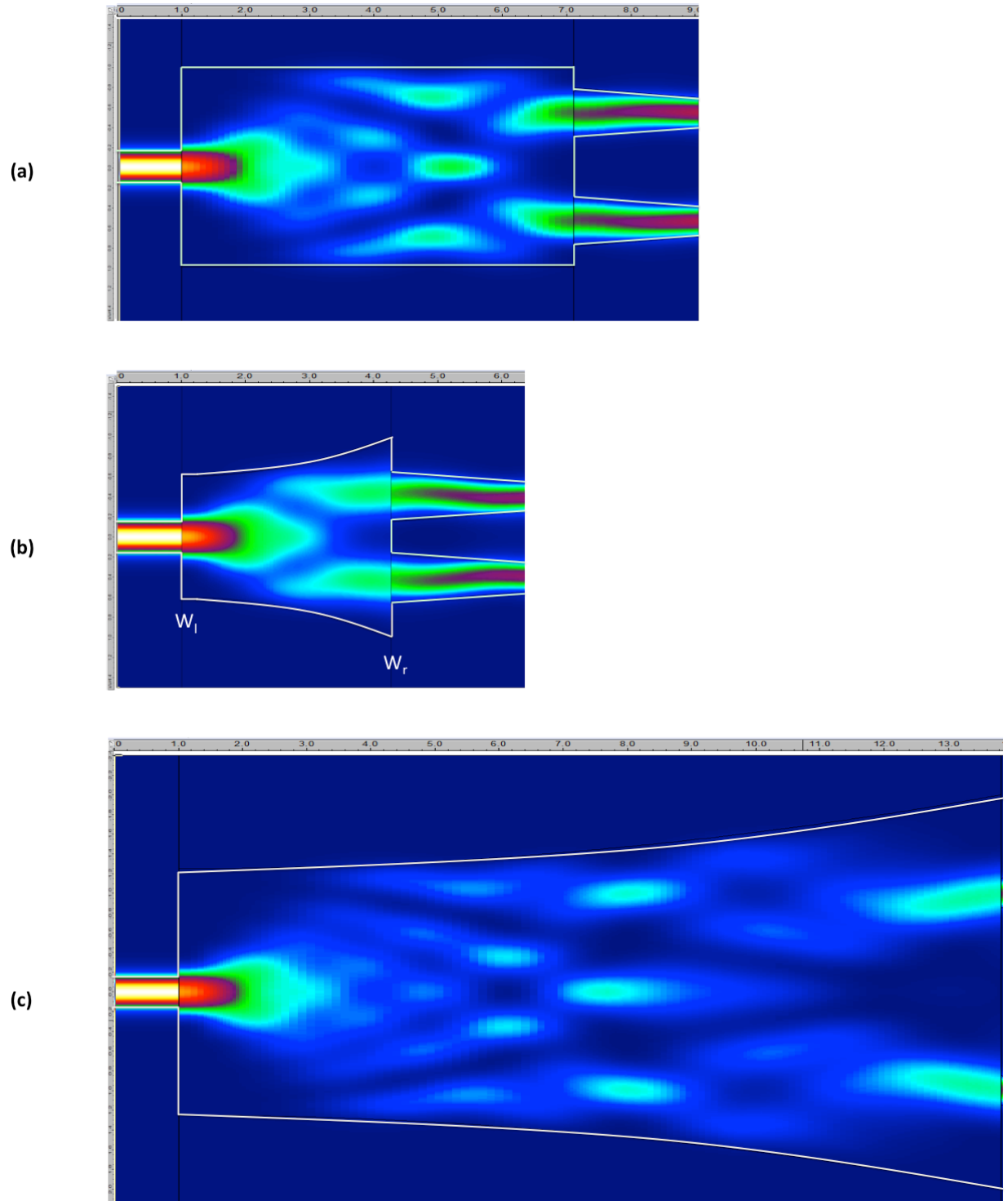


Figure III.29: Simulated light intensity patterns $I(y,z)$ in: (a). 2 μm -wide conventional MMI coupler; (b). 1.2 $\mu\text{m}/2 \mu\text{m}$ -wide parabolic MMI coupler; (c). 2.4 $\mu\text{m}/4 \mu\text{m}$ -wide parabolic MMI coupler. In (a) and (b), the output tapers have length of 2 μm and width of 0.5/0.3 μm . For all cases, the input waveguide's width is set to 0.3 μm .

The parabolic MMI coupler's half-beat length (L_{π}') with a phase shift of π is analogous to (III-19) and have following integral expression [WEI01]:

$$\pi = \int_0^{L_{\pi}'} (\beta_0(z) - \beta_1(z)) dz \quad (\text{III-25})$$

with

$$\beta_0(z) - \beta_1(z) = \frac{3\pi\lambda_0}{4n_{eff1D}W_{em}^2(z)} \quad (\text{III-26})$$

Substituting (III-23) and (III-26) into (III-25) yields

$$L_{\pi}' = \frac{4n_{eff1D}(W_r + W_{GH})^2}{3\lambda_0\eta} \quad (\text{III-27})$$

with a weighting factor

$$\eta = \frac{W_r^2}{2(W_l + W_{GH})(W_r + W_{GH})} + \frac{W_r^2 \tan^{-1} \sqrt{\frac{W_r - W_l}{W_l + W_{GH}}}}{2\sqrt{W_r - W_l}(W_l + W_{GH})^{\frac{3}{2}}} \quad (\text{III-28})$$

As shown in Figure III.29.(a), the 2 μm -wide conventional MMI coupler has an optimized length of 6.2 μm instead of the theoretical L_m of 6.5 μm according to Figure III.21. However as shown in Figure III.29.(b), the length of the parabolic MMI coupler is reduced to 3.3 μm . Therefore the division of conventional MMI coupler's length over the parabolic MMI coupler's length is 1.88. This value could be regarded as the simulation obtained weighting factor, noted as η_s . On the other hand, the theoretical weighting factor calculated according to (III-28) is noted as η_t . We list in Table III-6 the dimensions and parameters of the simulated parabolic 1 \times 2 MMI beam splitters shown in Figure III.29.(b) and (c), respectively.

Table III-6: Simulation parameters of parabolic MMI beam splitter as shown in Figure III.29.

Case	W_l	W_r	L_m	η_t	η_s
(b)	1.2 μm	2 μm	3.3 μm	1.72	1.88
(c)	2.4 μm	4 μm	12.8 μm	1.85	1.93

In conclusion, the parabolic MMI coupler provides a more compact solution to realize a symmetric beam splitter. Meanwhile, the self-imaging patterns in such a parabolic MMI coupler show a very interesting tilt angle about the middle line of devices (see the two split light spots shown in Figure III.29.(c)). This tilt effect could be due to the parabolically varying

width in the MMI section. This feature could be useful to extract the split beams into an inclined outward waveguides, in order to expand quickly the vertical spacing between the two output waveguides. However, this re-configured design increases the EL value in our simulation. For instance, with the same parameters of $W_g = 0.3 \mu\text{m}$, $W_t = 0.5 \mu\text{m}$ and $L_t = 2 \mu\text{m}$, the EL in the $1.2/2 \mu\text{m}$ -parabolic MMI coupler and in the conventional $2 \mu\text{m}$ -wide MMI coupler (not shown here) is 0.55 dB and 0.36 dB, respectively. It would thus be worthy of applying this parabolic MMI coupler's design within a high integration rate PIC.

c. Design of 1×4 MMI couplers

We have designed also the conventional symmetric 1×4 MMI couplers. Similarly to the 1×2 MMI coupler, based on the theoretical dimensions according to the self-imaging principle, we scanned the length of MMI coupler to find an optimized L_m . The simulated intensity pattern is presented in Figure III.30 with a list of simulation parameters presented in Table III-7. This conventional 1×4 MMI coupler with the theoretical dimensions has an additional EL of 0.41 dB comparing to the un-optimized conventional 1×2 MMI coupler. Meanwhile, the intensity difference between the split beams at the position of $y = \pm 0.5 \mu\text{m}$ and $y = \pm 1.5 \mu\text{m}$ results in a NU of 0.04 dB.

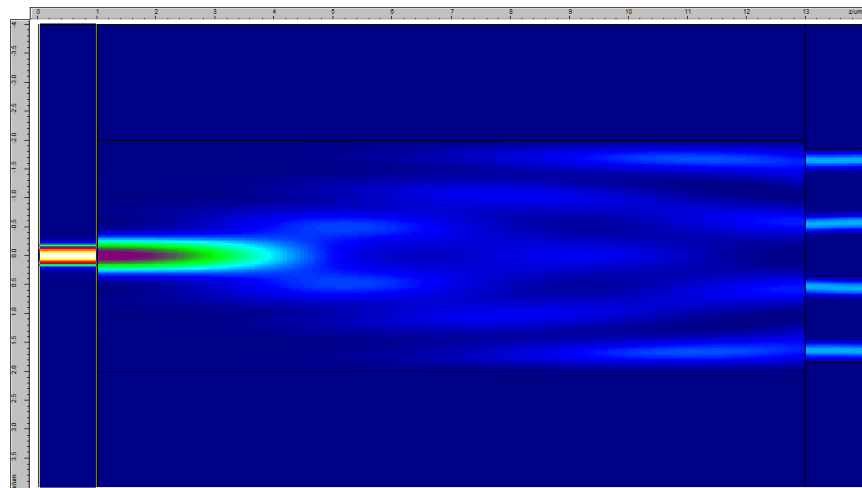


Figure III.30: Simulated light intensity patterns $I(y,z)$ in a basic MMI 1×4 beam splitter.

Table III-7: Simulation parameters and EL results of conventional 1×4 MMI beam splitter.

Parameters	W_m	L_m	P_g	W_g	EL	NU
Values	$4 \mu\text{m}$	$12.1 \mu\text{m}$	$0.5 \mu\text{m}/1.5 \mu\text{m}$	$0.4 \mu\text{m}$	1.8 dB	0.04 dB

Similarly to the 1×2 conventional MMI coupler's optimization, we have at first scanned the length of the MMI coupler within a range of $2 \mu\text{m}$. The EL and NU characteristic curves as a function of L_m are presented in Figure III.31.

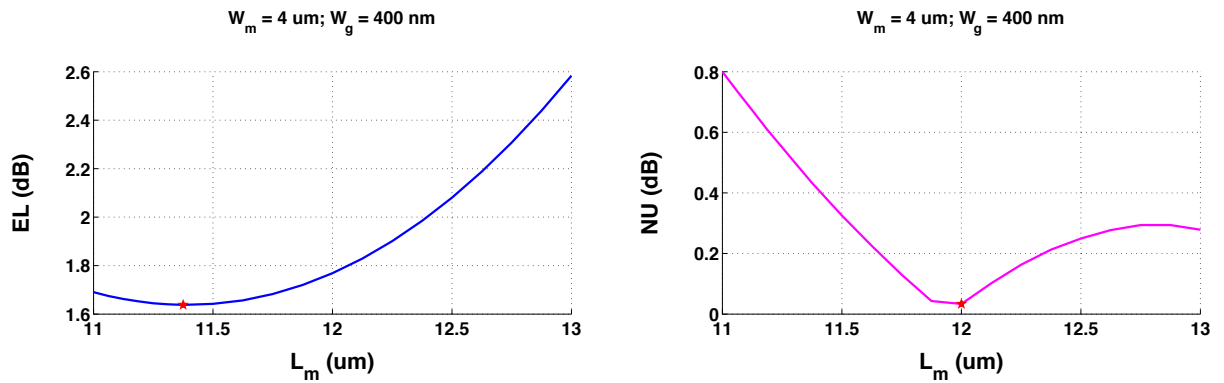


Figure III.31: EL and NU characteristic curves as a function of L_m of basic 1×4 MMI beam splitter.

As shown in Figure III.31, an exponential growth of EL has been observed as well as in the case of 1×2 MMI coupler. The lowest EL is found with $L_m = 11.4 \mu\text{m}$. At the same time, from the split uniformity view of point, the lowest NU is located at $L_m = 12 \mu\text{m}$. We added then the taper section in the 1×4 MMI coupler in order to continuing the optimization for the EL and NU. The simulated intensity pattern of tapered 1×4 MMI coupler is presented in Figure III.32. We compared two dimensions of taper, the modeling parameters and simulation results in listed in Table III-8.

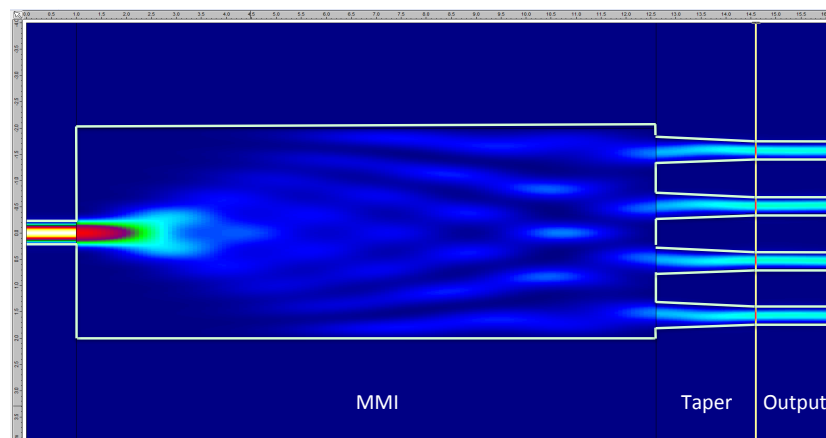


Figure III.32: Simulated light intensity patterns $I(y,z)$ in a tapered ($0.5 \mu\text{m} \times 2 \mu\text{m}$) MMI 1×4 beam splitter.

Table III-8: Simulation parameters and results of tapered MMI 1×4 beam splitter.

	W_m	L_m	W_t	L_t	EL	NU
Small-taper	4 μm	11.6 μm	0.5 μm	2 μm	0.63 dB	0.05 dB
Large-taper	4 μm	11.6 μm	0.7 μm	5 μm	0.51 dB	0.33 dB

In conclusion, the lowest EL could be obtained with a theoretical length of MMI coupler slightly shorter than according to (III-20). Indeed for the calculation of half beat length and the output waveguide position, it seems that the *Goos-Hänchen* shift correction is excessive, maybe due to the large difference between the MMI coupler's width and the leaked mode's penetration length. Meanwhile, an important NU comes out in the optimized case based on the minimization of EL. There is thus a trade-off condition between the EL and NU for the symmetric 1×4 MMI beam splitter. Comparing with the other $1 \times N$ ($N > 2$) MMI beam splitter mentioned in III.2.1-d.2, increasing the number of the output N would result in a growth of NU. For purposes of keeping a high uniformity among all the split outward waveguides and making the arrangement of each elementary beam splitter more flexible within the whole planar device, we have to limit the number of the MMI coupler's output. In this situation, we plan to cascade 1×2 or 1×4 MMI couplers for future beam splitter on our Si_3N_4 waveguide platform.

d. Design of $1 \times N$ symmetric PHASAR

Inspired by the PHASAR's design, we have designed and simulated a monochromatic PHASAR-like beam splitter based on our Si_3N_4 waveguide platform. Its instantaneous E-field distribution in the yz plane of the propagation modes is presented in Figure III.33. We set the access waveguide's width to 300 nm and PHASAR's width to 15 μm . There are 11 symmetric outputs arranged at uniformly spaced positions along the propagative wavefront-like arc, and each outward waveguide is perpendicular to the tangent of the arc. We suppose the propagative wave have a Gaussian E-field distribution along the y -direction. Then the right hand side of the PHASAR has been designed as an arc with radius of curvature of 7 μm , which is analogous to the Gaussian-like propagative wavefront with a diffraction angle of 30° . Similarly to the decomposition of sub-wavefronts issuing from a punctual source, every split sub-wave could continue to propagate along its wave vector's direction.

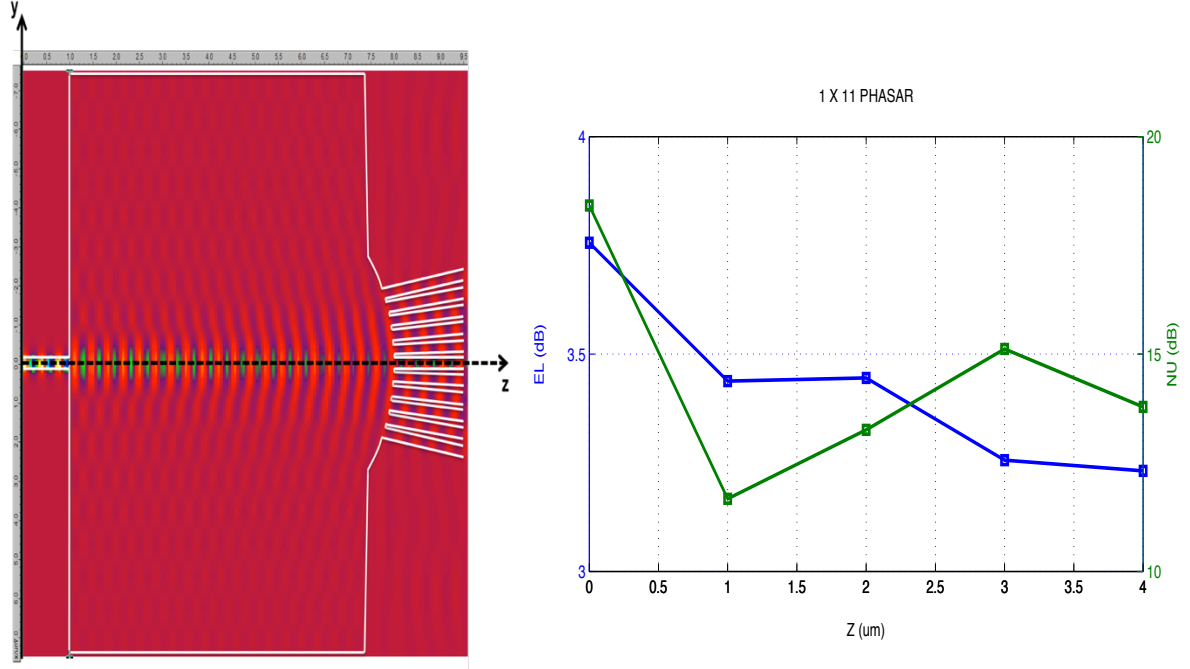


Figure III.33: FIMMPROP simulated Phasar-based 1×11 beam splitter's E-field instantaneous distribution and the EL and NU characteristic curves as a function of the output's location z from the vertex of the arc.

We calculated the output optical intensity distributed in each outward waveguides. Similarly to the analysis in the MMI coupler, we plot in Figure III.33 the EL and NU evolution curves as a function of the location z from the vertex of arc. In fact, the split beams' intensity has also a Gaussian-like distribution along the y -direction. That means the split beam in the middle output waveguide has the strongest intensity, on the opposite, the furthest pair of split waveguides from the z -axis with a tilt angle of 15° have the weakest intensity. As seen in Figure III.33, this single input PHASAR has a high-level excess loss (> 3 dB) and non-uniformity (> 10 dB) among the split beams in the 11 output waveguides. It cannot be regarded as a good candidate for the expected $1 \times N$ uniform beam splitter.

e. Design of 1×2^N cascade MMI coupler

As we know, it's possible to generate a symmetric 1×2^N (N is an integer) cascade MMI coupler based beam splitter. We study here only the simplest case, in which there are 2-stage MMIs and 4 outputs. As mentioned before, we could take advantage of the elementary 1×2 beam splitter's flexibility, in order to provide various device's layout. We present here the schematic illustrations of optical intensity patterns in two types of cascade MMI beam splitter.

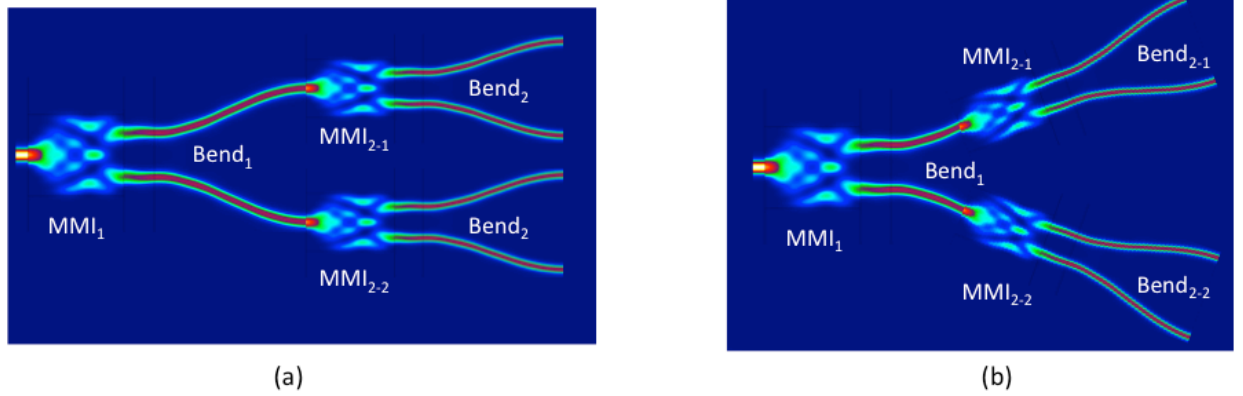


Figure III.34: Schematic configuration of a 2-stage cascade 1 x 2 MMI coupler based 1 × 4 beam splitter.

The first design shown in Figure III.34.(a) has 4 horizontal symmetric output waveguides on the right-hand side of the 2nd-stage MMI₂₋₁ and MMI₂₋₂, in which the Bend₁ have also horizontal inputs and outputs to connect with the 1st and 2nd stage 1 × 2 MMI beam splitters. On the other hand as shown in Figure III.34.(b), the 2nd stage MMI couplers are arranged with a tilt angle about the horizontal axis, which is aligned with the inclined outputs of the Bend₁. Consequently, the 2nd stage MMI couplers expand much more vertical space within the whole planar device.

From the dimensions point of view, the transition bent waveguides need to occupy more space than the elementary 1 × 2 beam splitters (i.e.: 2 μm × 10 μm) in order to reserve enough interval space between each neighboring output waveguide at the terminal. For the purpose of avoiding inter-waveguide interference, we suppose to separate the terminal-stage output waveguides with a security interval. For instance, the Bend₂ should space its input and output side a distance of several ten microns. Therefore, in order to make the whole cascade beam splitter more compact, we have to design some specific low loss bent waveguides within the beam splitting PIC.

III.2.3 Design and evaluation of bent waveguides

As mentioned before, the bent waveguides are dominant of the space's occupation within the expected beam splitting devices. We will introduce our design and evaluation of these bent waveguides in this part. Firstly, we will define two types of curves, which have analogous bended optical path. Secondly, we will introduce two theoretical approaches to analyze the

radiation losses due to the bend. Finally, we will evaluate the bent waveguide's propagation performances and propose an efficient design within our targeted PIC.

a. Definition of plan curve-based bent waveguides

a.1 The S-Function bend

The S-Function bend is pre-defined as a default bent waveguide's design except for the constant-radius of curvature arcs within FIMMPROP. Assuming the origin of the coordinate system is the beginning of the S-Function bend (see Figure III.35), we can define the vertical expanding space along the bent waveguide's path as follows:

$$y(Z) = T_m \sin^2\left(\frac{\pi Z}{2}\right) \quad (\text{III-29})$$

where T_m is the spacing distance between the two shifted straight waveguides, which links one output branch of the m^{th} -stage MMI coupler's output with the $(m+1)^{\text{th}}$ -stage MMI coupler's input (see Figure III.34) and Z is the fractional z -coordinate normalized by the horizontal length of m^{th} -stage bend ($Z = z/L_m$).

Moreover, the S-Function also affects the width of the waveguide along Z in order to maximize the optical transmission through the bent waveguide:

$$W(Z) = W_{lhs} \left(1 - \sin^2\left(\frac{\pi Z}{2}\right)\right) + W_{rhs} \sin^2\left(\frac{\pi Z}{2}\right) \quad (\text{III-30})$$

where W_{lhs} and W_{rhs} are the width of the left-hand side and the right-hand side of the bent waveguide, respectively. In our case, we have $W_{lhs} = W_{rhs} = W_g$.

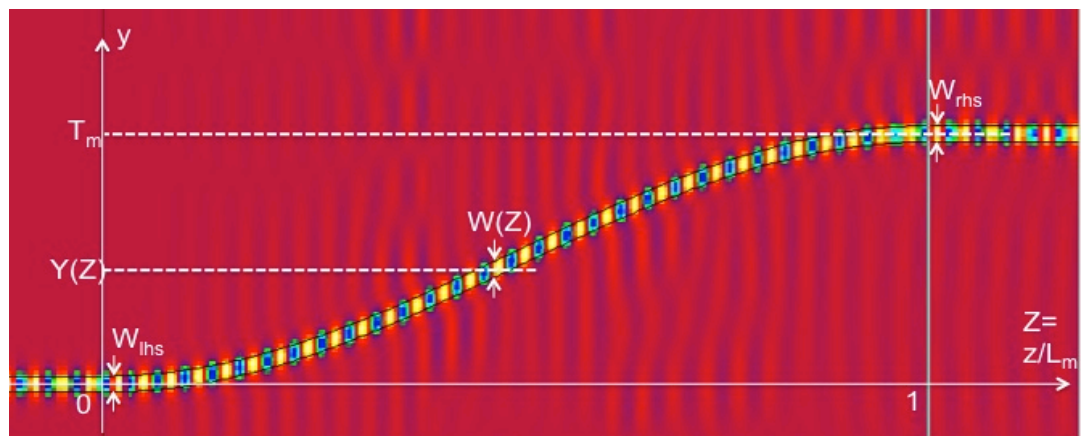


Figure III.35: Simulated E-field amplitude distribution in a S-Function bended Si_3N_4 rectangular waveguide.

We can deduce from the function shown in Figure III.28), the radius of curvature of the S-Function [WEISS]:

$$R_c(z) = \frac{\left[1 + \left(\frac{dy}{dz}\right)^2\right]^{3/2}}{\left|\frac{d^2y}{dz^2}\right|} \quad (\text{III-31})$$

We will compare the evolution of the radii of curvature along the propagation path with other curves afterwards.

a.2 The lemniscate-like bend

We have investigated some other plan curves, such as the lemniscate of Bernoulli. In fact, the lemniscate-like bend's design is widely used for the design of curved roads and tracks due to its featured mathematical properties [LABRO03]. Lemniscate of Bernoulli is a special case of the famous plan curve *Cassini oval* and firstly described by *Jakob Bernoulli* in 1694. It has the locus of points for which the sum of the distances to each of two fixed focal points is a constant. Classic lemniscate of Bernoulli in polar and Cartesian coordinates shown in Figure III.36 follows the 2D polar equation and parametric equations, respectively:

$$r^2 = 2a^2 \cos 2\theta \quad (\text{III-32})$$

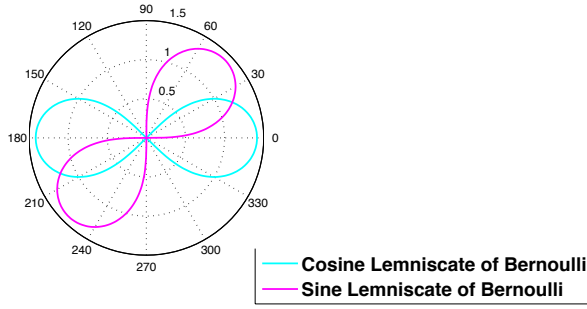
$$\begin{aligned} x(t) &= \frac{a\sqrt{2}\cos(t)}{1 + \sin^2(t)}; \\ y(t) &= \frac{a\sqrt{2}\cos(t)\sin(t)}{1 + \sin^2(t)}. \end{aligned} \quad (\text{III-33})$$

Considering a counterclockwise rotation of 45°, we obtain a sine-type lemniscate of Bernoulli with similar equations in polar and Cartesian coordinates:

$$r^2 = 2a^2 \sin 2\theta \quad (\text{III-34})$$

$$\begin{aligned} x(t) &= \frac{a\cos(t)(1 - \sin(t))}{1 + \sin^2(t)}; \\ y(t) &= \frac{a\cos(t)(1 + \sin(t))}{1 + \sin^2(t)}. \end{aligned} \quad (\text{III-35})$$

Full-period Lemniscate of Bernoulli in Polar coordinate



Full-period Lemniscate of Bernoulli in Cartesian coordinate

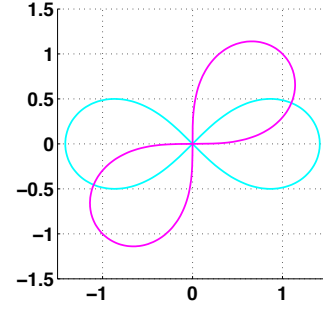


Figure III.36: Full-period ($0 \leq \theta \leq 180^\circ$) cosine-type and sine-type lemniscate of Bernoulli (with $a=1$) presented by solid line in cyan and in magenta, respectively.

Schematical illustration of lemniscate based bent waveguide's design is presented in Figure III.37. As an example, we generate a fractional part of normalized ($a = 1$) sine-type lemniscate with $\theta = 30^\circ$. It's trace starts from the origin in both coordinate systems and will end at an inflection point with a radius of curvature R_c and a tangential angle θ_c . The geometric parameters at the inflection point could be easily calculated in the polar coordinates as follows:

$$\begin{aligned} R_c &= a^2/3r \\ \theta_c &= 3\theta \end{aligned} \tag{III-36}$$

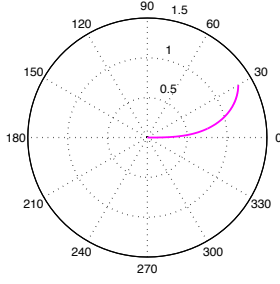
Since we have $\theta = 30^\circ$ and $r = 1.32$ in the polar coordinates, at the inflection point, $R_c = 0.44$ and $\theta_c = 90^\circ$. Then we combine the anti-symmetric image of this fractional lemniscate curve in Cartesian coordinates to form a complete end-to-end bend, which is analogous with the propagation path of guided modes in the bend section of our PICs. Therefore, the horizontal and vertical spacing between the endpoints are 2.28 and 1.32, respectively.

By the way, we could also deduce the radius of curvature for this sine-type lemniscate by using the parametric equations in the Cartesian coordinates [WEISS]:

$$R_c(t) = \frac{\left[\left(\frac{dx(t)}{dt} \right)^2 + \left(\frac{dy(t)}{dt} \right)^2 \right]^{3/2}}{\left| \frac{dx(t)}{dt} \frac{d^2y(t)}{dt^2} - \frac{dy(t)}{dt} \frac{d^2x(t)}{dt^2} \right|} \tag{III-37}$$

where the horizontal and vertical displacements along the curve can be calculated according to (III-35).

1/6-period Lemniscate of Bernoulli in Polar coordinate



Lemniscate of Bernoulli based bend in Cartesian coordinate

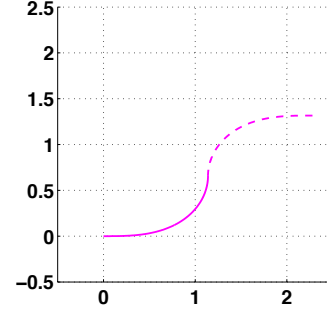


Figure III.37: 1/6-period ($0 \leq \theta \leq 30^\circ$) sine-type lemniscate and its application in combining with its mirror symmetric image at an inflection point with $\theta_c = 90^\circ$ to design a bent waveguide.

b. Modeling and analysis methods of the bend loss

In our single-mode rectangular waveguide, the index-contrast between the cladding (SiO_2) and the core (Si_3N_4) is identical along the y-direction and along the x-direction (see Figure III.4). Therefore we must consider the leakage effect in both directions. We will introduce here two rough analysis methods in order to evaluate the bend losses in a dielectric waveguide.

b.1 1st approximation method: velocity approach

Marcatili and Miller introduced the velocity-delay approach to analyze the radiation loss due to bent waveguides [MARCA69a]. This velocity approach is based on the physical effect that the low-loss propagative modes confined in the waveguide would imply propagation above the velocity of light at a distance far from the center of curvature of the bend. As shown in Figure III.38, in order to keep the integrity of the propagation's modal field in a curved waveguide with a radius of curvature R_c and a propagation constant k_z , the phase velocity of fields in the wavefront is proportional to the distance from the center of curvature O_c . Therefore we obtain a proportional formula as follows:

$$\frac{k_0}{k_z} = \frac{R_c}{R_c + \Delta R} \quad (\text{III-38})$$

where k_0 and $R_c + \Delta R$ are respectively the propagation constant and the radius of curvature at which the phase velocity exceeds the velocity of light in the cladding.

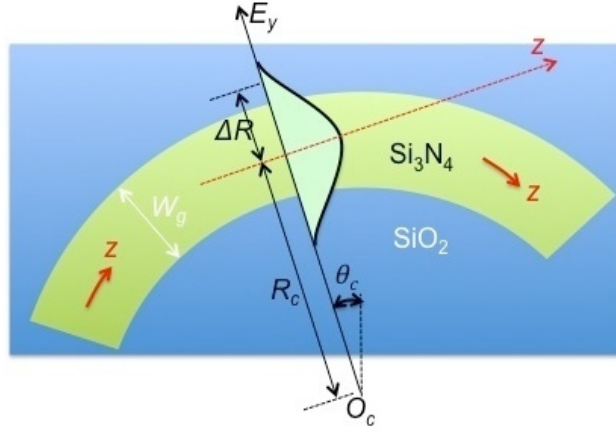


Figure III.38: Schematic illustration of the propagation mode in a bent waveguide. W_g is the width of the waveguide. R_c and θ_c are the radius of curvature and the angle of arc, respectively.

Along with moving further from (around) the middle (z -axis) to the edge of the waveguide, the phase velocity will be increased quickly and the effective index will go down abruptly. As a result, the modal field's confinement to the waveguide will become weaker. Once ΔR is increased to a threshold, the effective index could be close to the refractive index of the cladding. The Si_3N_4 waveguide has thus no more confinement for the mode.

According to this velocity approach, we can present the attenuation coefficient in a simplified form as follows [GOELL74]:

$$\alpha = C_1 \exp(-C_2 R_c) \quad (\text{III-39})$$

where C_1 and C_2 are constants depending on the dielectric waveguide's geometric dimensions and refractive indexes. As shown in (III-39), the bend-related attenuation coefficient varies as an exponential of the radius of curvature. Thus the radiation loss could change abruptly from considerably large to negligibly small when we increase the minimal radius of the curvature of the bent waveguide. The values for C_1 and C_2 play also an important role in the calculation of the theoretical bend loss.

b.2 2nd approximation method: 2D modal analysis

Marcatili quantitatively analyzed the propagative modal fields in a bended dielectric waveguide [MARCA69b]. This modal analysis theory can be used to deduce the accumulated bend loss in a TE single-mode SiO_2 cladded Si_3N_4 waveguide. The main difference of this model with respect to the elementary “velocity approach” method presented before, is the fact that the dependence of C_2 with R_c is taken into account in the equation (III-39). As explained

in the following, this dependence comes from the possible excitation of higher order leaky modes when R_c significantly decreases. As mentioned before, the cross-section of the considered Si_3N_4 waveguide should be close to the cut-off dimension (i.e.: $250 \text{ nm} \times 300 \text{ nm}$). Only TE_{00} mode could thus propagate with a high confinement in the Si_3N_4 medium. We modeled in Figure III.39 a 2D rectangular waveguide with a turning angle of θ and a fixed radius of curvature R_c .

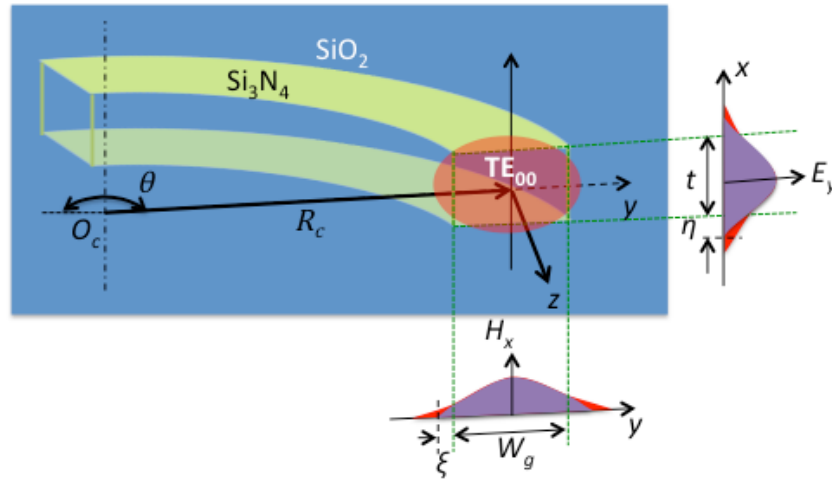


Figure III.39: Schematic illustration of a curved SiO_2 cladded Si_3N_4 rectangular waveguide. W_g and t are the dimensions of the waveguide's cross-section, R_c and θ are the radius of curvature and the angle of arc about the origin of the curvature O_c , respectively.

As shown in Figure III.39, When the optical wave goes through a bend with a radius of curvature R_c , the only large modal field components, such as TE_{00} -like mode's E_y (H_x) are perpendicular to the curved z -axis. All of these components have a sinusoidal distribution along x or y direction within the Si_3N_4 medium and an exponential decay in the cladding SiO_2 media. The penetration depth along the y and x -axis are noted as ξ and η , over which the modal fields decrease by $1/e$. The propagation constant is related with the free space wavelength by the expression:

$$k_z = \sqrt{k_0^2 - k_y^2 - k_x^2} \quad (\text{III-40})$$

where $k_0 = 2\pi n_{\text{Si}_3\text{N}_4} / \lambda$ with λ the free space wavelength i.e.: $0.633 \mu\text{m}$ in our case; k_x and k_y are the propagation constant's component along x and y axis, respectively. k_x is identical in the straight and curved waveguides and equal to $2\pi n_{\text{effIDTE}} / \lambda$. In fact, the model analysis theory is based on a theoretical study of the TE or TM-like propagative modal field's evolution in a bend. The attenuation mechanism can be supposed to be linked to the fact that the

fundamental or low-order modes could be coupled to higher-order modes in the curved section and result in a loss of confinement for the propagative modes. Consequently, this mode's conservation would finally excite the leakage of energy from the guidance material to the cladding layers. [MARCA69b] has given the relation between the portions of the guided mode's power coupled to high-order modes as a function of the radius of curvature in the transition section between a straight waveguide and a curved waveguide:

$$f(R_c) = \frac{k_{y0}}{4} \left(\frac{k_{z0} W_g}{k_{y0}} \right)^2 \frac{1}{R_c} \quad (\text{III-41})$$

where k_{y0} is the propagation constant along y-axis in straight waveguide and k_{z0} the axial propagation constant, which equals $2\pi n_{\text{eff}2D_TE}/\lambda$ (see Figure III.14). Since the field component in a straight waveguide's cladding media decays almost exponentially away from the guide, we can calculate it as a function of the penetration length ξ by the following expression:

$$k_{y0} = \sqrt{k_0^2 - k_1^2 - \left(\frac{1}{\xi}\right)^2} \quad (\text{III-42})$$

where $k_1 = 2\pi n_{\text{SiO}_2}/\lambda$. By using FIMMPROP's MOLAB, we can easily find this penetration length for different cross-section waveguides. We present in Figure III.40 the TE_{00} E-field distribution along y-axis in the straight SiO_2 cladded Si_3N_4 rectangular waveguides with different cross-section dimensions.

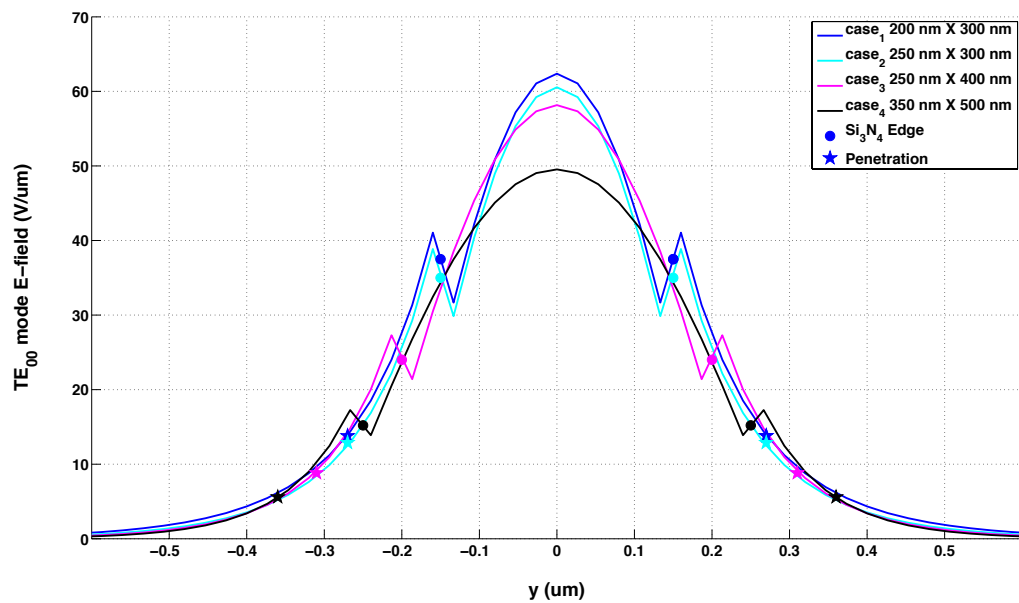


Figure III.40: Modal fields distribution along y-axis in the straight rectangular waveguide of several cross-section dimensions. Dots present the edge location of the waveguide and pentagons present the location of ξ , over which the modal fields decrease by $1/e$.

In fact, we find that the horizontal penetration length ξ for the TE₀₀ mode doesn't vary a lot with the increasing of the cross section dimensions. In case1 and case2, $\xi = 0.12 \mu\text{m}$; in case3 and case4, $\xi = 0.11 \mu\text{m}$. At the same time, we found a 'pulse' near the edge of the waveguide. It should be due to the E_y component discontinuity at interface. In the case of the shortest R_c values (strongly bent waveguides) this description is incomplete, since the guided mode maximal intensity is no more centered in the middle of the waveguide, but shifted in its outer middle part, similarly to a centrifuge effect. We have neglected this effect, and we have considered that the penetration depth of the guided mode is the same as in the case of a straight waveguide. This approximation is considered as valid for moderate bends, which will be chosen in any case in order to limit excess losses.

Finally, based on TE₀₀-like mode's analysis in the curved rectangular dielectric waveguide, we deduced the equation (19) in [MARCA69b] to put the R_c dependent attenuation coefficient α_c into a simplified expression, which is similar to (III-39). This general expression of attenuation coefficient α_c can be noted as follows:

$$\alpha(R_c) = C_1 \exp(-C_2(R_c)R_c) \quad (\text{III-43})$$

with a R_c-independent constant:

$$C_1 = \frac{\left(\frac{k_{y0}W}{\pi}\right)^2 \frac{W}{\pi W_g} \left[1 - \left(\frac{k_{y0}W}{\pi}\right)^2\right]^{\frac{1}{2}} \frac{k_0^3}{k_{z0}^2} \left(1 - \frac{n_{SiO2}^2}{n_{Si3N4}^2}\right)}{1 - 2 \left(1 - \frac{n_{SiO2}^2}{n_{Si3N4}^2}\right) \left(\frac{k_{y0}W}{\pi}\right)^2 + \frac{2W}{W_g} \left[1 - \left(\frac{k_{y0}W}{\pi}\right)^2\right]^{\frac{1}{2}}} \quad (\text{III-44})$$

and a R_c-dependent constant:

$$C_2(R_c) = \frac{2\pi^3 \left[1 - \left(\frac{k_{y0}W}{\pi}\right)^2 \left(1 + \frac{2f(R_c)}{k_{y0}W_g}\right)^2\right]^{\frac{3}{2}}}{3k_{z0}^2 W^3} \quad (\text{III-45})$$

where W is the multimode cut-off width, which relies on the wavelength and the refractive indexes:

$$W = \frac{\lambda}{2\sqrt{n_{Si3N4}^2 - n_{SiO2}^2}} \quad (\text{III-46})$$

In order to avoid redundancy, we could substitute several symbol variables shown in (III-44) by the numerical values, which are applied for the presented Si₃N₄ bent waveguides (see Figure III.39). We obtain thus:

$$C_1 = \frac{A}{\lambda} \left(\frac{k_0}{k_{z0}} \right)^2 \frac{(1-A)}{1 + \frac{W_g}{2W} A^3} \quad (\text{III-47})$$

$$C_2(R_c) = \frac{2k_{z0}}{3} \left[\left(\frac{\pi}{k_{z0}W} \right)^2 - \left(\frac{k_{y0}}{k_{z0}} \right)^2 \left(1 + \frac{k_{z0}^2 W_g}{k_{y0}^2 2R_c} \right)^2 \right]^{\frac{3}{2}}$$

with

$$A = 1 - \left(\frac{k_{y0}W}{\pi} \right)^2 \quad (\text{III-48})$$

b.3 Discussion and analysis of C_1 and C_2

We list in Table III-9 a table of substituted material-dependent constants and parameters and in Table III-10 the numerical values for the dimension dependent variables.

Table III-9: Values for the material-dependent variables in the studied Si_3N_4 waveguide.

Variable	λ (μm)	$n(\text{Si}_3\text{N}_4)$	$n(\text{SiO}_2)$	W (μm)	k_0 ($\text{rad } \mu\text{m}^{-1}$)	k_1 ($\text{rad } \mu\text{m}^{-1}$)
Values	0.633	2.0	1.44	0.22	19.85	14.29

Table III-10: Values for the geometry-dependent variables in rectangular Si_3N_4 waveguide.

Case	Waveguide ($t \times W_g$: nm)	$n_{\text{eff}2D}$	C_1 (μm^{-1})	C_2 (μm^{-1})	R_c (μm , for $C_2=0$)
(1)	200 × 300	1.63	0.514	$10.79 \times \left[0.78 - 0.46 \left(1 + \frac{0.33}{R_c} \right)^2 \right]^{3/2}$	1.08
(2)	250 × 300	1.68	0.471	$11.12 \times \left[0.73 - 0.43 \left(1 + \frac{0.35}{R_c} \right)^2 \right]^{3/2}$	1.15
(3)	250 × 400	1.74	0.439	$11.51 \times \left[0.68 - 0.36 \left(1 + \frac{0.56}{R_c} \right)^2 \right]^{3/2}$	1.47

As shown in Table III-10, the bigger the cross-section of the rectangular dielectric waveguide is, the smaller the constant C_1 is in the formula of the bend losses calculation. Supposing the cladding material is homogenous and symmetric about the rectangular waveguide, C_1 is inversely proportional to the 2D effective index for the TE_{00} mode. Meanwhile, in our case, within a variation of 200 nm of the waveguide's cross-section, C_1

always stays at the same order of magnitude i.e.: several tenths per micron. In order to qualitatively analyze the evolution of C_2 , we present also in Figure III.41, the characteristic curves of C_2 as a function of the radius of curvature.

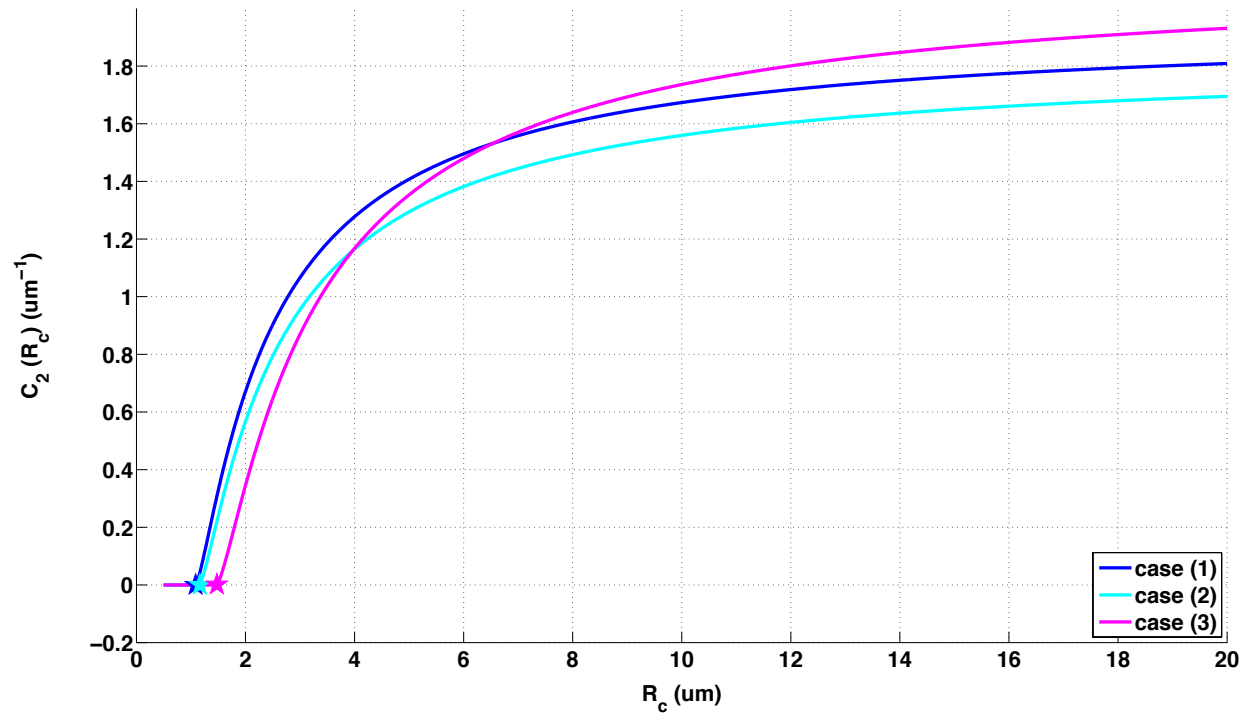


Figure III.41: Characteristic curves of C_2 as a function of the radius of curvature.

As shown in Figure III.41, C_2 is a piecewise function of the radius of curvature. If R_c is inferior to a threshold value, C_2 could be very close to zero. Consequently, the attenuation coefficient would no longer depend on R_c but only rely on C_1 . Otherwise, when R_c exceeds the threshold, C_2 will increase as a function of R_c . Comparing with different cases, we firstly found a proportional relation between the dimensions of rectangular waveguide and this threshold value of R_c to make $C_2 = 0$. The larger cross-section the rectangular waveguide has, the longer the threshold radius of curvature is. Physically speaking, we need to design a curved waveguide with a relatively larger radius of curvature, in order to decrease the radiation loss for a larger rectangular waveguide. By the way, we have also applied this modal analysis method to calculate the bend loss for a known InP rectangular waveguide, in which the bend losses have been measured. The theoretical calculation result matches well with the experimental results.

We will thus apply this approximation method to evaluate the mentioned S-Function and lemniscate-like bended Si₃N₄ rectangular waveguide's radiation loss, in which the R_c is varied along the whole bend section and has a minimal value at least equal to 10 μm, in order to satisfy the approximation condition.

III.2.4 Evaluation of lemniscate-like and S-Function bent waveguides

a. Definition of the optical transmission in a bent waveguide with varied radius of curvature

Similarly to the other attenuation coefficient, α_c can be defined as the decay of optical power P in a bent waveguides along z-axis by the expression:

$$\alpha_c = -\frac{dP}{Pds} \quad (\text{III-49})$$

Since in a bent waveguide, the wave vector's direction is varied along its optical path, we use thus **s** as a curvilinear displacement instead of the horizontal displacement z. In the both studied bent waveguides (i.e.: lemniscate-like or S-Function bend) with varying radius of curvature, the calculation principle consists in the decomposition of the full curve into successive elementary curves with constant R_c, and in the application of the function (III-45) for each elementary transition. As shown in Figure III.37, the bent waveguide's optical path is defined to be analogous to a pair of anti-symmetric fractional lemniscate of Bernoulli. By computing the integration and substituting (III-39) we obtain the optical transmission in a parametric expression for the lemniscate-like bent waveguide as shown in (III-37):

$$T = \frac{P_{out}}{P_{in}} = e^{-\int_{t_1}^{t_2} \alpha_c(t) \left(\frac{ds}{dt}\right) dt} \quad (\text{III-50})$$

with

$$\frac{ds}{dt} = \sqrt{\left(\frac{dx}{dt}\right)^2 + \left(\frac{dy}{dt}\right)^2} \quad (\text{III-51})$$

On the other hand, for the S-Function bent waveguide as shown in (III-31), we can also calculate the radius of curvature dependent transmission along z-axis:

$$T = \frac{P_{out}}{P_{in}} = e^{-\int_{z_1}^{z_2} \alpha_c(z) \left(\frac{ds}{dz}\right) dz} \quad (\text{III-52})$$

with

$$\frac{ds}{dz} = \sqrt{1 + \left(\frac{dy}{dz}\right)^2} \quad (\text{III-53})$$

Therefore, the accumulated radiation loss due to the bend's radius of curvature in both cases could be evaluated through an analytic expression of the attenuation coefficient, which is varied along the whole bend section. By the way, we will use the same definition of excess losses shown in (III-21) to evaluate the bent waveguides.

b. Modeling of optical path of bent waveguides

The evaluation aims at comparing the occupation size (horizontal and vertical spacing between the 2 endpoints, which are analogous to the input and output of the bent waveguides) and the accumulation loss between the S-Function bends and lemniscate-like bends. In the beginning, we need to design the dimensions of bent waveguides based on both types. We suppose here the expected vertical spacing Δy between the start point (on the bottom-left side) and the endpoint (on the top-right side) is fixed to 50 μm , which matches the expected spacing between the last-stage split waveguides shown in Figure III.34.(a).

The analogue optical paths made by a pair of anti-symmetric fractional lemniscates and the corresponding S-Function curves are presented in Figure III.42. We have chosen a serial of tangential angles θ_c at the inflection point for the lemniscate-like curves (i.e.: $\theta_c = 60^\circ, 90^\circ$ and 180°). Meanwhile, we generate also a S-Function bend corresponding to each lemniscate case, in order to link the start point with the 3 different endpoints. Consequently, in the smaller θ_c case, we need more horizontal spacing along z-axis in order to lay down the whole curve.

For the purpose of making the cascaded beam splitter more compact and distributing the split waveguides more uniformly in a square-like plan, we hope to increase the aspect ratio of device, which is defined as the division of the horizontal spacing over its vertical spacing. In this context, the design of lemniscate-like bent waveguides with a bigger θ_c could be more interesting for us. However, we will begin our evaluation and analysis with the case of the smallest θ_c . We suppose that both types of curves are totally anti-symmetric about the inflection point, we will thus present the evolution of optical path and its radius of curvature and calculate the accumulated bend losses only along the first-half of optical path shown in Figure III.42.

Comparison between lemniscate-like and S-Function bends

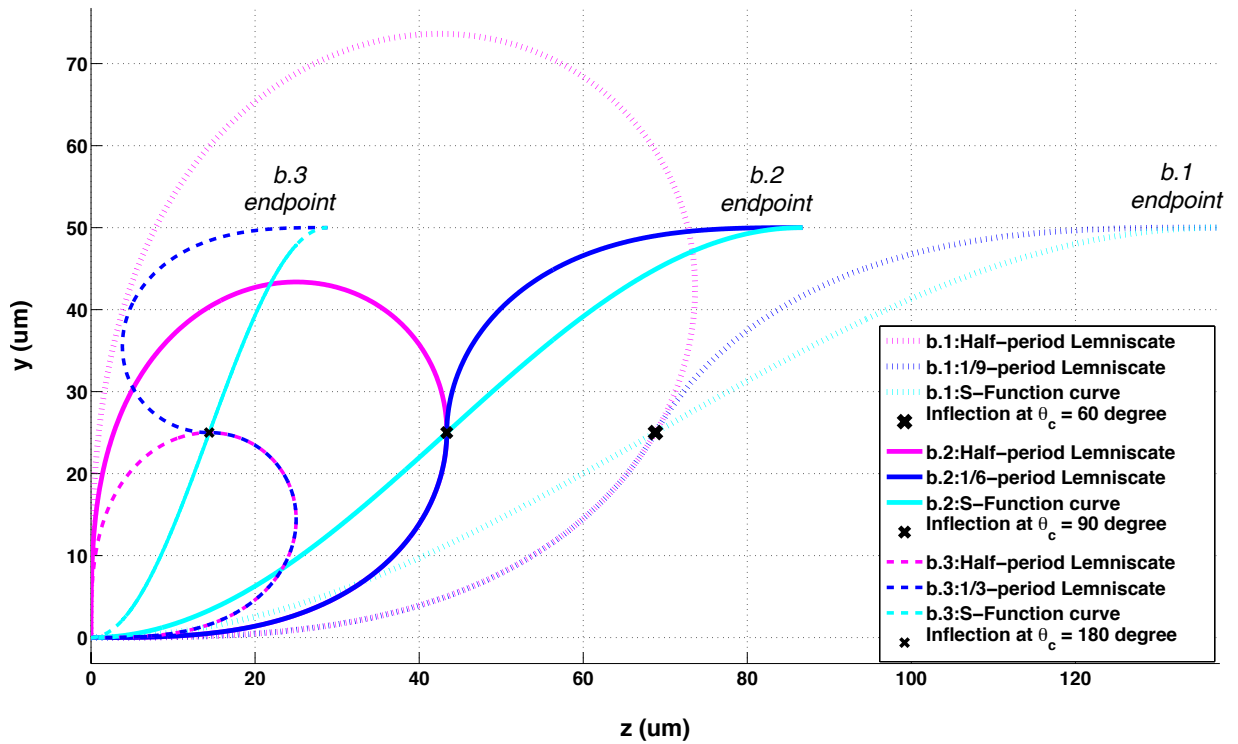


Figure III.42: Comparison between lemniscate-like and S-Function curves with the inflection point with $\theta_c=60^\circ, 90^\circ$ and 180° for a vertical spacing of $50 \mu\text{m}$ between the endpoints.

b.1 $\theta_c = 60^\circ$

As shown in Figure III.43, our first remark is that the lemniscate-like bend has an extremely large R_c (much larger than $500 \mu\text{m}$) in the beginning of the curve and goes down to its minimum at the inflection point. On the contrary, the S-Function curve's radius of curvature begins with its minimal R_c and arrives to the maximum at the inflection point. Secondly, the minimum of lemniscate's radius of curvature is about 50% smaller than that of S-Function's. However, comparing with the mentioned threshold radius of curvature ($C_2 = 0$), both curves are far away from the high attenuation zone. The accumulated bend losses along the lemniscate bend and the S-Function bend, according to (III-50) and (III-52), in 3 different cross-section rectangular waveguides (see Table III-10) are presented in Figure III.44.

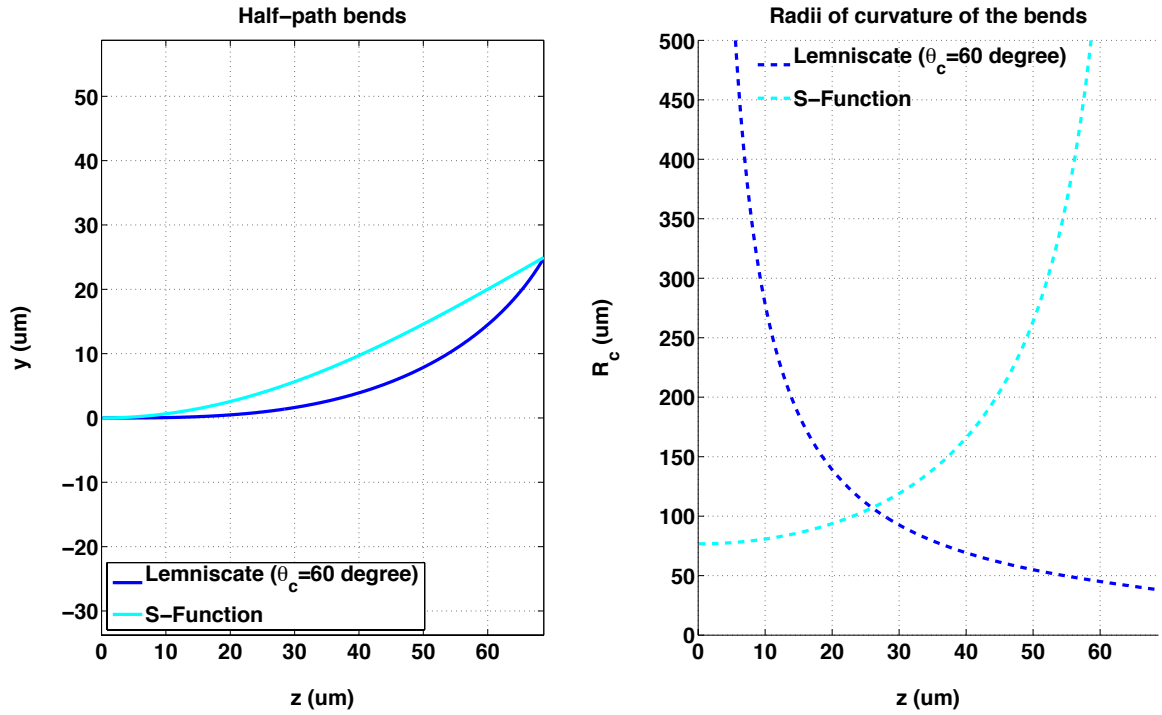


Figure III.43: Trace of half-path bend and evolution of radii of curvature between the lemniscate bend (with $\theta_c = 60^\circ$) and S-function bend for a vertical displacement of $25 \mu\text{m}$.

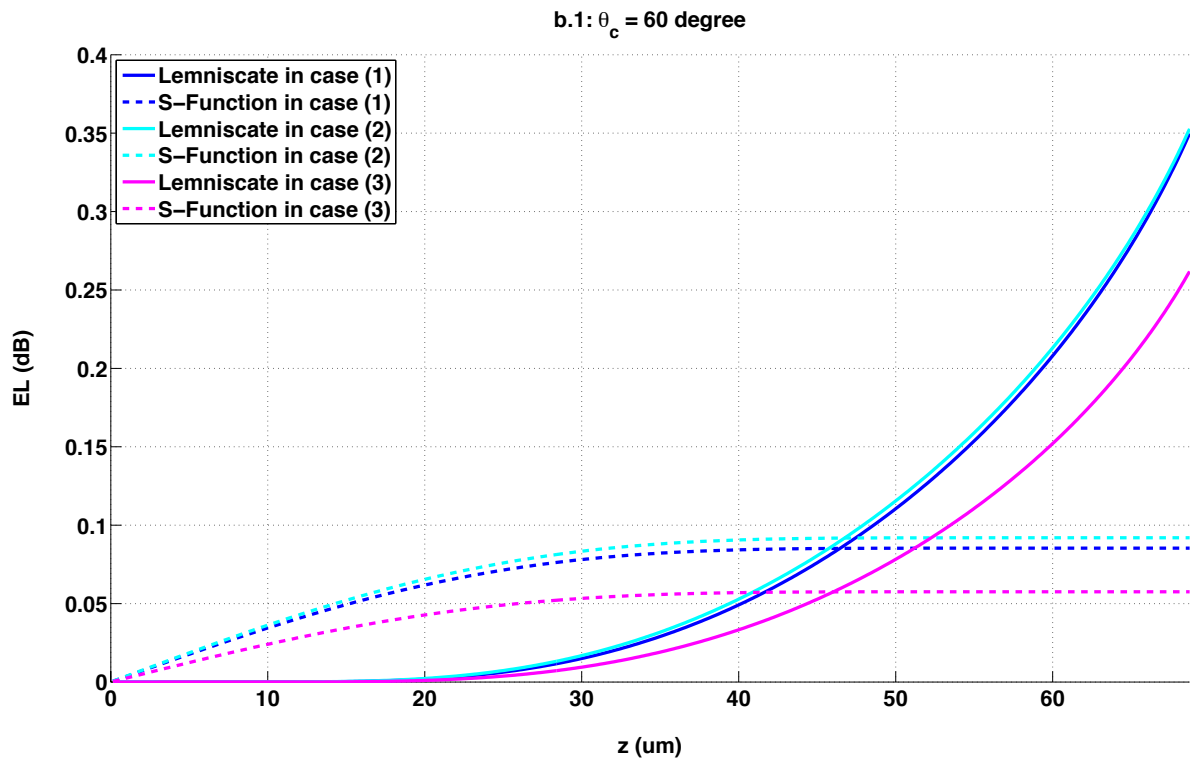


Figure III.44: Theoretical cumulated EL of the bent waveguides (with $\theta_c = 60^\circ$ and $\Delta y_{1/4} = 25 \mu\text{m}$).

As shown in Figure III.44, the radiation loss in the lemniscate bend will exponentially arise up to the maximum at the inflection point, and for the S-Function bend, the accumulated losses will arrive a limit value in the middle of the path. Comparing with different size of waveguide's cross-sections, it has been seen that the TE₀₀ mode propagation losses along the half-path bent waveguide can be reduced about 1/3 by increasing the width of the waveguide (see Table III-10).

b.2 $\theta_c = 90^\circ$

As shown in Figure III.45, the lemniscate bend with $\theta_c = 90^\circ$ is featured by the fact that the wave vector of the propagation modes can turn 90° at the inflection point. Meanwhile, the S-Function bend has a tangential angle of 45° . Comparing with the case b.1 with $\theta_c = 60^\circ$, the length of the bend along the z-axis has been cut off more than one third, although both curves have a comparable minimal R_c (i.e.: $25\ \mu\text{m}$ for lemniscate bend and $40\ \mu\text{m}$ for S-Function bend). The accumulated bend loss along the bend section is presented in Figure III.46. Similarly to the precedent case, the attenuation threshold of the lemniscate-like bent waveguide is located at about one third of the 1st half path. By exceeding the threshold, the R_c will keep descending and the bend loss will arise with exponential growth. During the last few microns along the propagation path, the bend loss in a lemniscate-like bent waveguide will be increased straightforwardly and thus result in a notable growth of the bend's accumulated losses.

By the way, comparing with different cross-section sizes of waveguide presented in case (1)-(3) (see Table III-10), we find the same tendency as the precedent situation with $\theta_c = 60^\circ$: the smaller the dimensions of rectangular waveguide are, the more important the bend loss of the guided TE₀₀ mode becomes. This property fully consists in the characteristic curves C_2 (R_c) curves shown in Figure III.41. Once the minimal R_c of the bends is larger than about $7\ \mu\text{m}$, $C_2(R_c)$ in case (3) will always be larger than that in case (1) and (2), on the opposite, C_1 in case (3) is the smallest among all the cases. Consequently, the bent waveguide in case (3), which has a largest cross-section has the smallest accumulated bend loss. On the other hand, since the minimal R_c of the S-Function bend is at the start point, the EL characteristic curves will also arise quickly during the first few microns of the bend section and arrive at a saturated level of 0.1-0.2 dB, which is almost doubled comparing with that of b.1.

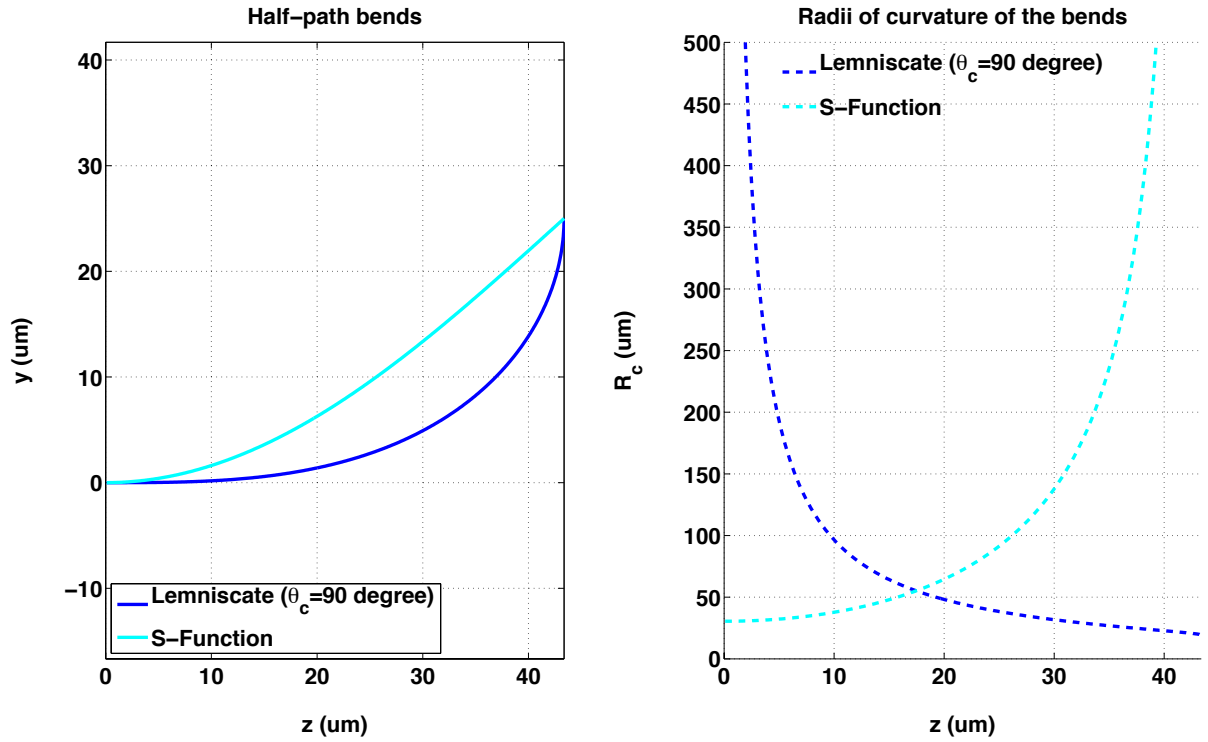


Figure III.45: Trace of half-path bend and evolution of radii of curvature between the lemniscate bend (with $\theta_c = 90^\circ$) and S-function bend for a vertical displacement of $25 \mu\text{m}$.

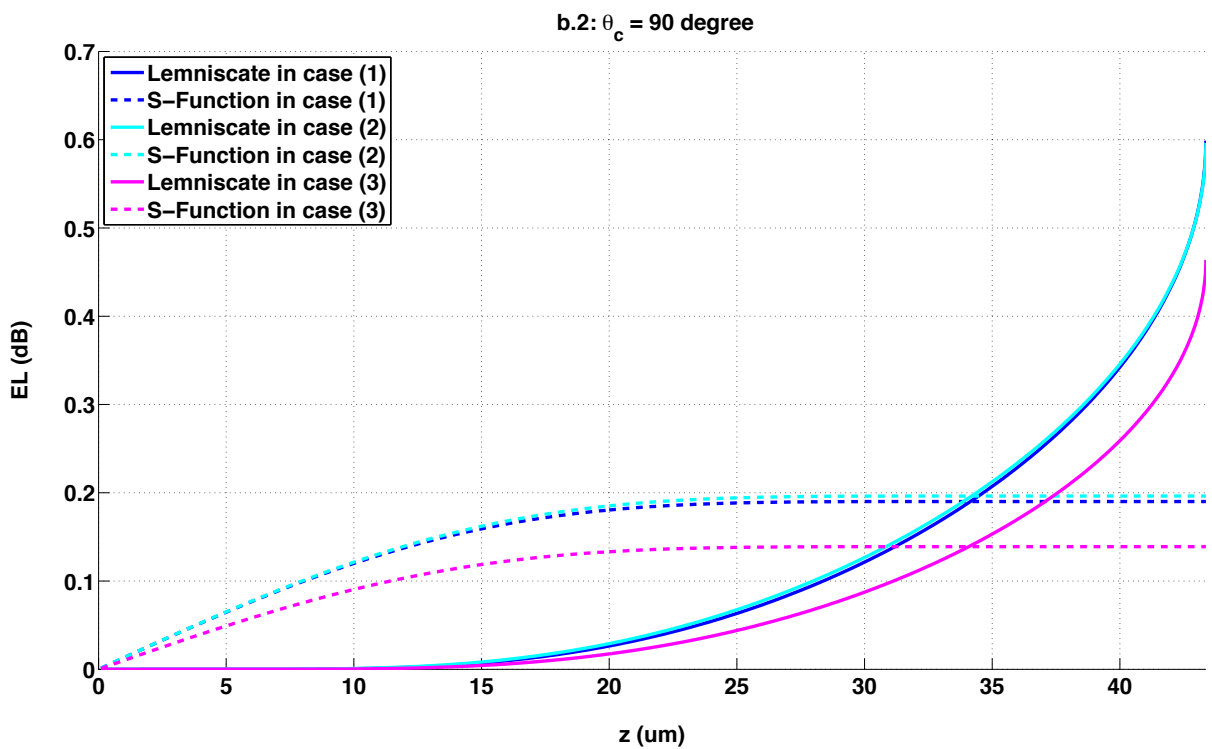


Figure III.46: Theoretical EL of the bent waveguides (with $\theta_c = 90^\circ$ and $\Delta y_{1/2} = 25 \mu\text{m}$).

To sum it up, the accumulated bend loss in a lemniscate with $\theta_c = 90^\circ$ has a lossless propagation within its first third of the 1st half path for the TE₀₀ mode. However, this advantage over the corresponding S-function waveguide will be straightforwardly eliminated by the quick growth of accumulated loss involved in an exponential decay of R_c within the last few microns of the half-path close to the inflection point. However, the S-Function design could also encounter an abrupt change of radius of curvature in the very beginning of the bend section due to the fact that there is always a straight access waveguide used to link the precedent device's output with the bent waveguide. In this case, if the S-Function bend's EL arises quickly to a comparable value, caution should be also taken for the design of the joint straight waveguide.

b.3 $\theta_c = 180^\circ$

The last case we studied is with $\theta_c = 180^\circ$. As shown in Figure III.47, the lemniscate-like bent waveguide could reverse the propagation wave vector's direction at the inflection point. After combining its anti-symmetric twin curve as shown in Figure III.42.b.3, the finally horizontal displacement from the start point to the endpoint b.3 could be remarkably reduced to about 30 μm . In this case, we can save about 2/3 of the z distance with respect to the case with $\theta_c = 90^\circ$, and even 4/5 with respect to the case with $\theta_c = 60^\circ$. Along with the propagation in the lemniscate bend, at the location near the intersection point with the S-Function bend ($z = 22 \mu\text{m}$), the radius of curvature is decreased to the minimum of magnitude of 10 μm , and then R_c will arise very slightly to 11 μm , in where we can find the inflection point. As a result, as shown in Figure III.48, the lemniscate-like bent waveguide will begin to suffer relatively huge losses, when it goes across the turning point at $z = 25 \mu\text{m}$ until the inflection point.

By the way, the influence of the waveguide's cross-section could be also noticed: the EL curves would be separated with more and more difference along the propagation path between the smallest cross-section waveguide in case (1) and the largest cross-section waveguide in case (3). As shown in Figure III.48, the bend loss in the 250 nm \times 400 nm-waveguide will be reduced of 0.3 dB with respect to the 200 nm \times 300 nm-waveguide. For the S-Function, the tangential angle at the inflection point has exceeded 45° . As a result, within the very beginning of the bent waveguide the EL could be already up to 0.2 dB and 0.3 dB for the larger and the smaller cross-section waveguides, respectively.

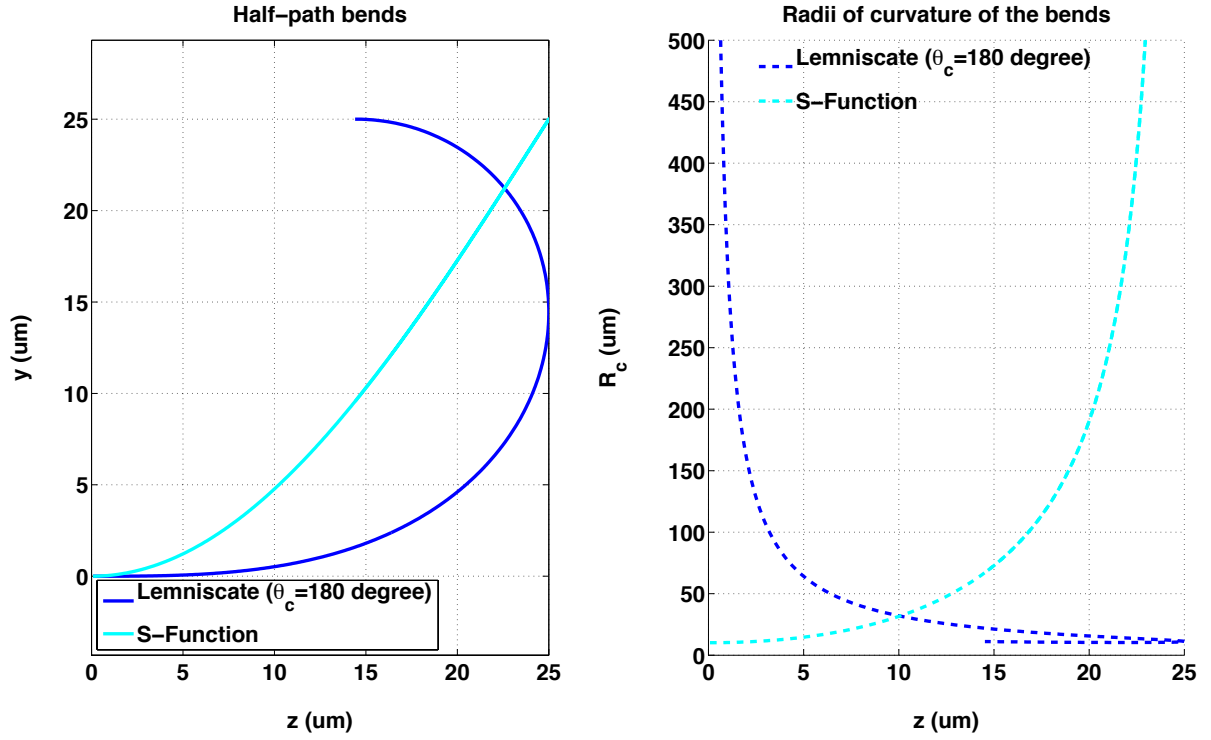


Figure III.47: Trace of half-path bend and evolution of radii of curvature between the lemniscate bend (with $\theta_c = 180^\circ$) and S-function bend for a vertical displacement of $25 \mu\text{m}$.

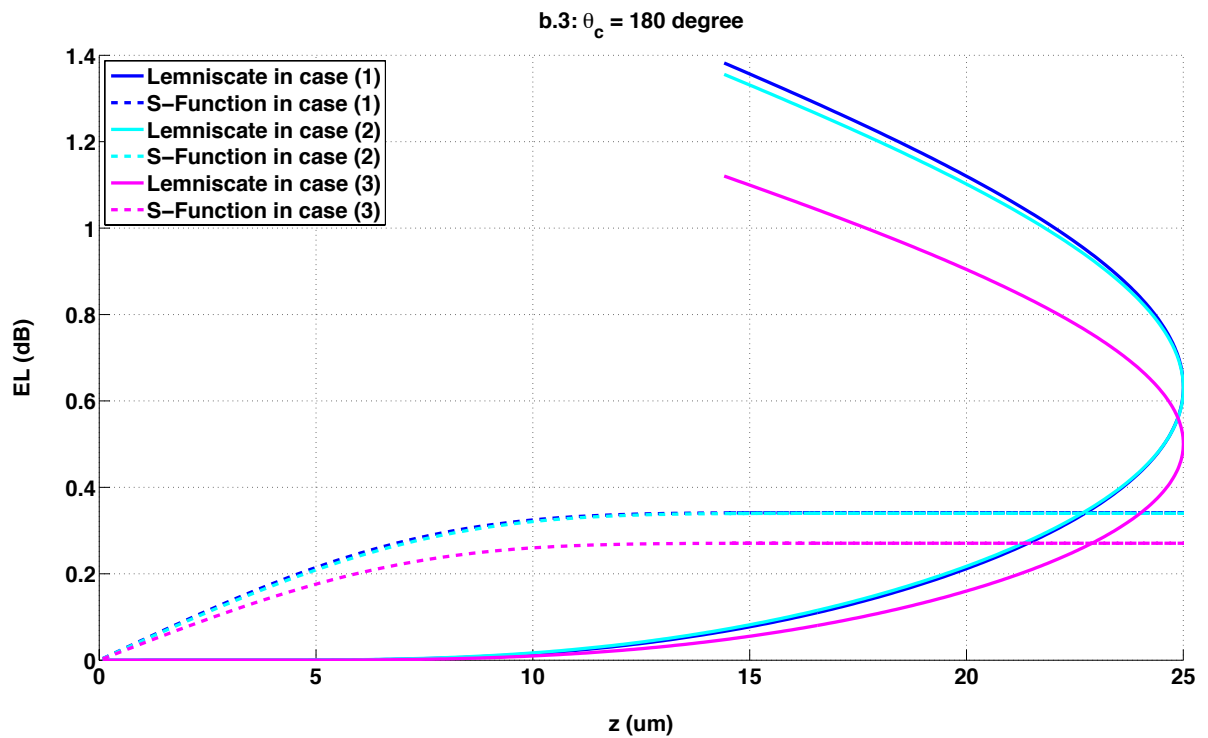


Figure III.48: Theoretical EL of the bent waveguides (with $\theta_c = 180^\circ$ and $\Delta y_{1/2} = 25 \mu\text{m}$).

Finally, we may propose here a new design based on the lemniscate with $\theta_c = 180^\circ$ and $\Delta y_{1/2} = 25 \mu\text{m}$. Considering the first $20 \mu\text{m}$ just before arriving at the intersection point along the propagation in the bent waveguides as shown in Figure III.48, the accumulated bend loss in the lemniscate bend is smaller than in the S-Function bend. We can take this advantage in order to design a low loss (i.e.: for $250 \times 400 \text{ nm}$ Si_3N_4 waveguide $\text{EL} < 0.2 \text{ dB}$) routing device and realize a wave vector's turning of 60° .

Furthermore, we can also choose an arbitrary endpoint with an expected tangential angle θ_c , along the lemniscate curve in order to increase the flexibility of the arrangement of the mentioned cascade devices. In that case, it can be relevant to successively position one lemniscate, one S-function (with inflexion point) and again one lemniscate, with continuous R_c value at the junctions, in order to benefit of the highest R_c values along the whole bend section. Moreover this combination allows connections with “infinite” radius at sensitive interfaces (straight waveguide-lemniscate bend and then the inflexion point inside the S-function bend). This type of wave vector turning device could easily be integrated in the cascade beam splitter as shown in Figure III.34.

III.2.5 Conclusion

In the part III.2, we introduced the design of some elementary passive devices, which are based on the mentioned SiO_2 cladded Si_3N_4 waveguide platform. Firstly, we designed and optimized different types of MMI coupler-based 633 nm single-mode 1×2 beam splitters, in which the simulated EL (excess losses) could be reduced to 0.1 dB and be comparable with the other state-of-the-art 1×2 beam splitters. The complete final 1×16 splitter can be made of a cascade of such 1×2 splitters. Then we systematically studied the bend loss's mechanism based on Marcatili's mode analysis theory. The bend attenuation coefficient has been established as a function of radius of curvature for the studied waveguide platform. By applying this analytic model, we evaluated then the S-Function and lemniscate of Bernoulli-based bent waveguide's design. Finally, the combination of lemniscates and S-function bends has been proposed as a low loss and compact optical routing device to be integrated into a cascade beam splitter system, which could be used to realize the uniform and coherent light distribution on a planar PIC.

III.3 CONCLUSION

This chapter was dedicated to the design of the Si_3N_4 PIC for the 633 nm light uniform repartition on a square-like plate, to match the size and shape of the holographic plate, thanks to a waveguide array, which is composed by different elements as single-mode straight and bent waveguides, and power splitters.

The first step consists in designing single-mode waveguide, or wider “almost” single-mode waveguide in order to limit excess propagation losses. First dimensions of such a SiO_2 cladded Si_3N_4 waveguide were determined at 250×300 nm. As an additional result, by this complete study using vectorial mode calculation software, we also showed that almost square section waveguides lead to first order-like TE/TM hybrid Eigenmode with circular symmetrical intensity repartition. Such a waveguide must be avoided here since it should favour TE/TM conversion.

The second step aimed at choosing and designing the 1×16 power splitter. By a comparison based on excess losses and power non-uniformity properties of different splitters, the 4-stage cascaded 1×2 MMI coupler was identified as the most relevant solution. Such geometry needs then efficient bent waveguides in order to connect the different MMIs and to uniformly position the waveguides and future emitters on the PIC surface.

The last part of this chapter was thus concerned with the bent waveguide design. Especially a full comparison was done on two kinds of bend shape, the S-function and the lemniscate bend. Both have progressive curvature radius, with a different evolution of this radius along the curve. We showed finally that the optimal case should be an accurate combination of the both shapes in order to ensure optimized connection with the straight waveguides, and at the inflexion points. This leads to a typical combination of lemniscate – S-function – lemniscate, which allows connections with “infinite” curvature radius at each interface.

The three main building blocks of the PIC have thus been designed. The experimental performance of these elements should be now evaluated.

CHAPTER IV: FABRICATION AND CHARACTERIZATION OF Si₃N₄ WAVEGUIDES

The fabrication of our samples was realized at the Centrale de Technologie Universitaire (CTU) IEF-MINERVE in the Université Paris-Sud. In this chapter, we will introduce the cleanroom techniques and the process of SiO₂ cladded Si₃N₄ rectangular waveguides as well as some other passive PICs based on the same planar device platform. Meanwhile, we will discuss on some critical parameters within the fabrication process and also present the process optimization. Then we will introduce the characterization methods and analyze some preliminary measurement results. At the end, we will discuss outlooks of this work.

IV.1 CLEANROOM FABRICATION PROCESS

Our integrated photonic devices were fabricated on 4” silicon wafers. The whole flowchart of cleanroom fabrication is shown in Figure IV.1. We will describe the main processes corresponding to the steps of the flowchart in this part.

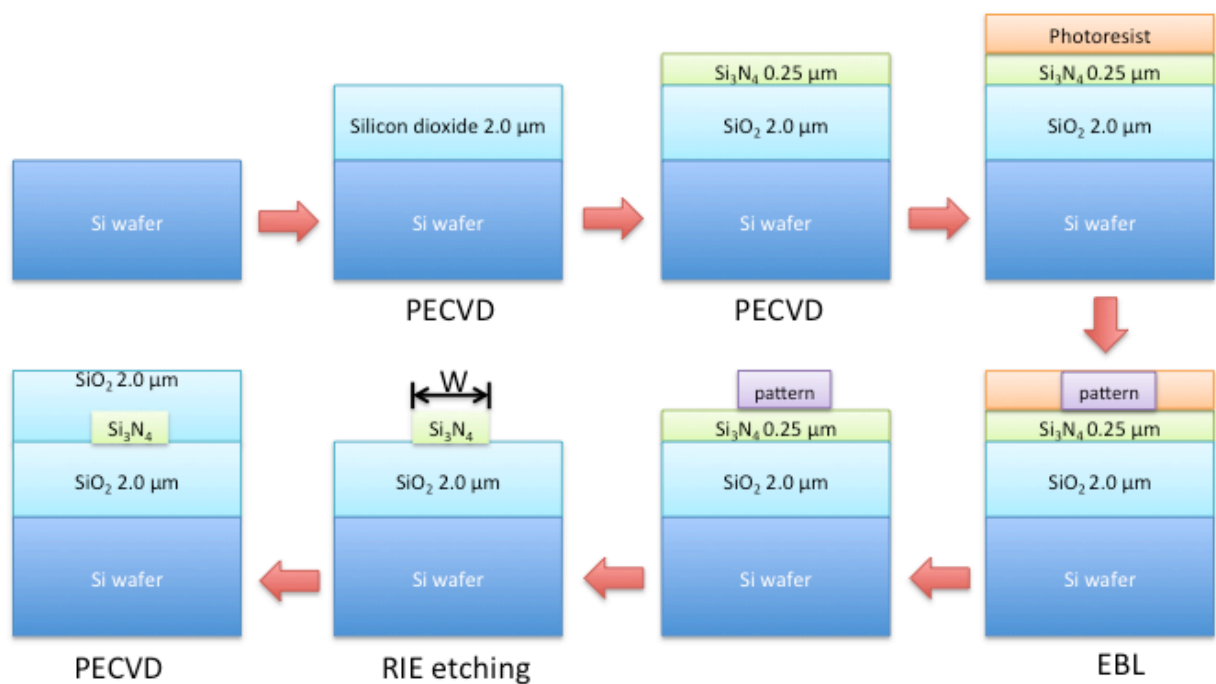


Figure IV.1: Flowchart of the fabrication process in cleanroom.

IV.1.1 Deposition of materials

As mentioned in the Chapters II & III, due to low losses in the visible spectrum, we used the silicon nitride and silicon dioxide as the dielectric waveguide's "core" and "cladding" materials. Meanwhile, the refractive indexes and the physic dimensions of these dielectric materials play a very important role for the propagation of guided modes in the waveguides. We introduce here the deposition process of the sub-micron or several-microns thick silicon nitride and silicon dioxide layers on top of the standard 2" and 4" Si substrate.

a. Principle of LPCVD and PECVD techniques

Usually, there are 2 conventional chemical vapor deposition methods for the silicon nitride and silicon oxide: the low-pressure chemical vapor deposition (LPCVD) [MELCH05, HOSSE09] and the plasma-enhanced chemical vapor deposition (PECVD) [GORIN08, IKEDA08, DAI12]. We will briefly review both CVD techniques and discuss respectively their goodness and weakness.

a.1 LPCVD

For a slab dielectric waveguide, the dominant intrinsic losses are due to the surface scattering, which is generally proportional to the square of the ratio of the surface roughness to the operating wavelength. According to the cited reports, stoichiometric Si_3N_4 layers grown by LPCVD exhibit remarkable refractive index uniformity, highly controllable thickness, and extremely small interface roughness. The LPCVD made slab SiO_2 waveguide contributes of about 0.5-5 dB/cm to the losses of the fundamental guided mode, and more for higher-order modes [HUNSP09]. Meanwhile, for a 2D cross-section dielectric waveguide, LPCVD has also shown its advantage for the purpose of low loss propagation. For instance, the LPCVD made Si_3N_4 channel waveguides had propagation losses of 1 dB/cm for the single-mode regime and down to 0.1 dB/cm in multimode regime at 1.55 μm [SHAW05]. However, this technique for Si_3N_4 is limited by the maximum deposited layer thickness, which is less than 350 nm due to the large internal tensile stress of this material (around 1.3 GPa) [DALDO04b].

a.2 PECVD

The PECVD process is attractive in our application due to the low temperature of the deposition chamber (usually 300-400 °C for PECVD and 800 °C for the LPCVD). It is used to deposit thin films from a gas state (vapor phase) to a solid state on a substrate within the

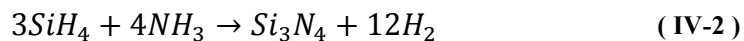
chemical reaction induced by the plasma. The plasma is created by radiofrequency between two electrodes, i.e.: HF-PECVD usually works at a high frequency of 13.56 MHz and LF-PECVD works at a low frequency from 10 kHz to 500 kHz. The chamber is filled with reacting gases and plasmas typically operate at pressures from a few mTorr to a few Torr. For LF-PECVD process, low-mass ions can follow the applied radio frequency electromagnetic field so as to cross the plasma sheath and directly bombard the substrate leading a change of structural and physical properties of the deposited films. *Gorin et al.* reported their preference of this low-frequency technique to deposit silicon nitride materials for application of channel waveguides, due to a higher optical index and a lower absorption coefficient over the visible wavelength-range in comparison with HF-PECVD [GORIN08]. In our process, we chose LF-PECVD technique to deposit both oxide and nitride layers.

b. Deposition of SiO₂ and Si₃N₄ by PECVD

Deposition process of SiO₂ cladding layer on silicon wafer is as follows: once a voltage is dropped across a thin sheath region between the plasma and the sample in its contact, all the ionized atoms or molecules that diffuse to the edge of the sheath region are attracted by an electrostatic force and are accelerated towards the neighboring surface. Thus all surfaces exposed to the plasma receive energetic ion bombardment. Especially when high-density plasma is formed, the density of ions can be high enough to result in a significant sputtering of the deposited films. The chemical reactions involved in this process are presented as follows:



The formed film of silicon dioxide contains hydrogen impurities from the silane precursor. Then, a new vacuum pumping with the initialization of the ambience in the reaction chamber will be executed to eliminate the N₂O and N₂ before the nitridation reaction happens as follows:



During this reaction, if the silane percentage and ion bombardment are increased, a film of silicon rich silicon nitride will be formed, thus the composition of the Si and N elements is not as precise as the subscripts of Si₃N₄. But a low deposition temperature would be helpful to stabilize the nonstoichiometric Si_{3+x}N_{4-y}. As seen in Chapter II, an ellipsometric measure of refractive indexes of both deposited layers has been done to give a reference for our fabricated materials. The process parameters of our PECVD recipes could be found in Table IV-1.

Table IV-1: Parameters¹³ of PECVD processes at the CTU IEF-MINERVE.

Recipe	P_{op}	T_p	T_{sh}	Gas (flux)	t_{op}	Th_{ellip}	n_{ellip}
LFSIO	550 mTorr	300 °C	250 °C	N ₂ O (1420 sccm)	30'	2272.55 ±	1.438 ±
				SiN ₄ (400 sccm)		10.182 nm	0.003
LFSIN	550 mTorr	300 °C	250 °C	NH ₃ (20 sccm)	5'30"	262.12 ±	1.9995
				SiH ₃ (2000 sccm)		0.711 nm	± 0.006

The silicon nitride film seems to contain hydrogen impurities, which are probably introduced by silane and could result in absorption effect in the NIR range. According to references, by applying a high-temperature annealing, i.e.: at 800°C or at 1000°C, some of the stress and trapped gases could be removed from the deposited layers [GONDA10]. Recently, *Romero-Garcia et al.* reported cladded single-mode photonic wire with low waveguide loss (< 0.7 dB/cm) at 660 nm fabricated within a CMOS pilot-line using PECVD technology, while *Subramanian et al.* also reported low loss silicon nitride waveguide for 532-900 nm application [ROMER13, SUBRA13]. Thus, with an optimization of PECVD by adjusting the ratio of the reactive gases and processing and using an additional annealing step after the deposition, we believe that high quality SiO₂ clad Si₃N₄ rectangular waveguides should be obtained (not applied here).

IV.1.2 Electron beam lithography

Electron beam lithography (EBL) is the key step for the cleanroom fabrication of sub-micron integrated devices. Within an ultra-vacuum and stable room-temperature environment, EBL set-up exposes a thin film of chemical resist (usually with a thickness of several hundred nm to several μm) and writes down the design patterns (with a feature size down to several nm) by moving a high-voltage electron beam gun, in which the exposure dose of electron beam and displacement step-size can be precisely controlled. *Shawn et al.* reviewed and compared the mainstream high-energy EBL techniques [SHAWN10] to show the outstanding writing precision of EBL technique comparing with the conventional projection optical lithographic

¹³ P_{op} : Operation Pressure in the reaction chamber; T_p : Temperature of platen; T_{sh} : Temperature of showerhead; t_{op} : Processing Time; Th_{ellip} : Ellipsometry measured thickness of deposited layer; n_{ellip} : Ellipsometry measured refractive index.

techniques. Finally, by applying a corresponding development solution, the expected patterns with a fine feature size could be thus transferred to the resist layer, which is made of some specific polymer materials.

a. Preparation of substrate and spin-coating of resists

A step of substrate cleaning should be done before the spincoating of resist. Typically, we use firstly the PICO plasma cleaner to clean the surface of the PECVD made Si_3N_4 samples. The pressure of oxygen is set to 0.7 mBar and the generator’s power is 160 W at 40 kHz. After 5-minute oxygen plasma cleaning, the substrate is rinsed with acetone, Isopropyl alcohol (IPA) and de-ionized water. Then we dry them with nitrogen.

A widely used negative photoresist MaN-2403 is used as our e-beam resist. The choice of negative resist is based on the fact that waveguide-occupied effective writing area should be very small comparing to the whole pattern frame with a distribution of planar-geometry split waveguides. Meanwhile, according to the characteristic of MaN-2403, we found it to be readily used to pattern narrow and long ridge-like waveguide with a featured size down to 25 nm and to be nearly independent on the dose of e-beam in the case we keep the feature size of pattern at the same order of magnitude. To improve EBL performances, a HMDS¹⁴ Prime promoter layer of several ten nanometers is used to increase adhesion between silicon nitride surface and MaN-2403 layer by reacting with the substrate material, removing absorbed water and reducing surface energy. Another layer of E-spacer 300Z has been spun on top of the MaN-2403 in order to prevent internal charge build-up in the dielectric materials during the e-beam writing process. The parameters of spincoating processes are summarized in Table IV-2.

Table IV-2: Parameters of spincoating program for the resist deposition.

Material	Speed	Acceleration	Delay	Thickness	T_{bake}(@90°C)
HMDS	5000 rpm	5000 rpm/s	60’’	several nm	None
MaN-2403	4000 rpm	5000 rpm/s	60’’	≈250 nm	90’’
E-spacer	4000 rpm	5000 rpm/s	60’’	Several nm	120’’

¹⁴ HMDS: Hexamethyldisilazane.

Caution should be taken when we put the HMDS on the Si₃N₄ deposited samples. Since the methyl groups of the HMDS fragment form a monolayer of hydrophobic-like surface on top of the water-free Si₃N₄ substrate accompanied with the release of NH₃, a N₂ bubbler oven step has to be done to HMDS for the water-free substrate. In our case, only spin-coater is available to deposit HMDS, so we have to make sure that a very thin thickness is deposited by increasing the speed of the spinning. Otherwise, a too thick HMDS film will make the through-developing process impossible [MICRO13].

b. Nano-beam lithography

We have used the NanoBeam© nB4 to write the waveguide patterns at the CTU IEF-MINERVE.

b.1 Operational parameters and writing strategy

The mentioned nB4 facility uses an acceleration voltage from 30 kV to 100 kV. According to the database, a guaranteed writing beam size down to 8 nm could be obtained for an operating voltage at 80 kV. We use a negative resist (i.e.: MaN-2403) for the EBL process due to the fact that the effective writing area is small. A relatively low writing current (i.e.: 1.6 nA) has been thus chosen to write our patterns. In fact, the criterion of operational current relies on the exposure dose and the writing areas. For the conventional EBL technique, we can define the dose of exposure D as follows:

$$D = \frac{IT}{A} \quad (\text{IV-3})$$

where I is the beam current, T is the dwell time of exposure, A is the exposed area and D has usually an order of magnitude of $\mu\text{C}/\text{cm}^2$. By the way, once we choose the operation current, we can use (IV-3) to estimate the writing time. Since the contact between the electron beam and the surface of electron sensitive resist is diffusive, the dose of exposed electron beam is a decisive factor in order to precisely control the exposed area, which results in the determination of pattern's dimensions in the resist layer. The EBL's exposure process of a typical tapered waveguide is schematically illustrated in Figure IV.2.

The first wider rectangular section is used for coupling the input light from the micro-lensed optical fiber with a diameter of 2 μm ; the second taper section is used to transmit progressively the input light beam into a 300 nm-wide single-mode Si₃N₄ waveguide, which is illustrated in the 3rd section. Meanwhile, we suppose the length of each section is variable from several μm to several mm. In fact, within a sub-field writing zone (typical 20 $\mu\text{m} \times 20$

μm), the e-beam gun only adjusts its emission angle to leave the exposure trace following a vector-scan mode along a referenced direction and finally covering the whole sub-field pattern zone. The nB4 system chooses the shorter side of a rectangular pattern zone with a default setting. For example, in the case shown in Figure IV.2 the vector-scan starts with the top-left of the pattern, then moves vertically from top to bottom, and finally turns 90° to the second column. This repeatable round-way scanning lasts within the whole sub-field area.

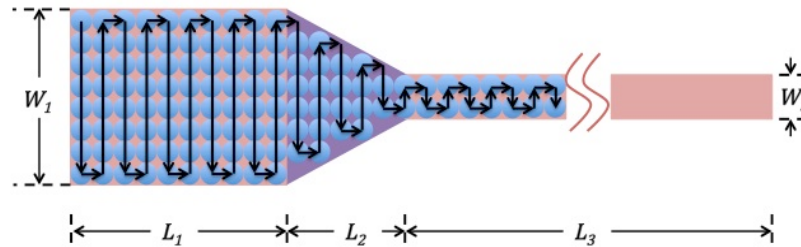


Figure IV.2: Schematic diagram of the EBL exposure spot routing to write a tapered rectangular waveguides.

b.2 Field stitching errors

Once the emission angle leans towards its limit where the exposure spot arrives at the edge of the first sub-field, the e-beam emission will move into the next sub-field pattern area without mechanical move. At this moment, a mismatch of focus and an abrupt variation of e-beam's location could probably cause "sub-field stitching". As shown in Figure IV.3.(a), these field-stitching effects occur occasionally within the section of straight 300 nm-wide waveguides. As a result, a lateral shift of patterned resist is observed, and the measured spacing distance is varied from several nm to tens of nm. From the light beam propagation point of view, this fabrication error could result in considerable loss due to misalignment and also discontinuity.

Similarly, once the e-beam gun finishes writing the whole main-field (typical $500 \mu\text{m} \times 500 \mu\text{m}$), nB4 system will send to the stepping motor a driving command to move the beneath chuck with a step size of $500 \mu\text{m}$. This mechanical movement of heavy metallic chuck probably causes another type of pattern's mismatching or discontinuity called "main-field stitching". In fact, a non-optimized "main-field stitching" has also a feature dimension of several tens of nm, or even more. Consequently, a discontinuity near a main-field's boundary has also been observed (see Figure IV.3.(b)).

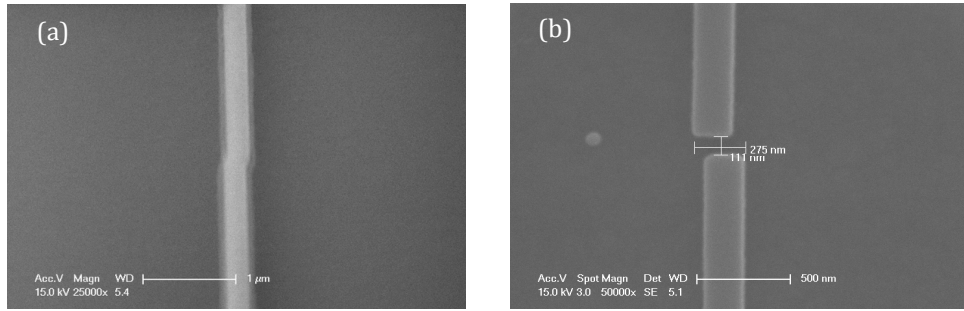


Figure IV.3: Micrograph of resist after developing: (a). a lateral shift caused by the sub-field stitching; (b). a discontinuity of pattern caused by the main-field stitching.

b.3 Stitching error's overcoming with alignment marks

Although the errors due to sub or main-field stitching are relatively smaller than the feature dimensions of the patterned waveguides, we need after all to correct effectively it to optimize propagation performances. We introduce here a self-focusing method assisted by additional alignment marks. Before applying the spin-coating of the EBL resist, we have deposited a series of Au rectangular marks (typically $6 \mu\text{m} \times 8 \mu\text{m}$ with a spacing of $200 \mu\text{m}$) on the top of the Si_3N_4 layer by UV lithography and lift-off techniques (see Figure IV.4.(a) and (b)).

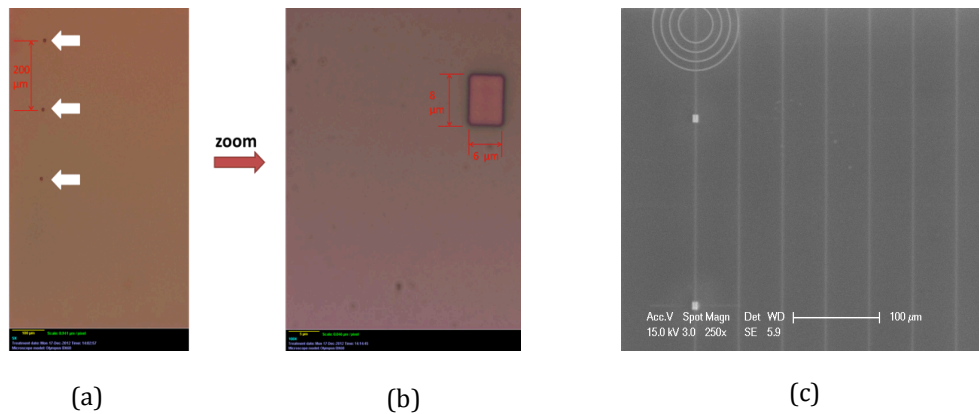


Figure IV.4: (a). & (b). Optical microscopic photos of Au alignment marks deposited on silicon nitride samples; (c). Micrograph of alignment marks with EBL patterned resist.

These 3-element metallic marks can be found in a line every 2 mm in horizontal and vertical directions. An identification program of nB4 is thus executed to verify the alignment marks by refocusing on them with the EBL's scanning electron microscope. If the size of rectangular match, the location and the updated focus value for each alignment mark are

registered in order to generate a new and more precise focus map within the whole substrate. It means that with a displacement of 2 mm during the EBL writing, the focus can be updated by using the data of the neighboring alignment marks taken from the new focus map. By the way, in our case, we defined also the EBL's writing coordinates by linking the locations of two horizontally arranged alignment marks with a relative large spacing distance for example, 4 mm. The idea is to write down our straight waveguides in parallel with the horizontal abscissa in the EBL's writing coordinates. Furthermore, these alignment marks can be used during the sample's cleavage process, since the μm -wide marks are easily observed and localized by the assistance optical microscope in the dicing saw, rather than the nm-wide waveguides.

b.4 Analysis of the charge effects

Moreover, if we consider the reaction between the e-beam and the electron sensitive resist deposited on top of the dielectric materials, there should be others "charge effects" due to the secondary electrons and the back-scattered electrons, which will expose a certain area around the principal e-beam spot (see Figure IV.5). Each exposure of nB4's with a Gaussian-like e-beam profile forms a spot with a nominal size of 2 nm. If we apply a relatively large current or choose a small dose for the EBL process, the exposure time would be thus increased. According to (IV-3), we have to enlarge the step size, in order to avoid exceeding the nominal frequency of exposure (typical 50 MHz). In this case, we need to delete the residual effects of charge due to the secondary and back-scattered electrons. Indeed these residual electrons are totally diffusive in the resist and they could straightforwardly modify the shape of exposed resist. As a result, the lithographic quality could be degraded. That's why an additional E-spacer layer is realized on top of the MaN resist in order to prevent the internal charge build-up of the residual electrons.

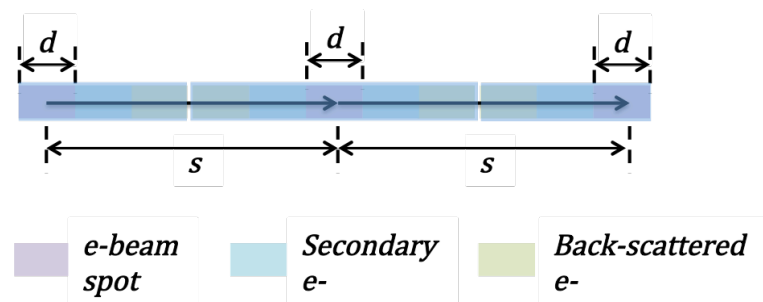


Figure IV.5: Schematic diagram of charge effects in the resist due to the principal and residual electron beams during the EBL writing process. d is the typically diameter of the e-beam spot and s is the experimental step size of EBL exposures.

c. Resist development

We use AZ-726 MIF to develop the EBL exposed MaN-2403 resists. It contains a wetting agent for fast and uniform wetting of the wafer. This helps ensuring good uniformity when short developing duration is chosen. Based on our test results, 30 seconds are enough to remove the unexposed resist with a thickness of 250 nm. In addition, the sample has been submerged in the de-ionized water for 20 seconds before developing to wet and dilute E-spacer layer. Slightly jiggle of the sample is useful to optimize the contact between the organic solution and the sample during the developing. The sample should be always placed horizontally and jiggle from side to side along the parallel direction with the straight waveguide's pattern. After the developing, we rinse the sample with de-ionized water for more than 2 minutes and then dry it with nitrogen.

d. Optimization of EBL process

We can firstly evaluate the EBL's performances by observing the cross-section's profile of the developed resist. By the way, a thin layer of Au can be deposited on top of the developed samples, in order to avoid the unfavorable charge effect in the scanning electron microscope (SEM) and enhance thus contrast of the micrograph.

d.1 Discussion on the vector-scan mode

In our EBL optimization process, we firstly aim at overcoming the discontinuity and unfavorable pattern shifting due to the sub-field(s)-stitching. By applying the alignment marks, these issues could be effectively improved. On the other hand, since the fabricated straight waveguides have a length of at least 800 μm and a cross-section of 250 nm \times 300 – 400 nm, which are then cleaved and measured in an optical loss characteristic platform, the main-field stitching could be still detected from the transmission spectrum. We will discuss on this issue afterwards.

Secondly, the influence of the dose and stepsize of the e-beam exposure on the developed resist's cross-section's profile has to be investigated. By the way, we must point out that nB4's vector-scan mode may introduce gentle undulations along the sidewall of developed resist (see Figure IV.6). In fact, if the step size of exposure is slightly larger than the experimental exposure spot size, the time-domain convolution of the dose profile along the horizontal axis is smoother than the one along the sidewall of waveguides. Because nB4 chooses the shortest side of pattern zone as its trajectory of writing, the abrupt change of writing direction occurs

along the vertical side of pattern. This wave-like dose profile would thus be transferred into the resist. According to the optical loss theory [GOELL77], the surface scattering loss due to the roughness of waveguide's sidewall would be dominant in the propagation losses of the dielectric waveguide.

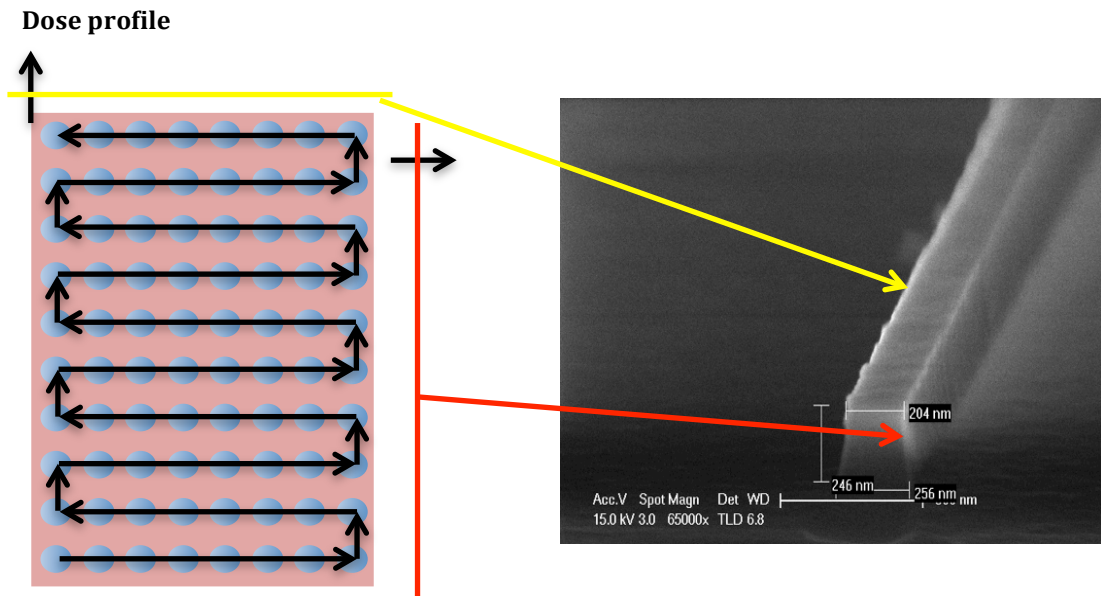


Figure IV.6: Schematic illustration and SEM photo of etched sample show the undulation of the rectangular waveguide's sidewall and top face due to the vector-scan writing mode.

d.2 EBL's dose and stepsize tests

In the very beginning of our EBL tests, we tried varying doses and step-sizes. Typically, doses from 2.0 C/m^2 to 5.0 C/m^2 and exposure step size from 5 nm to 15 nm were tried. The tested pattern was a series of 350 nm-wide straight and curved waveguides and some of the results are presented in Figure IV.7. As shown in Figure IV.7 (a) and (b), in the case of a large step size of 10 nm, there are two sloping facets on the top of the waveguide and the cross-section is not rectangular with expected dimensions. Especially when the dose of exposure is small at 3.1 C/m^2 (see Figure IV.7 (a)), the difference between topside and bottom side of the developed resists is large. On the other hand, in the case of a higher dose as shown in Figure IV.7.(b) and (d), the profiles of resist are closer to a rectangular and their cross-section are closer to the expected dimensions with extremely vertical sidewalls. By comparing a large amount of samples with different EBL doses and step-sizes, we have found the same tendency even if influence of the dose is weak on the developed resist's profile.

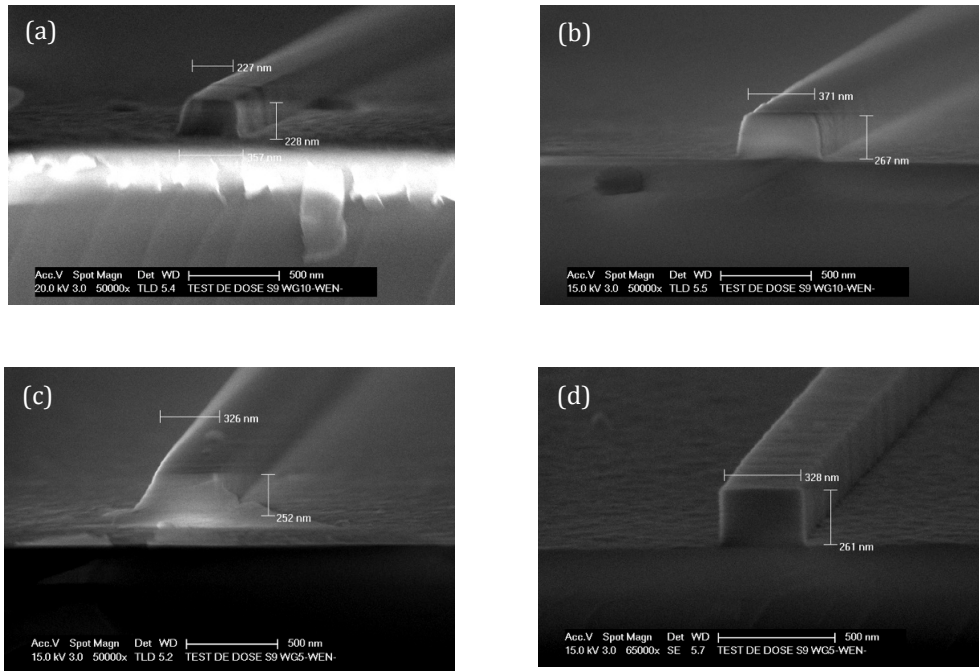


Figure IV.7: Micrograph of cross-section and sidewall of resists after developing. The pattern is 350 nm-wide straight waveguides: (a). $s = 10$ nm and $D = 3.1$ C/m²; (b). $s = 10$ nm and $D = 4.1$ C/m²; (c). $s = 5$ nm and $D = 3.1$ C/m²; (d). $s = 5$ nm and $D = 4.5$ C/m².

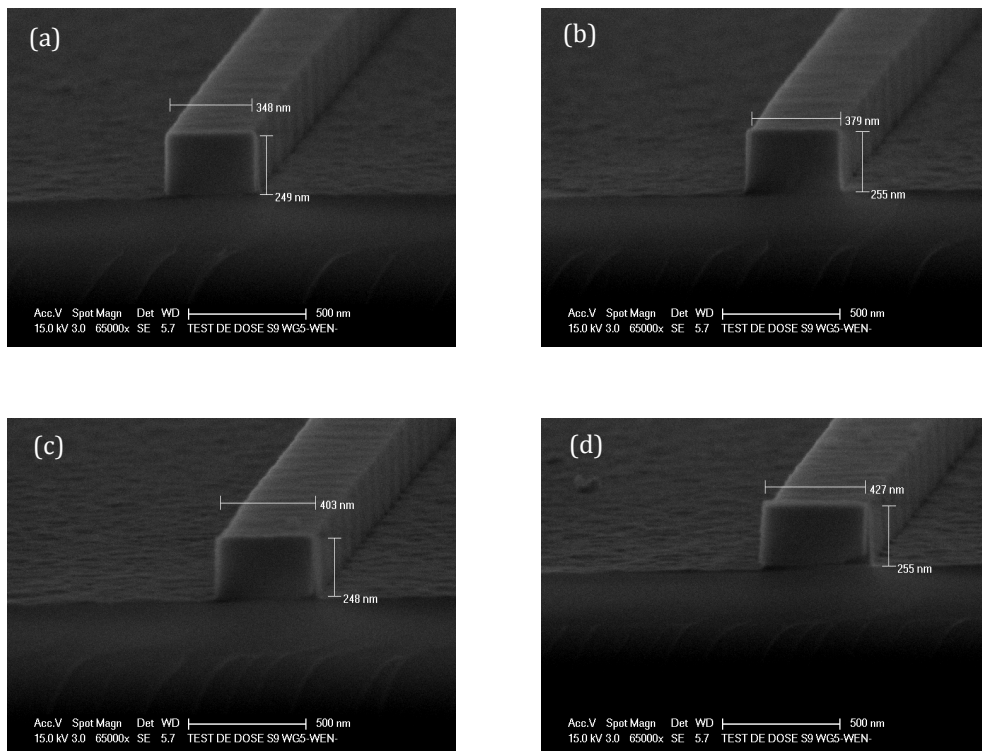


Figure IV.8: Micrograph of cross-section and sidewall of resists after developing for the pattern design with different widths of waveguide w . The EBL's parameters are $s = 5$ nm and $D = 4.5$ C/m²: (a). $w = 380$ nm; (b). $w = 400$ nm; (c). $w = 420$ nm; (d). $w = 450$ nm.

To sum it up, we need firstly to decrease the step-size of the EBL as small as possible, in order to improve the uniformity of the profile. If we fix the operation current at 1.6 nA and a step-size of 5 nm, the optimized dose is 4.5 C/m². In Figure IV.8, SEM photos of width-varied samples in these conditions are shown. Similarly to the case of Figure IV.7 (d), the cross-section profiles of developed resists are close to a rectangle with a thickness of the developed MaN layer around 250 nm. Comparing with the expected width of the patterns, the developed resist has only a mean tolerance of 20 nm, which is acceptable considering the nB4's minimal nominal precision of 8 nm. However, the presences of mentioned undulations due to nB4's intrinsic vector-scan writing still persist on top and along the sidewalls of the resist.

IV.1.3 Reactive ionic etching

Reactive ion etching (RIE) uses chemically reactive plasma to remove, in our case, dielectric materials deposited on the silicon wafer. Due to the vertical delivery of most reactive ions, RIE, as inductively coupled plasma (ICP) combined with RIE, can produce anisotropic profiles, in order to realize a high aspect ratio silicon etching [WU10]. Meanwhile, the RIE and ICP-RIE etchings for the rectangular Si₃N₄ waveguides with good properties have also been reported in [GONDA10]. We introduce here the RIE process applied for our EBL samples and evaluate the etching performance by analyzing the influence of different parameters of RIE process.

a. Principle of RIE plasma etching

A schematic illustration of the RIE facility and RIE plasma etching process is presented in Figure IV.9. In the reaction chamber and within a varied-pressure atmosphere, the precursor gases i.e.: CHF₃ and CF₄, are dissociated with the energized plasma's electrons, generated at radiofrequency. The reactive species i.e.: CF₃⁺ and F diffuse into the dielectric layer(s) of the samples along a certain flux direction. The Si₃N₄ layer adsorbs the reactive species and its Si-N bonds are also broken and replaced by the SiF₄. Therefore, the solid Si₃N₄ is transferred into gases and leave the sample's surface. Meanwhile, a high-density reactive gas flux causes a physical collision in the Si₃N₄ layers. A combination of these chemical and physical effects can consequently etch the Si₃N₄ layer with a controllable etching rate. Once the whole Si₃N₄ layer has been totally removed, the beneath SiO₂ layer can suffer from the precursor gases. However, the SiO₂ layer should have a different etching rate, usually faster than the Si₃N₄ one

because it's easier for the Si-O bonds to adsorb the fluorine ions and form the SiF_4 gas. As a result, by choosing an appropriate etching selectivity, we can obtain an expected rectangular Si_3N_4 etched structure on top of the SiO_2 layer.

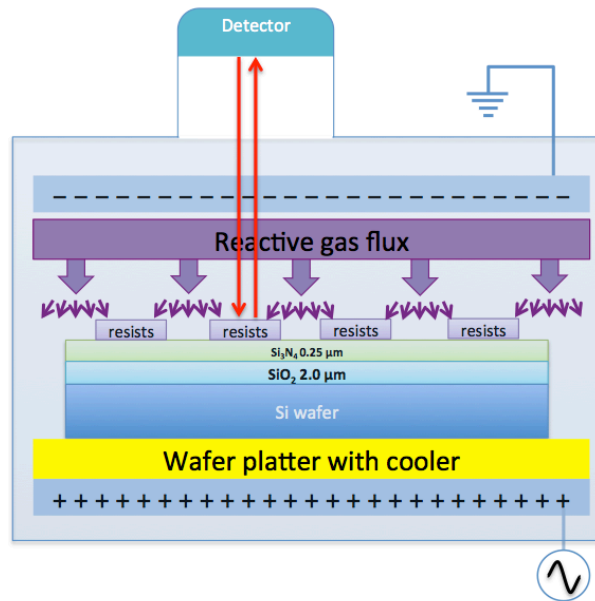


Figure IV.9: Schematic illustration of the RIE set-up and plasma etching processing.

b. Laser interferometer based end-point detection

By using a Jobin Yvon 633 nm laser interferometer based RIE end-point detection system (shown as “detector” and red-line laser beams in Figure IV.9), we can monitor in real-time the etching process, which is presented by the interference fringe’s evolution as a function of operation time.

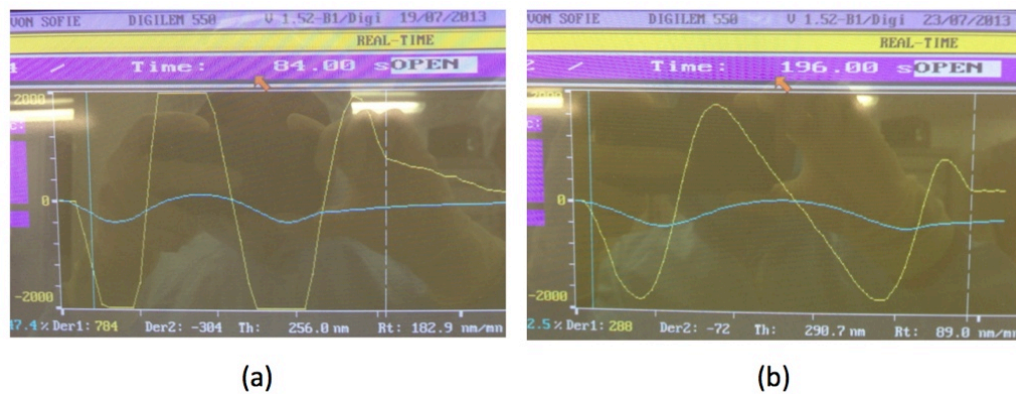


Figure IV.10: Jobin Yvon’s end point detection laser interferometer experimental data: (a). with 30 mTorr and 450 W; (b). with 20 mTorr and 150 W.

Based on some precedent test recipes at IEF, we have started our RIE tests with the precursor gases of CF_4 and CHF_3 flux values of, respectively, 42 and 10 Standard Cubic Centimeters per Minute (scm). In this situation, we evaluated the etching rate (ER) as a function of chamber pressure and RF power. As shown in Figure IV.10, we found clearly a shift of interference fringe's periods after certain duration of RIE etching. In the case (a), the first periodic oscillation ends at 84 s, and it corresponds to the RIE condition of 30 mTorr and 450 W. On the other hand shown in the case (b), the shift of oscillation period occurs at 196 s due to a decreased RF power and chamber pressure. As the reactive gas flux is diffused homogeneously in the environment where our Si_3N_4 samples is, etching effect in the same dielectric materials could be considered to be uniform from a macroscopic point of view. Thus the RIE etching rate is supposed approximately a constant within the Si_3N_4 layer. Therefore, a study of the influence of RF power (chamber pressure: 40 mTorr; RF power: from 100 to 600 W) and chamber pressure (RF power: 450 W; chamber pressure: 15 to 40 mTorr) on Si_3N_4 ER was carried out and the results are shown on Figure IV.11.

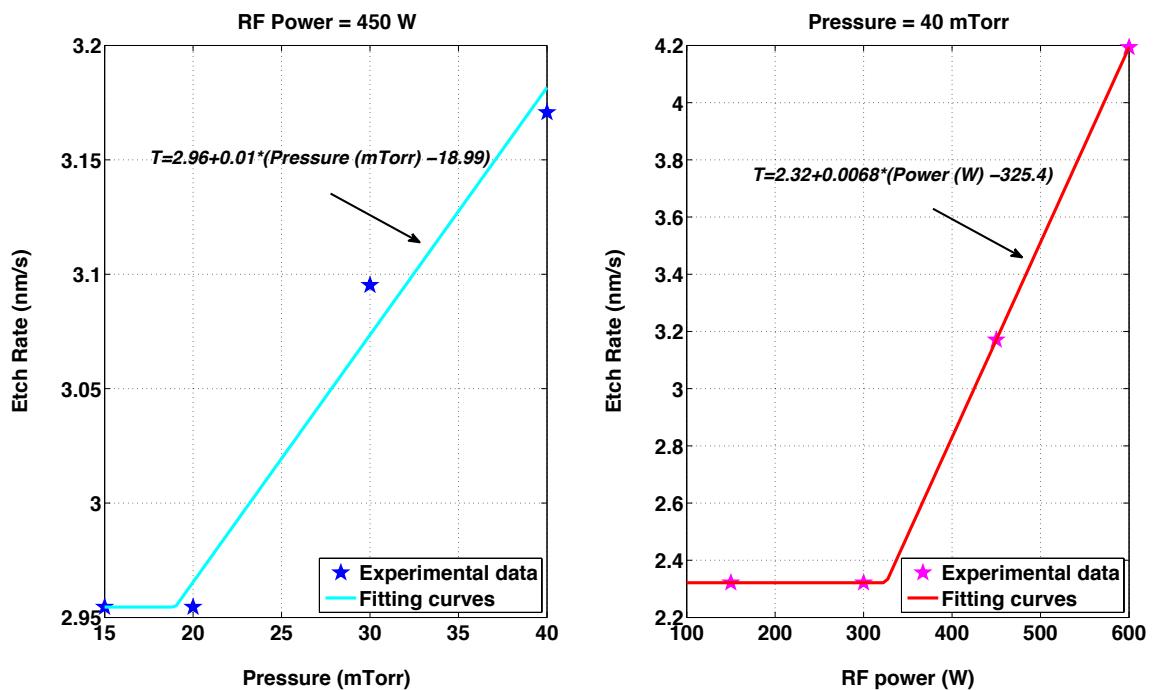


Figure IV.11: Characteristic curves of etch rate as a function of chamber pressure and RF power in the RIE process for the 260 nm-thick Si_3N_4 waveguide samples.

As shown in Figure IV.11, both characteristic experimental data are linear. In the chamber pressure-dependent ER curve, there is a threshold around 20 mTorr with constant ER

of 2.95 nm/s below and a linear growth with a slope of 0.01 nm/s/mTorr above. On the other hand, in the RF power-dependent ER curve, we found a threshold RF power of 325 W with constant ER of 2.32 nm/s below and linear growth with a slope 0.0068 nm/s/W above.

c. Evaluation of the cross-section profile

The pattern for EBL is composed of width-varied straight waveguides, optimized EBL process conditions have been applied ($D = 4.5 \text{ C/m}^2$ and $s = 5 \text{ nm}$) and a recipe with 42 sccm of CF_4 and 10 sccm of CHF_3 has been used for etching. The test of RIE is aiming to optimize the etched waveguide's cross-section's profile by varying the chamber pressure and RF power and to obtain an 260 nm-thick Si_3N_4 rectangular waveguides with sidewalls as vertical as possible for the purpose of TE_{00} mode's E-field symmetry. Meanwhile, the etched waveguides are expected to have minimal sidewall roughness, in order to decrease the surface scattering loss. We present here some representative samples with 3 different RIE recipes. By the way, since there were still some unconsumed Man-2403 resists persisting on top of the patterned Si_3N_4 waveguide with a thickness of several tens of nm, samples have been firstly washed by the acetone + IPA solution and then loaded in the *PICO* plasma cleaner.

c.1 Sample 10: Pressure = 40 mTorr, RF power = 300 W and etching time = 112 s

As shown in Figure IV.12, the sidewall bowing effect is observed, which means the etched waveguides have a pair of hyperbola-like sidewalls. According to [RANGE03], the general reason to form such a sidewall bowing is the non-uniform charging effect due to the electron shading. Upper parts of the sidewalls are locally charged and would reduce the flux of etching species reaching the bottom of the samples. As a result, the horizontal moving flux of etching species could be denser than the vertical flux, which is going down. Since the expected rectangular has a low aspect ratio, the lateral etching effect on the middle part of sidewalls become more important in this case. Consequently, both chemical reaction and physical collision of the etching species have more impact in the middle part of the sidewalls. Meanwhile the top part suffers from less etching effect than the middle because of the protection by the resists, and the foot of the Si_3N_4 received less etching species. Finally, a bowing-like cross-section is formed. From the propagation mode's distribution view of point, such a bowing-like Si_3N_4 ridge waveguide would have no longer a horizontal symmetry for the fundamental modes.

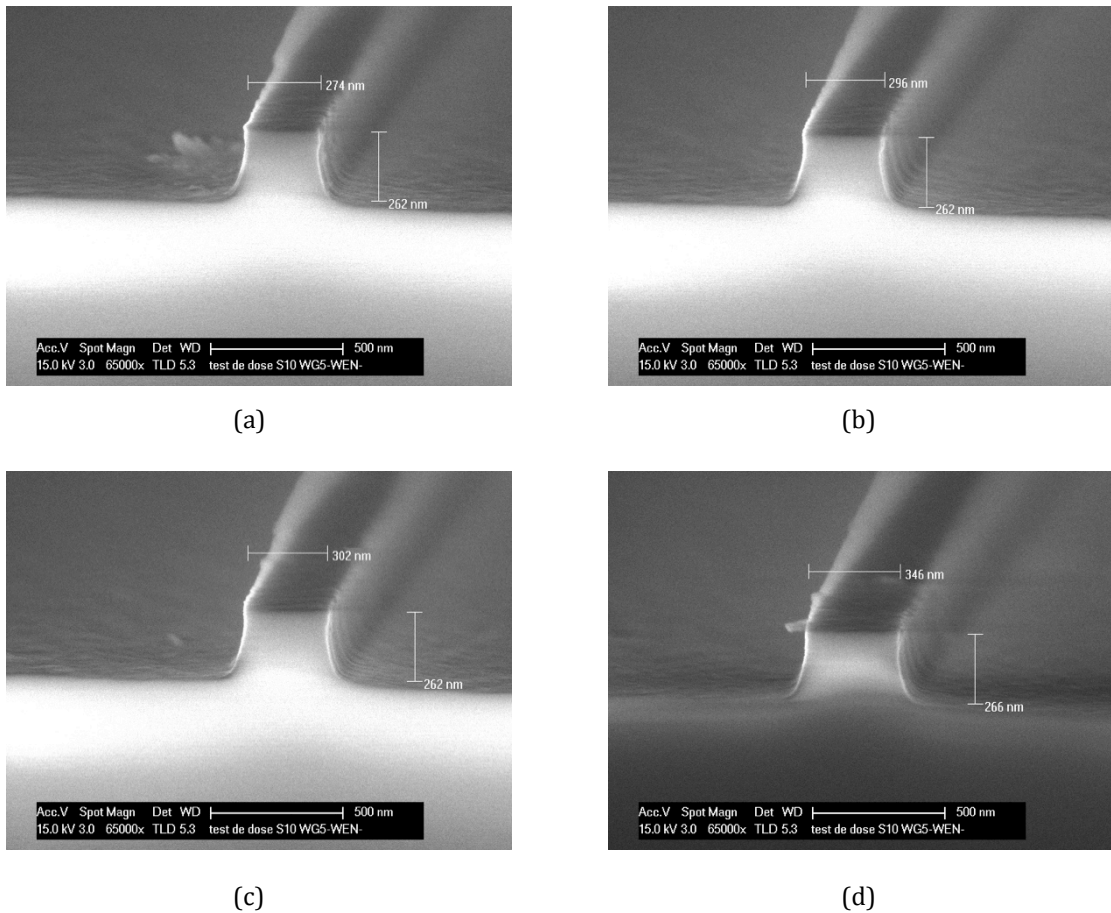


Figure IV.12: Micrograph of cross-section and sidewall of RIE etched Si_3N_4 waveguide sample S10 with different widths w . The EBL's parameters are $s = 5 \text{ nm}$ and $D = 4.5 \text{ C/m}^2$: (a). $w = 380 \text{ nm}$; (b). $w = 400 \text{ nm}$; (c). $w = 420 \text{ nm}$; (d). $w = 450 \text{ nm}$.

c.2 sample 10-2: Pressure = 30 mTorr, RF power = 450 W and etching time = 84 s

Based on the analysis of sample 10, we tried to increase the RF power, in order to increase the verticality of etching species' flux going across the plasma sheath and moving towards the bottom. At the same time, we decrease also the chamber pressure for the purpose of dilute the atmosphere, in which the neutrals and other non-biased reactants have less probabilities to hinder the reactive gases flux going downward. As shown in Figure IV.13, the retrograde sidewalls have been obtained. Comparing the width of the cross-section with Figure IV.12, the etched waveguide's topside has an average reduction of 50 nm. Meanwhile, the waist of the cross-section profile has been raised from the middle to a location close to the topside. Although the laterally moving etching species have etched more Si_3N_4 than the precedent case, the sidewalls have no longer hyperbola shape but an improved verticality. However, the retrograde effect should also be eliminated to avoid deforming the propagating modes.

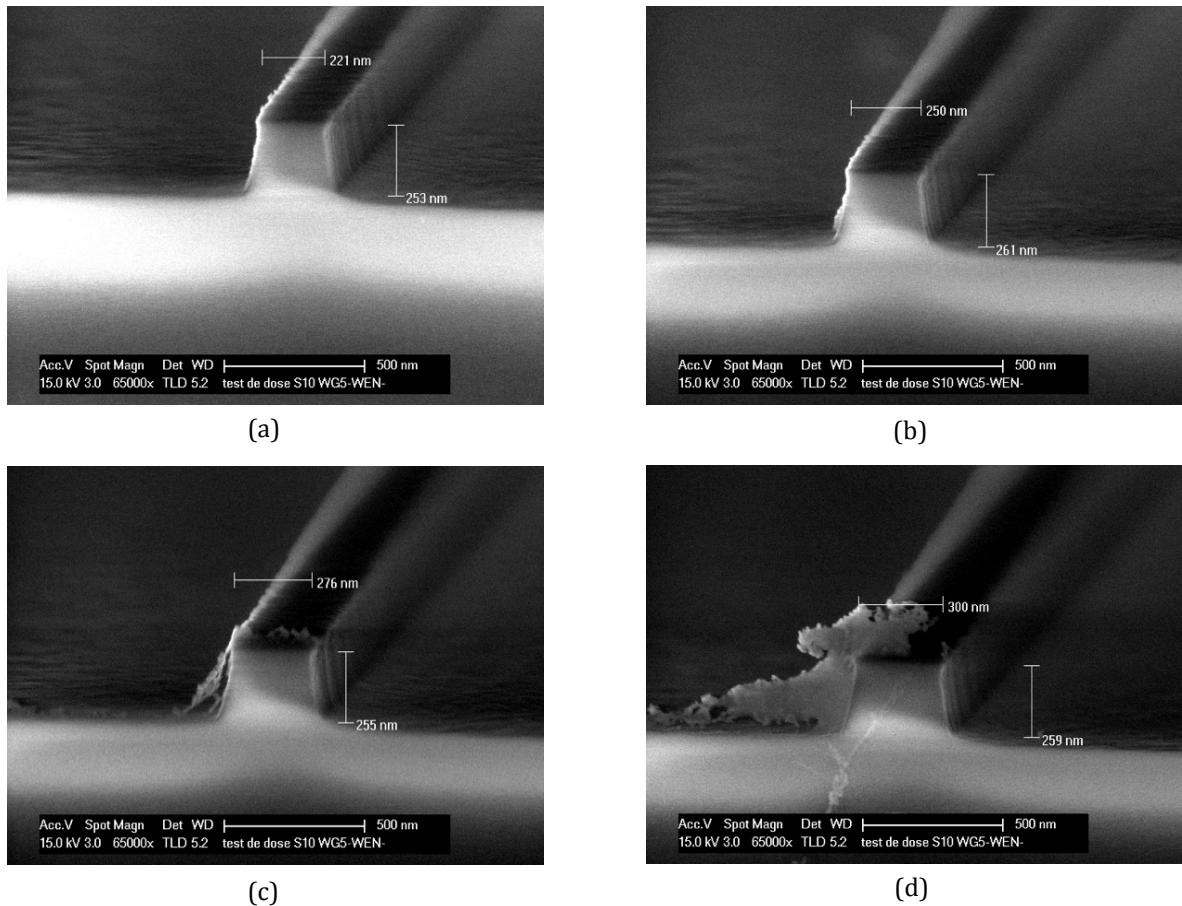


Figure IV.13: Micrograph of cross-section and sidewall of RIE etched Si_3N_4 waveguide sample S10-2 with different widths w . The EBL's parameters are $s = 5 \text{ nm}$ and $D = 4.5 \text{ C/m}^2$: (a). $w = 380 \text{ nm}$; (b). $w = 400 \text{ nm}$; (c). $w = 420 \text{ nm}$; (d). $w = 450 \text{ nm}$.

c.3 sample 12: Pressure = 15 mTorr, RF power = 450 W and etching time = 88 s

In fact, as a tendency observed in the precedent cases, the smaller the chamber pressure is, the more vertical sidewall is obtained. However, the RIE set-up has a limitation of the chamber's pressure to have an auto-assigned gases flux angle, which is 15 mTorr for any RF power. As shown in Figure IV.15, we obtain an etched waveguide with sidewalls more vertical than the previous ones. As it can be seen in Figure IV.14, width has a maximal value at the bottom side, which has been reduced to more or less 80 nm comparing with the pattern's drawing width.

However, the topside's faceting effect must be caused by the angular dispersion of ions and neutrals, which have more chances to have collisions within the plasma sheath because the light density atmosphere makes the etching depending more on the angle of ion incidence [RANGE03].

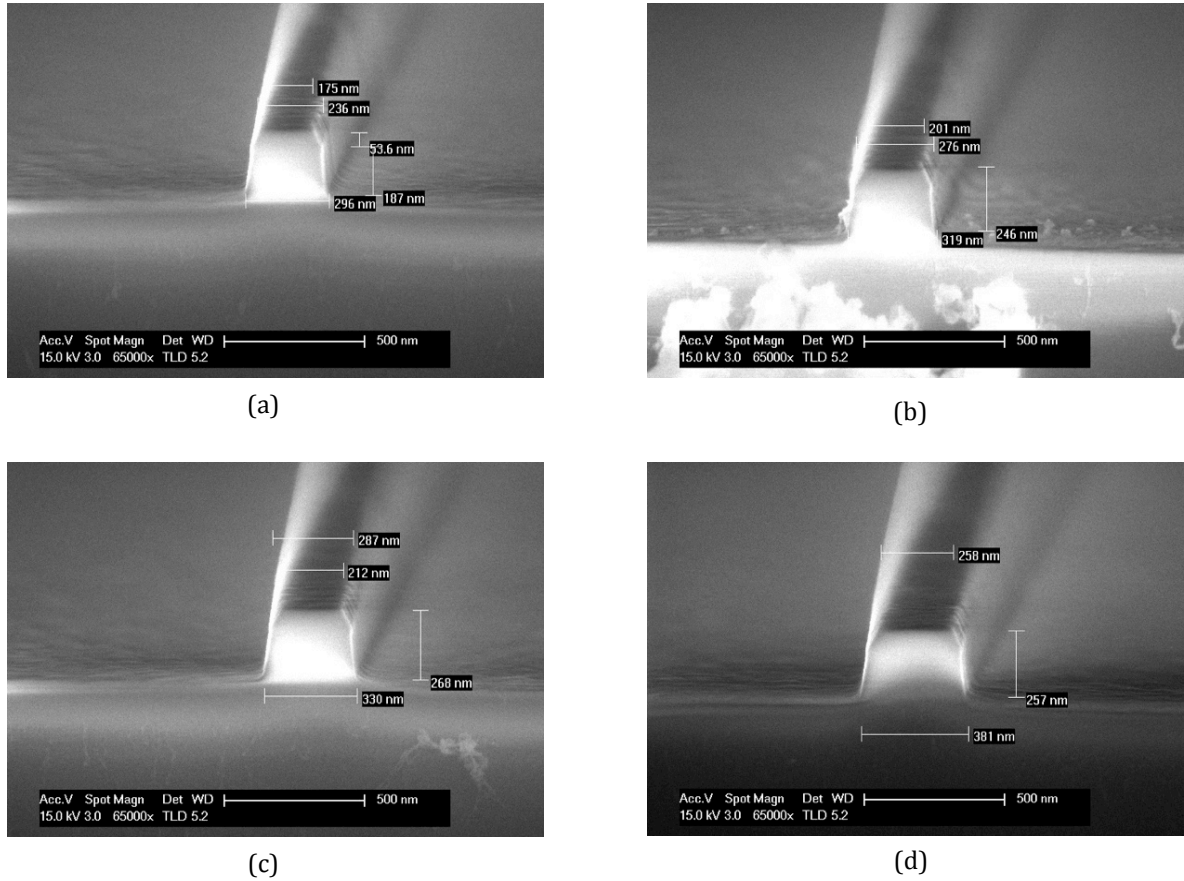


Figure IV.15: Micrograph of cross-section and sidewall of RIE etched Si_3N_4 waveguide sample S12 with different widths w . The EBL's parameters are $s = 5$ nm and $D = 4.5$ C/m^2 : (a). $w = 380$ nm; (b). $w = 400$ nm; (c). $w = 420$ nm; (d). $w = 450$ nm.

IV.1.4 Cut and cleavage of the samples

a. Dicing saw cutting

Disco dicing saw system DAD 641 has been used to cut the samples based on a $1\text{ cm} \times 3\text{ cm}$ Si substrate. The used 56 mm-diameter dicing blades with a plane edge of $30\text{ }\mu\text{m}$ are installed with a 54 mm-diameter metallic support. In fact, we made some rectangular alignment marks in the same layer as Si_3N_4 waveguide, in order to observe and localize easily the cutting positions on the sample's edge. A SEM photo of the sample's boundary with alignment marks is presented in Figure IV.16.(a) and the side view scheme of the dicing saw's cutting in Figure IV.16.(b). The depth of the cutting is inferior to the whole thickness of the sample, in order to keep the bottom part of each cleaved section getting together and also improve the uniformity of the cleaved sidewalls. Since a pair of adhesive plastic film encloses the substrate after a batch of cutting process, we can easily recover all the divided sections by lightly pressing the

samples from its backside. And besides, we can program all the information concerning the start point's location and moving route of the blade for each cut, and realize an automatic batch process, especially for a length-varied waveguide samples.

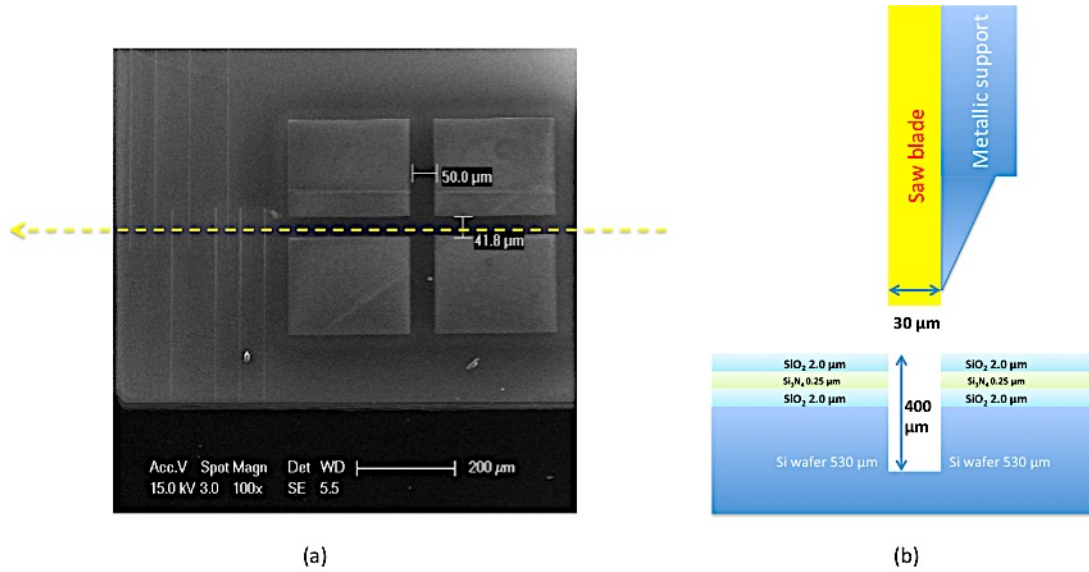


Figure IV.16: (a). SEM photos of the plan view of cleavage zone on the substrate of SiO_2 cladded Si_3N_4 waveguide samples. (b). Schematic illustration of the side view of the dicing saw cleavage.

Moreover, we tested also different feed speeds (i.e.: 0.1, 0.3 and 0.5 mm/s) along the cutting direction and also different revolution speeds of the spindle (i.e.: 18000, 24000 and 30000 rpm). We present some representatives photos of the cut waveguide's samples in Figure IV.17.

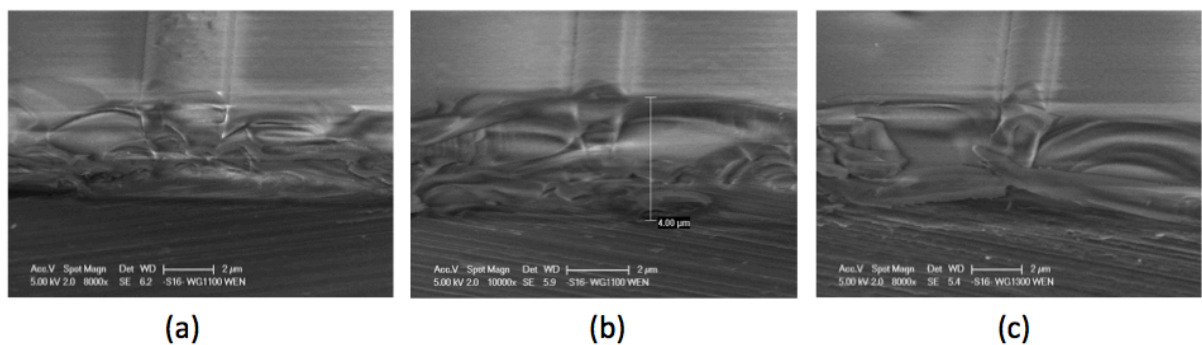


Figure IV.17: Dicing saw cut cladded waveguide's samples: (a). with 0.1 mm/s and 24000 rpm; (b). 0.5 mm/s and 18000 rpm; (c). 0.5 mm/s and 30000 rpm.

As shown in Figure IV.17.(a), with a slower feed speed, the dicing saw caused along cutting interface many bursts and brought a lot of curdling with a feature size of 1 μm . We can hardly find out the Si_3N_4 rectangular waveguide's profile under SEM. Once we increase the feed speed, the feature size of the bursts becomes bigger and there are less bursts as shown in Figure IV.17.(b) and (c). However, all of the samples cleaved by this blade could introduce an important coupling loss due to the roughness of the cleaved facets.

b. Scriber cleavage

We have also tried the direct cleavage using the scriber set-up under an assistant optical microscope. By producing a groove with the diamond tip at the predefined position of the sample, the crystalline Si wafer could be cleaved following the trace of the grooves. In fact, the substrate comes from the standard 4" Si wafer, which has a thickness of 530 μm . So we need firstly to make the sample thinner by using a conventional polishing setup. We usually remove a thickness of 400 μm in order to satisfy the operation condition of scriber. If we thin it more, we would obtain a curving substrate sample. Then we can adjust the force of scriber's tip, with ranges from several grams to several hundred grams. Some SEM photos of the scriber cleaved sample's cutting edge are presented in Figure IV.18.

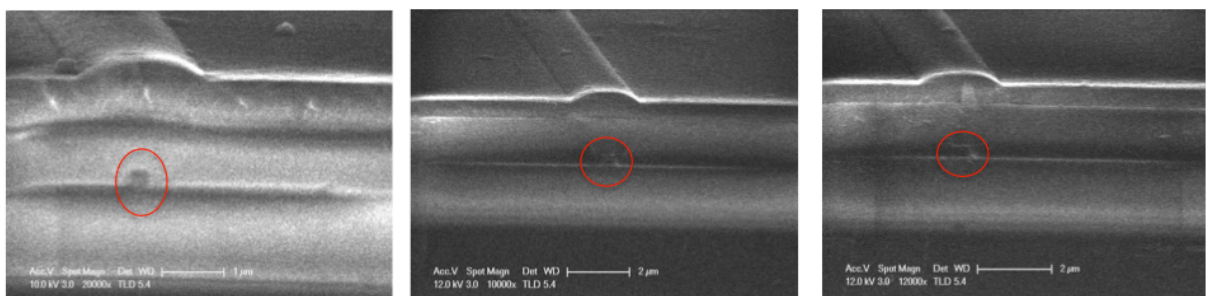


Figure IV.18: SEM photos of optimized scriber cleaved samples' cutting edge.

As shown in Figure IV.18, the scriber's cleavage of samples is better than the dicing saw's cutting. We can find out clearly the rectangular-like Si_3N_4 waveguide's cross-section profile. Meanwhile, the cleaved edge in the whole field of view looks neat and uniform which is favorable to couple the light source with less loss due to the surface scattering. However, the weakness of this scriber based cleavage techniques is a high dependence of the operator's manual precision because alignment of the sample's edge and localization of the groove's

position have to be done manually. At the same time, much attention should be taken when we intend to separate the cleaved sections from the initial substrate by manually pressing the backside of the extremely thin samples. Consequently, we can barely obtain a perfect fraction of waveguide samples with a length inferior to 1 mm.

IV.1.5 Conclusion

In this part, we presented the principal cleanroom fabrication techniques and processes of the 633nm single-mode Si_3N_4 rectangular waveguides. The critical steps are the PECVD, EBL and RIE. By scanning a great number of variable parameters and qualitatively evaluating the samples under a SEM, we have optimized each elementary process step and finally obtained measurable SiO_2 cladded Si_3N_4 straight and curved waveguides with a ~ 260 nm-thick rectangular cross-section and different widths, as well as MMI couplers based beam splitters. At the end of the technological process, the cleavage is also a critical step for such structures.

IV.2 CHARACTERIZATION OF FABRICATED WAVEGUIDES

In the precedent chapters, we have systematically introduced the design, simulation and fabrication of the SiO_2 cladded Si_3N_4 rectangular waveguide, which is intended to be single-mode at 633 nm. Since this waveguide is the basic element within the targeted 1×16 beam splitting planar integrated device, we must measure the fabricated samples propagation losses. In this part, we will firstly present our experimental characterization platform, and then show the loss measurement results for different lengths of straight waveguides. Lastly, we will analyze these experimental results and discuss on the prospective optimization involving the design, fabrication and also characterization.

IV.2.1 Characterization platform

a. 635 nm laser diode test

Since we are interested in TE propagation modes in the fabricated Si_3N_4 waveguides, the first step of the characterization is to make the 633 nm laser source with a TE linear polarization state. The experimental set-up for the TE polarization calibration is schematically presented in Figure IV.19.

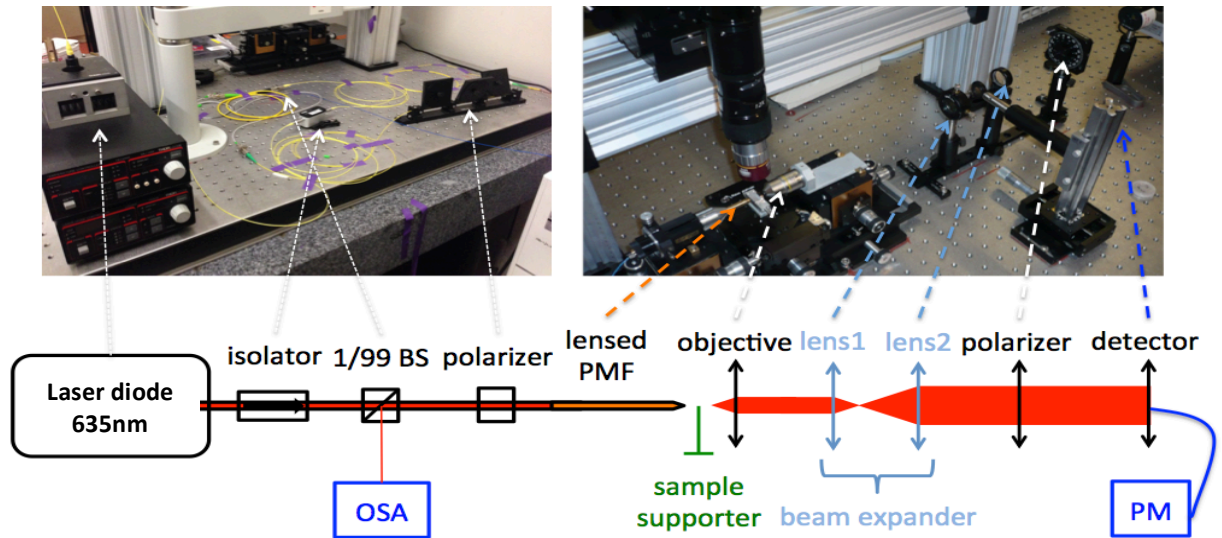


Figure IV.19: Schematic illustration and photos of the TE polarization calibration set-up.

We have used the laser diode (THORLABS TCLDM-9) with a TEC 2000 temperature controller and LDC 500 laser diode controller. The noticed central wavelength of this laser diode is 635 nm with a microwatt optical power. Firstly, we characterized this laser diode's output spectra measured by an optical spectral analyzer (OSA) ANRITSU MS-9710C. The OSA has an effective operation wavelength range from 0.6 to 1.75 μm . We tested several stabilized operation temperatures, which are varied from 25°C to 38°C. Meanwhile, we varied also the driving current from the threshold (i.e.: 25 mA) to the limited maximum (i.e.: 90 mA). The fibered output of the laser diode has been connected with a 2 μm -diameter micro-lensed fiber (AMS technologies AG: TPMJ-3A-633-4/125-1-5-2-10-1-AR). Then we coupled the output beam from the micro-lensed polarization-maintaining fiber into a 10 \times objective and a set of beam expander, which is based on 2 convergent lenses as shown in Figure IV.19. The parallel propagative beam is collected by a fiber collimation packages (THORLABS F230FC-B) and finally sent to the OSA's input by a 633 nm single mode optical fiber. We list in

the OSA's parameters for the laser diode's test. The diode laser's output characteristic spectra as a function of current at an operation current of 27°C are presented in Figure IV.20.

Table IV-3: Parameters of OSA for the diode laser's characterization.

Parameters	λ_{center}	Span	Resolution	VBW	P_{tavg}	Sampling
Values	636.5 nm	5.0 nm	0.2 nm	1000 Hz	10	501 pts

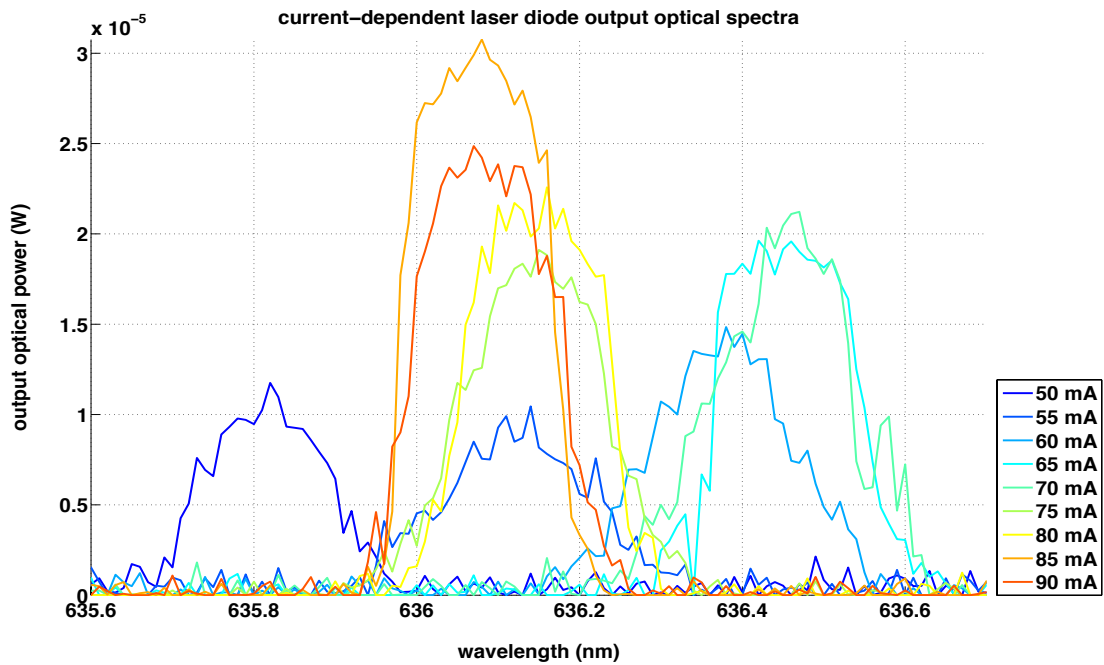


Figure IV.20: Current-dependent output optical power spectra of the laser diode.

The maximal output optical power is decreased by 2 orders of magnitude comparing with the optical output of the diode laser. This attenuation has been probably introduced during the coupling of optical signal between the fibered propagation and inter-lens transmission. As shown in Figure IV.20, the central wavelength is shifted from 635.8 nm to 636.4 nm when the current is increased from 50 mA to 65 mA at 27°C. Then the output peak has a blueshift about 0.2 nm when the current continues arising to 80 mA. We studied also the time-dependent stability of this diode laser without any stabilization operation. In fact, an average wavelength-shift of 0.3 nm has been observed during 10 minutes in keeping all the parameters unchanged. The instability of the measured diode laser's spectra is probably caused by the interference effect between the current-driven diode laser and the reverse-path optical signals, which are reflected by some smooth ends of fiber interconnectors and inputs of the measurement instrument (i.e.: OSA). To do a reliable measurement of optical transmission, we should thus improve the stability of the diode laser source.

b. Stabilization of the light source

Firstly, in order to eliminate the mentioned internal interference affected by the reverse-path optical signal, we installed an isolator (THORLABS IO-F-660) as shown in Figure IV.19. Secondly, we slightly pulled out a few mm on both optical ends within the first interconnector,

which is used to link the diode laser's fibered output and the isolator's input in order to induce a constant feedback. Moreover, a 1%/99% beam splitter (THORLABS FC-632-99B) has also been inserted following the output of the isolator in the optical path. Its 1% output has been connected directly with the OSA. Finally, we fixed the operation temperature of 25°C and driven current of 80 mA and measured the time-dependent laser diode's output optical power spectra as shown in Figure IV.21. The applied laser diode's parameters are presented in Table IV-4. By the way, the output of this 1%/99% beam splitter has been used as the reference signal for the transmission measurement of the waveguide samples.

Between each neighboring measurement, we wait 5 minutes. Generally speaking, by applying the mentioned stabilization operations, the laser diode could send relatively stable optical spectra spanning from 635.5 nm to 636.3 nm. Meanwhile, due to the fluctuation of the driven current and also the controlled operation temperature, these reference optical spectra don't show a good stability as a function of time. During half an hour, the optical power peaks have an average fluctuation of 20%, although these power peaks didn't shift laterally in the spectra. However, for the next transmission measurement, we suppose each measurement of the transmitted signal and the reference signal has only an interval of time less than 1 minute, the division optical spectra should be out of the influence of this instability.

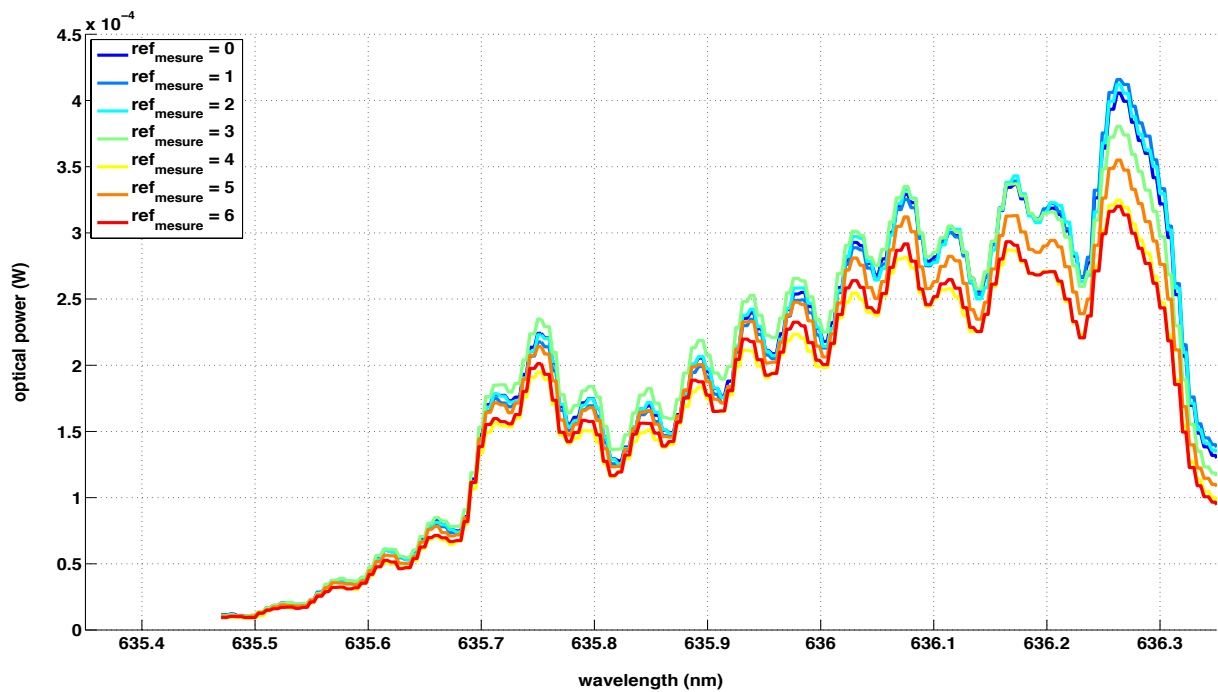


Figure IV.21: Time-dependence output optical power spectra of the stabilized laser diode (T=25°C).

Table IV-4: Parameters of OSA for the diode laser’s characterization.

Parameters	λ_{center}	Span	Resolution	VBW	Pt _{avg}	Sampling
Values	635.85 nm	1.0 nm	0.05 nm	1000 Hz	10	1001 pts

c. TE polarization state

As shown in Figure IV.19, the TE polarization of the guided modes can be realized by rotating the fibered polarizer, which is connected with the 99% output of the beam splitter. Since the micro-lensed fiber can maintain the state of polarization, the propagative light arriving the sample’s left-hand side would keep the same state of the polarization at the output of the fibered polarizer. On the right-hand side of the sample’s support, the second polarizer would filter the collected light through the objective and the beam expander.

IV.2.2 Transmission measurement of the straight waveguides

a. TE modes transmission measurement set-up

We present in Figure IV.22 the experimental set-up used to measure the transmission of waveguide samples. The diode laser is operated at 25°C and 80 mA. We used a visible camera with a 20 × zoom camera to monitor the plan view of the optical signal’s coupling between the lensed fiber and the on-a-chip waveguide samples. We used ELLIOT-MARTOCK 3-axis adjustable supportors to precisely move both the lensed fibers. Two camera-captured photos of the optical coupling between the lensed fibers and the waveguide are presented in Figure IV.23.

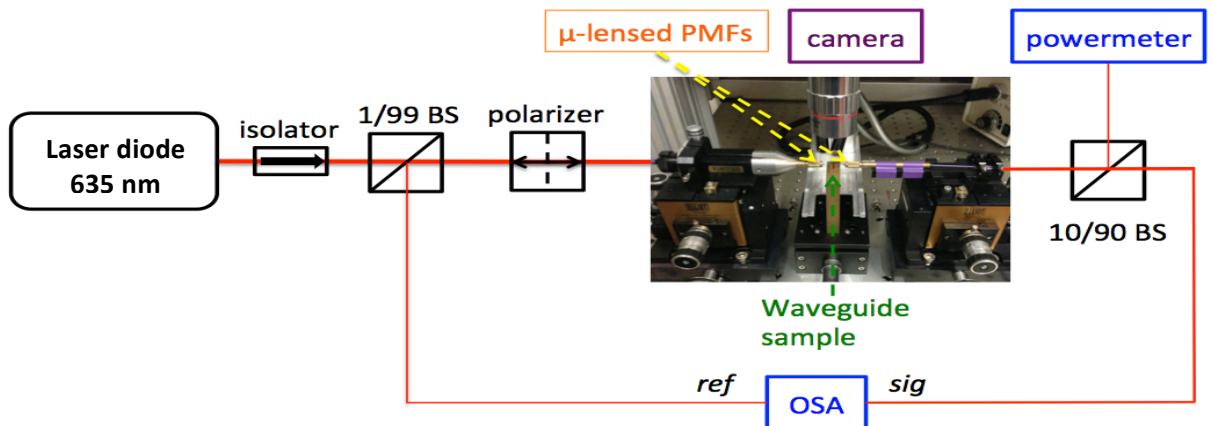


Figure IV.22: Schematic illustration of the waveguide’s optical transmission measurement.

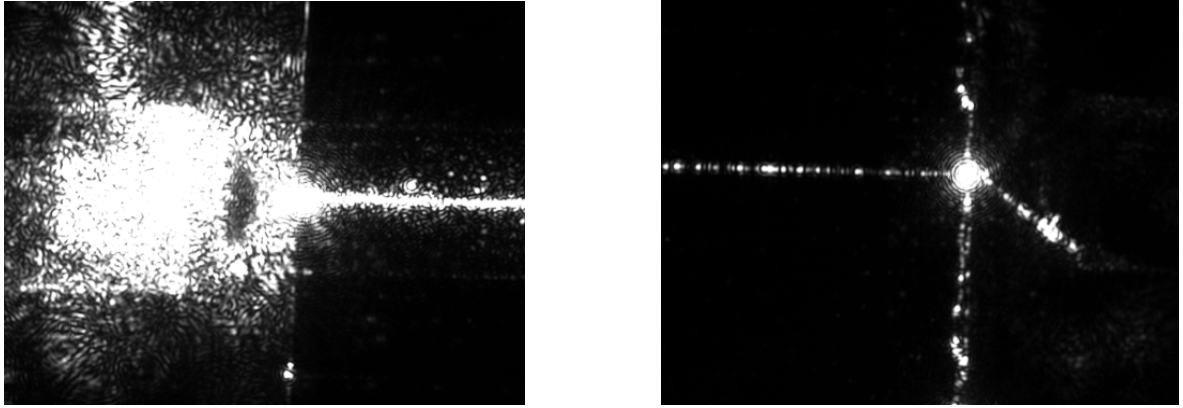


Figure IV.23: Views of the input (left) and output (right) coupling between the lensed fiber and the straight waveguide.

At the same time, we used another 10%/90% fibered beam splitter to do simultaneous measurement of the optical power and optical spectra. The idea is to optimize the coupling by real-time monitoring of the powermeter and then recording the stabilized optical spectrum.

b. Measurement of the transmission spectra and attenuation coefficient

By using this popular end-fire method, we measured the optical spectra for 5 straight waveguides with lengths from 500 μm to 900 μm . As we mentioned before, the scribe assistant cleavage is not reliable to prepare a sample with a certain predetermined length. Consequently, we present here only the measurement results for the straight waveguide samples realized with the optimized fabrication process shown in Figure IV.13.(d) and cut by the dicing saw with a non-optimized recipe. For each sample, we measured separately 3 times the “ref” and “sig” spectra and we redid every time the optimization of the optical coupling between the lensed fibers and the sample, in order to save only the maximized “sig” spectra. The OSA measured average transmission spectra are presented in Figure IV.24.

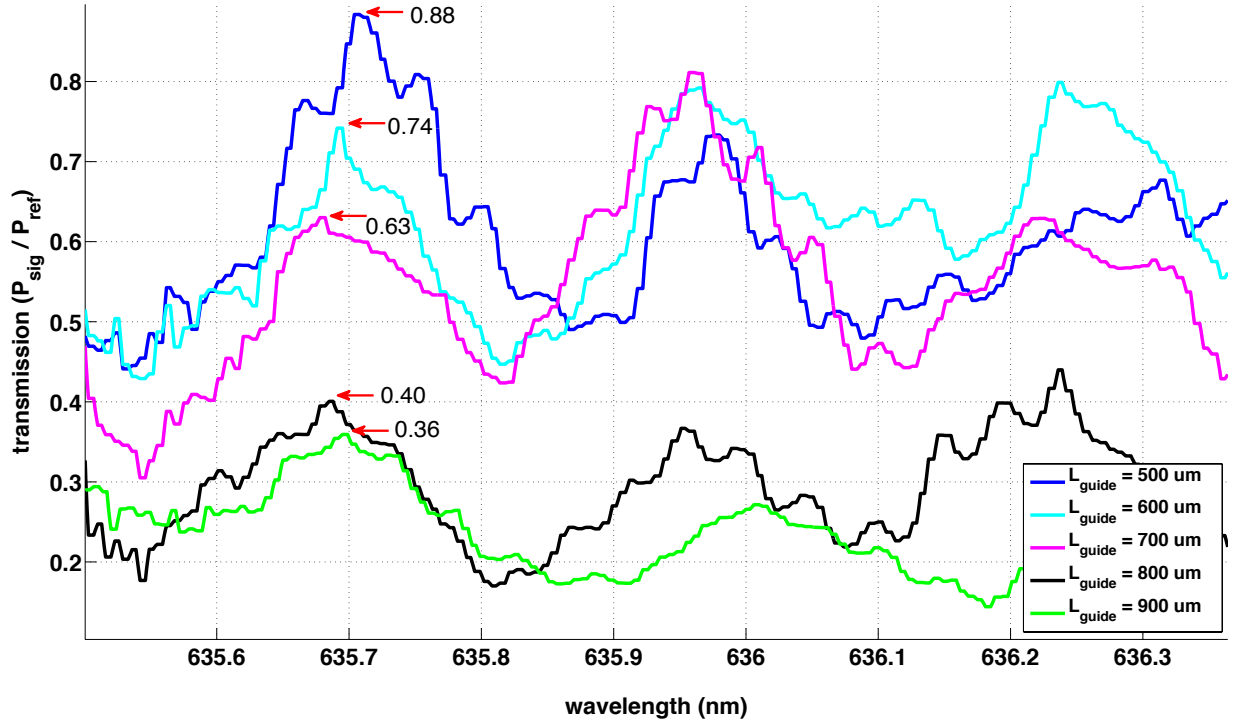


Figure IV.24: Transmission spectra of the different lengths straight waveguides.

As shown in Figure IV.24, the spectral transmission for each measurement is defined as follows:

$$T_{meas(\lambda)} = \frac{P_{sig}(\lambda)}{P_{ref}(\lambda)} \quad (IV-4)$$

This transmission value is the ratio of the transmitted power to the input power, including the contribution of the two splitters (1:99 and 10:90, before and after the sample) as shown in Figure IV.21. The fiber-to-fiber transmission is thus obtained by correcting this value as follows:

$$T_{ftf}(\lambda) = 0.01 \times \frac{T_{meas(\lambda)}}{0.99 \times 0.9} \quad (IV-5)$$

Supposing that the attenuation coefficient due to the straight waveguide length should be constant, we present in Figure IV.25, a characteristic curve showing the relation between the fiber-to-fiber transmissions at 635.7 nm (expressed in dB) as a function of the waveguide's length. We fitted it with a linear function since the relation between the transmission (in dB) and the linear losses can be expressed by:

$$T_{ftf}(dB) = 4.343 \times (-aL + c) \quad (IV-6)$$

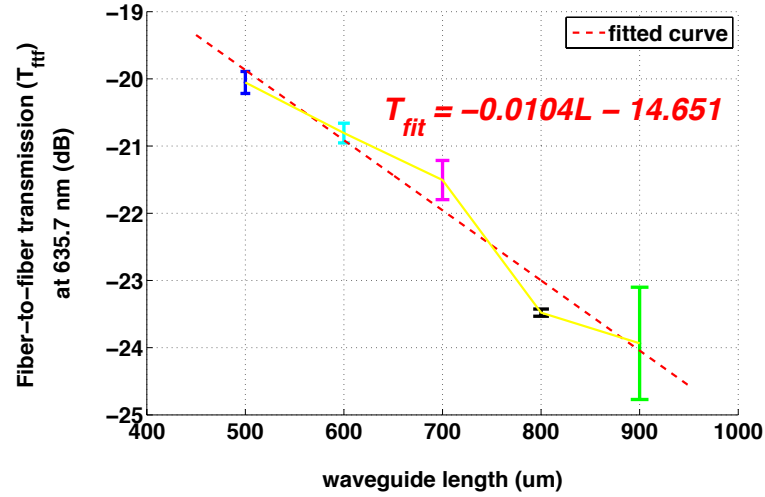


Figure IV.25: Relation between the fiber-to-fiber transmission and the waveguide's length at 635.7 nm.

The slope of the linear fit leads to the linear attenuation coefficient of the waveguide, which is estimated at 10.4 dB/mm. Taking into account the fluctuation of the 3-times measurement, the error bar is as follows: 10.4 +/- 0.9 dB/mm. The constant part c is related to the optical injection coupling, which is evaluated at 7.2 +/- 0.3 dB/facet, in accordance with the mismatch size between the waveguide and the fiber spots. This result must be considered as a very first estimation, whose range is anyway in accordance with literature results (see Figure II.12).

c. Fabry-Perot oscillation effect

As shown in Figure IV.24, a serial of periodic oscillation (period = 0.2 nm – 0.3 nm) has been observed in the transmission spectra. The Fabry-Perot theory can be used to analyze this oscillation effect. At first, we can define a group index of the propagative modes as follow:

$$n_g = \frac{\lambda^2}{2\Delta\lambda L} \quad (\text{IV-7})$$

where $\Delta\lambda$ is the Fabry-Perot oscillation's step size, and L is the cavity length. By deducing the 1st order dispersion relation, we obtain the relation between this group index and the effective index for the propagative modes:

$$n_g = n_{eff} - \lambda \frac{\partial n_{eff}}{\partial \lambda} \quad (\text{IV-8})$$

where n_{eff} is the guided mode's effective index. Here we suppose the fabricated rectangular Si₃N₄ waveguides have a fixed thickness of 250 nm and a variable width from 250 nm to 400

nm. By applying the EIM, we can estimate approximately the theoretical group index for the TE_{00} mode's propagating in such a rectangular Si_3N_4 waveguide. We present in Figure IV.26 the wavelength-dependent group index of the TE_{00} mode function of the wavelength and also the analogue FP cavity's theoretical $\Delta\lambda$ as a function of the FP cavity's length for different widths.

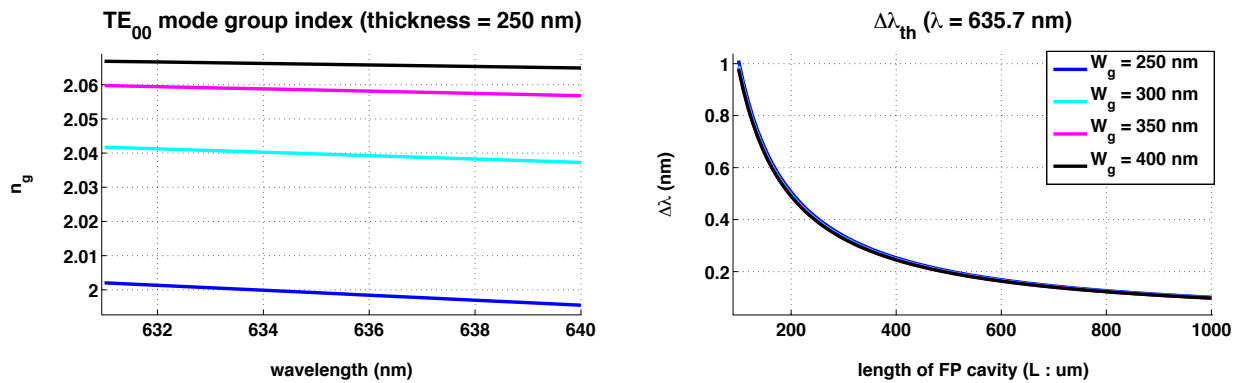


Figure IV.26: Group indexes as a function of wavelength and analogue FP1 cavity's oscillation step-size as a function of cavity's length for the TE_{00} mode for different width of SiO_2 cladded Si_3N_4 waveguides.

As shown in Figure IV.26, the TE_{00} mode's group index changes little within the wavelength range (i.e.: 630 nm – 640 nm). It could be increased when we enlarge the waveguide's cross-section. On the other hand, according to the formula shown in (IV-7), we can estimate the FP cavity's length, which is supposed to be equal to the straight waveguide's length if there is no discontinuity along the waveguide.

d. Discussion on the measurement results

Based on the observed oscillation step-size in the transmission spectra, we can estimate the corresponding straight waveguide's length by applying the FP cavity theory. However, we can hardly exclude the possibility that the coupled light beam has also be guided and propagated within the enclosed SiO_2 layers. In this case, we can estimate also the FP cavity's length by replacing the n_{eff} of Si_3N_4 by the refractive index of SiO_2 . We present in Figure IV.27, the FP cavity's theoretical $\Delta\lambda$ as a function of the SiO_2 waveguide's length. We list a comparison between the FP cavity's lengths corresponding to the observed oscillation step-size in the transmission spectra in Table IV-5.

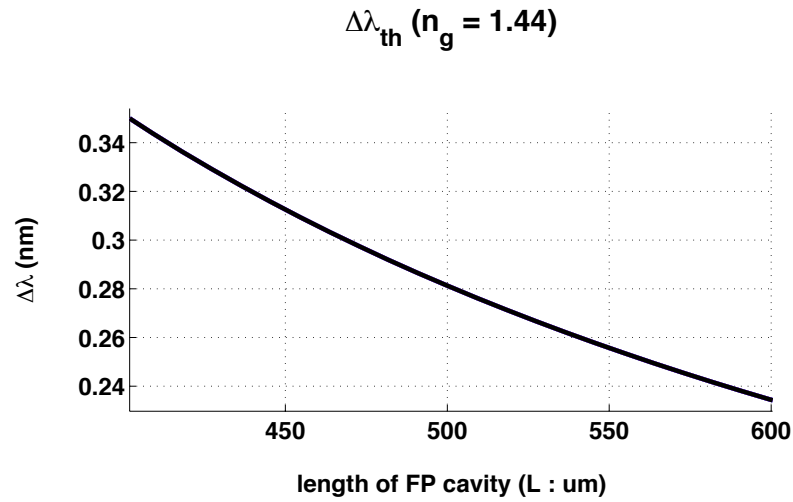


Figure IV.27: FP2 cavity's oscillation step-size as a function of cavity's length for the propagative mode with a constant group index of 1.44.

Table IV-5: Comparison between the measured sample's lengths by microscope and the theoretically deduced FP cavity's lengths for two waveguides effective indexes.

Samples	500	600	700	800	900
L_{cut} (μm)	470±30	570±30	670±30	770±30	870±30
$\Delta\lambda$ (nm)	0.32	0.26	0.26	0.25	0.3
L_{FP1}^{15} (μm)	317	390	390	405	338
L_{FP2} (μm)	440	540	540	564	473

As shown in Table IV-5, firstly the reduction of the sample's length measured under an optical microscope is due to the dicing saw's cutting. In fact, the width of the cutting blade is about 30 μm and thus a potential error of 30 μm during the cutting operation could be considered. Secondly, the observed FP cavities corresponding to different-sample transmission spectra have a comparable theoretical length even in different length waveguide samples, i.e.: for the samples of 600, 700 and 800. It should be reasonable to suspect that this FP cavity is due to the presence of the main-field stitching with a certain interval of EBL's main-field size (i.e.: 500 μm) along the straight waveguides.

¹⁵ FP1: corresponding to the 250 nm × 250 nm SiO₂ cladded Si₃N₄ straight waveguides; FP2: corresponding to the SiO₂ slab waveguides.

In fact, as a result of combined guiding effect in both the SiO₂ slab waveguide and Si₃N₄ rectangular waveguide propagating within a main-field section of 500 μm, we could probably find an FP oscillation in the transmission spectral with a step-size of 0.25-0.26 nm. However, for the sample 500 and 900, we suppose that there should be a discontinuity point along the waveguide, by which the straight waveguide could be split into 2 sections, and one of them corresponds to the calculated analogue FP cavity's length. Finally the comparison of LFP1, LFP2 and main-field section of 500μm may reveal that the effective index of the guided mode is intermediate between the silica waveguide and the targeted Si₃N₄ waveguide. One possible reason is that the realized waveguides are smaller (and less confined) than expected.

IV.2.3 Discussion, conclusion and perspectives of fabrication

In conclusion, for these first measurement results of straight waveguide samples, we obtained a linear attenuation coefficient estimated at 10.4 dB/mm and a 2-facet optical coupling loss of 15 dB due to the coupling between the lensed fibers and the unpolished sample. An interpretation of the high linear attenuation coefficient measured in the fabricated waveguide can be given as follows:

- Firstly, RIE-etched waveguide's sidewall has an optically unacceptable roughness as shown in Figure IV.6. As a result, the scattering due to the undulation along the waveguide's sidewalls causes enormous optical losses.
- Secondly, in our case, the measured width of the fabricated waveguide is about 260 nm and the Si₃N₄ waveguide is totally under the single mode condition to only support the fundamental transverse mode as TE₀₀. Comparing with a wider waveguide, the effective index of the guided TE₀₀ mode is abruptly decreased as shown in Figure.III.12, as well as its confinement coefficient as shown in Figure.III.13. The FP oscillation measurements also suggest that the confinement of the fabricated waveguides could be lower than expected. Now, as shown in Figure II.12, the attenuation coefficient is expected to “exponentially” increase with the decrease of waveguide's width to very small values.
- Thirdly, inner FP oscillations caused by a main-field stitching have also been observed in the measured transmission spectra.

Based on our analysis, we have planned to further optimize the EBL based fabrication process, in order to eliminate the unfavorable e-beam writing field stitching effect and also to

improve the sidewall roughness along the waveguides. By the way, we are intended to enlarge the width of fabricated waveguide in order to decrease the linear propagation attenuation. Considering the single mode condition at 633 nm, the expected width of etched waveguide can arise 350 nm.

Then we would continue optimizing the dicing saw based cutting technique, for the purposes of improving the cut side's roughness and further increasing the optical coupling efficiency with the lensed fibers. In fact, we are currently testing the dicing saw system with different types of blades and also different operational parameters. The idea is to execute a 2-step cutting by two different blades with two different precisions of roughness. Meanwhile, a fine polishing process has also been considered to make further progress in the sample's cutting quality. Moreover, we also plan to fully characterize the other designed PIC devices, such as the bent waveguides (shown Figure IV.28) and the MMI coupler based beam splitters.

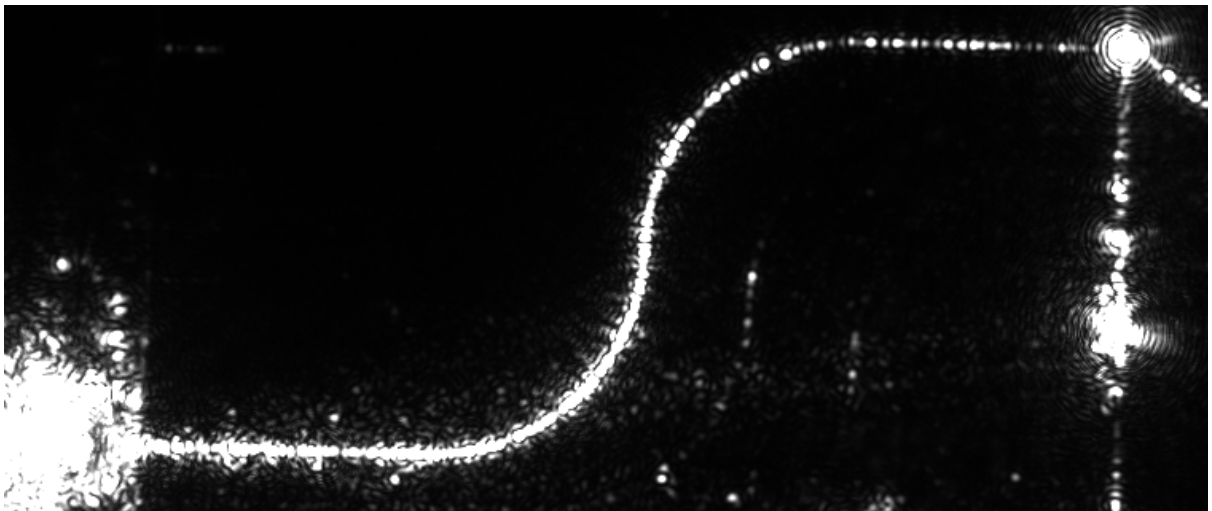


Figure IV.28: View of the input (left) and output (right) coupling between the lensed fiber and a curved waveguide combined by 2 anti-symmetric quart circles ($R = 400 \mu\text{m}$).

IV.3 CONCLUSION

Chapter IV was dedicated to the experimental part of this work. The realization of single-mode optical waveguides, and more generally integrated circuits, for visible light operation remains today a real challenge in terms of fabrication and performance for several reasons: core and cladding materials must be of optical quality (low intrinsic losses and roughness), they must be patterned without additional roughness or defaults and with challenging dimensions (waveguides of typically 300 nm width on several mm length).

The main obtained results are as follows:

- Fabrication of straight and bend Si_3N_4 waveguides buried in SiO_2 with estimated width of 300 nm and thickness of 260 nm: in addition to usual technological process optimization, this includes work on the e-beam lithography (new) setup control to reduce some beam writing effects (lateral pattern roughness due to vector scan mode, stitching errors, pattern widening due to electronic charge). Solutions have been proposed and applied, like mark alignment use, writing step size control and additional conductive layers.
- Preparation of sample for test: dicing saw cutting has been chosen.
- Optical test: despite technological defaults, straight waveguide losses have been estimated at 10.4 dB/mm. This very first result is in accordance with literature results, taking into account the dimensions of the waveguide and the material and etching quality.

In this context we have also tried to show here the extreme rigor required to obtain acceptable performances and to improve this first result: the PECVD technique of dielectric layers should be accompanied by thermal post-treatment for better material quality; the alignment procedure in e-beam lithography must be rigorously applied to avoid stitching and misalignment; the device cleavage and preparation for test must be improved by combining saw cutting and facet polishing.

CHAPTER V: COUPLING BETWEEN MNP CHAIN AND Si_3N_4

WAVEGUIDE

As explained in the first chapter of this manuscript, the visible silicon nitride PIC we are developing includes sections dedicated to light radiation from the device surface toward a specific direction. This directional radiation can be obtained with structures like gratings or nano-antennas. We have chosen the latter type of structures, especially nano-antennas made of metallic nanostructures supporting localized surface plasmons, because of expected better (mono-) directionality control.

In this chapter, we will firstly review some representative research work on the hybridized photonic-plasmonic modes generated in a metallic nanoparticle (MNP) chain, which is deposited on the top of a dielectric waveguide. We will especially focus on the cases with a visible resonant wavelength. Then, we will present the state-of-the-art optical antennas, which are based on the MNP chains. Secondly, we will theoretically study the coupled photonic-plasmonic modes between Si_3N_4 rectangular waveguides and gold and silver MNP chains. An analytic method of MNP's resonance calculation will be introduced in the first step. Then we will use the FDTD method to simulate the hybridized waveguide. Finally, based on the analysis of the simulation results, we will propose a value's range of the MNP's dimensions, which can be used to effectively couple the TE fundamental mode of the beneath Si_3N_4 waveguide into the 5-element MNP chain at a visible resonant frequency.

V.1 BASIC KNOWLEDGE AND STATE OF THE ART

V.1.1 Surface plasmonic modes in a metallic nanoparticle (MNP) chain

The surface plasmon (SP) at the interface between a metal and dielectric materials has been deeply investigated in theory since the pioneering work of *Ritchie* [RITCH57]. The plasmons can be considered as elements of a plasma wave, which is analogous to the metal's electron gas's oscillation induced by an electromagnetic (EM) field. Metal's permittivity is thus strongly involved in the SP mode and determines the plasmon resonance wavelength. So we will introduce some basic notions and knowledge on surface plasmon.

a. Basics of the surface plasmon

Most of noble metals have a complex permittivity and its real part is negative. The Drude model is the common analytic method to describe the permittivity and further the refractive index of metals as follow:

$$\varepsilon_m(\omega) = 1 - \frac{\omega_p^2}{\omega(\omega + i\gamma)} \quad (\text{V-1})$$

where ω_p is the plasma pulsation and γ is the relaxation time of the metal's electrons. Due to the presence of the imaginary part of the permittivity, the attenuation of the SP mode in the metal would gradually grow when the oscillation frequency is inferior to the plasma frequency of metal. However, in a high frequency domain, the imaginary part can be negligible. As a result, we can thus define a critical wavelength below which the metal is transparent:

$$\lambda_c = \frac{2\pi c}{\omega_p} \quad (\text{V-2})$$

where c is the light velocity in vacuum. For the bulk plasmon, once the incident EM wave has a wavelength smaller than λ_c , metal allows for the propagation of EM wave. For the surface plasmon confined to the interface of the dielectric and the metal, the strong coupling with the EM field of the light forms a surface plasmon polariton (SPP). This SP mode has a momentum of $\hbar\omega_{sp}/c$. The principle of the excitation of the SP mode is presented in Figure V.1.

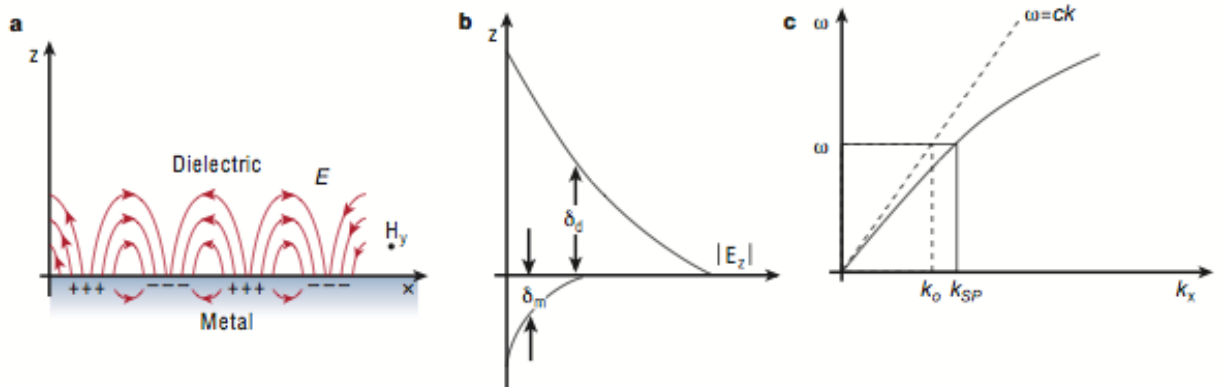


Figure V.1: Configuration of the surface plasmon at the interface between a metal and a dielectric material (taken from [BARNE03]).

As shown in Figure V.1, due to the combination influences affected by both the z-direction component of the electric field and the y-direction magnetic field of the light wave's transverse mode, the SP mode has a state of polarization TM and the surface charges enhance

E_z at the interface. However, the optical power will be partly localized at the surface in the inner part of both materials performing an evanescent wave. E_z has thus an exponential decay in both sides of the interface and is characterized by the metal's skin depth δ_m and the dielectric penetration length δ_d , respectively. Consequently, the SP mode's momentum will exceed the light cone at a photonic frequency. The dispersion relation of the SP modes can be found by solving Maxwell equations with boundary conditions and presented as [RAETH88]:

$$\omega_{sp} \triangleq \omega_0 \sqrt{\frac{\epsilon_d \epsilon_m}{\epsilon_d + \epsilon_m}} \quad (\text{V-3})$$

where ω_0 is the pulsation of propagative light in air, ϵ_d and ϵ_m are the permittivity of the dielectric and metal, respectively. In fact, $\epsilon_d = n_d^2$ for a non-absorption dielectric and $\epsilon_m = \epsilon_m' + i\epsilon_m''$ for noble metals according to (V-1). A summary of the SP's ω - k dispersion curves into three different cases is presented in Figure V.2.

Moreover, once the feature dimension of the metallic structure is decreased by one or two orders of magnitude comparing with the wavelength, we can excite the localized surface plasmon (LSP). This LSP mode can't propagate but can be considered as a "resonator". The resonant Eigen modes depend strongly on the shape and material of the metallic structure.

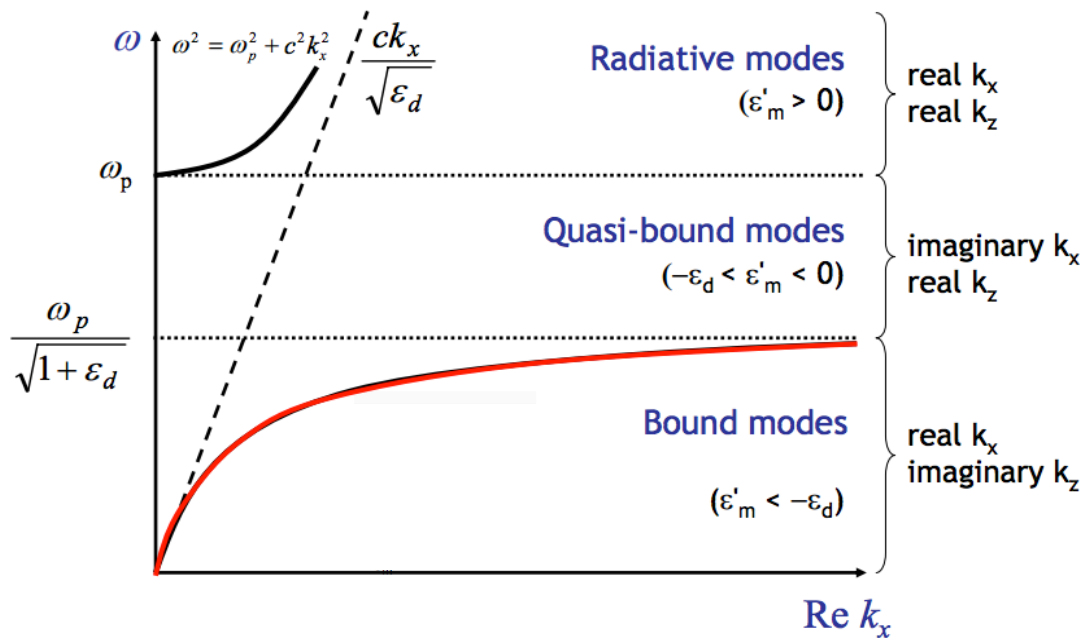


Figure V.2: Summary of the SP dispersion relation (taken from [LUCHT]).

b. Plasmonic waveguide made of a metallic nanoparticle chain

As one representative plasmonic waveguide, the LSP mode based MNP chain has been deeply investigated for the last decade. As mentioned before, since the MNP's dimensions are probably far smaller than the wavelength, we can treat each sphere or ellipse MNP as a punctual dipole. Based on this hypothesis, *Quinten et al* theoretically studied the dipolar model within the silver nanoparticle chain based on the generalized Mie theory, since silver has the lowest material losses within the visible wavelength range and the SP propagation length is typically several tens of μm . According to [QUINT98], there are two propagation modes, the 1st one is longitudinal, in which the oscillation field is in parallel with the MNP chain as shown in Figure V.3.(a) and (c). The other one is transverse, where the oscillation field is perpendicular to the MNP chain as shown in Figure V.3.(b) and (d). The best guiding condition with a $1/e$ attenuation length of 900 nm can be achieved in that case when the spacing distance between two neighboring MNPs is 25 nm, which is comparable with the NP's dimensions (the diameter of the Ag NP is 50 nm).

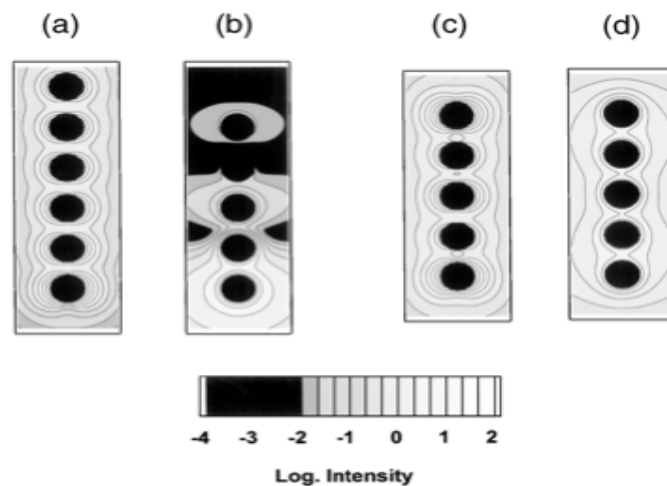


Figure V.3: E-field intensity distribution along a chain of Ag NP (25 nm-radius sphere) for (a) and (c) horizontal polarization direction, and (b) and (d) vertical polarization direction in a 50 Ag NP chain and a 5 Ag NP chain, respectively (taken from [QUINT98]).

With the development of the cleanroom fabrication and high-resolution microscopic techniques, the samples of MNP chains could be prepared and then observed. *Krenn et al* presented the experimental observation of near-field optical effects close to Au MNP using a photon scanning tunneling microscope (PSTM) [KRENN99]. The measured optical near-field intensity distribution had an agreement with the predicted theoretical computation as shown in

Figure V.4. By the way, the bright spots shown in Figure V.4.(b) are not on top of the MNP but localized in the space between neighboring MNP, and correspond to the SP Eigen mode of the chain.

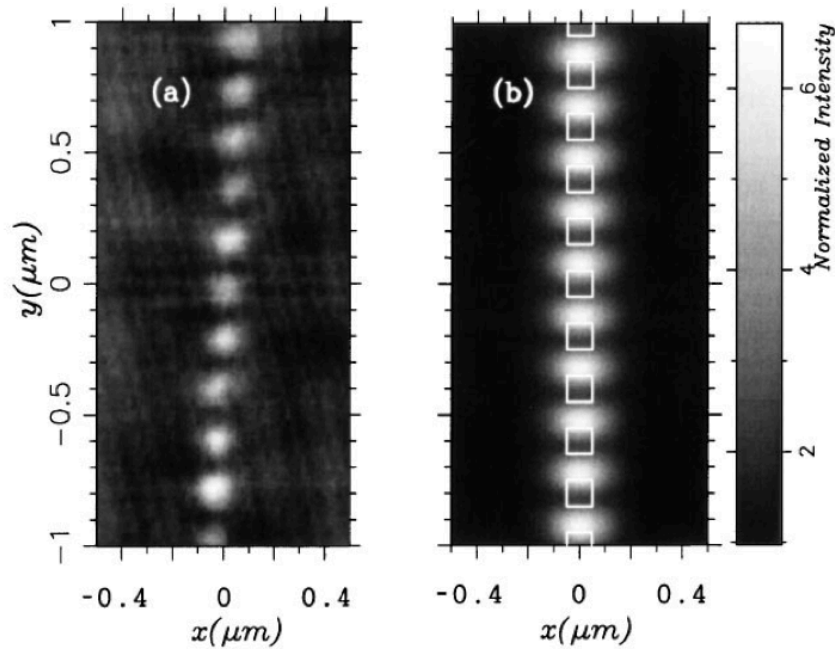


Figure V.4: Comparison between the intensity distribution above the central 10 Au NP ($100 \times 100 \times 40 \text{ nm}^3$) chain deposited on an ITO substrate (a) detected by photon scanning tunneling microscope (PSTM) and (b) simulated by mode-calculation numerical method.

Maier et al also experimentally demonstrated an Ag NP chain plasmonic waveguide by using a near-field optical microscope's tip to excite the 1st silver nanoparticle, and inserting a dye fluorescent nano-sphere in the center of the MNP chain in order to detect the electromagnetic energy transport in far-field. They have observed the plasmonic guiding along 500 nm from the localized source to the localized detector and estimated the losses coefficient of the plasmonic waveguide about $30 \text{ dB}/\mu\text{m}$ [MAIER03].

Brongersma et al introduced the punctual dipole coupling theory with an approximate condition of quasi-static response to analytically model the MNP chain's LSP modes [BRONG00]. However, the quasi-static approximation didn't consider a retardation effect due to the inter-particle coupling. Other researchers have confirmed the presence of this delay effect by theoretical and experimental study.

Weber and Ford calculated the dispersion relation by solving the full Maxwell equations for the propagation modes in a finite Ag NP (with a very small ratio of particle's radius over

the spacing i.e. $< 1/3$) chain [WEBER04]. Differently from the observed SP mode in the quasi-static approximation, they found a strong interaction between the transverse modes and the light line and a larger bandgap developed by the longitudinal modes as shown in Figure V.5. Indeed only photons with a transverse mode can propagate along the MNP chain.

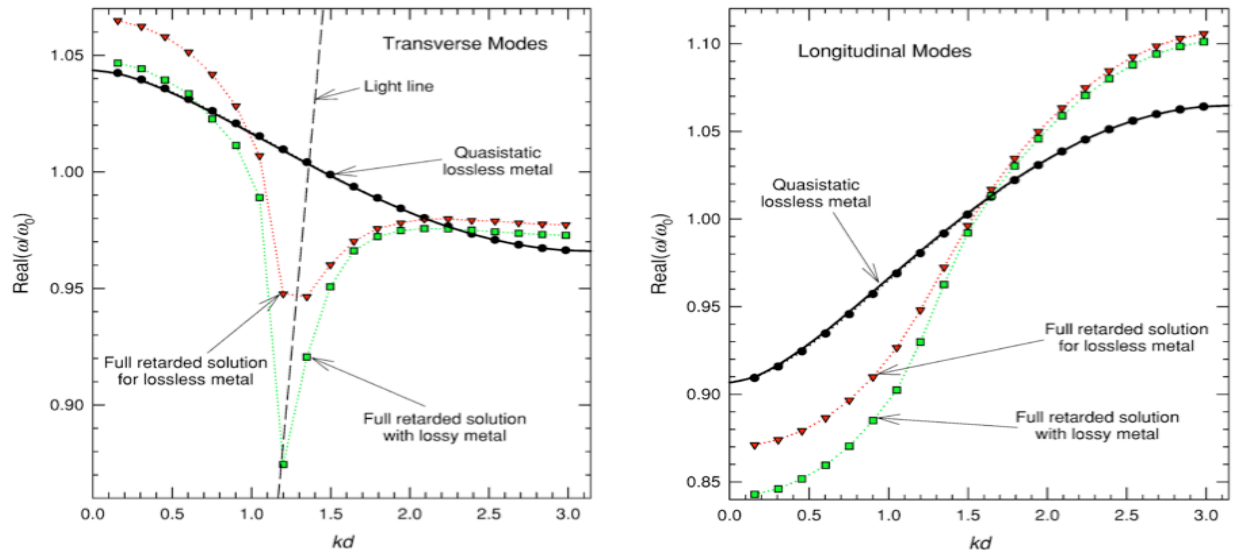


Figure V.5: Dispersion curves for transverse and longitudinal excited SP modes in a finite 20-Ag sphere chain (taken from [WEBER04]).

Moreover, *Femius* and *Polman* theoretically studied an infinite MNP chain by considering all the influences involved in ohmic damping, radiation damping, and retardation [KOEND06]. They have observed split anti-crossing branches in the transverse modes dispersion relation curve, while the retardation losses occur above the light line. They noted also for any resonant linear dipole arrays, such as any chain of dipole MNP, this retardation should not be ignored. An experimental evidence for these dynamic effects is then presented in [KOEND 07].

Crozier et al have pushed forward the coupling mode's study by including the influence of the beneath substrate. They have experimentally observed [CROZI07] and theoretically formulated [SIMSE10] two orthogonal transverse modes into the computation of dispersion relation. The 1st one is named as T1, which is parallel with the chain and the 2nd one with a name of T2, which is perpendicular to the chain as shown in Figure V.6. It can be seen that T1 and L modes occur within the frequency range between the theoretical dispersion curves corresponding to the cases where the NP are in air or in glass.

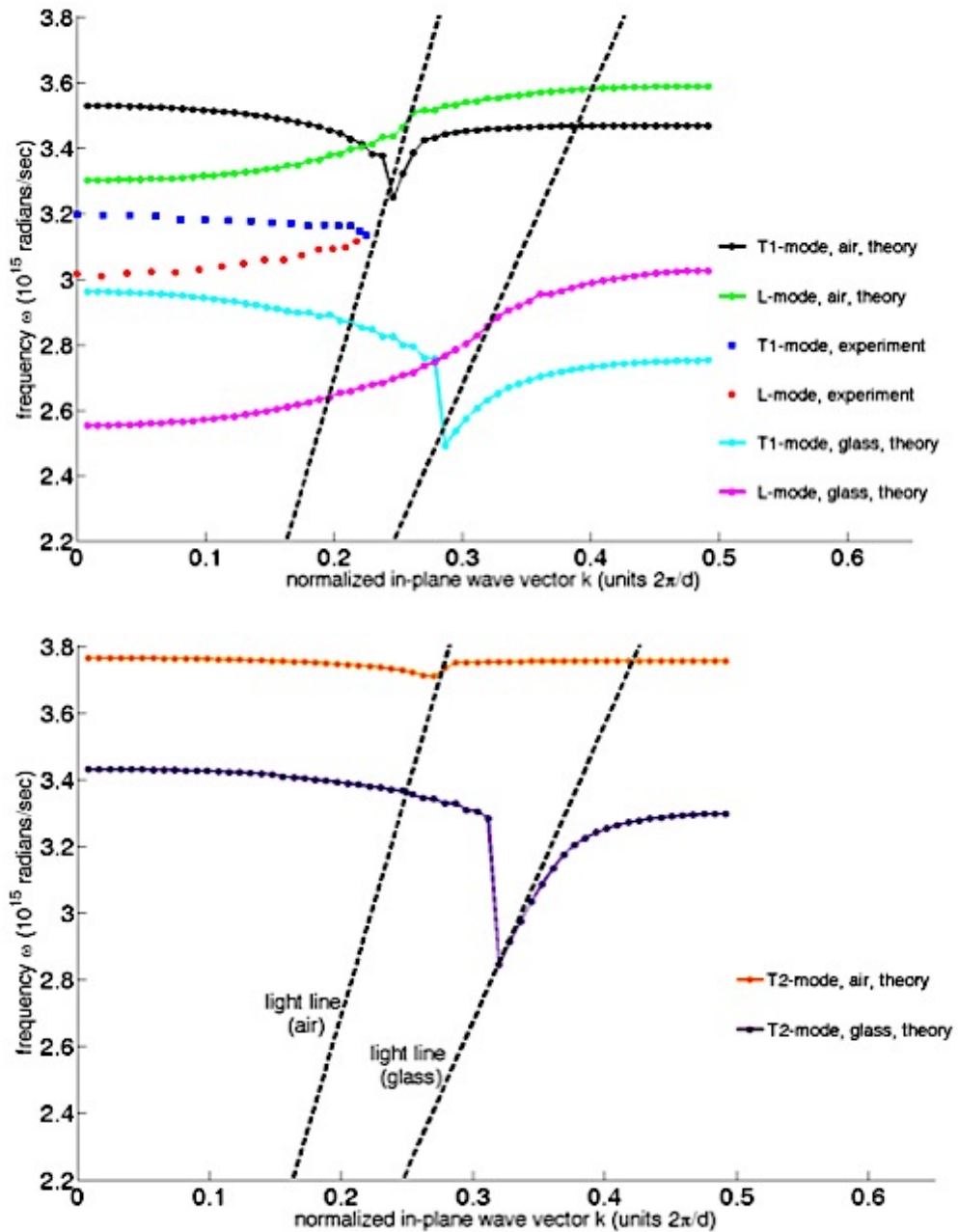
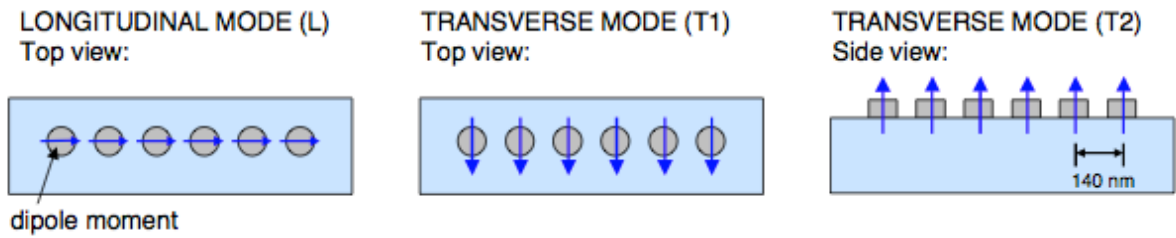


Figure V.6: Dipole moments orientation and dispersion curves for the transverse and longitudinal SP modes in an Au NP chain. Theoretical simulation is based on fully-retardation model for 2 different environments: in air and in homogeneous glass (taken from [CROZI07]).

V.1.2 Coupling between plasmonic waveguides and 2D dielectric waveguides

Once the substrate on which the MNP chain is deposited supports also the propagation of the light frequency wave, the mentioned fully-retardation model of MNP based dipole arrays should thus be reconsidered and updated by adding the coupling effect between the guided photonic modes and the MNP's SP modes. In this context, some more powerful computing methods should be applied to simulate the hybrid waveguide structure because it's no longer easy to find an analytic solution to calculate the dispersion relation of the SP modes.

a. Slab and ridge metal/dielectric plasmonic waveguides

Weeber et al experimentally demonstrated by using the PSTM the SPP modes sustained by a limit width (i.e: 1 μm to 3.5 μm) Ag stripes deposited on a glass substrate [WEEBE01]. At first, they launched SPP modes by a focused beam on a homogeneous slab metal/glass area. Then they characterized the coupling effects between the incident SPP modes and the excited stripes guided SPP modes at visible frequencies as a function of the width of the Ag stripes. Finally they observed a direct excitation of the SPP modes by the incident focused beam for a 3.5 μm Ag stripe. *Hochberg et al* introduced the coupling effect of hybrid waveguide's between the guided photonic modes and the metallic SP modes by studying the silicon-on-insulator (SOI) waveguide and a silver slab (film) waveguide. Thanks to the coupling effect operating at 1.55 μm , they fabricated a plasmonic PIC device to realize a 90° turning of propagative TE modes with a measured EL of 1.2 dB/ μm [HOCHB04]. *Goykhman et al* optimized this hybrid plasmonic waveguide to increase the propagation length by 2 orders of magnitude and also the coupling efficiency up to 80% [GOYKH10].

2D ridge metallic waveguide combined with a Si based waveguide has been investigated in order to localize propagative light wave's energy along the hybrid waveguide with a high coupling efficiency. This realizes densely-integrated plasmonic devices which are totally compatible with the traditional Si based PIC platform. *Wu et al* presented a conductor-gap-silicon plasmonic waveguide along compact S-bend curved propagation path and Y-junction beam splitters. The theoretical and experimental investigation shows a sub-wavelength confinement of light along a long propagation length [WU10]. *Zhu et al* developed a series of Cu-SiO₂-Si₃N₄-SiO₂-Cu-based plasmonic waveguides and other passive devices such as tapers, couplers, power splitters, bent waveguides and ring resonators [ZHU13]. The measured propagation loss is 0.37 dB/ μm and coupling efficiency is of 52%. In a word, the hybridization between the structured metal and dielectric waveguides opens the way to make more compact

PIC devices and realize some specific functions which are not easy to achieve based on the traditional Si based waveguide platform.

b. MNP chain/dielectric plasmonic waveguides

Combining a 2D dielectric photonic waveguide and the MNP chains, the excited SP mode's EM field would interact strongly with the guided mode's field. *Fevrier et al* theoretically and experimentally studied SOI/Au NP chain supported LSP resonances. The LSP mode allows a sub-wavelength confinement of light frequency EM wave within a short length. The giant coupling effect from the guided optical mode to the stationary LSP mode at an IR resonance wavelength has been observed by using the near-field characteristic technique as shown in Figure V.7 [FEVRI12]. This giant coupling results from waveguide coupling mechanism between the dielectric and the chain waveguide. The other closely-related result is the demonstration of highly efficient excitation of such LSP collective mode, from a waveguide. This work provides a potential solution to realize an ultra-compact hybridized PIC component, used as optical tweezers and sensors.

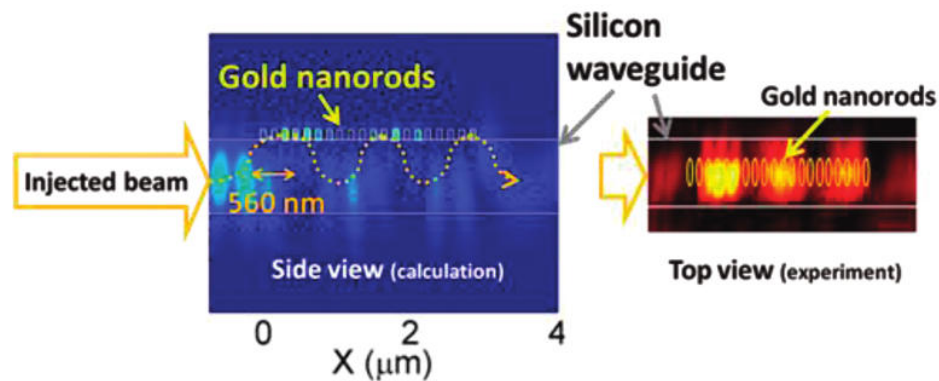


Figure V.7: TraNSOM observed giant coupling effect between MNP chain and SOI waveguide.

V.1.3 Applications based on hybrid dielectric/MNP chain waveguides

a. Nanoparticle(s) based localized surface plasmon resonances

Since the plasmon resonance frequency is also strongly dependent on the size and shape of the nanostructure, the plasmonic scientific community is also interested in the topic of different shape of single or chained nanoparticles. A variety of shape of nanoparticles could be prepared

and realized by a series of wet chemical synthesis methods or cleanroom fabrication process. Besides the traditional sphere or ellipse nanoparticles mentioned before, some other geometries of MNP have also been introduced i.e.: triangles, prisms, rods and cubes. However, for non-spherical particle, the electron oscillation is non-isotropic and localized along the principle axis or at the edge or corners or even both of the nanoparticles.

Lal et al presented qualitatively the dependence of LSP energy and corresponding wavelength function of the structured nanoparticle's shape [LAL07]. As shown in Figure V.8, by varying the shape of the fabricated nanoparticles, the excited plasmon resonances can cover the whole visible range and up to the mid IR range of the electromagnetic spectrum. It is of great interest for the whole scientific community to develop new lab-on-a-chip application, i.e.: sensing, manipulation and guiding of light. However, there is still challenge to realize the controlled assembly and integration of nanoparticles in order to match the expected demands of design.

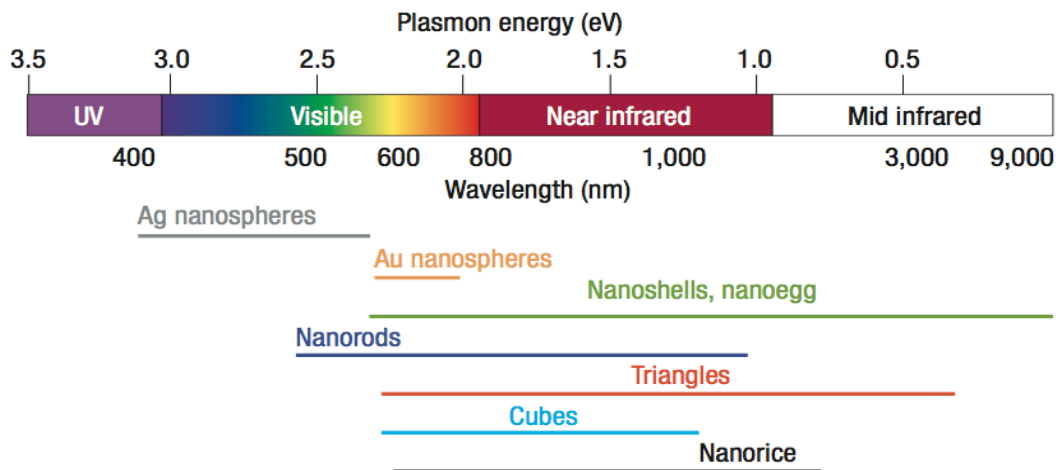


Figure V.8: Excited plasmon's resonance as a function of the particle's morphologies (taken from [LAL03]).

b. Plasmonic antennas

Following the demonstration of a high-efficiency coupling effect that transfer the dielectric guided photonic modes into a MNP chain transverse LSP mode [FEVRI12], researchers were encouraged to vary each elementary MNP's shape and dimensions, in order to develop some new functional devices. The optical antennas are one of the most representative applications [KOSAK10, CURTO10, NOVOT11].

Curto and *Taminiau* presented the design of plasmonic antenna inspired by the common radio-frequency Yagi-Uda antenna based on MNP chain as shown in Figure V.9 [CURTO10, TAMIN08]. The objective is to transfer the functions of high-directionality and efficiency receiving and sending of propagative EM wave from the RF domain to the light frequency domain. Therefore, the classic 5-elements design remained in the prototype of the optical Yagi-Uda antenna. However, comparing to the microwave application, optical antennas have to present dimensions reduced by 5 to 6 order of magnitude to be used in the visible and IR range.

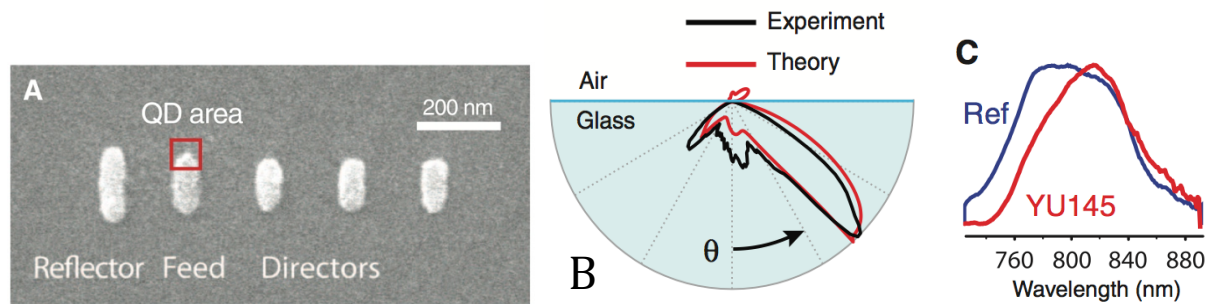


Figure V.9: Optical 5-element Yagi-Uda antennas driven by quantum dots. (A). Scanning electron microscopy image; (B). Angular radiation pattern; (C). Luminescence spectra of QDs coupled to the reference and Yagi-Uda antennas shown in (A) (taken from [CURTO10]).

As shown in Figure V.9, the fabricated 5-elements Yagi-Uda antenna is made of a reflector, a feed and a series of directors. It can be driven by quantum dots (QD) placed besides the top of the feed. The unidirectional emission of the QD coupled to the optical antenna makes it resonant at a certain frequency and bandwidth. The angular radiation spectra in the polar angle (θ) show a frontward emission and backward emission in both sides of the interface. Due to the index contrast, the radiation lobe emerged in the SiO_2 could be dominant and with a preferred direction. The intensity ratio between the point with maximum emitted power and the point diametrically opposite is called front-to-back (F/B) ratio. This ratio is used to evaluate the directional performance. Meanwhile, this antenna has a redshift detuned from the QD's emission as shown in the luminescence spectra, and the operation wavelength is about 820 nm. Finally the experimental results are in agreement with the theoretical predictions and calculations, which can be found in [TAMIN08].

Moreover, most of the recent advances in the study of unidirectional optical nanoantennas and relative applications have been summarized in [MAKSY12]. In fact, the metallic nano-rod or nanoparticle based optical or plasmonic antennas have shown their potentials to realize

more compact emitters or sensors which can be effectively embedded in a functional PIC device. Meanwhile, the application of nanoantenna can cover most fields of active nanoparticle circuits, i.e.: quantum information technology, high-density data storage, biologic sensing and imaging, photovoltaic and photodetection system.

Instead of a homogeneous environment, *Arango et al.* reported their Yagi-Uda like plasmonic antennas, which are composed of 5 Au nano-rods with different widths and also different spacings. Si_3N_4 rectangular waveguide is used to support the conventional 5-element Yagi-Uda like MNP chain. A natural idea of operation is to address a hot spot at a visible wavelength from the cleaved cross-section of the Si_3N_4 waveguide based on the conventional end-fire fiber-coupled techniques, in order to study the coupling and radiation effect within the zone where we can find the MNP chain. The Si_3N_4 waveguide has a width of 1 μm and thickness of 600 nm, quite larger than the multimode cut-off condition. According to our EIM calculation, this waveguide can support several high order TE/TM modes.

Coupling the guided light wave from the dielectric waveguide into the MNP chain can drive the antenna's radiation effect. *Arango et al* compared a single-element antenna and multi-element antenna. An approximate analytic method was introduced to calculate the polarizability with a dynamical correction based on a static model of a prolate spheroid. On one hand, for the single MNP, only the one-dipole scatterer needs to be considered: there, the extinction power is proportional to the imaginary part of the product of the incident E-field's conjugate and the dipole's polarization. On the other hand, for the multi-MNP case, two-step analysis should be executed. In the 1st step, the induced dipole moments in N particles will take influence of not only the incident E-field, but also the summation of the product of the quantified dipolar interaction's Green function and the polarization of the neighboring dipole. The 2nd step is to coherently superpose the E-fields for each dipole-like MNP by calculating the summation of the product of the nth dipole's Green function with its own polarization.

Finally, a scattering radiation spectra for the re-emitted SP modes by the nanoantenna has been shown in Figure V.10.(a). This Yagi-Uda antenna shows a resonance at a wavelength of 830 nm. Comparing with single MNP's resonance, this multi-element LSP resonance is red-shifted due to the 2 facts that the fabricated nano-rods have a length slightly larger than the designed value (i.e.: 100 nm) and the predicted Yagi-Uda antenna's response is red-shifted by plasmon hybridization. Meanwhile, by scanning the confocal microscopy with different frequencies over the sample plane of the scattering and by focusing at different positions in the same plane as shown in Figure V.10.(b), the scattering spectra show a dependence of

wavelength. This effect shows that the Yagi-Uda antenna plays a role of phased array in the light frequency spectral range and can be driven coherently by the beneath waveguide mode.

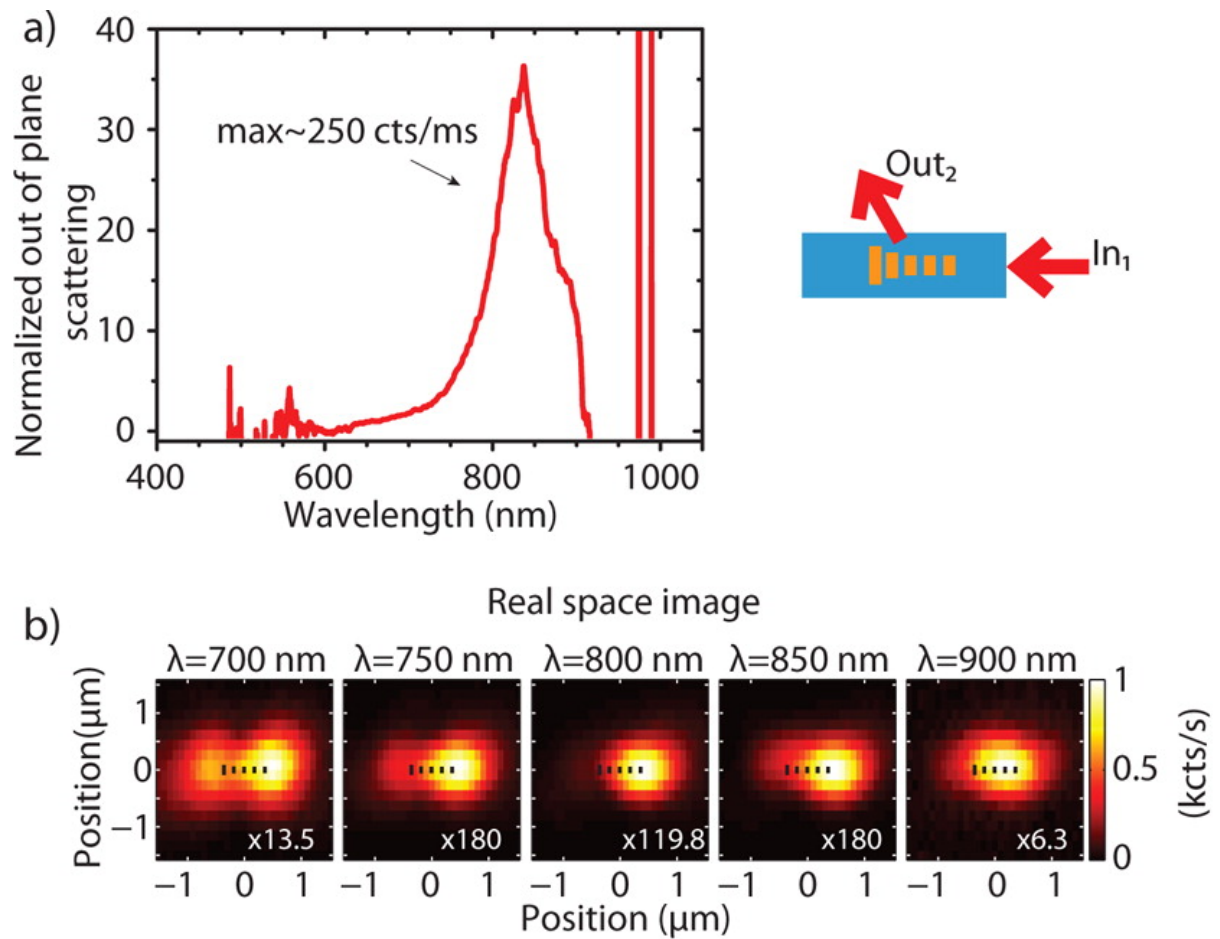


Figure V.10: Measurements of the scattering of the guided mode to free space modes carried out on a 5-element Yagi-Uda antenna on top of a 1000 nm-width Si_3N_4 waveguide. (a). Normalized spectrum of the scattering into the free space; (b). Confocal scans over the sample plane of the scattering due to the antenna; (c). Fourier images of the Yagi-Uda antenna for the scattered light coming from the guided modes (taken from [ARANG12]).

Recently, *Arango et al.* presented a cathodoluminescence experiments to study the robustness of the mentioned Si_3N_4 waveguide supporting 5-Au MNP nano-antenna. The realized 5000 nano-antenna samples are supposed to have the same designed geometry and fabrication conditions, but in reality, the fabricated and tested nano-antennas show a disordered distribution in geometry. By applying the local density of states (LDOS) analysis method, they presented experimental results for directivity of all 5000 size-predetermined Yagi-Uda nano-antennas [ARANG15]. As shown in Figure V.11, all antennas show their

maximum forward emission in the red part ($\lambda_c = 810$ nm and span = 40 nm). On the opposite, the backward beaming with maximum presents a backward directivity at blue-shift wavelength ($\lambda_c = 675$ nm and span = 25 nm). However, the obtained directivities¹⁶ for the backward beams vary a lot in values from 2.4 to 4.0, as well as for the forward beams, which are from 2.5 to 5.0.

In conclusion, although the fabricated nanoantennas suffered from disorder of size, the obtained directivity of radiation in both backward and forward direction is robust for a given dimension. However, a more precise geometry control during the fabrication of MNP should be asked in order to achieve a reasonable control of radiation directivity.

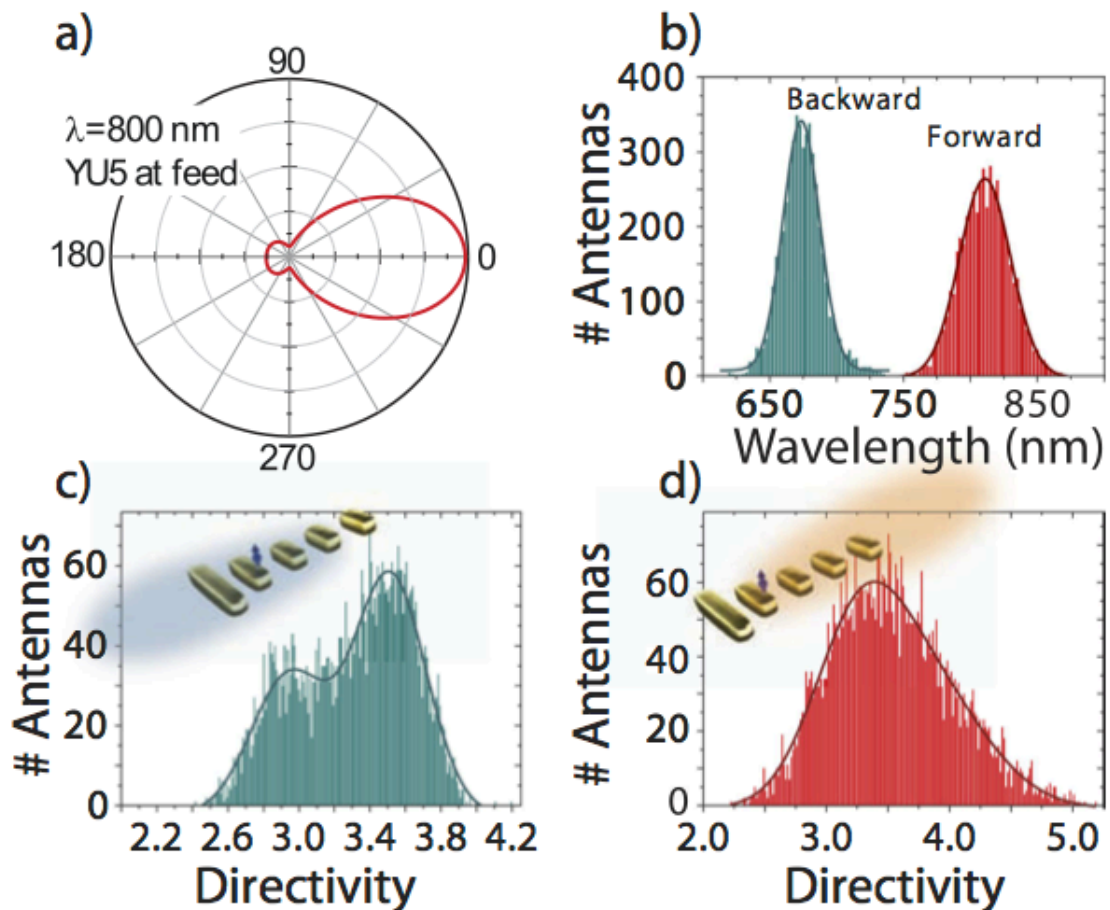


Figure V.11: (a). Angular radiation pattern for an ideal Yagi-Uda antenna in free space driven at 800 nm; (b). Distribution of wavelengths at which the directivity is maximum for forward and backward directions; (c). Distributions of maximum directivity for backward and forward radiation, respectively (taken from [ARANGO15]).

¹⁶ Directivity: synonym for directive gain, which can be defined as the radiation intensity of an antenna at a particular solid angle $U(\theta, \phi)$ divided by the radiation intensity of the analogous isotropic antenna which radiates average power all over all directions but has the same amount of total power [DIREC].

V.2 MODELLING OF MNP CHAIN INTEGRATED ON A Si₃N₄ WAVEGUIDE

In this part, we will introduce our theoretical and simulation work on the finite MNP chain deposited on top of the rectangular Si₃N₄ waveguide, which is then embedded into a SiO₂ environment. The main objective here is to optimize the dimension of the structures, which will allow efficient excitation of the nano-antennas by the silicon nitride guided mode, at resonance. The typical geometry of the full structure is represented in Figure V.12. Firstly, we will introduce the basic analytic method in order to study the MNP SP resonance in a homogenous environment. In this case, we suppose there is no beneath dielectric waveguide interacting with the excited SP modes. We are intended to find a logical tendency by varying the geometric dimensions of the MNPs, and compare with different metals, i.e.: Au and Ag. Secondly, we will present the FDTD simulation work on the expected hybrid MNP chain/dielectric waveguides. The 2D geometry (the radii of MNP on the horizontal plan)-dependent SP resonance will be studied for both Au and Ag MNP chains with 5 identical elements. In the end, we will discuss on the transmission spectra of these hybrid waveguides.

V.2.1 Punctual dipole model

For small particles with a feature size far smaller than the wavelength, it's possible to limit its excited LSPR's behavior to the polarization of the punctual dipole [VAN81, WEBER04]. The momentum for the single MNP can thus be presented as follows:

$$\vec{p}_n = 4\pi\epsilon_0\epsilon_d\alpha_s(\omega)\vec{E}_{loc} \quad (\text{V-4})$$

with α_s the polarizability of the nanoparticle which includes the quasi-static response and corrective terms. The quasi-static polarizability $\alpha_{s,u}$ has been proposed by [BOHRE08]:

$$\alpha_{s,u}(\omega) = a_x a_y a_z \frac{\epsilon_m - \epsilon_d}{3\epsilon_d - 3L_u(\epsilon_m - \epsilon_d)} \quad (\text{V-5})$$

where ϵ_m is the metal permittivity, a_x , a_y and a_z are the ellipsoid's radius along the x, y and z axis, and L_u is the form factor in each direction (u=x, y ou z):

$$L_u = \frac{a_x a_y a_z}{2} \int_0^\infty \frac{dq}{(a_u^2 + q)[\prod_{m=x,y,z}(a_m^2 + q)]^{1/2}} \quad (\text{V-6})$$

with:

$$\sum_{u=x,y,z} L_u = 1 \quad (\text{V-7})$$

As presented in §V.1, the quasi-static approximation is not relevant to take into account the interaction with electromagnetic wave. The full polarizability expression also includes radiation and dynamic depolarization effects [KELLY08]:

$$\alpha_s(\omega) = \left(\frac{1}{\alpha_{s,u}} - i \frac{2\omega^3}{3v^3} - \frac{\omega^2}{a_u v^2} \right)^{-1} \quad (\text{V-8})$$

where v is the phase velocity and ω the wave pulsation. We present in Figure V.12 (left) an illustration of the single MNP nano-ellipsoid whose resonance is modeled by (V-8). In Figure V.12 (right) is represented the 5-elements MNP chain deposited on top of the rectangular Si_3N_4 waveguide, which is the FDTD simulation modeling structure. Such a structure cannot be modeled by analytical approach (cylindrical MNP, inhomogeneous medium). The main behavior of the chain itself could be known thanks to the Coupled Dipole Approximation (CDA) method. The CDA considers that in the case of an assembly of resonant nanostructures, each one is a punctual dipole which is placed in an electric field made of radiation of all the other dipoles and of the applied external field (incident electromagnetic wave). The response of each MNP results from all these interactions.

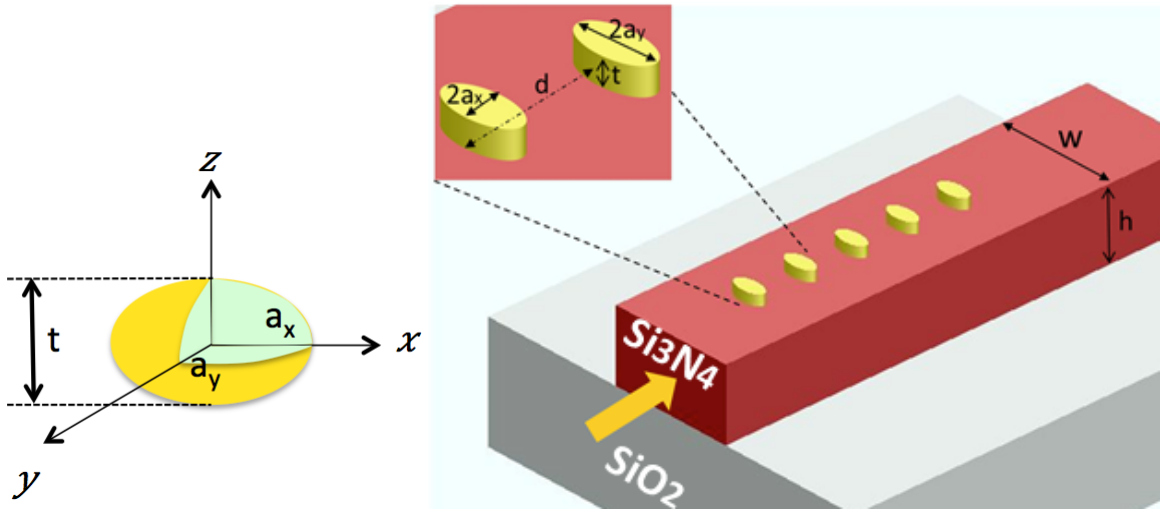


Figure V.12: Schematic illustration of the MNP chain's modeling in the theoretical calculation.

Meanwhile, the localized E-field applied to the n^{th} MNP consists of 2 parts:

$$\vec{E}_{loc} = \vec{E}_{ext} + \vec{E}_{dip} \quad (\text{V-9})$$

with the dipole excited E-field E_{dip} and the applied macroscopic field E_{ext} . If we consider the collectively excited E-field by all the other punctual dipoles, the total E_{dip} for the n^{th} MNP can be written as follow:

$$\vec{E}_{dip} = \frac{1}{4\pi\epsilon} \sum_{m \neq n} \left[\frac{\omega^2 \vec{p}_m - (\vec{p}_m \vec{R}) \vec{R}}{v^2 |n - m|d} + \left(1 - \frac{i\omega |n - m|d}{v} \right) \frac{3(\vec{p}_m \vec{R}) \vec{R} - \vec{p}_m}{(|n - m|d)^3} \right] e^{i\omega \frac{|n-m|d}{v}} \quad (\text{V-10})$$

with

$$v = \frac{C_0}{n_e} \quad (\text{V-11})$$

where n_e is the MNP environment refractive index. Considering the relations (V-4), (V-9) and (V-10), we can admit that the collective response of a chain made of identical nanostructures is significantly driven by the polarizability of each nanostructure, in an homogeneous medium. The dipolar (near to far field) interactions (V-10) between the different nanostructures of the chain will then add a correction to the resonant wavelength. In the real structure including the silicon nitride waveguide (Figure V.12) the polarizability will be much more strongly affected by the inhomogeneous medium. Anyway the consideration of the polarizability of a stand-alone ellipsoidal nanostructure in a homogeneous medium is sufficient to determine the “rough” dimensions of nano-cylinders resonant at the visible wavelength (~ 633 nm), as a starting point for FDTD simulations of the full structure. This will be done in § V.2.3.

V.2.2 Optical properties of the metals

Since the noble metals have a complex permittivity, as well as their refractive index, the *Drude* model is used to link the optical and electric properties for a metal as shown in (V-1). In reality, by using the ellipsometry techniques, we can measure the spectra of refractive indexes for the fabricated metals. A comparison of the refractive index between the fabricated Au or Ag samples and the FDTD software recommended *Palik* model is presented in Figure V.13. As shown the fitted model for FDTD is quite similar to *Palik* data [PALIK], especially at the shortest wavelengths (the most interesting here). Even if the cleanroom-deposited gold index real part is significantly different from *Palik* data, we have considered the fitted model of FDTD even for analytical calculation in order to ease further comparisons.

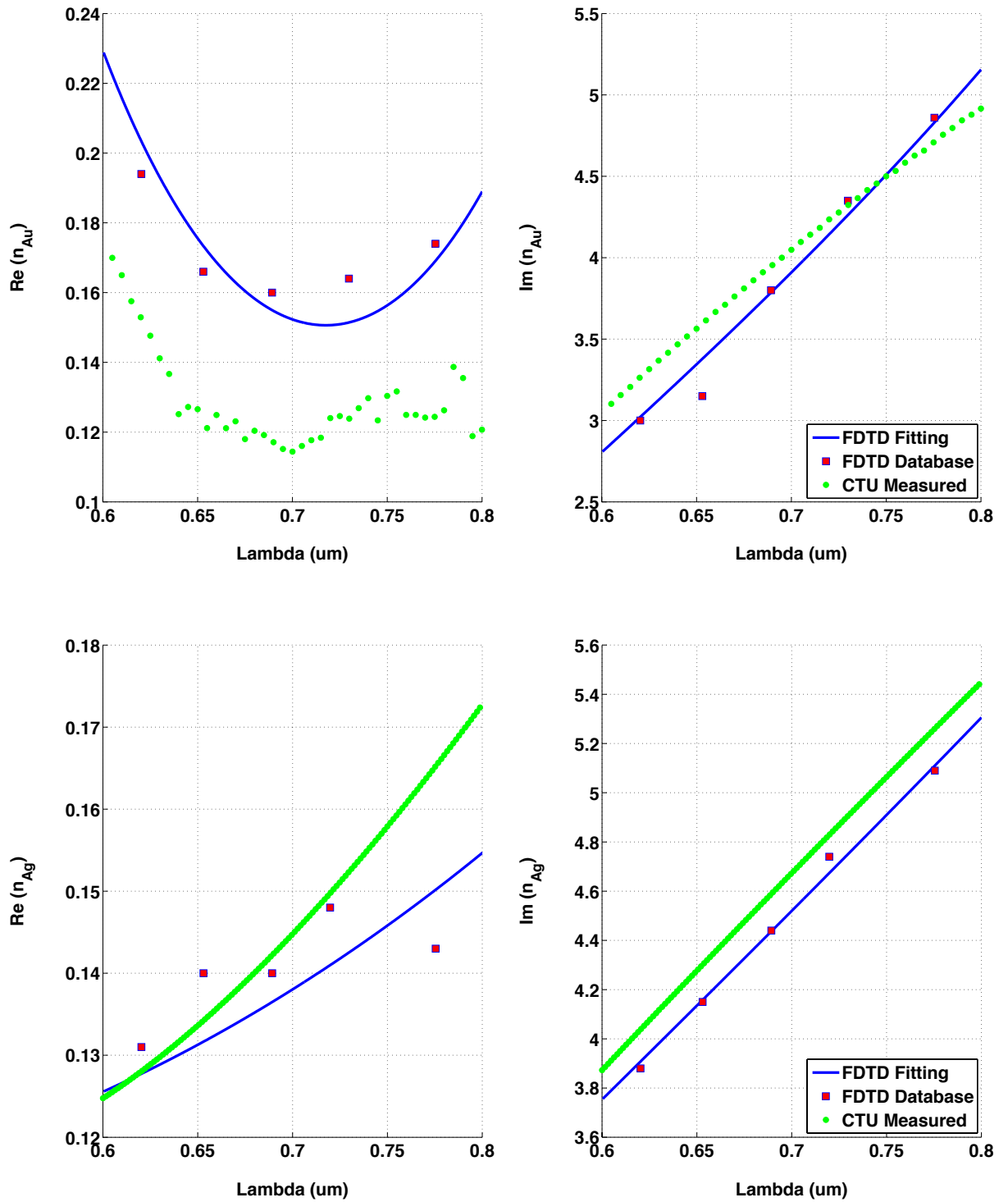


Figure V.13: Comparison of the refractive index between the cleanroom (CTU) fabricated Au or Ag samples and the FDTD software recommended Palik model.

V.2.3 Computed single MNP resonance

We applied the punctual dipole model to calculate the excited SP mode's polarizability of one single MNP. We will concentrate on the expected visible wavelength range, especially the red part. The objective is to determine the geometry of the single Au or Ag nano-ellipsoid, in order to adapt its resonance to an interested wavelength range, i.e.: 600 nm - 800 nm. The permittivity of Au or Ag is referred to the LUMERICAL fitted *Palik* material database [PALIK].

a. Polarizability in a full-retardation corrective mode

We present in Figure V.14 and Figure V.15, the computation results of the imaginary part of the single Au or Ag nano-ellipsoid's polarizability in considering the full-retardation losses, for two different thicknesses $t = 2a_z$.

a.1 Palik Au nano-ellipsoid

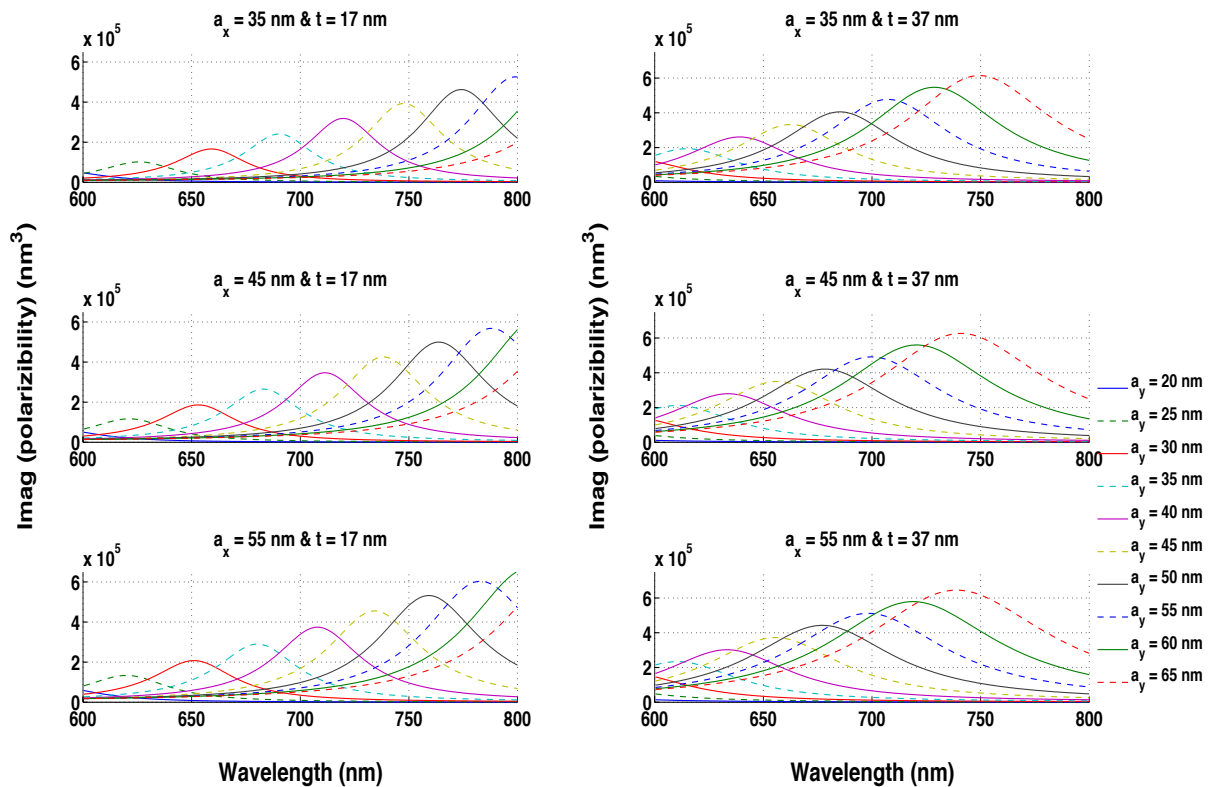


Figure V.14: Single ellipsoid-like Au nanoparticle's polarizability (imaginary part) as a function of its geometry (a_x , a_y , $t=2a_z$).

a.2 Palik Ag nano-ellipsoid

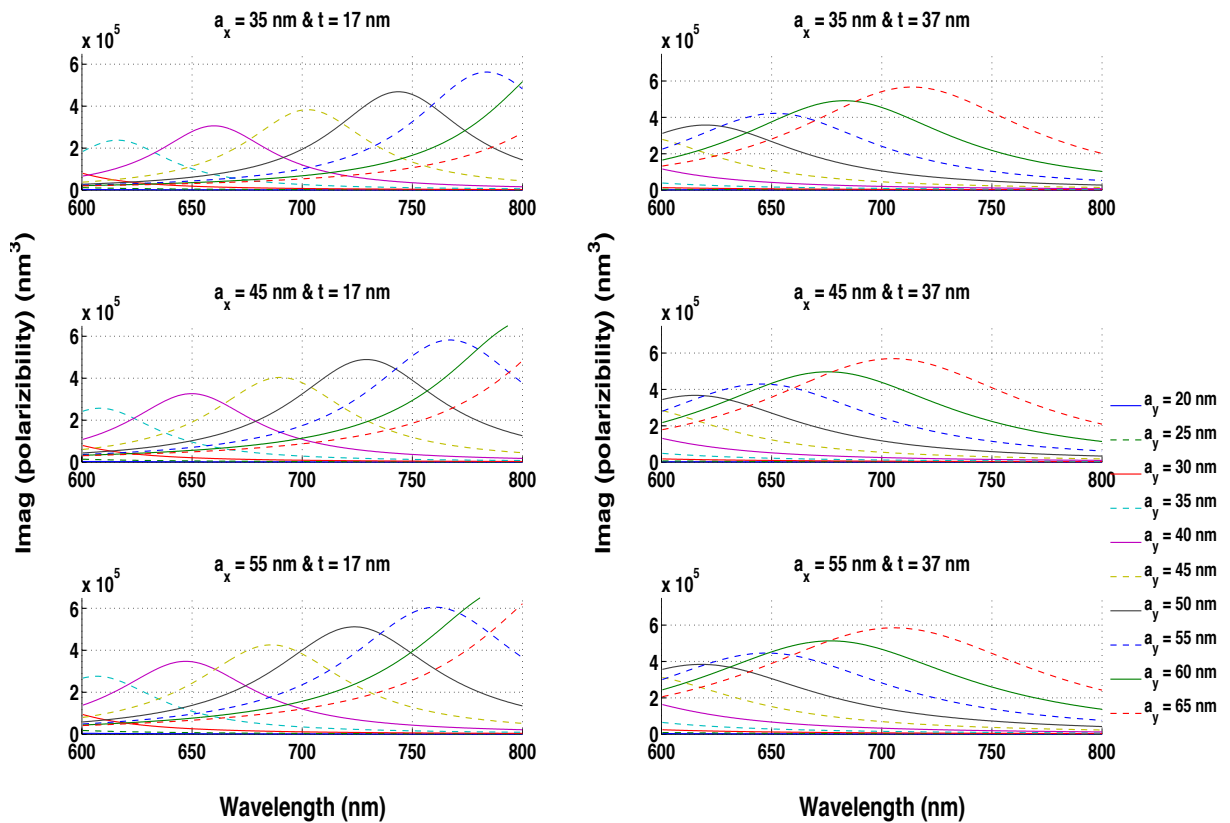


Figure V.15: Single ellipsoid-like Ag nanoparticle's polarizability (imaginary part) as a function of its geometry (a_x , a_y , $t=2a_z$).

a.3 Discussions

In both cases with two different thicknesses of Au or Ag ellipsoid, the polarizability will have a strong red-shift when the radius a_y is slightly increased. In the thinner case ($t = 17$ nm), the average ratio of the polarizability's red-shift over the increasing of a_y is about 30 nm / 5 nm for Au and 40 nm / 5 nm for Ag, and in the thicker case ($t = 37$ nm), this ratio is decreased to 20 nm / 5 nm for Au and 30 nm / 5 nm for Ag. It can be interpreted by the dominance of the transverse mode in the excited SP resonance. Once we change the MNP's y-axis size, the boundary conditions of the transverse SP mode will be straightforwardly changed and thus influence the SP resonant frequency. On the opposite, by increasing the other radius a_x , the polarizability resonance will reversely shift towards blue, although this blueshift is relatively much slower than the red-shift with the increasing of a_y . Meanwhile, the same tendency of blueshift occurs while increasing the thickness of the MNP.

b. Resonance calculation

We determine numerically the resonant wavelength by seeking the maximum value of the polarizability's imaginary part. In order to determine the Au or Ag nano-ellipsoid dimensions to obtain a resonance at 633 nm, we present in Figure V.16 and Figure V.17 this geometry-dependent Au or Ag (respectively) NP resonance for the two thicknesses 17 and 37 nm.

b.1 Palik Au nano-ellipsoid

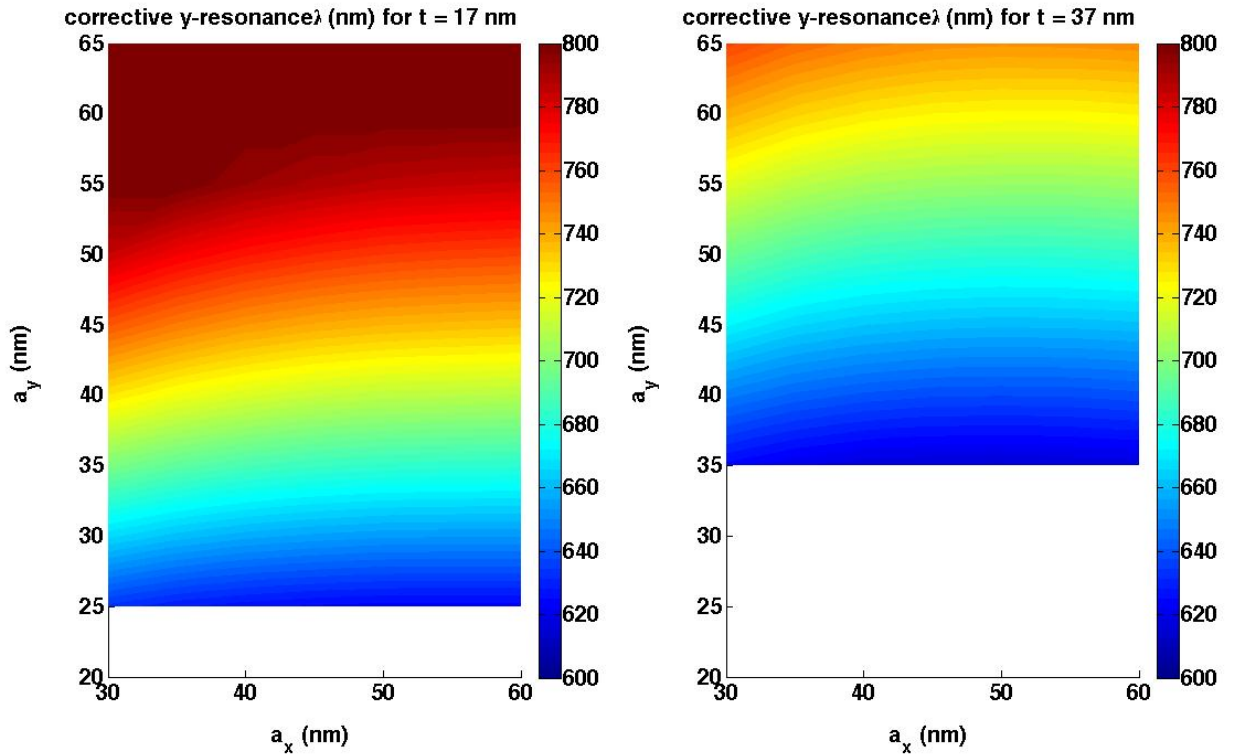


Figure V.16: Cartography of Au nano-ellipsoid resonance within the range 600-800 nm for a fixed thickness of 17 nm and 37 nm.

As shown in Figure V.16, a certain number of geometric solutions (a_x , a_y , a_z) can be determined to achieve an expected 633 nm resonance in the 17 nm-thick Au nano-ellipsoid. The corresponding radius a_x and a_y can be varied from 30 to 60 nm and from 23 nm to 27 nm, respectively. However, for a thicker Au nano-ellipsoid, the expected resonance requires a relatively large a_y (35-37nm) and a comparable a_x . In other word, by increasing the thickness of Au nano-ellipsoid, the resonance wavelength will be straightforwardly blue-shifted.

b.2 Palik Ag nano-ellipsoid

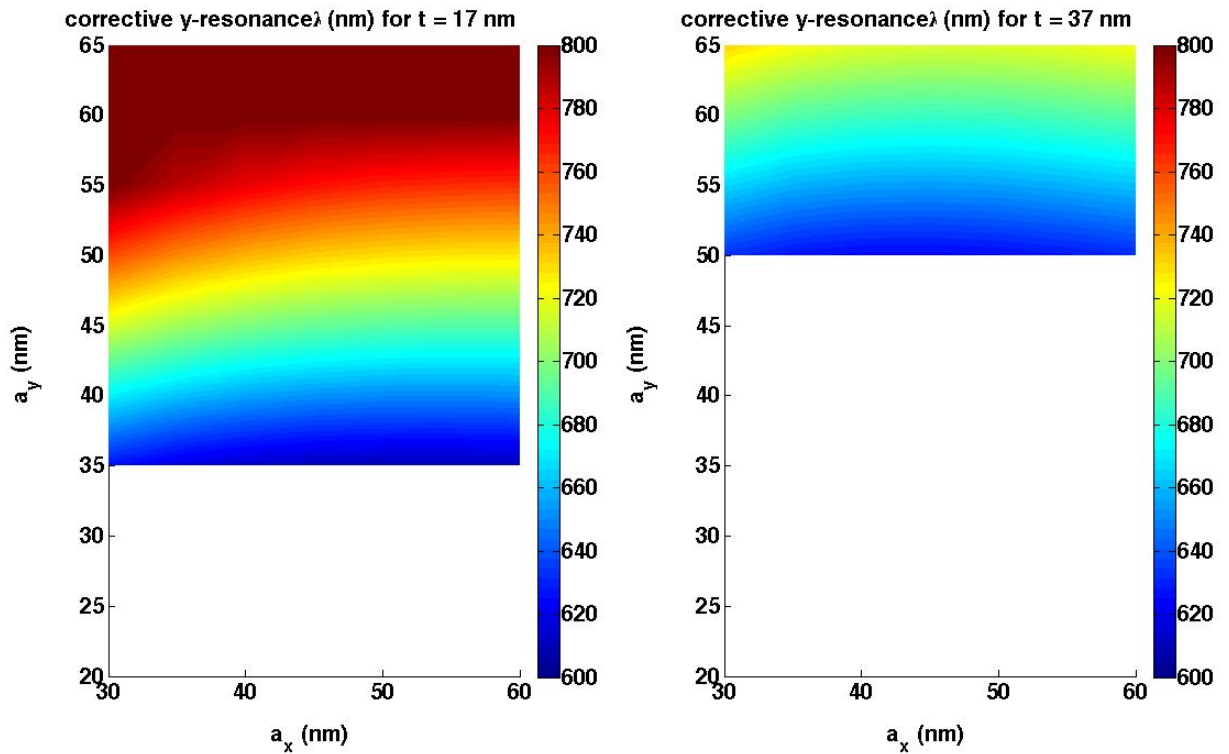


Figure V.17: Cartography of Ag nano-ellipsoid resonance within the range 600-800 nm for a fixed thickness of 17 nm and 37 nm.

As shown in Figure V.17, the same tendencies of the geometry-dependent resonance wavelength's evolution have been observed as in the Au nano-ellipsoid case. But comparing with Au NP, Ag nano-ellipsoid has a smaller resonance wavelength. Therefore, to achieve a resonance of 633 nm, the expected Ag's dimensions could be larger than Au. For instance, for a thinner Ag nano-ellipsoid ($t = 17$ nm), the expected resonance requires an a_y around 35 nm and for the thinner case ($t = 37$ nm), a_y can be increased up to 50 nm.

By the way, all of these geometric solutions are compatible with the current cleanroom fabrication techniques based on the high-precision e-beam lithography, but very good control is required for the a_y dimension. Based on our analysis, the use of Ag instead of Au to fabricate our MNP seems to be a better choice in order to decrease the influence due to the fabrication errors, because the expected resonance can be achieved with a larger Ag nano-ellipsoid, especially with comparable a_x and a_y of magnitude of 50 nm and a thickness of 37 nm.

V.2.4 FDTD simulation

We have used the LUMERICAL FDTD software to study the coupling effect between the MNP chain and the Si_3N_4 waveguide, in the full structure. The objective is to assess the coupling efficiency between the waveguide and the chain as well as the resonance of the chain. The principle of the study is to evaluate the transmission of a guided mode through the waveguide decorated by the MNP chain. The transmission spectrum, defined as the ratio between the output power and the input power versus the input wavelength, will reveal the coupling efficiency and the plasmonic resonance which both induce losses during the full transmission.

The dimensions of the Si_3N_4 waveguide are referred to the predetermined design, which has a rectangular cross-section of $250 \text{ nm} \times 300 \text{ nm}$ under the TE_{00} single-mode condition. The simulated Au and Ag have optical properties based on the Palik model, which is included in LUMERICAL's material database. The simulation zone is covered by a large number of stairs-step like mesh. The minimum meshgrid is set to 3 nm for both direction along x-axis and y-axis, and 5 nm along the z-axis. As shown in Figure V.12, we put the simulated MNP into a 2D+z structure, which means its cross-section on the x-y plan is a standard ellipse with two varied radii a_x and a_y , and is unchanged along the z-axis.

In the FDTD calculation, the light source has a normalized field distribution within a wavelength range from 600 nm to 800 nm. Therefore, the transmission spectra of the hybrid waveguide are supposed to be independent to the light source. The transmission spectra will be directly linked with the SP mode's resonance excited near the MNP chain and dielectric waveguide's interface. We will present the dependent relation between the 5-element MNP's geometry and the resonant wavelength. At the same time, the transmission spectra curves will be fitted by a Lorentzian mathematical model in order to calculate the factor of quality Q for each chain with different dimensions. The quality factor includes information on coupling efficiency and resonance depth, together. At first, we have studied the dependence of the transmission spectra as a function of the MNP's spacing. We present in Figure V.18 an example for the 5 Au MNP with a geometry of $50 \text{ nm} \times 35 \text{ nm} \times 37 \text{ nm}$.

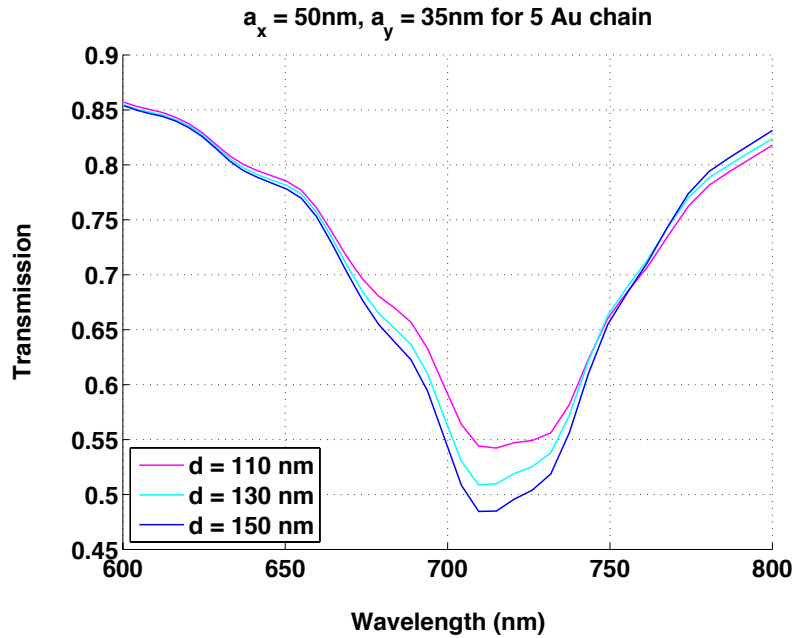


Figure V.18: FDTD simulated 5-element Au NP chain/ Si_3N_4 waveguide resonance spectra as a function of MNP's spacing.

As shown in Figure V.18, by increasing the MNP's spacing, the transmission would be decreased and also slightly blue-shifted. We suppose in these situations that the excited MNP chain's SP mode is always out of Bragg resonance's control, because the studied inter-NP's spacing are always inferior to the featured Bragg resonant period, which can be approximately estimated to a third of the resonant wavelength. Therefore, we will fix the inter-NP's space to 130 nm for the following simulation.

In the following we will present successively the transmission spectra, the resonant wavelengths and the quality factors versus the dimensions of NP, for 5-element Au NP chain/ Si_3N_4 waveguide (§ a.1 and a.2), and for 5-element Ag NP chain/ Si_3N_4 waveguide (§ b.1 and b.2), followed by a discussion on the results (§c).

a. 5-elements Au NP ($t = 37$ nm) Chain

a.1 Dependence of transmission spectra to the geometry of Au nanoparticle

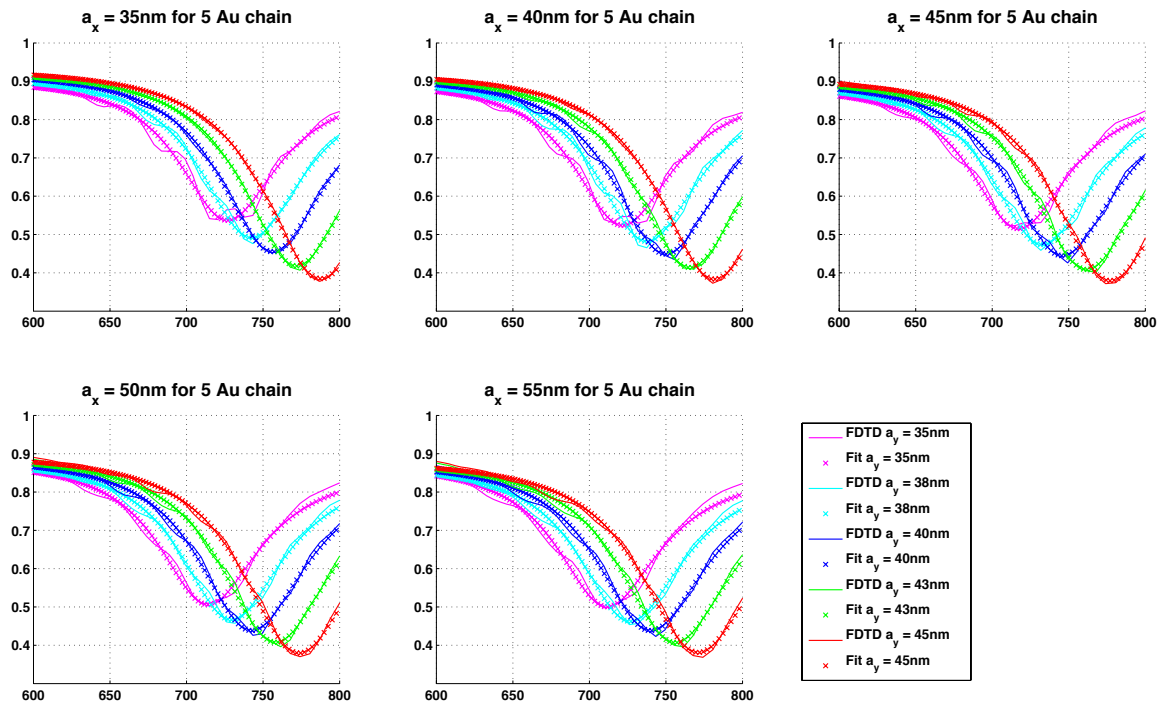


Figure V.19: Transmission spectra of FDTD simulated 5-element Au NP chain/ Si_3N_4 waveguide.

a.2 Dependence of resonance to the geometry of Au nanoparticle

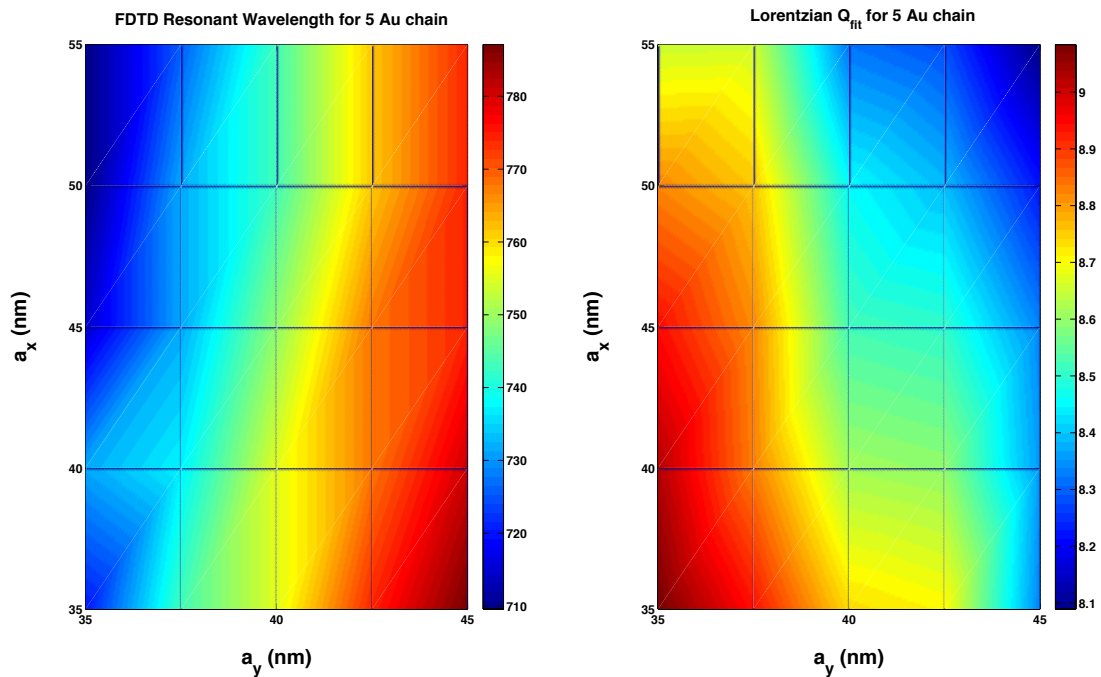


Figure V.20: Cartographies of the FDTD simulated resonance and the Lorentzian fitted factor of quality for the 5 Au NP/ Si_3N_4 waveguide.

b. 5-element Ag NP ($t = 37$ nm) Chain

b.1 Dependence of transmission spectra to the geometry of Ag nanoparticle

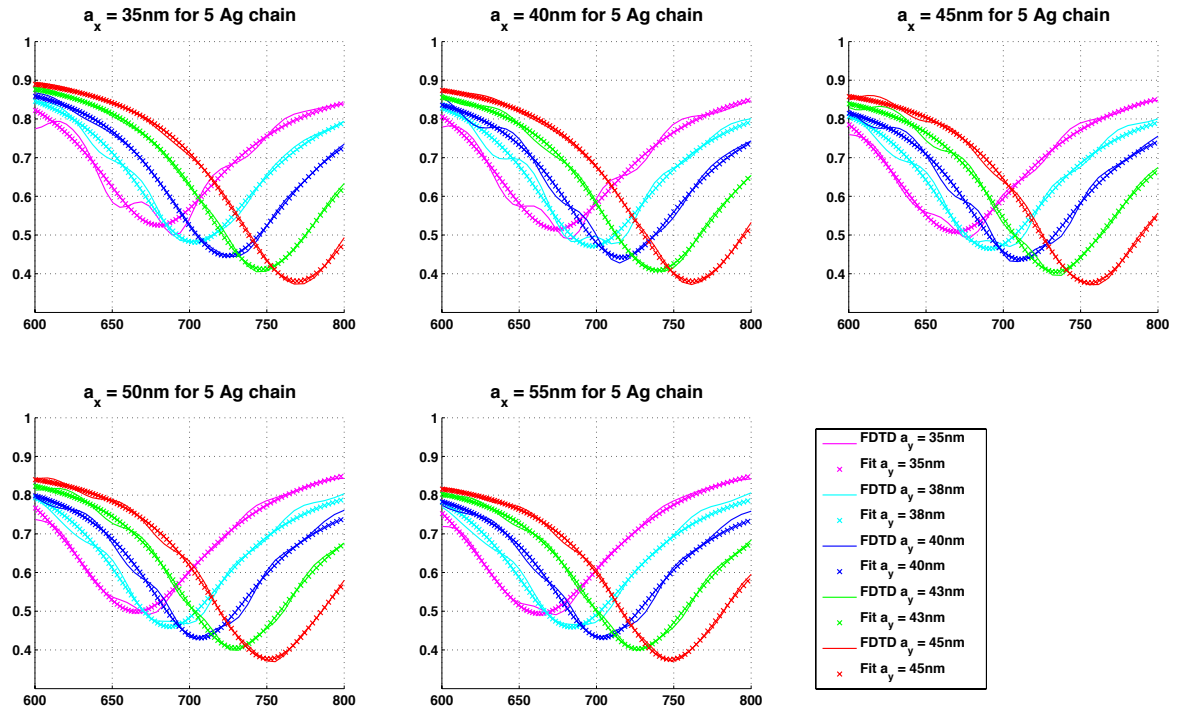


Figure V.21: FDTD simulated 5-element Ag NP chain/Si₃N₄ waveguide resonance spectra.

b.2 Dependence of resonance on the geometry of Ag nanoparticle

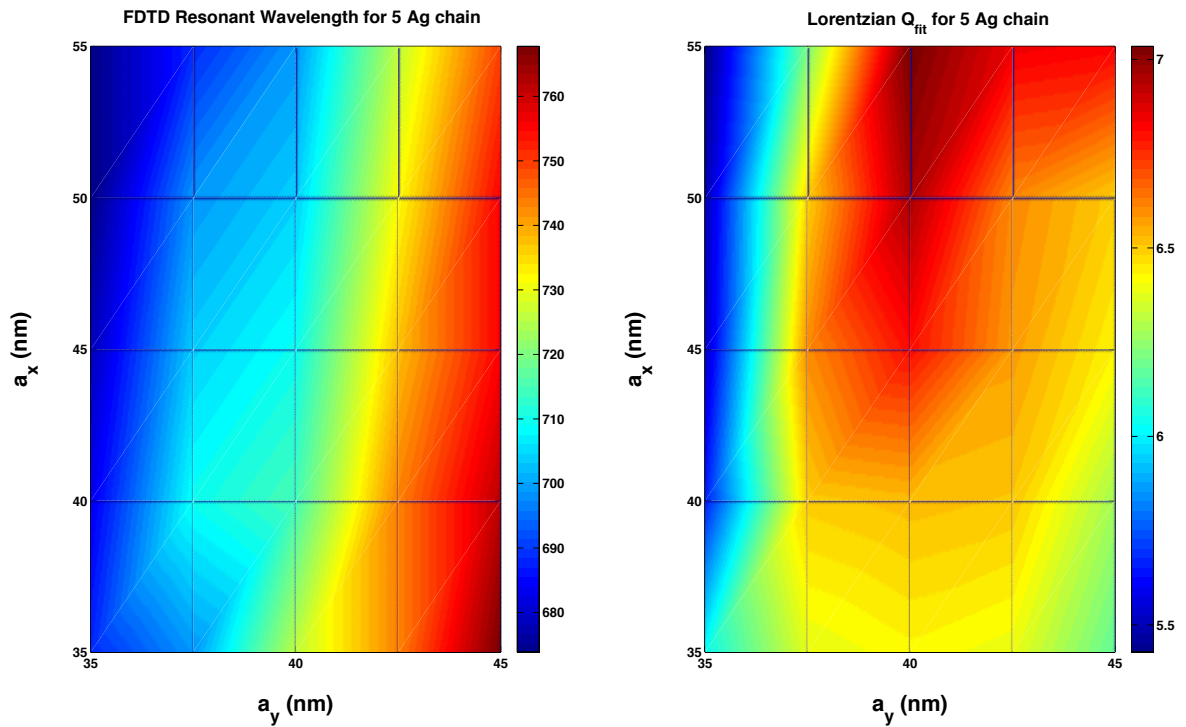


Figure V.22: Lorentz fitted factor of quality for the 5 Ag NP/Si₃N₄ waveguide.

c. Discussions

c.1 Observation of the transmission spectra

In all of the transmission spectra of both Au and Ag NP chains, there are the same geometry-dependent evolution tendencies for the peak wavelength as shown in the computed polarizability's imaginary part of a single Au nano-ellipsoid. In other words, by decreasing a_y or increasing a_x , the transmission peak wavelength will shift towards blue. Although the FDTD simulated transmission spectra show a disorder (not a Lorentzian shape) for the small size MNP chain, i.e.: $a_y = 35$ nm, we can estimate that with a larger a_x and a smaller a_y , the expected 633 nm resonance could be obtained with a transmission near 50%. Interestingly, this corresponds to a MNP shape with higher axes in the propagation direction than in the transverse polarization direction. We present in Figure V.23, one of this giant coupling effect at 664 nm for the Ag NP with dimensions of $a_x = 50$ nm, $a_y = 40$ nm and $t = 37$ nm. In fact, the first 4 MNPs have accomplished the localization for most of coupled energy.

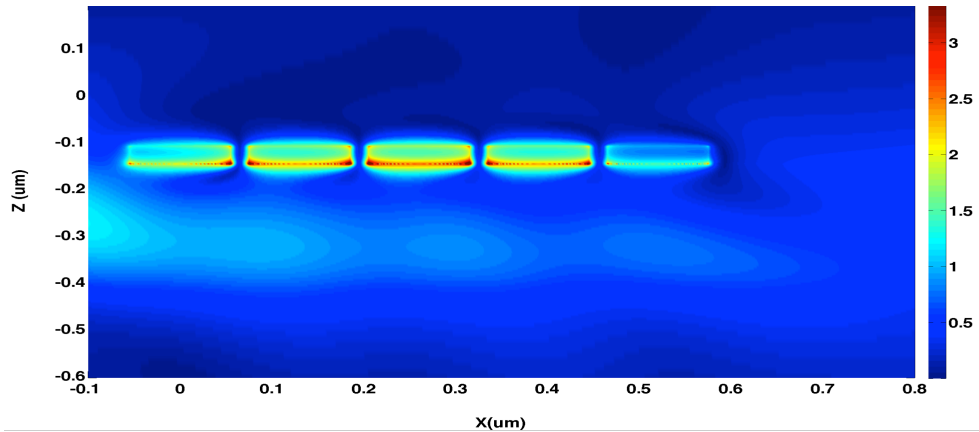


Figure V.23: FDTD simulated optical intensity distribution along the hybrid waveguide. Ag NP has dimensions of $a_x = 50$ nm, $a_y = 40$ nm and $t = 37$ nm. The resonant wavelength is 663 nm.

c.2 Fitting the transmission spectral curves to a Lorentzian model

Most of the transmission spectra have a similar shape as the standard Lorentzian model. We have studied the ratio between the resonant wavelength and the full width at half maximum (FWHM) in such a Lorentzian transmission spectrum. If we suppose the localized surface plasmon along the chain is analogous to a photonic cavity, the mentioned ratio can be defined as the factor of quality Q for the conventional cavity-like photon localization and oscillation system. Once the photon is coupled from a propagative guided mode to a localized surface plasmonic mode, the light energy remains confined at the interface of metal and dielectric

along the chain. The more this Q factor is, the more the energy stored within such a plasmonic waveguide is. Furthermore, it is also related to the coupling efficiency.

As shown in Figure V.20 and Figure V.22, the cartographies show the geometry-dependent factor of quality in the 5-element MNP chain, which is combined with the beneath Si_3N_4 rectangular waveguide. For the Au MNP chain, decreasing both radii a_x and a_y could increase the Q factor. It is anyway very low. A different evolution tendency has been observed in the Ag MNP chain. a_y plays a dominant role in this Q factor characteristic curve and shows a parabolic relation, in which the maximum of Q factor is situated at 40 nm. At the same time, a_x has a relatively low influence on the Q factor's variation. One possible reason of the different tendencies of Q for Au and Ag is the very different behavior of the permittivity of the both metal in the spectral range 600-800nm (Figure V.13). This must be anyway further investigated for better understanding of the resonance and the coupling efficiency.

V.3 CONCLUSION

In this chapter, we firstly reviewed the basic notions of surface plasmon and some state-of-the-art theoretical and experimental research work in this domain. We focused on the MNP chain based LSP resonance and the hybrid photonic-plasmonic waveguide formed by a combination of a MNP chain with a dielectric waveguide. It's of great interest for us to design and fabricate the optical nano-antennas based on this hybrid waveguide structure, for the purpose of realizing directional coherent emission. In the second part, we theoretically investigated the MNP's resonance and the hybrid waveguide's transmission by both analytic method and FDTD solutions. We proposed a geometric value range of the Ag nano-ellipsoids in order to obtain a resonance at 633 nm in such a single MNP based coupling dipole system, which is compatible with fabrication technology: typically comparable a_x and a_y values, of magnitude of 50 nm, and a thickness of 37 nm. Finally, we analyzed the geometry dependence of the hybrid waveguide's resonant wavelength and the coupling efficiency between the dielectric guided modes and the Au or Ag MNP formed LSP modes, notably by comparing Lorentzian Q factor. This parameter can be relevant for the optimization of integrated metallic chains on waveguides but has to be further evaluated, as well as its dependence with the metal permittivity properties. Future work on this PIC's element will be concerned with the application of such a chain to the function of re-emitters, i.e. its behavior as nano-antennas.

CONCLUSION AND PERSPECTIVES

The long-term objective of the research work presented in this manuscript is to develop a compact auto-embedded holographic illumination system, within a collaboration framework between PSA Peugeot Citroën and Institut d'Electronique Fondamentale.

The application background is described by a holographic signalling system patented by PSA [FR2949725(A1)] which aims at alerting following car drivers of too reduced security distance. However, the prototype of this system is composed of a series of bulky optical lens and mirrors and has a total length close to 1 m. Obviously, it's not compact enough to be installed easily in a passenger car. In this context, inspired by the rapid development of integrated optics and corresponding nanotechnologies, we proposed an alternative solution to replace all of these optical components by an ultra-compact visible photonic integrated circuit (PIC). The global design of this PIC has been patented in [WO2014106584(A1)].

The targeted device can be divided into 3 relatively independent subsystems: 1). 633 nm single-mode Si_3N_4 waveguides array, 2). metallic nanoparticle (MNP) chain based optical nano-antennas and 3). organic amplifiers. The 2 first subsystems have been studied and developed in a first-phase during this PhD. Meanwhile, the 3rd subsystem has been assigned to our project partner in the WNLO (China). In this manuscript, we have sequentially presented the 1st subsystem in Chapter II, III and IV and the 2nd subsystems in Chapter V.

More precisely the targeted PIC should guide and split the optical power of one single laser source at 633nm into 16 waveguides, occupying the whole PIC surface on a \sim square surface which has to match a holographic plate (first subsystem). Each of the 16 waveguides supports at least 1 (nano-antenna) emitter (second subsystem), precisely positioned in order to re-emit equal-power and in-phase guided light in a precise direction of 56° .

For the 1st subsystem, we firstly reviewed the evolution of design, fabrication and characterization of the visible light waveguides since last few decades and introduced some state-of-the-art visible rectangular waveguides, in order to show the feasibility of our expected 633 nm single-mode rectangular waveguide on Si_3N_4 (in Chapter II). Then we theoretically studied and designed the rectangular Si_3N_4 waveguides array (in Chapter III). The effective index method (EIM) has been used to optimize cross-section dimensions of waveguide. At the same time, we applied vectorial mode analysis software to study the modal profiles of the SiO_2 cladded Si_3N_4 waveguides. Finally, we found that the strict multimode cut-off dimensions should be close to $250 \text{ nm} \times 300 \text{ nm}$, with a guided TE_{00} confinement coefficient

of about 85%. Based on these expected dimensions of Si_3N_4 waveguide's cross-section, we designed also some other passive integrated devices as 1×16 beam splitters and bent waveguides for the purpose of realize an uniform repartition of 633 nm light on a square surface. Finally, we proposed a 4-stage cascaded 1×2 MMI couplers based solution aiming at achieving a low-loss and high-uniformity beam splitter. At the end of Chapter III, we compared the theoretical bend losses of the lemniscate-like and S-Function curved waveguides and consequently presented an accurate combination of both types of bend, in order to ensure a low-loss connection between the inputs and outputs of different beam splitting stages.

We fabricated the designed SiO_2 cladded Si_3N_4 waveguide in the CTU cleanroom at the IEF. In fact, the realization of single-mode optical waveguides, and more generally integrated circuits, for visible light operation remains still a real challenge in terms of fabrication and performance. Based on the EBL techniques, we realized a series of different-length straight waveguide samples, in which the optimization has also been taken into account, especially for the EBL writing process. The fabricated waveguide samples have an estimated width of 300 nm and a thickness of 260 nm. Finally, we measured their propagation attenuation coefficient by setting up a 635 nm optical characterization platform. Despite technological defaults, straight waveguide losses have been estimated at 10.4 dB/mm. This very first result is in accordance with literature results, taking into account the dimensions of the waveguide and the material and etching quality. However, we are intending to continue optimizing the fabrication process, including introducing a thermal post-treatment of PECVD, reducing EBL's stitching errors and roughness of etched sidewalls, and improving the dicing saw based facet cutting quality. These experimental works are presented and discussed in Chapter IV.

We presented in the last Chapter (Chapter V) our theoretical research work on the mentioned 2nd subsystem, which is intended to realize the propagative optical energy's coupling (from the Si_3N_4 waveguide) and re-emitting outward the plane. We firstly reviewed the basic notions of surface plasmon and some state-of-the-art research work of the hybrid photonic-plasmonic waveguide made by the MNP (Metal Nanoparticle) chain and a dielectric waveguide. It's of great interest for us to take advantage of Au or Ag nanoparticle chains to form an optical nano-antenna for the purpose of realizing directional coherent emission. In this context, we theoretically investigated the MNP's resonance and the hybrid waveguide's transmission by using both analytic method and FDTD simulation software. Finally, we compared different metal (Au and Ag) and different MNP's geometry (radii, thickness and spacing distance) in order to obtain a resonance at 633 nm and a suitable coupling efficiency between the dielectric guided modes and the MNP formed LSP modes. This investigation was

helpful to finally propose a geometric value range of the metal nano-ellipsoids chain for our on-a-chip application within the visible wavelength range. Typical nanostructures should be ellipsoid Ag nano-rods with comparable a_x and a_y values (i.e. 50 nm) and a thickness of 37 nm. The next step will be then the study of the far-field radiation from these nano-antennas, which could be controlled by the change of the elementary MNP's geometry. *Arango et al.* have already reported their experimental and theoretical investigation on this type of MNP chain based 5-elementary Yagi-Uda like nano-antennas [ARANG12, ARANG15]. However, there is still a lot of research work to improve the nano-antenna's directivity in order to precisely control the radiation angle.

The first perspective of this work will be the improvement of the technological fabrication in order to be able to lean on a reliable silicon nitride platform for visible PICs. Then the design of emitters has to be completed for directionality control. Immediately after will come the demonstration of the integrated device with the arrayed waveguides and splitters, and the directional nano-emitters. In parallel the insertion of amplifying sections, combined or not with the plasmonic structures should allow compensating losses. All these steps are already planned within a new PhD program, which will lean on the basis established in the present pioneer work.

In a longer term, the availability of such building blocks for visible PICs will be of great interest for several additional applications, like directional lighting, possibly with several colors, or integrated biological plasmonic sensors.

ANNEXE I: EFFECTIVE INDEX METHOD FOR 1D DIELECTRIC WAVEGUIDE

The effective index method (EIM) is a fast calculation method for the analysis of 1D layered and 2D rectangular waveguides [YARIV2006]. We can deduce from the equations of the transverse electromagnetic fields in the dielectric waveguides the propagative modes, which can be qualified by their effective index and their confinement ratio.

i.1 1D approximation of EIM

The very first step of approximation is to split the layered dielectric structures into 3 planar zones differed in refractive index and thickness (see Figure i.1).

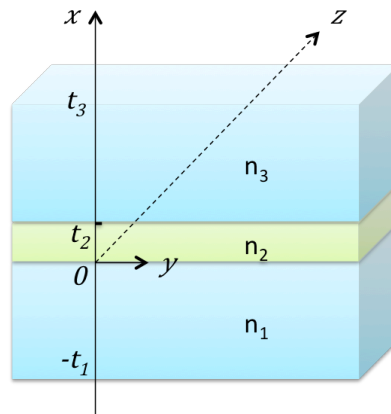


Figure i.1: Schematic of the layered 1D waveguide structures.

The propagation modes should be confined within the waveguide layer which has the highest refractive index and usually a thickness of the same order of magnitude as the wavelength. We consider here the general case of the refractive index distribution of each layer as following:

$$n(x) = \begin{cases} n_1, & -t_1 \leq x < 0 \\ n_2, & 0 \leq x \leq t_2 \\ n_3, & t_2 < x \leq t_3 \end{cases} \quad (\text{i-1})$$

where we suppose that $n_3 < n_1 < n_2$, and t_1 and t_2 “infinite”, i.e. large with respect to the wavelength. We can describe the monochromatic light wave propagating along the z-direction in the green layer by Maxwell equations:

$$\begin{cases} \nabla \times \mathbf{H} = i\omega\epsilon_0 n^2 \mathbf{E} \\ \nabla \times \mathbf{E} = -i\omega\mu \mathbf{H} \end{cases} \quad (\text{i-2})$$

We consider each layer as a homogenous medium to carrier the electromagnetic waves, so the solutions of (i-2) can be presented as following:

$$\begin{cases} \mathbf{E}(\mathbf{x}, t) = \mathbf{E}_m(\mathbf{x})e^{-i(\omega t - \beta z)} \\ \mathbf{H}(\mathbf{x}, t) = \mathbf{H}_m(\mathbf{x})e^{-i(\omega t - \beta z)} \end{cases} \quad (\text{i-3})$$

where β is the z-component of the wave vector, is also considered as the propagation constant decided by wave equation, and $\mathbf{E}_m(\mathbf{x})$ and $\mathbf{H}_m(\mathbf{x})$ are electric- and magnetic- wave functions of the guiding modes, which can be decomposed by several plane waves of different order \mathbf{m} . We deduce (i-3) to obtain the wave equation represented by the electric-component:

$$\left(\frac{\partial^2}{\partial x^2} + \frac{\partial^2}{\partial y^2} \right) \mathbf{E}(\mathbf{x}, y) + [k_0^2 n^2 - \beta^2] \mathbf{E}(\mathbf{x}, y) = 0 \quad (\text{i-4})$$

where $k_0 = \omega/c_0$ is the wave number in vacuum. Considering the continuities of the wave functions at the upper and lower interface of the waveguide layer, TE modes consist of E_y , H_x and H_z components and can be calculated by (i-4) in anywhere of the layered structure. Here we analyse qualitatively the TE modes in such a layered waveguide structure by solving the (i-4). The wave function $\mathbf{E}_m(\mathbf{x})$ can be presented as follows:

$$E_m(x) = \begin{cases} C \left(\cos(h(x - t_2)) - \frac{q}{h} \sin(h(x - t_2)) \right) e^{px}, & -t_1 \leq x \leq 0 \\ C \left(\cos(h(x - t_2)) - \frac{q}{h} \sin(h(x - t_2)) \right), & 0 \leq x \leq t_2 \\ C e^{-q(x-t_2)}, & t_2 \leq x \leq t_3 \end{cases} \quad (\text{i-5})$$

where C is a normalized constant, and h, p and q can be written as:

$$\begin{cases} p = \sqrt{\beta^2 - n_1^2 k_0^2} \\ h = \sqrt{n_2^2 k_0^2 - \beta^2} \\ q = \sqrt{\beta^2 - n_3^2 k_0^2} \end{cases} \quad (\text{i-6})$$

i.2 Analysis of E-field distribution

As shown in Figure i.2, we consider the dependence of the solution to the (i-4) on different value intervals of the propagation constant dependent on the light wavelength. When $n_3 k_0 < \beta < n_1 k_0$, the E-field decays exponentially in the zone of $x > t_2$ and displays a modulated sinusoidal distribution in the zone $x < t_2$. So most of energy can be penetrated into the bottom-clad layer, we call this radiation mode shown in Figure i.1.(a).

When $n_1 k_0 < \beta < n_2 k_0$, in the cladding layer, the E-field decays exponentially but in the waveguide layer, it follows a sinusoidal distribution. We name these analytic TE modes by adding the subscript m corresponding to the number of solutions of the wave function. For example, in Figure i.2.(b) there are two possible TE modes that are the fundamental mode TE₀ and the first-order mode TE₁. Once we solve the propagation equation, we can totally describe this E-field distribution along the x -axis. So a confinement coefficient of each TE mode can be used to evaluate its efficiency of wave's guiding capacity, which is represented by the confinement coefficient. The definition of the 1D confinement coefficient is:

$$\eta_m(t_2) = \frac{\int_0^{t_2} E_m(x) dx}{\int_{-t_1}^{t_3} E_m(x) dx} \quad (\text{i-7})$$

where we suppose that t_2 is largely smaller than t_1 and t_3 in order to match the real physical model of such a core-cladding layered waveguide, and t_2 is the only one variable involved in the analysis of 1D TE modes.

In the last situation shown in Figure i.2.(c), when $\beta > n_2 k_0$, $E(x)$ displays in the whole space exponential distribution, that means at $x = +\infty$ the E-field decays to 0 and at $x = -\infty$ the energy is supposed to be infinite. So this case doesn't correspond to any meaningful physical wave.

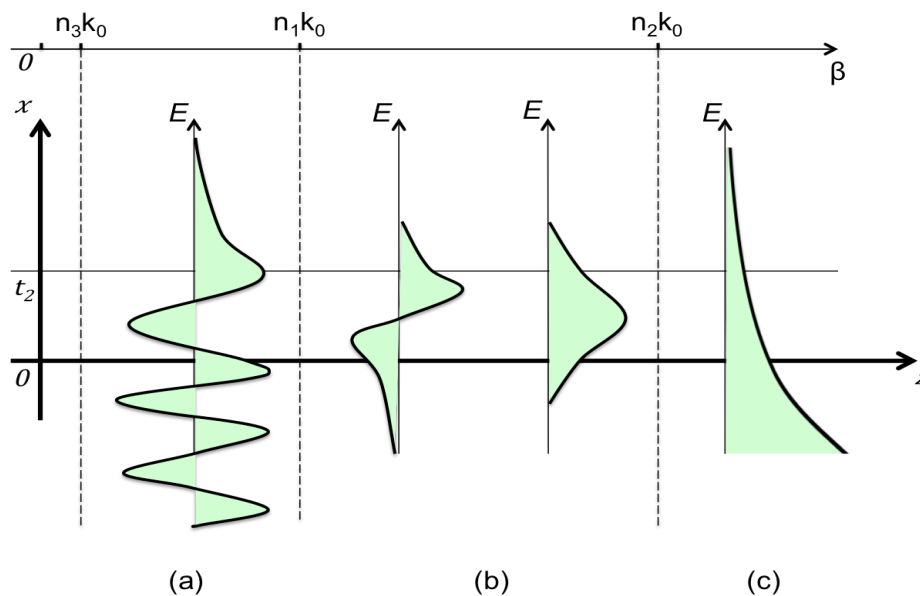


Figure i.2: Schematic of the electric field distributions in the x - z plan corresponding to different propagation constant: (a). radiation mode of cladding layer; (b). waveguide mode TE₀ and TE₁; (c). no physical meaning corresponding to an existed wave mode.

Considering the E_y and H_z 's continuities at the interface of $x = 0$ and $x = t_2$ as well as the partial derivatives of 1st degree of E_y , the Eigenvalue equations can be presented as follows:

$$\tan(ht_2) = \frac{p + q}{h(1 - pq/h^2)} \quad (\text{i-8})$$

According to this mode condition, we can obtain a finite number of propagative TE modes in such a layered waveguide. So the 1D effective index can be expressed by:

$$n_{eff}(t_2) = \beta(t_2)/k_0 \quad (\text{i-9})$$

RÉSUMÉ EN LANGUE FRANÇAISE

Le contexte industriel de cette thèse CIFRE est l'étude d'une structure d'éclairage surfacique à géométrie plane qui, associée à un système holographique 3D embarqué dans un véhicule, peut réaliser la fonction d'alarme de proximité. Le développement de cette structure d'éclairage surfacique répondra aux exigences de la reconstitution des images holographiques en 3D, qui nécessite une illumination par un faisceau cohérent, directionnel et uniforme. Ce type de système a été jusque-là réalisé par PSA Peugeot Citroën à base de composants optiques classiques comme des lentilles et des miroirs [FR2949725(A1)]. Le but de cette thèse est donc de proposer une solution plus compacte grâce à l'utilisation des (nano-) technologies d'intégration pour réaliser une émission cohérente, directionnelle et uniforme sur une grande surface à 633 nm en remplaçant les composants optiques volumineux par un circuit intégré photonique.

La thèse est divisée en 3 principales parties. Dans un premier temps, nous introduisons les applications des composants optiques et photoniques dans le domaine de l'automobile et décrivons la structure plane intégrée pour éclairer le système holographique visé. La deuxième partie porte sur les circuits intégrés photoniques à base des guides d'onde de nitrure de silicium. D'abord, nous introduisons les méthodes théoriques pour analyser les modes guidés et montrons les résultats de calcul des indices des modes 1D et 2D pour dimensionner un guide rectangulaire monomode (Chapitre II). Ensuite, nous détaillons les études théoriques et les travaux de simulation pour définir certains composants intégrés du circuit visé, comme le diviseur $1 \times N$ de faisceau et les guides d'onde courbes (Chapitre III). Enfin, nous présentons les travaux de fabrication en salle blanche des guides d'onde Si_3N_4 encapsulés dans le SiO_2 , précédemment conçus, et qui présentent une dimension autour de $250 \text{ nm} \times 300 \text{ nm}$, suivis de leur caractérisation à l'aide d'un banc d'optique guidée (Chapitre IV). La dernière partie est dédiée à l'étude théorique du couplage d'un mode photonique guidé à un mode plasmonique, qui est supporté par une chaîne de nanoparticules métalliques en Au ou en Ag déposée sur le guide d'onde Si_3N_4 (Chapitre V).

CHAPITRE I : INTRODUCTION GÉNÉRALE AU CONTEXTE ET À L'OBJECTIF DE LA RECHERCHE

I.1 Technologies optiques et photoniques dans l'automobile

Les composants optiques et photoniques ont été introduits dans le domaine de l'automobile dès 1880. Les phares se sont trouvés en avant de la voiture du fait de leurs fonctions d'illumination et de signalisation sur la route. Par la suite, beaucoup de travaux de développement des projecteurs de lumière ont été faits au niveau des matériaux et structures (i.e. : Halogène, Xénon, DEL et Laser) ainsi que leurs fonctionnalités (i.e. : lumières à l'extérieur, lumières à l'intérieur et systèmes d'assistance au conducteur avancés). Jusqu'à présent, les chercheurs et ingénieurs ont développé de nombreux composants optiques et photoniques avancés, qui peuvent être installés au sein d'un véhicule pour assister à la conduite sur la route et aussi pour rajouter de la valeur esthétique afin d'attirer les regards des consommateurs.

Par contre, il n'y a presque plus de place disponible pour rajouter des nouveaux systèmes optiques et photoniques à base de composants optiques classiques comme des lentilles et des miroirs à cause de leurs caractéristiques volumiques. Dans ce contexte, les technologies nanophotoniques permettent de nous amener de plus en plus d'opportunités pour que les circuits intégrés photoniques puissent être intégrés dans le design, les fonctionnalités et la fabrication des futures voitures. En effet les applications photoniques avancées seront le facteur le plus important pour la révolution technologique automobile qui compte trois priorités d'innovation: l'attractivité, les technologies propres et le véhicule autonome et connecté [BARAT]. Selon un rapport d'analyse de l'industrie, les systèmes d'assistance au conducteur avancés (ADAS) vont occuper environ un quart du marché des produits photoniques automobiles en 2018 et avoir une croissance la plus rapide par rapport aux autres applications [COCHA15]. Il y aura alors une énorme opportunité pour les technologies optiques et photoniques qui peuvent être utilisées au sein des systèmes ADAS.

I.2 Contexte de recherche de la thèse

I.2.1 Système holographique 3D embarqué

PSA Peugeot Citroën a développé un nouveau système holographique 3D, qui est installé dans le coffre arrière d'une voiture [FR2949725(A1)]. L'objectif de ce système d'alarme de

proximité est de générer des images holographiques prédéterminées, qui peuvent être donc visualisées par le chauffeur de la voiture suivante quand les deux voitures sont trop proches. Le principe de ce système est présenté dans la Fig.1. La reconstitution des images holographiques est réalisée par l'illumination d'une plaque holographique de manière cohérente, directionnelle et uniforme.

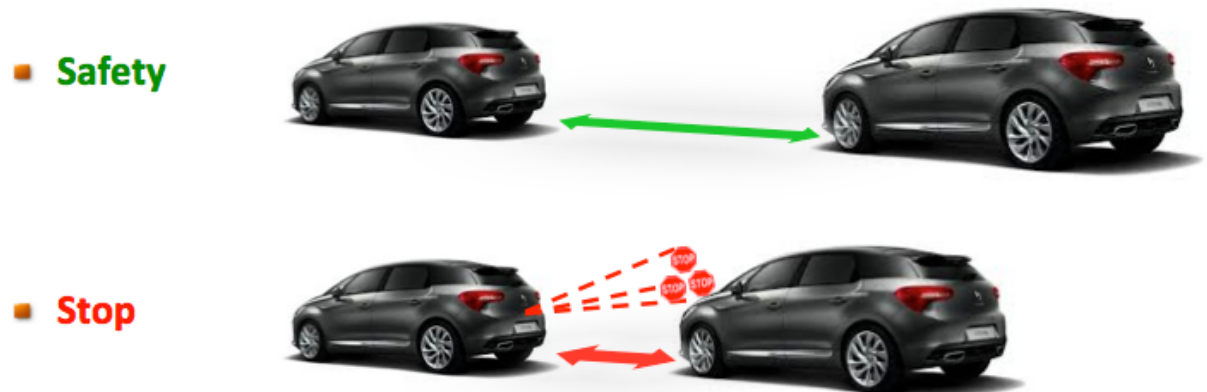


Fig.1: Schéma de principe du système de signalisation holographique développé par PSA Peugeot Citroën: (a). mode de sécurité : pas d'image holographique observée; (b). mode de danger: une image holographique « STOP » observée.

1.2.2 Reconstitution des images holographiques 3D

Le système d'illumination pour reconstituer les images holographiques se compose de composants optiques à base de verre, comme des lentilles cylindriques et miroirs. Comme la plaque holographique occupe une surface de 40 cm × 16 cm, le système total mesure environ 80 cm en raison de l'exigence d'expansion du faisceau d'une source ponctuelle à un large faisceau d'illumination qui peut couvrir toute la plaque holographique. Nous présentons un schéma du principe de la génération des faisceaux de reconstitution des images holographiques 3D dans la Fig.2.

Dans ce contexte, *Gonçalves et al.* ont proposé des solutions alternatives pour que le chemin d'optique du faisceau de reconstitution soit plié plusieurs fois en compressant le volume du système à l'aide de miroirs supplémentaires [FR3005011]. La longueur latérale du système est alors réduite effectivement jusqu'à une dizaine de centimètres. En revanche, nous visons à remplacer tous les composants optiques classiques (i.e.: miroirs et lentilles) par les circuits intégrés photoniques pour que tout le système d'illumination à géométrie surfacique

soit comprimé sur une puce planaire avec une épaisseur inférieure à 1 cm. Autrement dit, le but de cette thèse est d'étudier ce système d'illumination à géométrie surfacique ultra-compact à base de circuits intégrés photoniques.

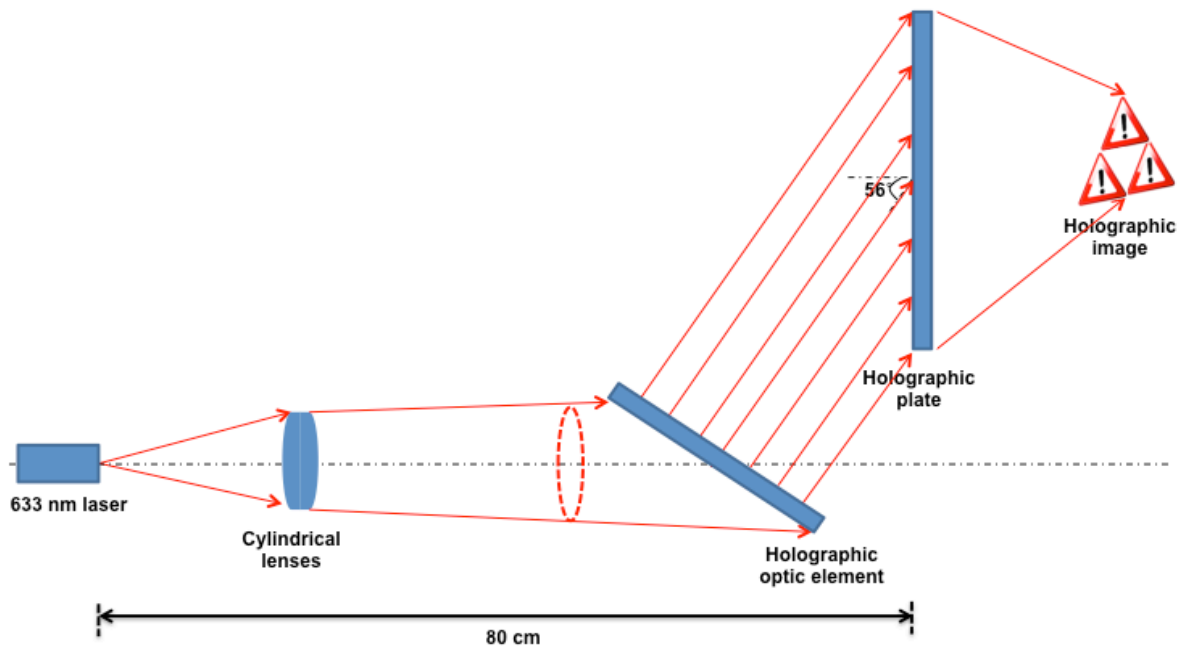


Fig.2: Schéma du système de reconstitution des images holographiques 3D réalisé par des composants optiques conventionnels.

1.3 Objectif et plan de recherche

Notre projet de recherche peut se diviser en 3 parties principales. Nous présentons dans la Fig.3 un schéma du système d'illumination visé et breveté [WO2014106584 (A1)]. Premièrement, le circuit intégré photonique est basé sur un réseau de 16 guides d'onde diélectriques, constitué par des diviseurs de faisceau (voir Fig.3.(a)). Deuxièmement, la lumière guidée dans le guide d'onde diélectrique est redirigée vers la surface par des émetteurs sous un angle précis (56° dans notre cas) et de manière cohérente et uniforme afin d'illuminer la plaque holographique (voir Fig.3.(b)). Troisièmement, des amplificateurs organiques situés entre les guides d'onde droits servent à compenser les pertes de propagation optiques dans les guides d'onde (voir Fig.3.(c)). Du fait des conditions de l'enregistrement des images holographiques 3D dans la plaque holographique, l'angle d'illumination est fixée à 56° (à 632.8 nm). D'autre part l'intensité optique pour la reconstitution holographique requise est de 16 W/m^2 en considérant la réglementation photométrique sur les feux STOP.

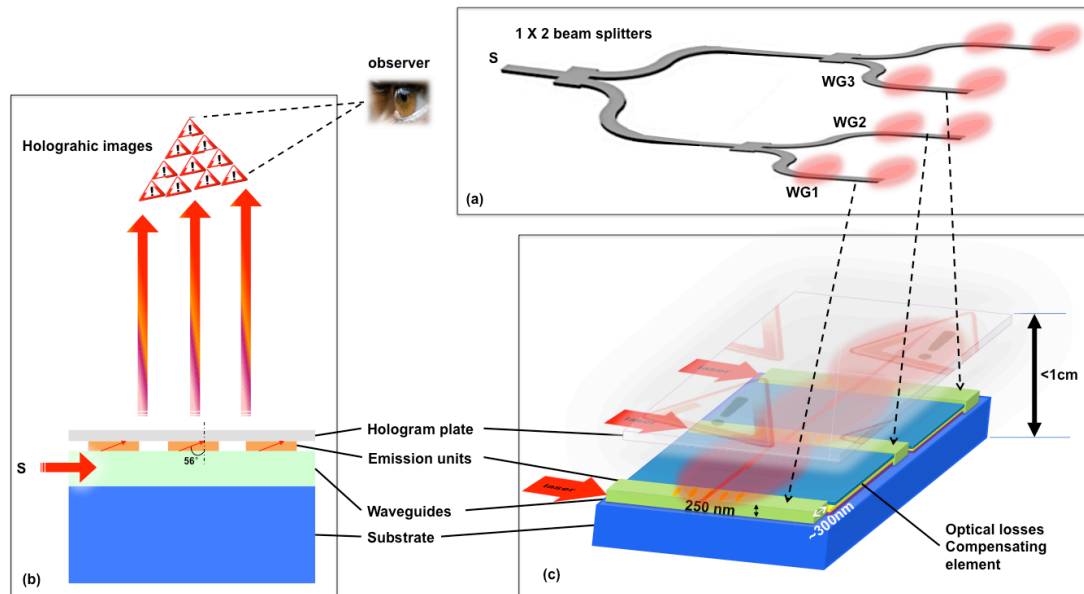


Fig.3: (a). Schéma du diviseur $1 \times N$ de faisceau et des émetteurs qui se trouvent au-dessus des guides d'onde. (b). Schéma du principe de la reconstitution des images holographiques 3D réalisé par l'illumination sur la plaquette holographique de manière cohérente, directionnelle et uniforme. (c). Schéma du système global d'illumination à géométrie surfacique visé.

CHAPITRE II : INTRODUCTION AUX GUIDES D'ONDE DE NITRURE DE SILICIUM

II.1 Contexte de la photonique silicium

Les circuits intégrés photoniques (PIC) à base de silicium ont fait l'objet de nombreuses recherches au cours de la dernière décennie. En effet, ces structures, transparentes aux longueurs d'onde de la gamme $1,3 \mu\text{m}$ - $1,6 \mu\text{m}$ sont particulièrement adaptées aux réseaux de télécommunications à base de fibre optique, et permettent d'intégrer des guides d'ondes à faibles pertes, des coupleurs et diviseurs du faisceau, des lignes à retard, déphaseurs, cavités à haut facteur de qualité etc. En revanche, l'oxyde (dioxyde) de silicium et le nitrure de silicium attirent de plus en plus l'attention d'aujourd'hui du fait de leurs propriétés optiques dans le visible, comme la transparence et la faible non-linéarité. Par exemple, le guide d'onde en nitrure de silicium encapsulé dans la silice permet de propager de manière efficace les ondes optiques dans la gamme du visible et du proche infrarouge. Dans un contexte de l'application automobile autour de la longueur d'onde de 633 nm , nous avons choisi le Si_3N_4 comme matériau pour fabriquer des guides d'onde et aussi des composants intégrés passifs.

II.2 Applications des PICs dans le visible

Le développement des PICs pour l'application du visible est beaucoup moins avancé que celui du domaine des télécoms. D'abord, la résolution de fabrication des composants intégrés en salle blanche à base de la lithographie optique conventionnelle est limitée à l'échelle au-dessus du micron [KLEIN70]. Il est donc nécessaire de recourir à la lithographie électronique pour les PICs visibles. D'autre part, il n'y a pas eu, jusqu'à présent, autant de demandes industrielles de réalisation de PICs dans le domaine visible que dans le domaine de proche infrarouge (de 1,3 μm à 1,6 μm) qui s'adapte particulièrement aux systèmes de fibre optique.

II.2.1 Guides d'onde 1D en Si_3N_4

Les premiers guides d'onde en nitrure de silicium encapsulé dans la silice proposés dans la littérature étaient 1D. Le dépôt des couches diélectriques peut être réalisé par des techniques matures, comme la PECVD et la LPCVD [IRENE77, STUTI77, SRIRA83].

II.2.2 Guides d'onde 2D en Si_3N_4

Grâce au développement des techniques de gravure, des guides d'onde 2D ont été ensuite réalisés et caractérisés [HENRY87, DALDO04b]. Les pertes de propagation mesurées à la longueur d'onde visible dépendent fortement des tailles du profil des guides ainsi que des techniques de gravure. L'encapsulation dans un autre matériau homogène comme la silice et l'optimisation de la rugosité des parois latérales ont été recommandées pour diminuer l'effet dû aux diffusions de Rayleigh. En particulier, le guide d'onde 2D du type de *Canal* gravé par plasma présente la meilleure performance de propagation. Les modes TE ont des pertes de propagation linéaires toujours plus faibles que les modes TM. D'ailleurs, quand l'ordre du mode guidé est élevé, le mode est moins confiné dans le guide. Par conséquent, le coefficient des pertes de propagation est plus grand. Autrement dit, la rugosité latérale devient un facteur très important quand les dimensions du profil des guides d'onde 2D sont plus petites que la longueur d'onde d'opération.

II.3 État de l'art sur les guides d'onde monomode en Si_3N_4

Subramanian et al. ont réussi à fabriquer les guides d'onde rectangulaires en Si_3N_4 avec une épaisseur fixée de 200 nm et des largeurs variées de 300 nm à 1 μm à l'aide de la photolithographique à 193 nm et la gravure ICP-RIE [SUBRA13]. Les pertes de propagation ont été

mesurées par la technique *cutback* dans les domaines visible et proche infrarouge (532 nm, 780 nm et 900 nm) sur les échantillons encapsulés et exposés dans l'air. En fait, le processus de la planarisation par la silice va améliorer la performance de propagation. En même temps, les pertes de propagation linéaires peuvent augmenter rapidement quand la largeur du guide d'onde diminue progressivement (voir Fig.4). En outre, la largeur de coupure du mode fondamental dépend fortement de la longueur d'onde d'opération. Finalement, ces guides d'onde monomodes en Si_3N_4 présentent des pertes de propagation linéaires de l'ordre de 1.5 dB/cm avec une dimension de $200 \text{ nm} \times 300 \text{ nm}$. En réalité, la mesure du type *cut-back* n'est pas assez précise, puisque les barres des erreurs restent très variées. En conclusion, ces résultats expérimentaux permettent de montrer la faisabilité de fabrication des guides d'onde 2D monomode à la longueur d'onde visible avec des faibles pertes.

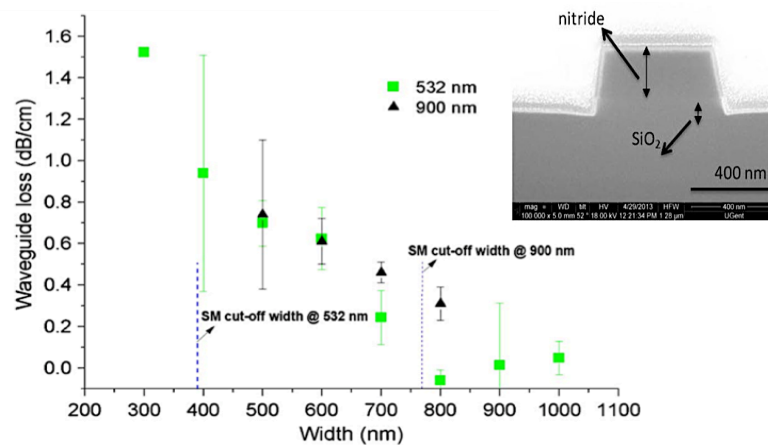


Fig.4: Pertes de propagation linéaires à 532 nm et 900 nm mesurées dans un guide d'onde 2D en Si_3N_4 encapsulé dans la silice en fonction de la largeur du guide.

CHAPITRE III : CONCEPTION ET SIMULATION DES GUIDES D'ONDE DE NITRURE DE SILICIUM

III.1 Dimensionnement du profil de guides d'onde

D'abord, nous évaluons les modes transversaux TE et TM d'un guide d'onde rectangulaire en Si_3N_4 encapsulé dans du SiO_2 . L'objectif est de dimensionner le profil du guide d'onde Si_3N_4 en respectant la condition monomode à 633 nm ainsi que maximisant le confinement du mode fondamental TE. Dans notre cas, le mode TE_{00} est préféré à TM_{00} pour qu'il puisse favoriser le couplage au mode plasmonique dans la chaîne de nanoparticules métalliques (voir chapitre

V). En même temps, le dimensionnement du guide d'onde doit être optimisé en considérant la capacité de fabrication en salle blanche.

La méthode la plus efficace pour évaluer approximativement des modes transversaux dans un guide d'onde diélectrique lamellaire est à base du calcul de l'indice effectif [YARIV06]. La valeur de l'indice effectif nous permet aussi d'étudier quantitativement la propagation du mode guidé en fonction de dimensions géométriques du guide d'onde. Selon la méthode de l'indice effectif (EIM), nous pouvons analyser pratiquement les modes guidés dans un guide d'onde rectangulaire. D'abord, nous divisons horizontalement et puis verticalement la structure du guide d'onde en plusieurs zones d'indice optique. Le schéma du guide d'onde en Si_3N_4 encapsulé dans SiO_2 est présenté dans la Fig.5.(a). Dans un premier temps, l'indice effectif de la structure lamellaire n_{eff1D} peut être calculé en fonction de son épaisseur t_2 , en déduisant l'équation de valeur propre de modes guidés TE et TM confinés par les deux couches de SiO_2 au-dessus et au-dessous de Si_3N_4 . En suite, la répartition de zones d'indice est effectuée latéralement en supposant que les deux zones à côté du guide d'onde de Si_3N_4 ont le même indice ($n_3 = n_1 = n_{\text{SiO}_2}$) et celle au milieu a l'indice effectif prédéterminé ($n_{\text{II}} = n_{\text{eff1D}}$). Étant donnée que seule la composante électrique avec une direction de polarisation parallèle à l'axe y est non-nulle, nous présentons en Fig.5.(b) la distribution du champ E_y du mode TE_{00} dans un guide d'onde de $250 \text{ nm} \times 300 \text{ nm}$ calculé par un logiciel de simulation utilisant un algorithme vectoriel.

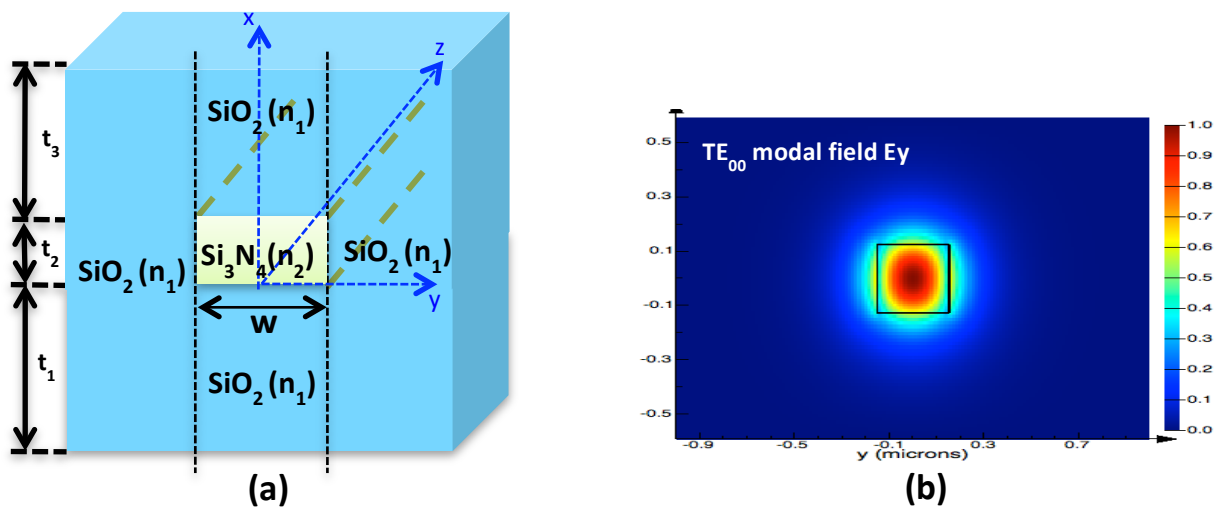


Fig.5 :(a). Schéma du principe de la méthode de l'indice effectif appliquée sur un guide d'onde en Si_3N_4 encapsulé dans SiO_2 ; (b). Profil du composant E_y du mode TE_{00} dans un guide d'onde de $250 \text{ nm} \times 300 \text{ nm}$.

Nous comparons le résultat de l'indice effectif des modes guidés aux dimensions du profil des guides d'onde calculé par l'EIM (présenté par trait plein et en ligne pointillée) et ceux obtenu par le logiciel de simulation vectorielle (présenté par rond et carré) sur la Fig.6. En fait, nous devons limiter l'épaisseur t_2 inférieure à 250 nm et la largeur w inférieure à 300 nm pour que le guide d'onde rectangulaire reste monomode. En suite, nous avons calculé le coefficient de confinement par l'EIM, qui permet de présenter quantitativement le confinement des modes guidés dans le Si_3N_4 . Il est défini en fonction de l'épaisseur t_2 et de la largeur w par la formule suivante:

$$\eta_{mn}(t_2, w) = \frac{\int_0^{t_2} E_m(x) dx \int_{-\frac{w}{2}}^{\frac{w}{2}} E_n(y) dy}{\int_{-t_1}^{t_3} E_m(x) dx \int_{-\infty}^{\infty} E_n(y) dy} \quad (1)$$

avec m l'ordre du mode transversal confiné verticalement et n l'ordre du mode confiné horizontalement. Dans le cas préféré (avec un profil de 250 nm × 300 nm), le confinement du mode TE_{00} est environs 80%. Par contre, nous pouvons encore agrandir w jusqu'à par exemple 400 nm, car les modes parasites à l'ordre plus élevés ne sont pas confinés de manière efficace.

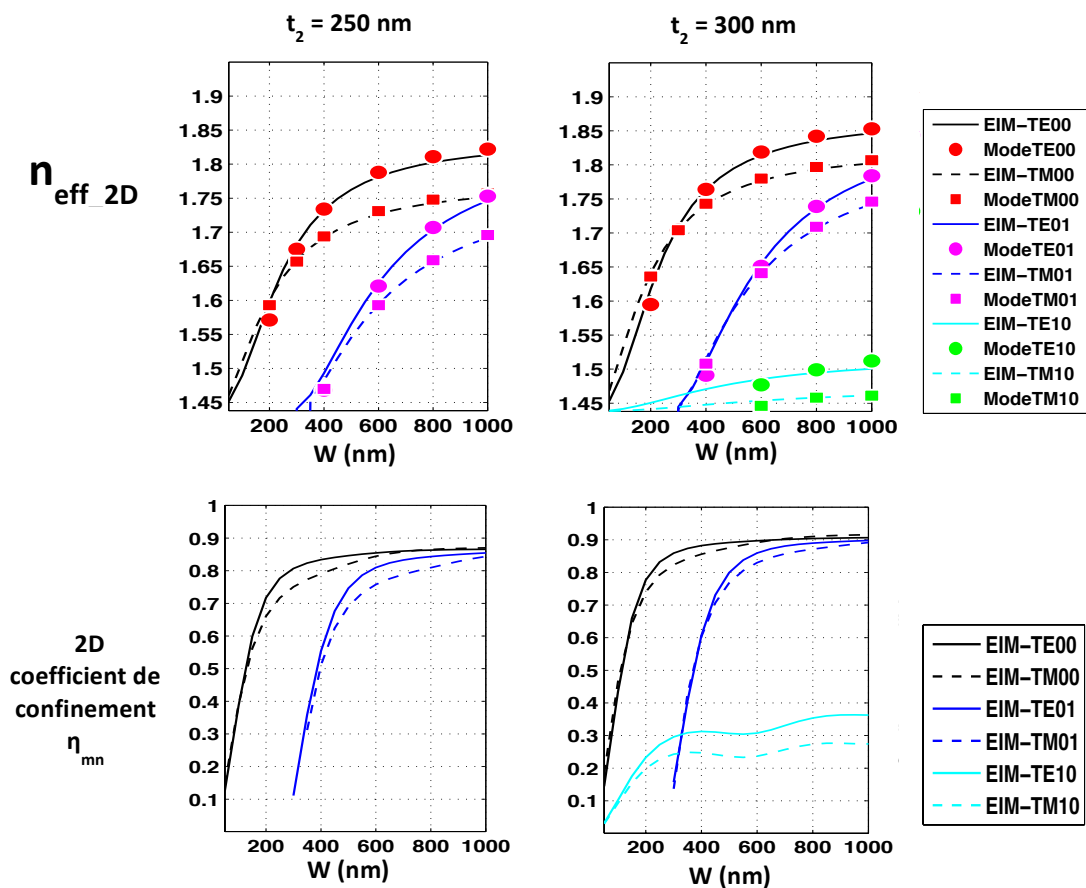


Fig.6 : Résultats du calcul EIM des indices effectifs des guides d'onde avec différentes largeurs et épaisseurs.

III.2 Design des diviseurs de faisceau et guides d'onde courbés

Afin de répartir la lumière visible (à 633 nm) en plusieurs guides d'onde de manière uniforme en amplitude et en phase, nous avons étudié des coupleurs d'interférence multimode (MMI). Nous présentons dans la Fig.7 le cas le plus simple, c'est-à-dire un coupleur MMI avec une seule entrée et deux sorties identiques. Nous calculons d'abord les valeurs initiales de ce type de coupleur MMI, surtout la longueur de MMI L_m en fonction de sa largeur W_m à l'aide des formules du dimensionnement de coupleur MMI symétrique proposé par *Soldano et al.* [SOLDA95].

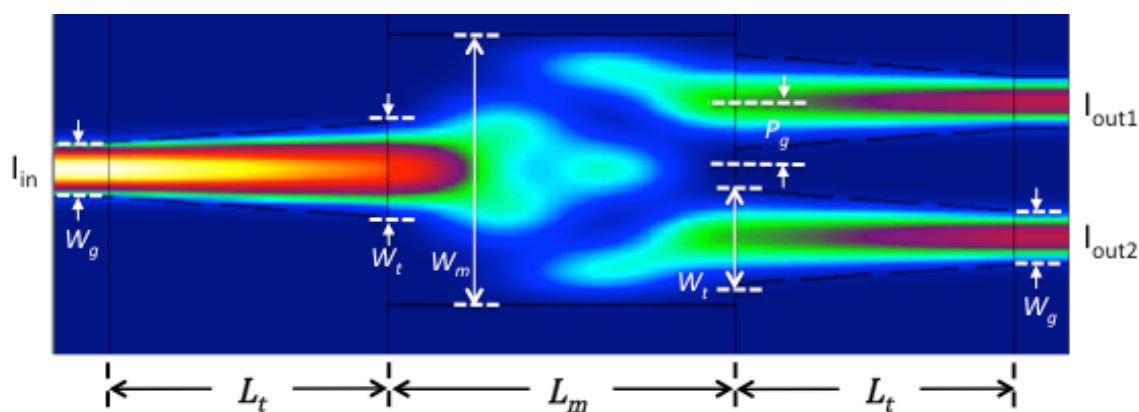


Fig.7 : Dimensionnement d'un diviseur 1×2 à base d'un coupleur MMI avec des tapers.

Ensuite, nous utilisons un logiciel de simulation du type 2D+z pour évaluer les performances de propagation en considérant les pertes excessives et la non-uniformité définies par les expressions suivantes :

$$\text{pertes excessives (EL)} = -10 \log_{10} \left(\frac{\sum_{i=1}^N I_i}{I_{in}} \right) \quad (2)$$

$$\text{non uniformité (NU)} = 10 \log_{10} \left(\frac{I_{max}}{I_{min}} \right) \quad (3)$$

avec I_i l'intensité optique du faisceau dans le $i^{\text{ème}}$ guide d'onde divisé, et I_{min} et I_{max} respectivement l'intensité minimale et maximale parmi tous les guides d'onde divisés. L'objectif de la conception assistée par la simulation FIMMPROP est d'optimiser le dimensionnement de diviseurs conçus à base de coupleur MMI en diminuant ces deux paramètres de simulation le plus possible.

III.2.1 Diviseur de faisceau 1 × 2

Nous arrivons à diminuer les pertes du diviseur de faisceau jusqu'à 0,11 dB en ajustant les dimensions du MMI et des tapers (voir Fig.7). La configuration optimale du design de ce diviseur élémentaire est présentée au Tab.1. D'autres types de diviseur 1 × 2 sont aussi étudiés dans la thèse, comme le MMI parabolique [LEVY98, WEI01], la Y-branche [WANG02] et le coupleur en étoile [KOSTE04, RASIG10]. Finalement, la conception comme présentée dans la Fig.7 devrait faciliter la fabrication et aussi rendre le composant plus stable.

Tab.1 : Configuration du diviseur de faisceau 1 × 2 à base du coupleur MMI et des tapers correspondant à la Fig.7.

	W_m	L_m	P_g	W_g	W_t	L_t	EL
Initial	4 μm	6.51 μm	0.54 μm	0.3 μm	--	--	1.39 dB
Optimal	4 μm	6.2 μm	0.5 μm	0.4 μm	2.11 μm	6.51 μm	0.11 dB

III.2.2 Diviseur de faisceau 1 × 4

Nous proposons ensuite deux solutions indépendantes pour réaliser un diviseur avec un nombre de sorties 1×2^N , par exemple $N = 2$. La première conception est à base du montage en cascade présenté dans la Fig.8.(a). Il y a 3 coupleurs MMI 1 × 2 au total et deux sections des guides d'onde courbés. Les pertes excessives optimales égalent donc $3 \times 0,11$ dB plus les pertes de courbure. D'un autre côté, nous présentons un MMI coupleur 1 × 4 direct avec des tapers. Dans ce cas optimal, les pertes en excès sont d'environ 0,51 dB et la non-uniformité est 0,33 dB. Suite à ces résultats de simulation, nous pensons que le design en cascade a des avantages. D'abord, il y a plus de flexibilité pour la disposition globale des composants. En outre, la non-uniformité peut être complètement négligée grâce à la symétrie par rapport à la ligne centrale.

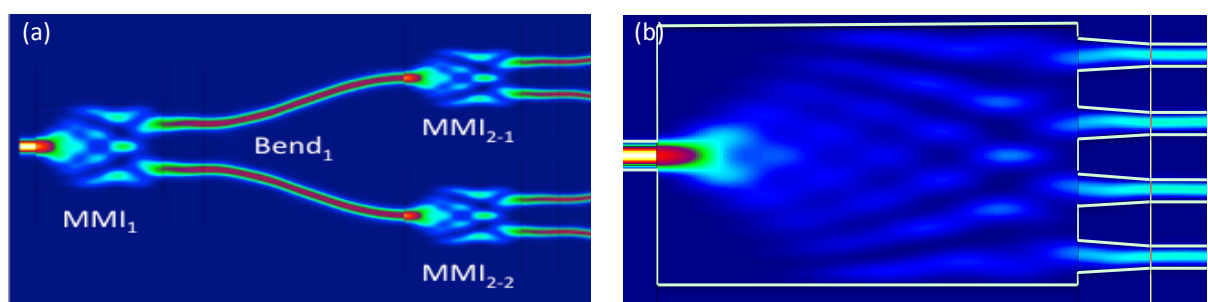


Fig.8 : Schéma des diviseurs de faisceau 1 × 4 : (a). Design en cascade ; (b). MMI coupleur 1 × 4.

III.2.3 Design des guides d'onde courbés

Comme nous choisissons le design en cascade pour réaliser un diviseur de faisceau 1×16 , la conception et l'évaluation des pertes de radiations liées aux guides d'onde courbés sont très importantes pour optimiser le design global au niveau de la taille de dispositif et de la performance de propagation optique. Nous étudions d'abord un type de courbes progressives usuel, la fonction S dont le rayon de courbure varie progressivement en fonction de sa coordonnée cartésienne horizontale. Nous présentons dans la Fig.9 une illustration schématique de la propagation de lumière guidée dans ce genre du guide d'onde courbé.

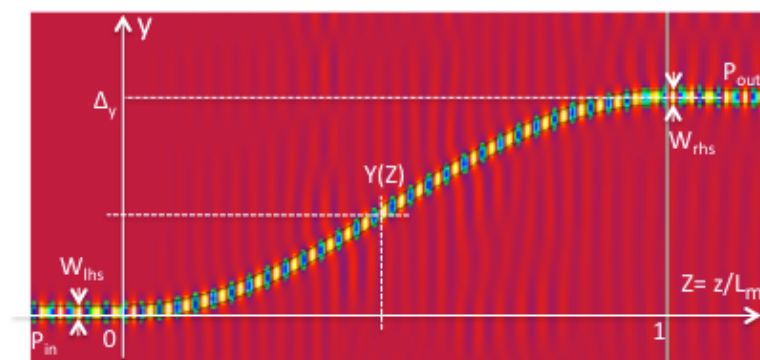


Fig.9 : Propagation de lumière guidée dans un guide d'onde courbé à base de fonction S.

Nous étudions un autre type de courbe progressive, la lemniscate qui a été décrite par *Bernoulli* en 1694. Une paire de lemniscates fractionnelles peut constituer un guide d'onde courbé complet, avec point d'inflexion. Nous présentons un exemple de guide courbé à base de lemniscate en Fig.10.

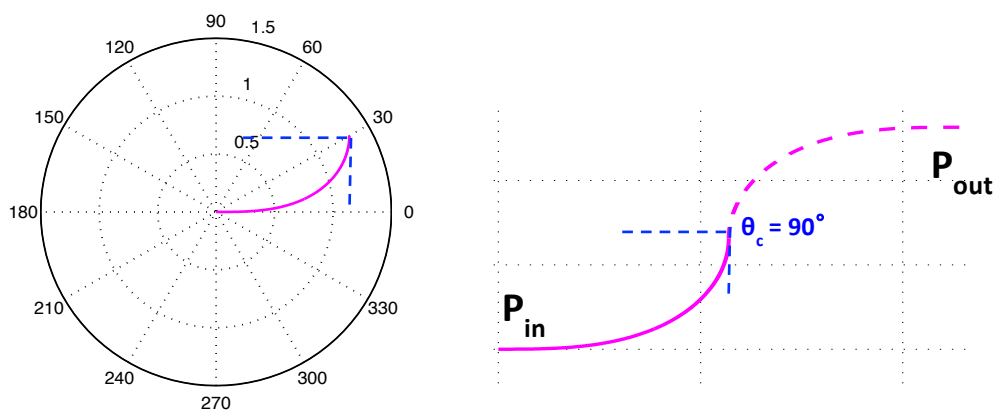


Fig.10 : Schéma de courbes progressives à base d'une lemniscate fractionnelle du type sinusoidal.

En fait, la lemniscate ne peut s'exprimer qu'en coordonnées polaires ou par des équations paramétriques. Dans notre cas, nous préférons étudier l'évolution de la trajectoire et du rayon de courbure de la lemniscate à l'aide des équations paramétriques. De toutes façons, nous pouvons analyser quantitativement les deux types de courbes progressives, y compris leurs trajectoires et rayons de courbures qui détermineront alors la taille et les pertes de courbure des guides d'onde. Nous pouvons donc étudier la transmission de propagation dans la section courbée, qui est dédiée au calcul de pertes de courbures. Par exemple, nous avons l'expression de la transmission liée à la courbe du type fonction S :

$$T = \frac{P_{out}}{P_{in}} = e^{-\int_{z_1}^{z_2} \alpha_c(z) \left(\frac{ds}{dz}\right) dz} \quad (4)$$

avec un paramètre curvilinéaire s et un coefficient de pertes de courbure α_c , qui évolue aussi en fonction de son déplacement sur le trajectoire courbé. Par conséquent, les pertes accumulées dues au guide d'onde courbé peuvent être calculées dès que nous sommes capable de formaliser ce coefficient α_c .

III.2.4 Évaluation des guides d'onde courbés

Nous utilisons la théorie de *Marcatili* pour modéliser approximativement une section des guides d'onde courbés avec un profil rectangulaire dont la taille est constante. Cette méthode est basé sur l'analyse modal TE ou TM dans un guide d'onde diélectrique 2D [MARCA69b]. Le principe d'analyse du mode TE_{00} est présenté dans la Fig.11.

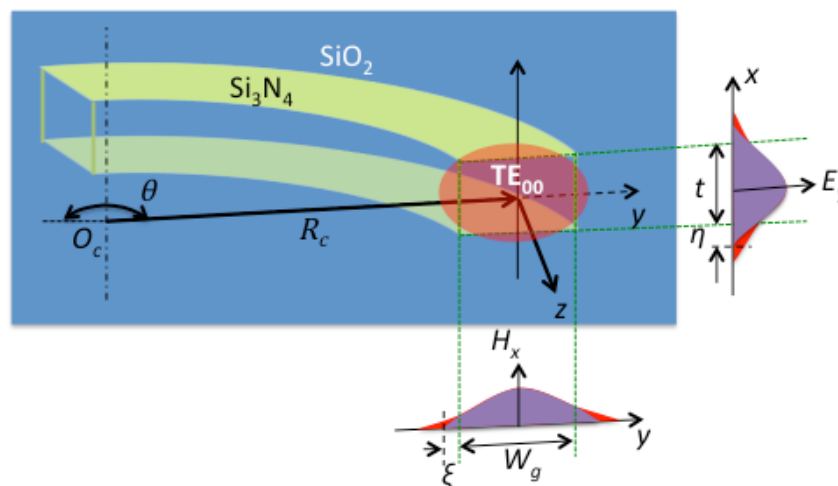


Fig.11 : Schéma de l'analyse modal 2D à base de la théorie de Marcatilli pour évaluer les pertes de courbure du guide d'onde rectangulaire 2D.

D'après *Marcatilli*, le coefficient de pertes de propagation du guide d'onde courbé s'exprime en fonction du rayon de courbure dans l'expression suivante:

$$\alpha(R_c) = C_1 \exp(-C_2(R_c)R_c) \quad (3)$$

avec deux constantes C_1 et C_2 qui dépendent fortement des dimensions et des indices du guide d'onde. En particulier, C_2 évolue aussi en fonction du rayon de courbure et donc progressivement sur la trajectoire. Nous considérons ici un guide d'onde monomode en Si_3N_4 encapsulé dans la SiO_2 . Par ailleurs, on suppose que le rayon de courbure est beaucoup plus grand que la distance de pénétration ξ and η .

Nous comparons les deux types des guides d'onde courbés. En fait, nous fixons le point au départ et le point final avec un décalage vertical de $50 \mu\text{m}$. Et même temps, nous varions l'angle tangente ($\theta_c = 60^\circ, 90^\circ$ et 180°) au point d'inflexion dans le cas des lemniscates pour générer trois trajectoires avec différents longueurs. En suite, nous traçons aussi trois courbes du type de fonction S qui ont les mêmes points de départ et d'arrivée que les lemniscates. Les trajectoires de différentes courbes mentionnées sont présentées dans la Fig. 12.

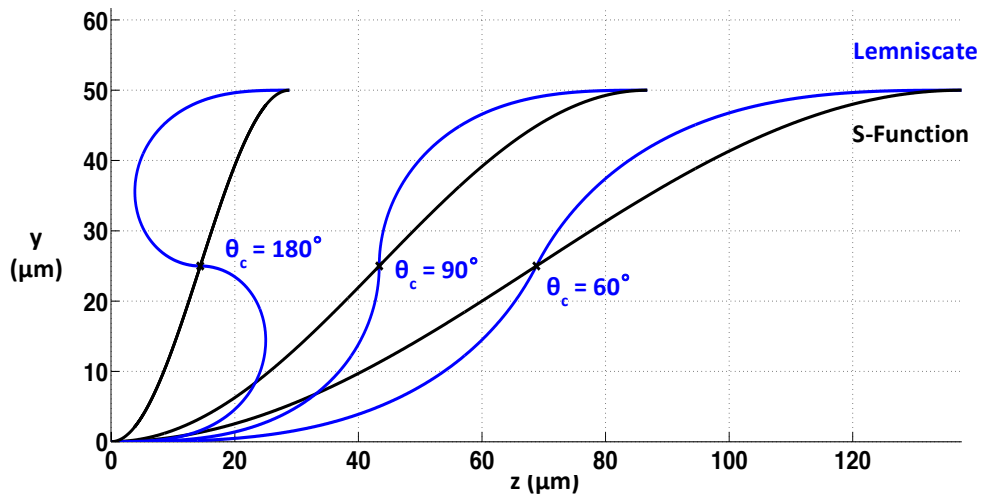
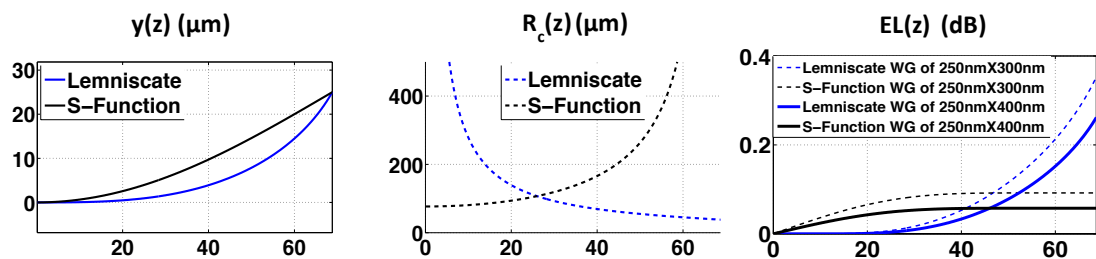


Fig.12 : Trajectoire des courbes lemniscate et du type fonction S.

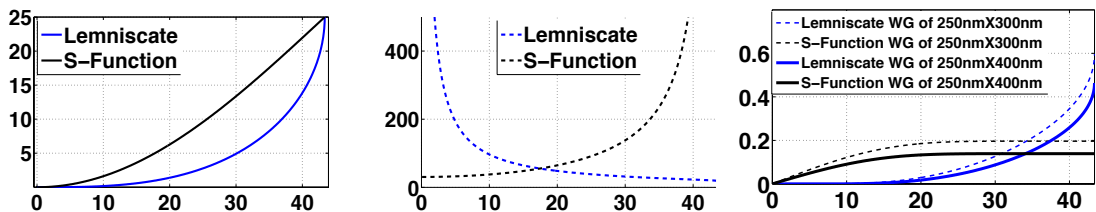
Pour simplifier l'évaluation des pertes de courbure accumulées dans les guides d'onde courbés, nous ne calculons que les pertes accumulées sur la première moitié de trajectoire complète en supposant que la valeur soit doublée pour toute la section courbée. Les résultats du calcul sont présentés dans la Fig.13. En conclusion, plus l'angle tangent au point d'inflexion est grand, plus le guide d'onde courbé est compact, plus les pertes de courbure

sont accumulées. C'est à dire que l'évolution des rayons de courbure minimaux influe beaucoup sur le coefficient de pertes de courbure. Par conséquent, les pertes de propagation accumulées deviennent très importantes si le rayon est assez petit. Par contre, une différence apparait sur l'évolution de pertes accumulées entre la lemniscate et la fonction S. Comme la fonction S a toujours son rayon minimal au début de trajectoire, les pertes de courbure augmentent rapidement et atteint une valeur saturée lorsque la propagation atteint environ un tiers de la demi-trajectoire. Au contraire, les pertes dues aux courbes des lemniscates augmentent rapidement seulement dans le dernier tiers de propagation. Finalement, nous proposons la conception d'une courbe combinant le premier tiers de la lemniscate et le dernier tiers de la fonction S qui permet de profiter des avantages des deux courbes au niveau de l'évolution des rayons de courbure et donc des pertes accumulées.

$\theta_c = 60^\circ$



$\theta_c = 90^\circ$



$\theta_c = 180^\circ$

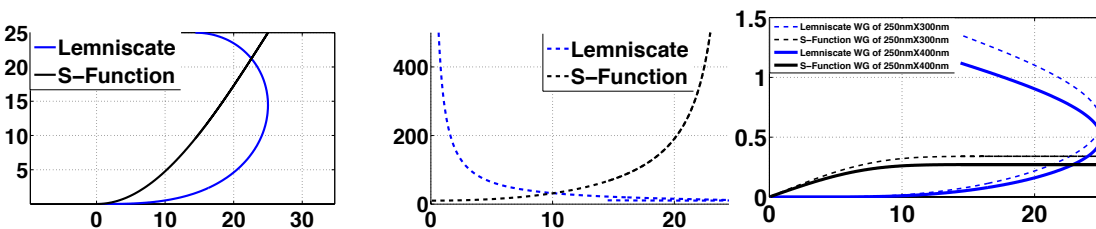


Fig.13 : Évolution des trajectoires, des rayons de courbure et des pertes de propagation accumulées dues aux différentes courbes sur la première moitié des guides d'onde courbés.

CHAPITRE IV : FABRICATION ET CARACTERISATION DES GUIDES D'ONDE DE Si_3N_4

IV.1 Procédé de fabrication en salle blanche

La fabrication des échantillons de guides d'onde est effectuée en salle blanche à la Centrale de Technologie Universitaire (CTU) IEF-MINERVE. Le schéma du procédé de fabrication est présenté Fig.14.

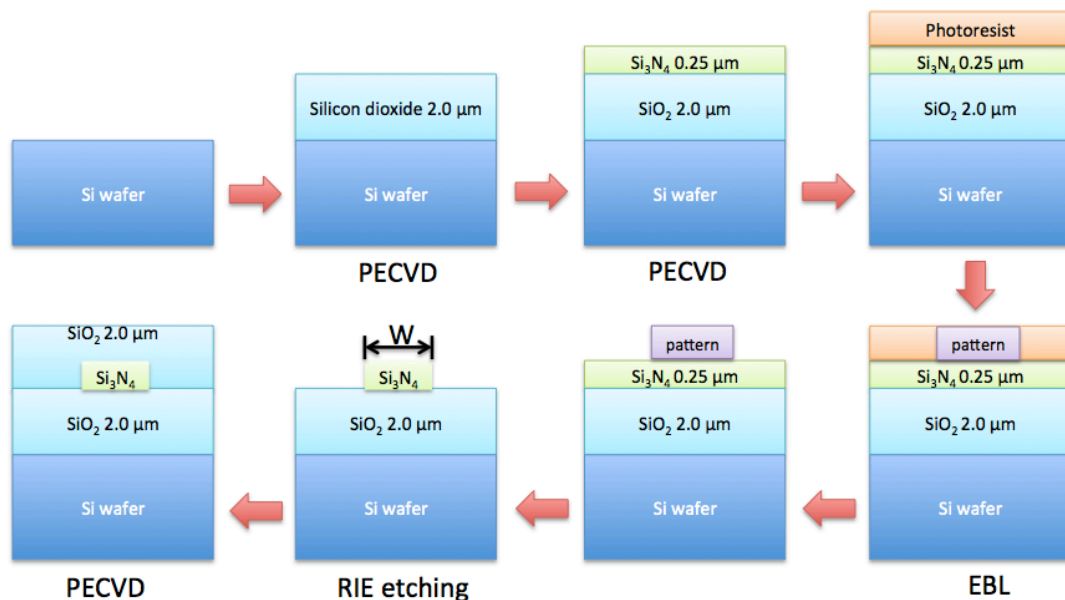


Fig.14: Schéma du procédé de fabrication des guides d'onde en Si_3N_4 encapsulés dans du SiO_2 .

IV.1.1 Dépôt des diélectriques

Le dépôt des couches minces diélectriques est réalisé en PECVD à basse fréquence sur un substrat du silicium de 4 pouces. Pour la formation des couches de nitrure dioxyde de $2\ \mu\text{m}$, nous utilisons des gaz de SiH_4 et N_2O . En revanche, ce processus peut introduire des impuretés parasites d'hydrogène provenant du silane précurseur. Ensuite, nous générons la couche de nitrure de silicium de $250\ \text{nm}$ par SiH_4 et NH_3 . Pendant cette réaction chimique, la composition des éléments Si et N n'est pas aussi précise que les indices de Si_3N_4 . En même temps, les échantillons déposés peuvent aussi contenir des impuretés d'hydrogène. Dans ce cas, un recuit supplémentaire à haute température est recommandé pour enlever une partie des gaz piégés [GONDA10].

IV.1.2 Lithographie

La lithographie à faisceau d'électrons (ou lithographie e-beam) est une étape importante dans le processus de fabrication car elle détermine la résolution des dimensions géométriques des guides d'onde et des composants intégrés visés. D'abord, un processus de nettoyage des échantillons de Si_3N_4 doit être fait à l'aide de plasma d'oxygène et de solutions d'acétone et d'alcool isopropylique. Nous enrésinons par la suite avec une couche de la résine négative MaN-2403 pour faire la lithographie. En fait, pour renforcer la force d'adhésion entre la surface de Si_3N_4 et la résine organique, nous rajoutons une couche de promoteur HMDS Prime au-dessous. En suite, pour éviter l'effet de charge à l'intérieur de la résine, nous enrésinons une couche de E-spacer 300Z au-dessus. Nous présentons d'ici la problématique due à la lithographie e-beam effectuée par la machine de Nanobeam NB4. Au début de notre test de dose de la lithographie e-beam, des décalages et discontinuités (voir la Fig.15) au long du guide d'onde visé ont été observés au microscope électronique à balayage (MEB) après la révélation de la résine lithographique et le dépôt d'une couche mince d'or.



Fig.15 : Problématique de la fabrication des échantillons des guides d'onde due à la lithographie.

En outre, des ondulations le long des bords de la résine sont aussi observées au MEB. Autrement dit, la rugosité latérale due au procédé d'écriture par défaut du système NB4 doit aussi être pris en compte pour diminuer l'effet de diffusion de Rayleigh. Finalement, une série de processus d'optimisation liés à la lithographie e-beam est effectuée, portant sur les tests de résine déposée en spin-coating, les doses d'exposition d'e-beam, et le « step-size » d'écriture du « sub-field ». Nous présentons des photos MEB des profils de résine des guides d'onde rectangulaires avec une épaisseur fixée à environ 250 nm. Typiquement, le meilleur cas correspond à une dose d'exposition autour de $4\text{-}5 \text{ C/m}^2$. Plus le « step-size » du « sub-field » d'écriture est petit, plus le profil de résine est en mesure d'avoir les bonnes verticalité et rugosité latérale.

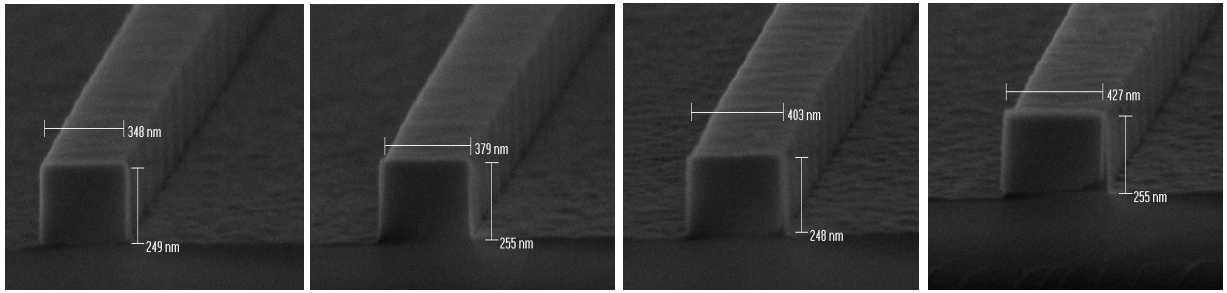


Fig.16 : Photos du MEB des profils de résines révélées à base de la lithographie des guides d'onde droits avec un « step-size » $s = 5 \text{ nm}$ et une dose d'exposition $D = 4.5 \text{ C/m}^2$ en variant la largeur du motif de guides d'onde.

IV.1.3 Gravure

La gravure assistée par ions réactifs (ou RIE abréviation pour *Reactive ion etching*) est utilisée dans notre cas pour transférer le motif de guides d'onde rectangulaires en résine dans le Si_3N_4 . L'avantage de la RIE est de générer un environnement de gaz de gravure isotrope. Donc la gravure se produit grâce aux réactions chimiques et attaques physiques entre les gaz de gravure CF_4 et CHF_3 et la couche de Si_3N_4 . Nous présentons dans la Fig.17 des photos MEB des profils de guides d'onde gravés par la RIE optimisée. En fait, nous pouvons contrôler pratiquement la largeur des guides d'onde en modifiant les dimensions des motifs car la gravure RIE optimisée consomme quasiment la même quantité de Si_3N_4 .

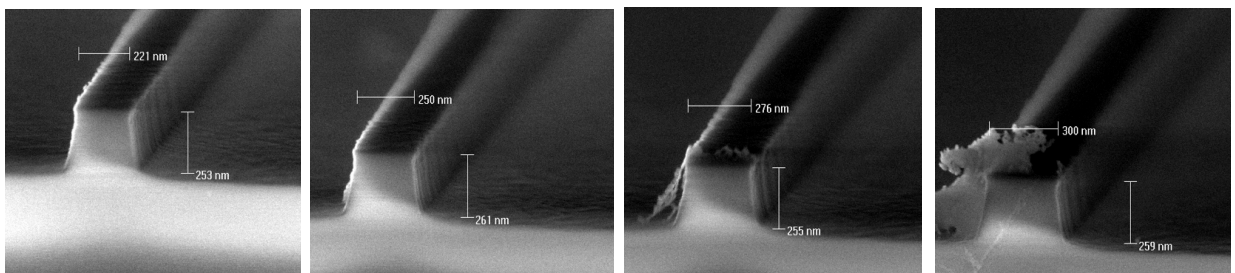


Fig.17 : Photos MEB des profils des guides d'onde gravés par RIE (échantillons présentés dans la Fig.16).

IV.2 Caractérisation d'échantillons à l'aide du banc optique

IV.2.1 Banc de caractérisation

Comme nous nous intéressons plutôt au mode transversal TE_{00} en raison du couplage efficace avec la chaîne de nanoparticule plasmonique, nous initialisons l'état de polarisation du banc

de caractérisation optique au mode TE à l'aide des polariseurs avant de tester la performance de propagation optiques des guides d'onde. Nous mettons en place aussi une série des dispositifs optiques pour aligner et puis calibrer le chemin d'optique à tester des échantillons fabriqués. La source lumière utilisée est basée sur une diode laser à 635 nm qui fonctionne à la température ambiante (25°C) et est polarisée par un courant de 80 mA. En revanche, le spectre de sortie de cette diode laser n'est pas très stable et étroit.

Nous utilisons une paire de fibres optiques micro-lentillées avec l'état de polarisation maintenu pour coupler la lumière TE₀₀ à 635 nm dans les échantillons de guides d'onde. Nous faisons la mesure des spectres optiques de transmissions fibre-à-fibre pour déterminer les pertes de propagation linéaires liées aux guides d'onde droits fabriqués. Un schéma du banc de mesure optique est présenté dans la Fig.18. Un support optique peut être bougé manuellement sur les trois axes avec une précision submicronique pour aligner le chemin d'optique guidé dans le guide d'onde rectangulaire de Si₃N₄ recouvert par SiO₂.

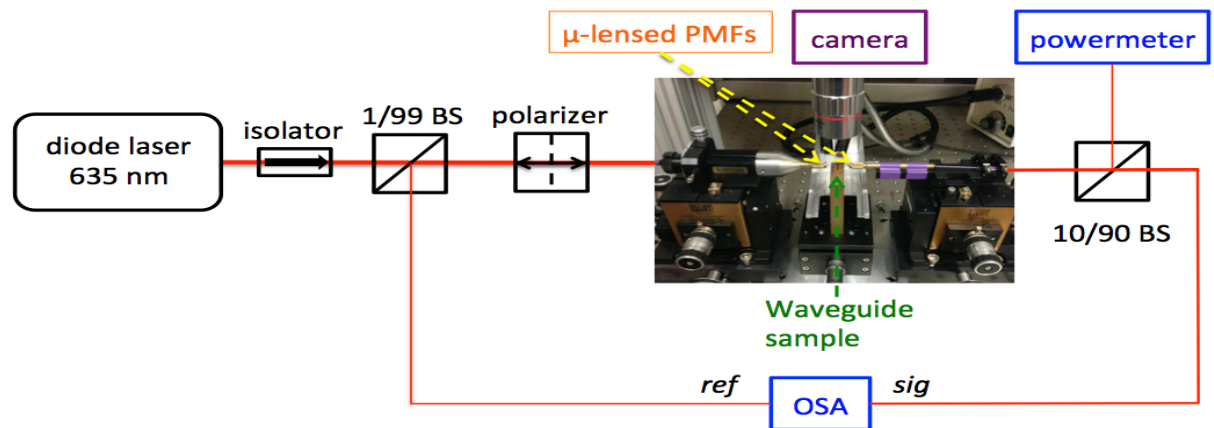


Fig.18 : Schéma du banc de caractérisation optique pour mesure les spectre de transmission fibre-à-fibre des guides d'onde fabriqués.

IV.2.2 Mesure des spectres de transmission fibre-à-fibre

Nous mesurons au moins de 3 fois des spectres de transmission fibre-à-fibre pour chaque échantillon de guides d'onde droits avec différentes longueurs en variant de 500 μm à 900 μm. Les résultats des spectres moyens sont présentés dans la Fig.19.

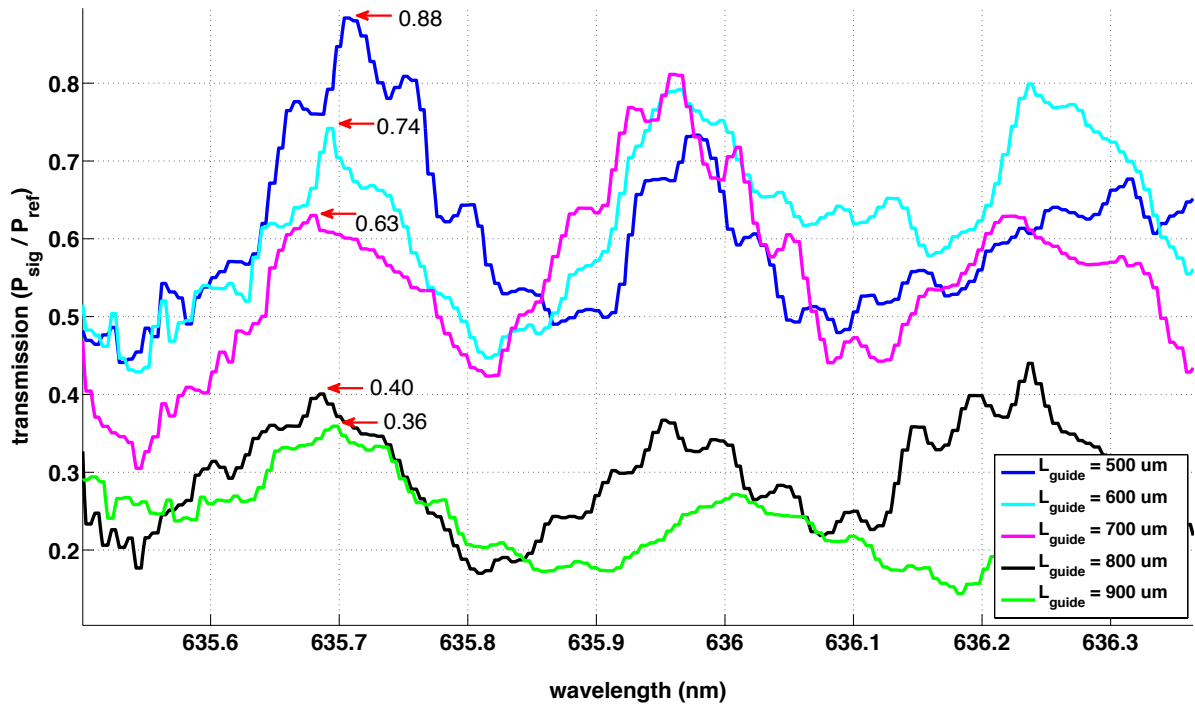


Fig.19 : Spectres optiques de transmission fibre-à-fibre en fonction de la longueur de guides d'onde droits.

En fait, le spectre de sortie de la source s'étend sur une plage de longueur d'onde d'environ 0,9 nm. Par conséquent, nous ne mesurons que les spectres de transmission sur cette plage de longueurs d'onde. Nous observons qu'il y a toujours des périodes d'oscillations d'environ 0,3 nm sur la Fig.19 pour différentes longueurs de guides d'onde. Donc la méthode de Fabry-Pérot ne peut pas s'appliquer dans ce cas. Nous pensons que ce phénomène est dû à la présence des raccords de champs de la lithographie e-beam qui génère des retours optiques le long des guides. Nous estimons alors le coefficient de pertes linéaires par une mesure du type de end-fire. Nous fixons une longueur d'onde d'opération, par exemple à 635,7 nm et puis comparons les puissances de crête en supposant que l'atténuation linéaire due à la propagation dans un guide d'onde droit soit constante. Nous pouvons calculer le coefficient des pertes linéaires α en utilisant la formule suivante:

$$T_{ftf}(dB) = 4,343(-\alpha L + c) \quad (4)$$

avec L la longueur des guides d'onde droit et C une constante liée aux atténuations parasites. Nous prenons aussi en compte l'effet de diviseurs de faisceau 1:99 et 10:90 dans cette formule. Les résultats expérimentaux de transmissions fibre-à-fibre en fonction de la longueur des échantillons des guides d'onde droits sont présentés dans la Fig.20.

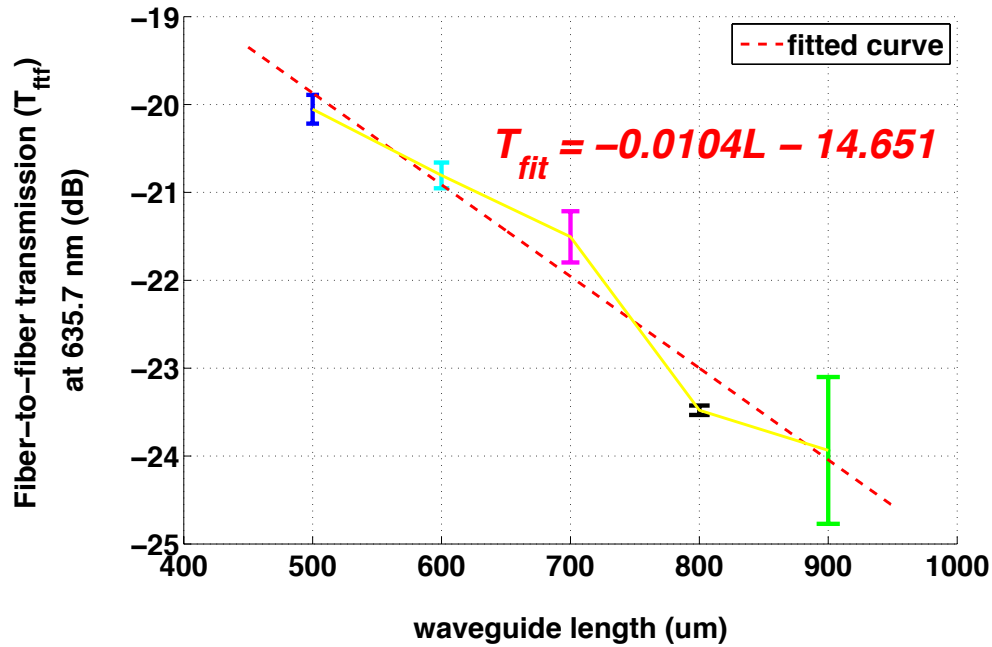


Fig.20 : Relation entre la transmission fibre-à-fibre à 635,7 nm et la longueur des guides d’onde fabriqués.

En conclusion, nous trouvons une pente de 10,4 dB/mm, qui représente le coefficient de pertes linéaires avec une barre d’erreur de 0,9 dB/mm. L’atténuation parasite due à la facette clivée par la scie est d’environ 7,2+/-0,3 dB/facette. En comparant avec la littérature, nous pensons que cette atténuation linéaire très élevée est surtout causée par le faible confinement du mode TE₀₀ dans un guide d’onde rectangulaire très étroit qui favorise les diffusions dues aux rugosités latérales, ainsi que les raccords de champ des « sub-field ». Il faudra donc améliorer la fabrication, et choisir des guides plus larges pour atténuer ces effets. En outre, nous visons aussi une autre mesure par la méthode top-view dans le futur.

CHAPITRE V : COUPLAGE PLASMONIQUE DU GUIDE D’ONDE DE Si₃N₄ À LA CHAÎNE DE NANOPARTICULES MÉTALLIQUES

V.1 Rappels sur les plasmons de surface et état de l’art

Les modes de plasmons de surface localisés (LSP) supportés par une chaîne de nanoparticules métalliques ont été profondément étudiés en théorie et en pratique depuis une dizaine d’années. Comme les dimensions géométriques de ce genre de nanoparticules métalliques sont inférieures à la longueur d’onde d’opération dans la gamme du visible et de l’infrarouge, ce

nouveau domaine appartient à celui de la nano-photonique. Au début de la recherche dans le domaine de la plasmonique, la théorie de Mie et le modèle dipolaire ont été largement appliqués pour expliquer analytiquement les modes plasmoniques propagatifs à base d'une chaîne de nanoparticules d'argent [QUINT98]. L'effet optique dans le champ proche a été aussi observé sur une chaîne d'or ou d'argent, qui est en accord avec la prédiction théorique [KRENN99, MAIER03]. Ensuite, la théorie du couplage dipolaire ponctuel et la méthode numérique basée sur les équations de Maxwell pour calculer la relation de dispersion de la chaîne infinie et finie de nanoparticules métalliques ont été aussi développées et puis confirmées expérimentalement [BRONG00, WEBER04]. Les effets telles d' « amortissement ohmique », de « rayonnement amorti » et de retard ont aussi été pris en compte dans le modèle analytique corrigé [KOEND06, KOEND07]. L'influence du substrat diélectrique a été considérée dans la théorie la plus avancée [CROZI07, SIMSE10].

V.1.1 Guides d'onde plasmoniques à base de la chaîne de nanoparticules métalliques

Dans un modèle physique de la chaîne de nanoparticules d'or déposé au-dessus d'un substrat SOI, un couplage géant entre un mode photonique guidé à une longueur d'onde de télécom et un mode plasmonique de surface (SP) localisé a été observé expérimentalement par *Février et al.* (voir Fig.21). L'excitation efficace de ce mode SP du guide d'onde rectangulaire de SOI peut être utilisé pour fabriquer des composants intégrés photoniques pour piéger ou détecter la lumière de l'infrarouge [FEVRI12].

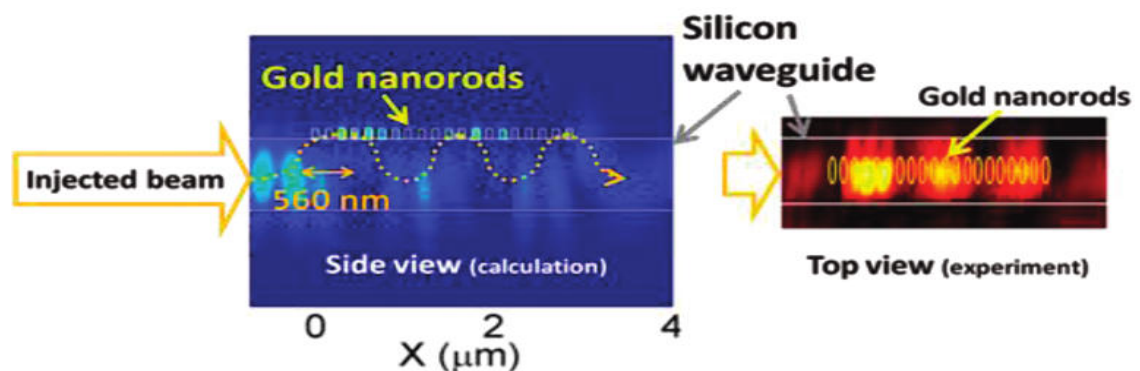


Fig.21 : L'effet du couplage géant entre la chaîne nanoparticules d'or et le guide d'onde SOI observée par TraNSOM.

V.1.2 Antennes plasmoniques du type Yagi-Uda

Suite à la démonstration du couplage efficace en transférant l'énergie optique à la résonance plasmonique localisée dans la chaîne de nanoparticules métalliques, des travaux de recherche sur le développement des nano-antennes plasmoniques ont été généralisés dans la gamme de longueur d'onde infrarouge et même visible [KOSAK10, NOVOT11]. Une des conceptions d'antennes plasmoniques les plus populaires est du type Yagi-Uda [TAMIN08, CURTO10]. *Arango et al.* ont présenté des études sur l'antenne plasmonique Yagi-Uda à base d'une chaîne de nanoparticules d'or et un guide d'onde monomode de Si_3N_4 visée pour la détection et l'émission directionnelle à la longueur d'onde autour de 850 nm. Ces composants intégrés ont toujours une taille compacte et une caractéristique de fonctionnalité d'émission et/ou de détection efficace et directionnelle [ARANG12, ARANG15].

V.2 Études sur la structure guidée à base d'une chaîne de nanoparticules métalliques et d'un guide d'onde de Si_3N_4

V.2.1 Approximation du dipôle ponctuel

Nous étudions d'abord la polarisabilité d'une seule nano-ellipsoïde d'or et d'argent dans un environnement homogène à l'aide de la méthode d'approximation du dipôle couplé (CDA). Nous cherchons la tendance de la variation de la longueur d'onde résonante en fonction des dimensions géométriques de nanoparticules. Un schéma du dimensionnement d'une seule nanoparticule métallique est présenté dans la Fig.22 (à gauche). Nous nous intéressons ici à la plage de longueur d'onde entre 600 nm et 800 nm. Les permittivités des métaux sont issues de la base de donnée du type de Palik du logiciel de simulation FDTD LUMERICAL.

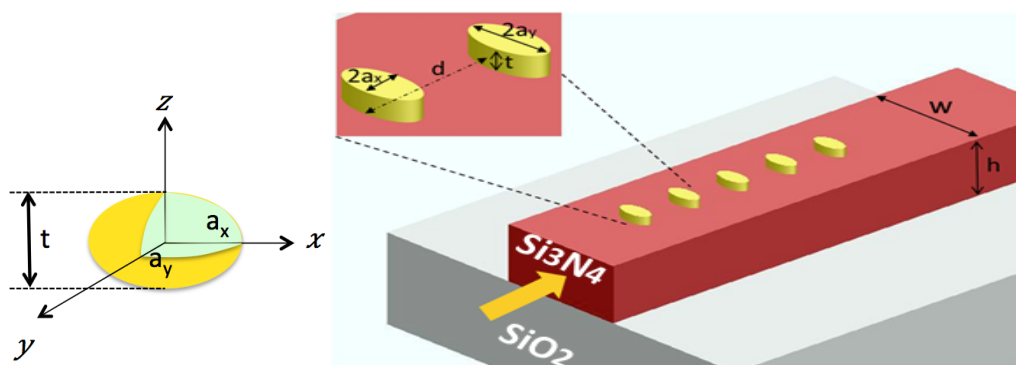


Fig.22 : Schéma du dimensionnement des nanoparticules métalliques pour le calcul CDA (à gauche) et pour la simulation FDTD (à droite).

Nous présentons dans la Fig.23 la polarisabilité (partie imaginaire) calculée par la méthode de CDA correctrice d'une seule nano-ellipsoïde d'or et d'argent en fonction de ses rayons sur l'axe x et l'axe y.

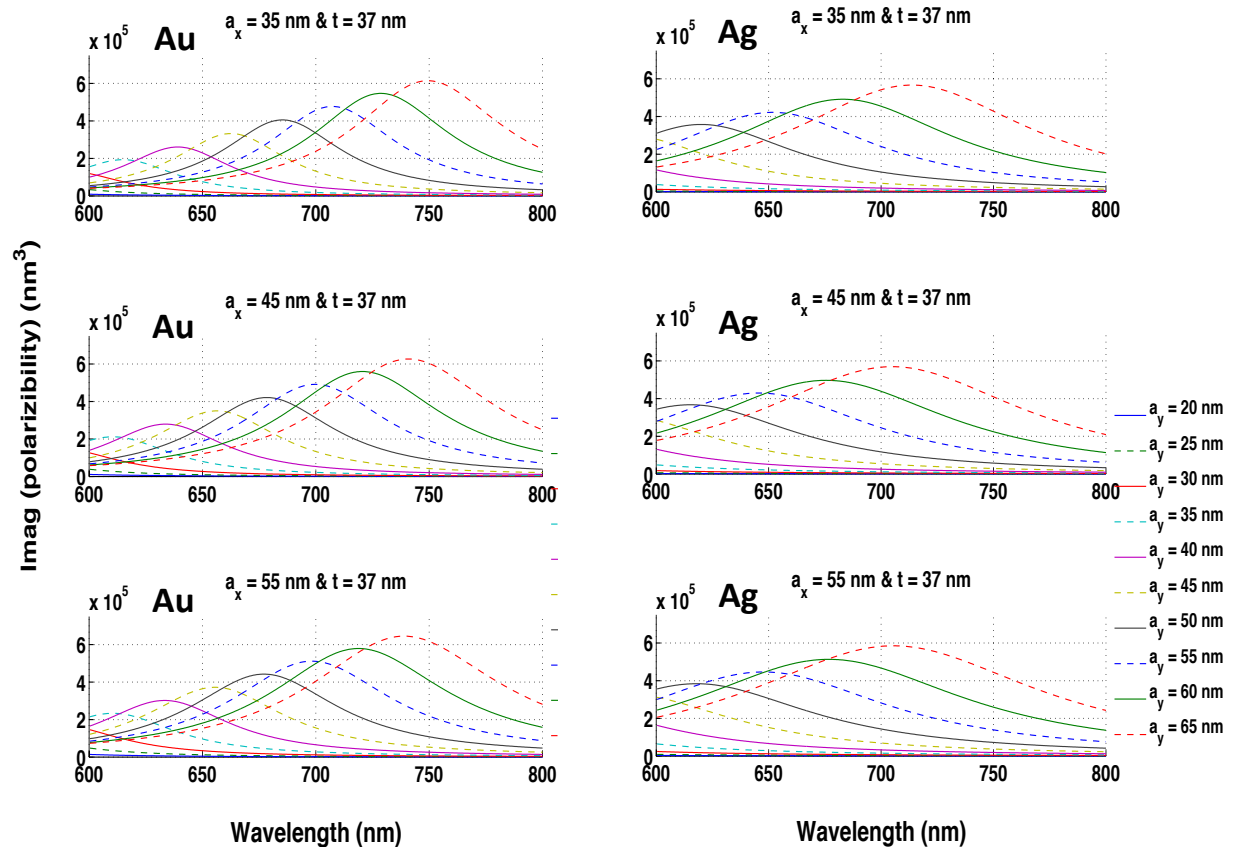


Fig.23 : Polarisabilités (partie imaginaire) d'une seule nano-ellipsoïde d'or (à gauche) et d'argent (à droite) en fonction de ses dimensions géométriques calculées par la CDA correctrice.

En général, le spectre de la polarisabilité est décalé vers le rouge quand a_y augmente. Au contraire, il y a un peu de décalage vers le bleu quand a_x augmente. En même temps, le spectre de la polarisabilité bouge vers le bleu si nous remplaçons l'or par l'argent.

V.2.2 Simulation par le logiciel FDTD

Nous utilisons un logiciel de simulation FDTD LUMERICAL pour étudier l'effet du couplage entre la structure guidée du mode plasmonique à base de la chaîne de nanoparticules métalliques déposée sur le guide d'onde de Si_3N_4 et recouverte par le SiO_2 . L'objectif est d'évaluer le coefficient du couplage entre le guide d'onde de Si_3N_4 et la chaîne de nanoparticules métalliques ainsi que la résonance plasmonique indiquée sur le spectre de transmission. D'ailleurs, les permittivités d'or et d'argent dans la simulation FDTD sont issues

de la base de donnée Palik. La taille du guide d'onde rectangulaire de Si_3N_4 est référée à la conception, c'est à dire que la taille de profil du guide d'onde concerné est fixée à $250 \text{ nm} \times 300 \text{ nm}$ pour un guide TE monomode à 633 nm . Les spectres de transmission en fonction des dimensions des nanoparticules d'or et d'argent sont présentés dans la Fig.24.

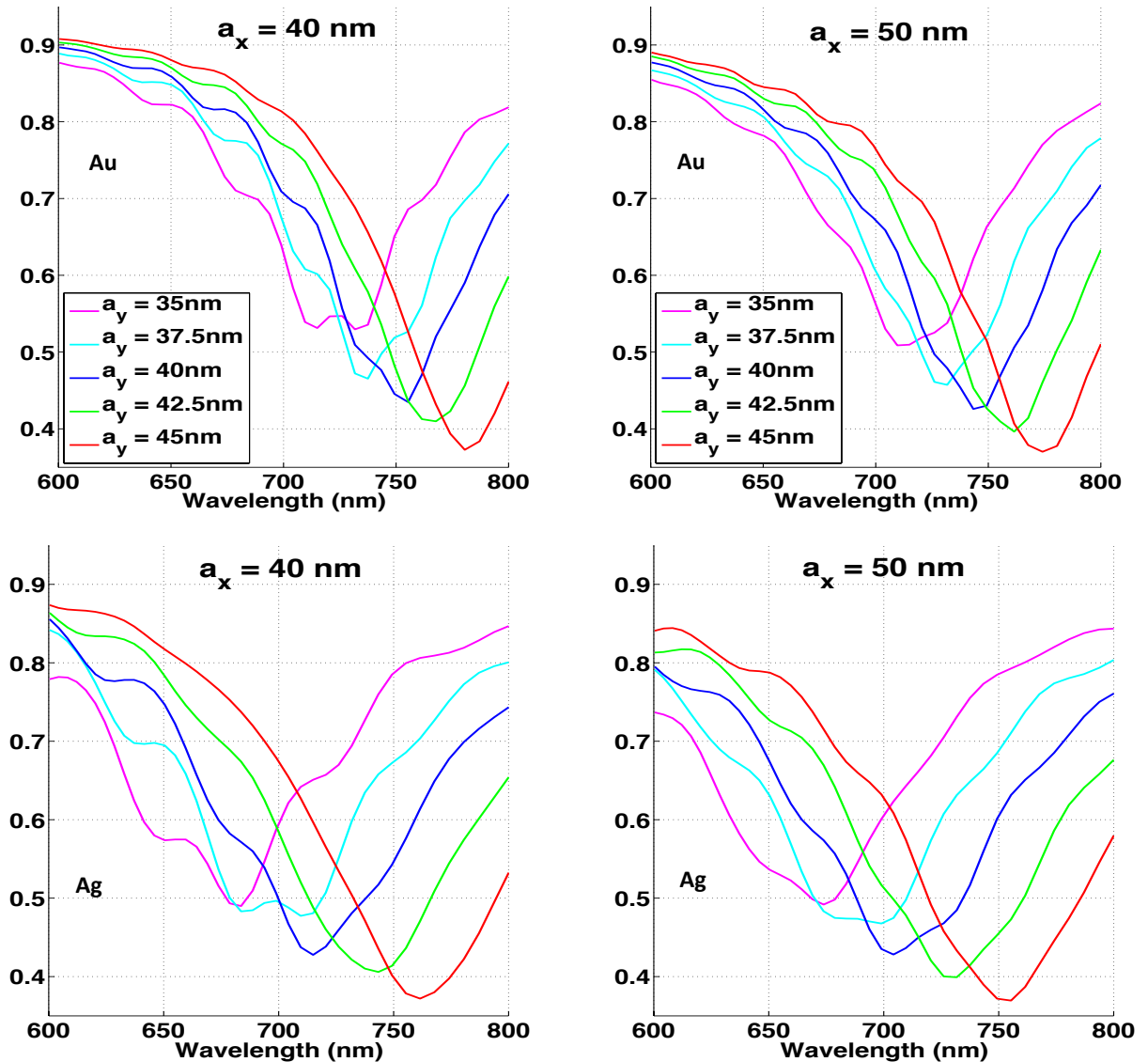


Fig.24 : Spectres de transmission en fonction des dimensions géométriques dans la structure guidée hybride avec des nanoparticules d'or et d'argent ($t=37 \text{ nm}$, $d=130 \text{ nm}$).

Selon les résultats de simulation FDTD, nous observons la même tendance d'évolution de la résonance en fonction des a_x et a_y de ces 5 nanoparticules identiques en chaîne que celle observée dans le cas d'une seule nano-ellipsoïde sous la CDA correctrice. Donc plus a_x est grand ou a_y est petit, plus le spectre de transmission bouge vers le bleu. Pour le cas avec des

grandes nanoparticules, le spectre de transmission ressemble beaucoup à une courbe Lorentzienne. Dans ce cas, nous étudions le ratio entre la résonance et la largeur spectrale à mi-hauteur (FWHM) en fonction des dimensions de nanoparticules en supposant que le plasmon de surface localisé est analogue à une cavité photonique dont le ratio mentionné représente le facteur de qualité Q.

Par contre, pour les petites nanoparticules, le spectre de transmission simulé est perturbé. Au niveau du pic de résonance, la dépendance des dimensions géométriques nous permet de prévoir une résonance visée à 633 nm avec une transmission de près de 60% excitée par la chaîne des nanoparticules d'argent dont $a_x = 50$ nm, $a_y = 35$ nm et $t = 37$ nm. Enfin, nous présentons dans la Fig.25 le profil du champ E_y résonant à 664 nm dans la chaîne d'argent simulé par LUMERICAL pour des dimensions $a_x = 50$ nm, $a_y = 40$ nm and $t = 37$ nm. En fait, le transfert d'énergie est déjà complètement terminé dans les premières 4 nanoparticules d'argent. Le plasmon de surface est bien localisé au-dessus du guide d'onde de Si_3N_4 et l'énergie optique non-couplée peut être guidée et continuer de se propager dans le guide d'onde de Si_3N_4 . L'étape suivante de notre recherche est donc d'étudier des émetteurs plasmoniques pour extraire la radiation directionnelle de la chaîne.

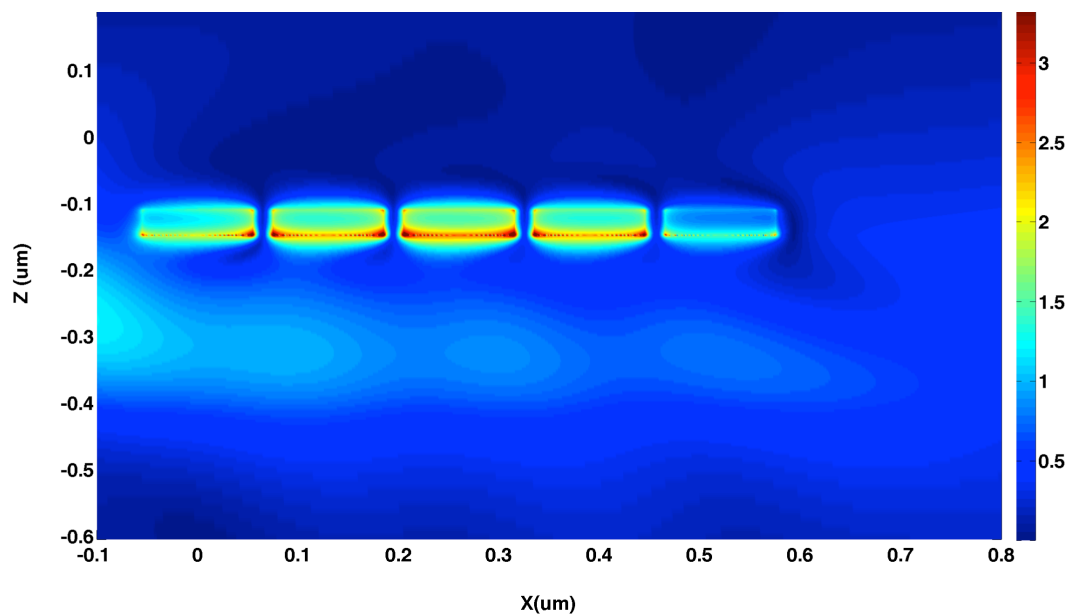


Fig.25 : Couplage du mode photonique dans le guide d'onde de Si_3N_4 à la chaîne de 5 nanoparticules d'argent avec des dimensions 50 nm \times 40 nm \times 37 nm résonné à 664 nm.

CONCLUSIONS ET PERSPECTIVES

Pendant ces trois ans de travaux de recherche dans la cadre d'une thèse CIFRE, nous avons visé à développer un système d'éclairage à géométrie surfacique ultracompact, qui est capable d'être embarqué facilement dans une voiture de passager à l'aide des circuits intégrés photoniques et des émetteurs plasmoniques. Nous avons d'abord dimensionné le guide d'onde de Si_3N_4 encapsulé dans la SiO_2 pour un fonctionnement monomode TE à 633 nm. Ensuite, nous avons proposé pour le diviseur de faisceau une structure en cascade à base de coupleurs MMI 1×2 . Les dimensions géométriques de ce coupleur MMI ont été optimisées par un logiciel de simulation. En même temps, nous avons développé des guides d'onde courbés en combinant deux types de courbes, la Fonction S et la lemniscate de Bernoulli. Nous avons aussi implémenté les processus de fabrication des guides d'onde rectangulaire de 250×300 nm en salle blanche. Par la suite, les échantillons fabriqués ont été caractérisés par la méthode de cut-back et le coefficient des pertes de propagation linéaires mesurées est d'environ 10 dB/mm. Enfin, nous avons étudié l'effet du couplage du mode photonique dans le guide d'onde de Si_3N_4 au mode plasmonique localisé dans la chaîne de nanoparticules d'or et d'argent dans le but de réaliser une résonance efficace autour de 633 nm.

Nous visons de continuer d'améliorer le dimensionnement et aussi la fabrication des échantillons de guides d'onde pour que les pertes linéaires mesurées puissent être réduites à un niveau acceptable dans un futur proche. Par ailleurs, nous allons finaliser la conception des guides d'onde courbés à faible perte et aussi le développement d'un outil numérique pour générer automatiquement des courbes progressives optimales. En parallèle, nous allons étudier la radiation directionnelle et efficace à base de chaînes de nanoparticules d'argent du type de l'antenne Yagi-Uda pour répondre à l'exigence de l'illumination cohérente et puissante à géométrie planaire. En outre, grâce à une collaboration internationale et interdisciplinaire, les perspectives à long terme consistent à développer des composants intégrés à base d'OLED pour compenser les pertes de propagation dues aux guides d'onde monomode de Si_3N_4 . Du côté de l'objectif industriel, nous visons aussi à généraliser le prototype de ce système intégré sur puce de l'ordre du mm à une grande surface de l'ordre du dm.

REFERENCE

- [AKEDO06] K. Akedo, A. Miura, H. Fujikawa, and Y. Taga, “Flexible OLEDs for Automobiles using $\text{SiN}_x/\text{CN}_x\text{:H}$ multi-layer Barrier Films and Epoxy Substrates,” *Journal of Photopolymer Science and Technology*, vol. 19, no. 2, pp. 203–208, 2006.
- [ARANG12] F. Arango, A. Kwadrin, and A. F. Koenderink, “Plasmonic Antennas Hybridized with Dielectric Waveguides,” *ACS Nano*, vol. 6, no. 11, pp. 10156–10167, Nov. 2012.
- [ARANG15] F. B. Arango, R. Thijssen, B. Brenny, T. Coenen, and A. F. Koenderink, “Robustness of plasmon phased array nanoantennas to disorder,” *Sci. Rep.*, vol. 5, Jun. 2015.
- [AZZAM87] R. M. A. Azzam and N. M. Bashara, *Ellipsometry and polarized light*, Elsevier Science Publishing Co., Inc., 1987.
- [BARAT] <http://www.opticsvalley.org/layout/set/sitemap/Les-Actualites/Newsletter-Lumiere/Newsletter-Lumiere-n-66-Photonique-et-Automobile/ETAT-DE-L-ART-ENJEUX/La-photonique-au-caeur-des-systemes-automobiles/L-automobile-un-concentre-de-composants-photoniques>.
- [BARNE03] W. L. Barnes, A. Dereux, and T. W. Ebbesen, “Surface plasmon subwavelength optics,” *Nature*, vol. 424, no. 6950, pp. 824–830, août 2003.
- [BENTO69] S. A. Benton, “Hologram reconstructions with extended incoherent sources,” in *Journal of the Optical Society of America*, vol. 59, p. 1545, 1969.
- [BESTW99] T. Bestwick, “ASOC silicon integrated optics technology,” 1999, vol. 3631, pp. 182–190.
- [BOHRE08] C. F. Bohren and D. R. Huffman, *Absorption and Scattering of Light by Small Particles*. John Wiley & Sons, 2008.
- [BOWER10] J. E. Bowers, D. Liang, A. W. Fang, H. Park, R. Jones, and M. J. Paniccia, “Hybrid Silicon Lasers: The Final Frontier to Integrated Computing,” *Opt. Photon. News*, vol. 21, no. 5, pp. 28–33, May 2010.
- [BRONG00] M. L. Brongersma, J. W. Hartman, and H. A. Atwater, “Electromagnetic energy transfer and switching in nanoparticle chain arrays below the diffraction limit,” *Phys. Rev. B*, vol. 62, no. 24, pp. R16356–R16359, Dec. 2000.
- [BULLA99] D. A. P. Bulla, B. V. Borges, M. A. Romero, N. I. Morimoto, L. G. Neto, and A. L. Cortes, “Design and fabrication of $\text{SiO}_2/\text{Si}_3\text{N}_4$ CVD optical waveguides,” in *Microwave*

and Optoelectronics Conference, 1999. SBMO/IEEE MTT-S, APS and LEOS - IMOC '99. International, 1999, vol. 2, pp. 454–457 vol. 2.

[CAILE12] A. Cailean, B. Cagneau, L. Chassagne, S. Topsu, Y. Alayli, and J.-M. Blosseville, “Visible light communications: Application to cooperation between vehicles and road infrastructures,” in *2012 IEEE Intelligent Vehicles Symposium (IV)*, 2012, pp. 1055–1059.

[CASSA03] E. Cassan, S. Laval, S. Lardenois, and A. Koster, “On-chip optical interconnects with compact and low-loss light distribution in silicon-on-insulator rib waveguides,” *IEEE Journal of Selected Topics in Quantum Electronics*, vol. 9, no. 2, pp. 460–464, 2003.

[CHANG10] H.-H. Chang, Y. Kuo, R. Jones, A. Barkai, and J. E. Bowers, “Integrated hybrid silicon triplexer,” *Opt. Express*, vol. 18, no. 23, pp. 23891–23899, Nov. 2010.

[CHUNG06] K. K. Chung, H. P. Chan, and P. L. Chu, “A 1×4 polarization and wavelength independent optical power splitter based on a novel wide-angle low-loss Y-junction,” *Optics Communications*, vol. 267, no. 2, pp. 367–372, Nov. 2006.

[COCHA15] J. Cochard, “Opportunités pour les technologies photoniques dans l’industrie automobile,” presentation at the Journée scientifique de la chaire UPSud/PSA, Orsay, France, May 2015.

[CROZI07] K. B. Crozier, E. Togan, E. Simsek, and T. Yang, “Experimental measurement of the dispersion relations of the surface plasmon modes of metal nanoparticle chains,” *Optics Express*, vol. 15, no. 26, p. 17482, 2007.

[CURTO10] A. G. Curto, G. Volpe, T. H. Taminiau, M. P. Kreuzer, R. Quidant, and N. F. van Hulst, “Unidirectional Emission of a Quantum Dot Coupled to a Nanoantenna,” *Science*, vol. 329, no. 5994, pp. 930–933, Aug. 2010.

[DAI12] D. Dai, J. Bauters, and J. E. Bowers, “Passive technologies for future large-scale photonic integrated circuits on silicon: polarization handling, light non-reciprocity and loss reduction,” *Light Sci Appl*, vol. 1, no. 3, p. e1, Mar. 2012.

[DAI08] D. Dai and S. He, “Design of an ultrashort Si-nanowaveguide-based multimode interference coupler of arbitrary shape,” *Applied Optics*, vol. 47, no. 1, p. 38, 2008.

[DALDO04a] N. Dalosso, M. Melchiorri, F. Riboli, F. Sbrana, L. Pavesi, G. Pucker, C. Kompocholis, M. Crivellari, P. Bellutti, and A. Lui, “Fabrication and optical characterization of thin two-dimensional Si_3N_4 waveguides,” *Materials Science in Semiconductor Processing*, vol. 7, no. 4–6, pp. 453–458, 2004.

- [DALDO04b] N. Daldosso, M. Melchiorri, F. Riboli, M. Girardini, G. Pucker, M. Crivellari, P. Bellutti, A. Lui, and L. Pavesi, “Comparison Among Various Si₃N₄ Waveguide Geometries Grown Within a CMOS Fabrication Pilot Line,” *J. Lightwave Technol.*, vol. 22, no. 7, p. 1734, Jul. 2004.
- [DEBRA91] G. N. De Brabander, J. T. Boyd, and H. E. Jackson, “Single polarization optical waveguide on silicon,” *IEEE Journal of Quantum Electronics*, vol. 27, no. 3, pp. 575–579, Mar. 1991.
- [DIREC] <http://www.antenna-theory.com/basics/directivity.php>
- [DOYLE08] J. K. Doyle, O. Cohen, M. R. Lee, O. Raday, S. Xu, V. Sih, H. Rong, and M. Paniccia; Tunable ring resonators for silicon Raman laser and amplifier applications. Proc. SPIE 6896, Integrated Optics: Devices, Materials, and Technologies XII, 68960Q, Feb. 12, 2008.
- [FANG12] A. W. Fang, G. Fish and E. Hall; Heterogeneous photonic integrated circuits. Proc. SPIE 8267, Optoelectronic Interconnects XII, 82670B, Feb. 9, 2012.
- [FARD14] S. T. Fard, K. Murray, M. Caverley, V. Donzella, J. Flueckiger, S. M. Grist, E. Huante-Ceron, S. A. Schmidt, E. Kwok, N. A. F. Jaeger, A. P. Knights, and L. Chrostowski, “Silicon-on-insulator sensors using integrated resonance-enhanced defect-mediated photodetectors,” *Opt. Express*, vol. 22, no. 23, pp. 28517–28529, Nov. 2014.
- [FEVRI12] M. Février, P. Gogol, A. Aassime, R. Mégy, C. Delacour, A. Chelnokov, A. Apuzzo, S. Blaize, J.-M. Lourtioz, and B. Dagens, “Giant Coupling Effect between Metal Nanoparticle Chain and Optical Waveguide,” *Nano Lett.*, vol. 12, no. 2, pp. 1032–1037, Feb. 2012.
- [GALLA03] Dominic F. G. Gallagher and Thomas P. Felici; Eigenmode expansion methods for simulation of optical propagation in photonics: pros and cons. Proc. SPIE 4987, Integrated Optics: Devices, Materials, and Technologies VII, 69, Jun. 17, 2003.
- [GAMET04] J. Gamet and G. Pandraud, “Ultralow-loss 1 × 8 splitter based on field matching Y junction,” *IEEE Photonics Technology Letters*, vol. 16, no. 9, pp. 2060–2062, Sep. 2004.
- [GONDA09] A. Gondarenko, J. S. Levy, and M. Lipson, “High confinement micron-scale silicon nitride high Q ring resonator,” *Opt. Express*, vol. 17, no. 14, pp. 11366–11370, Jul. 2009.
- [GORIN08] A. Gorin, A. Jaouad, E. Grondin, V. Aimez, and P. Charette, “Fabrication of silicon nitride waveguides for visible-light using PECVD: a study of the effect of plasma frequency on optical properties,” *Opt. Express*, vol. 16, no. 18, pp. 13509–13516, Sep. 2008.

- [GOYKH10] I. Goykhman, B. Desiatov, and U. Levy, “Experimental demonstration of locally oxidized hybrid silicon-plasmonic waveguide,” *Applied Physics Letters*, vol. 97, no. 14, p. 141106, Oct. 2010.
- [HARRI70] J. H. Harris, R. Shubert, and J. N. Polky, “Beam Coupling to Films,” *J. Opt. Soc. Am.*, vol. 60, no. 8, pp. 1007–1016, Aug. 1970.
- [HECK14] M. J. R. Heck, J. F. Bauters, M. L. Davenport, D. T. Spencer, and J. E. Bowers, “Ultra-low loss waveguide platform and its integration with silicon photonics,” *Laser & Photonics Reviews*, vol. 8, no. 5, pp. 667–686, Sep. 2014.
- [HENRY87] C. H. Henry, R. F. Kazarinov, H. J. Lee, K. J. Orlowsky, and L. E. Katz, “Low loss Si₃N₄-SiO₂ optical waveguides on Si,” *Appl. Opt.*, vol. 26, no. 13, pp. 2621–2624, Jul. 1987.
- [HIDA98] Y. Hida, T. Fukumitsu, F. Hanawa, Y. Enomoto, S. Sumida, and N. Takato, “Highly compact silica-based PLC-type 1 × 32 splitters using 127 [micro sign]m-spacing output and 0.4 %- waveguides,” *Electronics Letters*, vol. 34, no. 1, p. 75, 1998.
- [HOCHB04] M. Hochberg, T. Baehr-Jones, C. Walker, and A. Scherer, “Integrated plasmon and dielectric waveguides,” *Optics Express*, vol. 12, no. 22, p. 5481, 2004.
- [HOSSE10] A. Hosseini, H. Subbaraman, D. Kwong, Y. Zhang, and R. T. Chen, “Optimum access waveguide width for 1×N multimode interference couplers on silicon nanomembrane,” *Optics Letters*, vol. 35, no. 17, p. 2864, Sep. 2010.
- [HUNSP09] P. R. G. Hunsperger, “Losses in Optical Waveguides,” in *Integrated Optics*, Springer New York, 2009, pp. 107–128.
- [IKEDA08] K. Ikeda, R. E. Saperstein, N. Alic, and Y. Fainman, “Thermal and Kerr nonlinear properties of plasma-deposited silicon nitride/silicon dioxide waveguides,” *Opt. Express*, vol. 16, no. 17, pp. 12987–12994, Aug. 2008.
- [INUKA94] T. Inukai and K. Ono, “Optical Characteristics of Amorphous Silicon Nitride Thin Films Prepared by Electron Cyclotron Resonance Plasma Chemical Vapor Deposition,” *Jpn. J. Appl. Phys.*, vol. 33, no. 5R, p. 2593, May 1994.
- [IRENE76] E. A. Irene, “Residual stress in silicon nitride films,” *JEM*, vol. 5, no. 3, pp. 287–298, Jun. 1976.
- [ITO00] T. Ito and S. Okazaki, “Pushing the limits of lithography,” *Nature*, vol. 406, no. 6799, pp. 1027–1031, Aug. 2000.
- [IZUTS82] M. Izutsu, Y. Nakai, and T. Sueta, “Operation mechanism of the single-mode optical-waveguide Y junction,” *Optics Letters*, vol. 7, no. 3, p. 136, Mar. 1982.

- [KELLY03] K. L. Kelly, E. Coronado, L. L. Zhao, and G. C. Schatz, “The Optical Properties of Metal Nanoparticles: The Influence of Size, Shape, and Dielectric Environment,” *J. Phys. Chem. B*, vol. 107, no. 3, pp. 668–677, Jan. 2003.
- [KLEIN70] M. V. Klein, *Optics*, 2nd ed. New York: Wiley, 1970.
- [KOEND06] A. F. Koenderink and A. Polman, “Complex response and polariton-like dispersion splitting in periodic metal nanoparticle chains,” *Phys. Rev. B*, vol. 74, no. 3, p. 033402, Jul. 2006.
- [KOEND07] A. F. Koenderink, “Experimental evidence for large dynamic effects on the plasmon dispersion of subwavelength metal nanoparticle waveguides,” *Phys. Rev. B*, vol. 76, no. 20, 2007.
- [KOSAK10] T. Kosako, Y. Kadoya, and H. F. Hofmann, “Directional control of light by a nano-optical Yagi–Uda antenna,” *Nat Photon*, vol. 4, no. 5, pp. 312–315, mai 2010.
- [KOSTE04] A. Koster, E. Cassan, S. Laval, L. Vivien, and D. Pascal, “Ultracompact splitter for submicrometer silicon-on-insulator rib waveguides,” *J. Opt. Soc. Am. A*, vol. 21, no. 11, pp. 2180–2185, Nov. 2004.
- [KRENN99] J. R. Krenn, A. Dereux, J. C. Weeber, E. Bourillot, Y. Lacroute, J. P. Goudonnet, G. Schider, W. Gotschy, A. Leitner, F. R. Aussenegg, and C. Girard, “Squeezing the Optical Near-Field Zone by Plasmon Coupling of Metallic Nanoparticles,” *Phys. Rev. Lett.*, vol. 82, no. 12, pp. 2590–2593, Mar. 1999.
- [LABRO03] A. Labrousse, PhD Thesis « Conception et caractérisation d’interféromètres de Mach-Zehnder à base d’amplificateurs optiques à semiconducteur pour la régénération 3R “tout-optique” à haut débit (40Gbps) ». Rouen, 2003.
- [LAI97] Q. Lai, M. Bachmann, and H. Melchior, “Low-loss $1 \times N$ multimode interference couplers with homogeneous output power distributions realised in silica on Si material,” *Electronics Letters*, vol. 33, no. 20, p. 1699, 1997.
- [LAL07] S. Lal, S. Link, and N. J. Halas, “Nano-optics from sensing to waveguiding,” *Nat Photon*, vol. 1, no. 11, pp. 641–648, Nov. 2007.
- [LEE01] K. K. Lee, “Transmission and routing of optical signals in on-chip waveguides for silicon microphotronics,” Thesis, Massachusetts Institute of Technology, 2001.
- [LEVY99] D. S. Levy, K. H. Park, R. Scarmozzino, R. M. Osgood, C. Dries, P. Studenkov, and S. Forrest, “Fabrication of ultracompact 3-dB 2×2 MMI power splitters,” *IEEE Photonics Technology Letters*, vol. 11, no. 8, pp. 1009–1011, Aug. 1999.

- [LEVY98] D. S. Levy, R. Scarmozzino, Y. M. Li, and R. M. Osgood, “A new design for ultracompact multimode interference-based 2 x 2 couplers,” *IEEE Photonics Technology Letters*, vol. 10, no. 1, pp. 96–98, Jan. 1998.
- [LITTL97] B. E. Little, J.-P. Laine, and S. T. Chu, “Surface-roughness-induced contradirectional coupling in ring and disk resonators,” *Opt. Lett.*, vol. 22, no. 1, pp. 4–6, Jan. 1997.
- [LUCHT] R. P. Lucht, Drude Model for dielectric constant of metals, <http://optics.hanyang.ac.kr/~shsong/27-Metals.pdf>
- [MAIER03] S. A. Maier, P. G. Kik, H. A. Atwater, S. Meltzer, E. Harel, B. E. Koel, and A. A. G. Requicha, “Local detection of electromagnetic energy transport below the diffraction limit in metal nanoparticle plasmon waveguides,” *Nature Materials*, vol. 2, no. 4, pp. 229–232, Apr. 2003.
- [MAKSY12] I. S. Maksymov, I. Staude, A. E. Miroschnichenko, and Y. S. Kivshar, “Optical Yagi-Uda nanoantennas,” *Nanophotonics*, vol. 1, no. 1, pp. 65–81, Jul. 2012.
- [MARCA69a] E. a. J. Marcatili and S. E. Miller, “Improved Relations Describing Directional Control in Electromagnetic Wave Guidance,” *Bell System Technical Journal*, vol. 48, no. 7, pp. 2161–2188, Sep. 1969.
- [MARCA69b] E. a. J. Marcatili, “Bends in Optical Dielectric Guides,” *Bell System Technical Journal*, vol. 48, no. 7, pp. 2103–2132, Sep. 1969.
- [MASAN03] M. L. Masanovic, E. J. Skogen, J. S. Barton, J. M. Sullivan, D. J. Blumenthal, and L. A. Coldren, “Multimode interference-based two-stage 1 /spl times/ 2 light splitter for compact photonic integrated circuits,” *IEEE Photonics Technology Letters*, vol. 15, no. 5, pp. 706–708, 2003.
- [MELCH05] M. Melchiorri, N. Daldosso, F. Sbrana, L. Pavesi, G. Pucker, C. Kompocholis, P. Bellutti, and A. Lui, “Propagation losses of silicon nitride waveguides in the near-infrared range,” *Applied Physics Letters*, vol. 86, no. 12, pp. 121111–121111–3, Mar. 2005.
- [MICRO]
http://www.microchemicals.com/technical_information/substrate_cleaning_adhesion_photoresist.pdf
- [MOERM97] I. Moerman, P. P. Van Daele, and P. M. Demeester, “A review on fabrication technologies for the monolithic integration of tapers with III-V semiconductor devices,” *IEEE Journal of Selected Topics in Quantum Electronics*, vol. 3, no. 6, pp. 1308–1320, Dec. 1997.
- [MOORE98] D. Moore, “HEADLAMP HISTORY AND HARMONIZATION,” Ann Arbor, Michigan, USA, UMTRI-98-21, Jun. 1998.

- [MURPH01] T. E. Murphy, J. T. Hastings, and H. I. Smith, "Fabrication and Characterization of Narrow-Band Bragg-Reflection Filters in Silicon-on-Insulator Ridge Waveguides," *J. Lightwave Technol.*, vol. 19, no. 12, p. 1938, Dec. 2001.
- [NEUMA94] R. Neumann, "Improved Projector Headlamps Using HID (Litronic) and Incandescent Bulbs," SAE International, Warrendale, PA, SAE Technical Paper 940636, Mar. 1994.
- [NOVOT11] L. Novotny and N. van Hulst, "Antennas for light," *Nat Photon*, vol. 5, no. 2, pp. 83–90, Feb. 2011.
- [OHTAN92] M. Ohtani and M. Hanabusa, "Silicon nitride ridge-type optical waveguides fabricated on oxidized silicon by laser direct writing," *Appl. Opt.*, vol. 31, no. 27, pp. 5830–5832, Sep. 1992.
- [OKAMO99] K. Okamoto, "Recent progress of integrated optics planar lightwave circuits," *Optical and Quantum Electronics*, vol. 31, no. 2, pp. 107–129, Feb. 1999.
- [OKAZA91] S. Okazaki, "Resolution limits of optical lithography," *Journal of Vacuum Science & Technology B*, vol. 9, no. 6, pp. 2829–2833, Nov. 1991.
- [OMALL10] R. O'Malley, E. Jones, and M. Glavin, "Detection of pedestrians in far-infrared automotive night vision using region-growing and clothing distortion compensation," *Infrared Physics & Technology*, vol. 53, no. 6, pp. 439–449, Nov. 2010.
- [PALIK] E. D. PALIK, *Handbook of Optical Constants of Solids*. 1997.
- [PAUL] D. Paul, <http://userweb.eng.gla.ac.uk/douglas.paul/siphotonics.html>
- [PINTU13] P. Pintus, F. Di Pasquale, and J. E. Bowers, "Integrated TE and TM optical circulators on ultra-low-loss silicon nitride platform," *Opt. Express*, vol. 21, no. 4, pp. 5041–5052, Feb. 2013.
- [PRABH09] A. M. Prabhu, A. Tsay, Z. Han, and V. Van, "Ultracompact SOI Microring Add-Drop Filter With Wide Bandwidth and Wide FSR," *IEEE Photonics Technology Letters*, vol. 21, no. 10, pp. 651–653, May 2009.
- [QUINT98] M. Quinten, A. Leitner, J. R. Krenn, and F. R. Aussenegg, "Electromagnetic energy transport via linear chains of silver nanoparticles," *Optics Letters*, vol. 23, no. 17, p. 1331, Sep. 1998.
- [RANGE03] I. W. Rangelow, "Critical tasks in high aspect ratio silicon dry etching for microelectromechanical systems," *Journal of Vacuum Science & Technology A*, vol. 21, no. 4, pp. 1550–1562, Jul. 2003.

- [RASIG10] G. Rasigade, X. Le Roux, D. Marris-Morini, E. Cassan, and L. Vivien, "Compact wavelength-insensitive fabrication-tolerant silicon-on-insulator beam splitter," *Opt. Lett.*, vol. 35, no. 21, pp. 3700–3702, Nov. 2010.
- [RASMU95] T. Rasmussen, J. K. Rasmussen, and J. H. Povlsen, "Design and performance evaluation of 1-by-64 multimode interference power splitter for optical communications," *Journal of Lightwave Technology*, vol. 13, no. 10, pp. 2069–2074, Oct. 1995.
- [RAETH88] H. Reather, "Surface plasmons on smooth surfaces," in *Surface Plasmons on Smooth and Rough Surfaces and on Gratings*, Springer Berlin Heidelberg, 1988, pp. 4–39.
- [REIZM67] F. Reizman and W. van Gelder, "Optical thickness measurement of SiO₂- Si₃N₄ films on silicon," *Solid-State Electronics*, vol. 10, no. 7, pp. 625–632, Jul. 1967.
- [RITCH57] R. H. Ritchie, "Plasma Losses by Fast Electrons in Thin Films," *Phys. Rev.*, vol. 106, no. 5, pp. 874–881, Jun. 1957.
- [ROMER13] S. Romero-García, F. Merget, F. Zhong, H. Finkelstein, and J. Witzens, "Silicon nitride CMOS-compatible platform for integrated photonics applications at visible wavelengths," *Opt. Express*, vol. 21, no. 12, pp. 14036–14046, Jun. 2013.
- [RONG08] H. Rong, S. Xu, O. Cohen, O. Raday, M. Lee, V. Sih, and M. Paniccia, "A cascaded silicon Raman laser," *Nat Photon*, vol. 2, no. 3, pp. 170–174, Mar. 2008.
- [SAMMA00] A. Samman, L. Rimai, J. R. McBride, R. O. Carter, W. H. Weber, C. Gmachl, F. Capasso, A. L. Hutchinson, D. L. Sivco, and A. Y. Cho, "Potential use of near, mid and far infrared laser diodes in automotive LIDAR applications," in *Vehicular Technology Conference, 2000. IEEE-VTS Fall VTC 2000. 52nd, 2000*, vol. 5, pp. 2084–2089 vol.5.
- [SHAW05] M. J. Shaw, J. Guo, G. A. Vawter, S. Habermehl, and C. T. Sullivan, "Fabrication techniques for low-loss silicon nitride waveguides," 2005, vol. 5720, pp. 109–118.
- [SHAWN10] C. Shawn, Y. Makiuchi, and C. Che, "High-energy Electron Beam Lithography for Nanoscale Fabrication," in *Lithography*, M. Wang, Ed. InTech, 2010.
- [SIMSE10] E. Simsek, "Full Analytical Model for Obtaining Surface Plasmon Resonance Modes of Metal Nanoparticle Structures Embedded in Layered Media," *Optics Express*, vol. 18, no. 2, p. 1722, Jan. 2010.
- [SMIT96] M. K. Smit and C. Van Dam, "PHASAR-based WDM-devices: Principles, design and applications," *IEEE Journal of Selected Topics in Quantum Electronics*, vol. 2, no. 2, pp. 236–250, Jun. 1996.
- [SMIT88] M. K. Smit, "New focusing and dispersive planar component based on an optical phased array," *Electronics Letters*, vol. 24, no. 7, p. 385, 1988.

- [SOLDA95] L. B. Soldano and E. C. M. Pennings, "Optical multi-mode interference devices based on self-imaging: principles and applications," *Journal of Lightwave Technology*, vol. 13, no. 4, pp. 615–627, 1995.
- [SRIRA83] S. Sriram, W. D. Partlow, and C. S. Liu, "Low-loss optical waveguides using plasma-deposited silicon nitride," *Appl. Opt.*, vol. 22, no. 23, pp. 3664–3665, Dec. 1983.
- [STUTI77] W. Stutius and W. Streifer, "Silicon nitride films on silicon for optical waveguides," *Appl. Opt.*, vol. 16, no. 12, pp. 3218–3222, Dec. 1977.
- [SUBRA13] A. Z. Subramanian, P. Neutens, A. Dhakal, R. Jansen, T. Claes, X. Rottenberg, F. Peyskens, S. Selvaraja, P. Helin, B. Dubois, K. Leyskens, S. Severi, P. Deshpande, R. Baets, and P. Van Dorpe, "Low-Loss Singlemode PECVD Silicon Nitride Photonic Wire Waveguides for 532-900 nm Wavelength Window Fabricated Within a CMOS Pilot Line," *IEEE Photonics Journal*, vol. 5, no. 6, pp. 2202809–2202809, Dec. 2013.
- [TAKAH91] H. Takahashi, Y. Ohmori, and M. Kawachi, "Design and fabrication of silica-based integrated-optic 1×128 power splitter," *Electronics Letters*, vol. 27, no. 23, p. 2131, 1991.
- [TAMIN08] T. H. Taminiau, F. D. Stefani, and N. F. van Hulst, "Enhanced directional excitation and emission of single emitters by a nano-optical Yagi-Uda antenna," *Opt. Express*, vol. 16, no. 14, pp. 10858–10866, Jul. 2008.
- [TANG12] Y. Tang, J. D. Peters, and J. E. Bowers, "Over 67 GHz bandwidth hybrid silicon electroabsorption modulator with asymmetric segmented electrode for 1.3 μm transmission," *Opt. Express*, vol. 20, no. 10, pp. 11529–11535, May 2012.
- [TAO08] S. H. Tao, Q. Fang, J. F. Song, M. B. Yu, G. Q. Lo, and D. L. Kwong, "Cascade wide-angle Y-junction 1 × 16 optical power splitter based on silicon wire waveguides on silicon-on-insulator," *Optics Express*, vol. 16, no. 26, p. 21456, Dec. 2008.
- [THEMI04] C. Themistos, M. Rajarajan, B. M. A. Rahman, S. S. A. Obayya, and K. T. V. Grattan, "Rigorous Comparison of Parabolically Tapered and Conventional Multimode-Interference-Based 3-dB Power Splitters in InGaAsP/InP Waveguides," *Applied Optics*, vol. 43, no. 27, p. 5228, 2004.
- [TIEN11] M.-C. Tien, J. F. Bauters, M. J. R. Heck, D. T. Spencer, D. J. Blumenthal, and J. E. Bowers, "Ultra-high quality factor planar Si₃N₄ ring resonators on Si substrates," *Opt. Express*, vol. 19, no. 14, pp. 13551–13556, Jul. 2011.
- [ULRIC78] R. Ulrich and T. Kamiya, "Resolution of self-images in planar optical waveguides," *Journal of the Optical Society of America*, vol. 68, no. 5, p. 583, May 1978.

- [VAN81] H. C. van de Hulst, *Light Scattering by Small Particles*. New York: Dover, 1981.
- [WANG13] J. Wang, D. Liang, Y. Tang, D. Dai, and J. E. Bowers, “Realization of an ultra-short silicon polarization beam splitter with an asymmetrical bent directional coupler,” *Opt. Lett.*, vol. 38, no. 1, pp. 4–6, Jan. 2013.
- [WANG02] Q. Wang, J. Lu, and S. He, “Optimal design method of a low-loss broadband Y branch with a multimode waveguide section,” *Appl. Opt.*, vol. 41, no. 36, pp. 7644–7649, Dec. 2002.
- [WEBER04] W. H. Weber and G. W. Ford, “Propagation of optical excitations by dipolar interactions in metal nanoparticle chains,” *Phys. Rev. B*, vol. 70, no. 12, p. 125429, Sep. 2004.
- [WEEBE01] J.-C. Weeber, J. R. Krenn, A. Dereux, B. Lamprecht, Y. Lacroute, and J. P. Goudonnet, “Near-field observation of surface plasmon polariton propagation on thin metal stripes,” *Phys. Rev. B*, vol. 64, no. 4, p. 045411, Jul. 2001.
- [WEI01] H. Wei, J. Yu, X. Zhang, and Z. Liu, “Compact 3-dB tapered multimode interference coupler in silicon-on-insulator,” *Opt. Lett.*, vol. 26, no. 12, pp. 878–880, Jul. 2001.
- [WEISS] E. W. Weisstein, <http://mathworld.wolfram.com/RadiusofCurvature.html>
- [WOOLL99] J. A. Woollam, B. D. Johs, C. M. Herzinger, J. N. Hilfiker, R. A. Synowicki, and C. L. Bungay, “Overview of variable-angle spectroscopic ellipsometry (VASE): I. Basic theory and typical applications,” presented at the Optical Metrology, 1999, vol. 72, pp. 3–28.
- [WU10] B. Wu, A. Kumar, and S. Pamarthy, “High aspect ratio silicon etch: A review,” *Journal of Applied Physics*, vol. 108, no. 5, p. 051101, Sep. 2010.
- [XU00] J. Xu, G. Chen, and M. Xie, “Vision-guided automatic parking for smart car,” in *Proceedings of the IEEE Intelligent Vehicles Symposium, 2000. IV 2000*, 2000, pp. 725–730.
- [YARIV06] A. Yariv and P. Yeh, *Photonics: Optical Electronics in Modern Communications (The Oxford Series in Electrical and Computer Engineering)*. New York, NY, USA: Oxford University Press, Inc., 2006.
- [YOUN81] A. T. Young, “Rayleigh scattering,” *Appl. Opt.*, vol. 20, no. 4, pp. 533–535, Feb. 1981.
- [ZHU13] S. Zhu, G. Q. Lo, and D. L. Kwong, “Silicon nitride based plasmonic components for CMOS back-end-of-line integration,” *Opt. Express*, vol. 21, no. 20, pp. 23376–23390, Oct. 2013.

Résumé : la réalisation d'un système holographique 3D embarqué dans un véhicule nécessite le développement d'une structure d'éclairage surfacique à géométrie plane pour générer un faisceau cohérent, directionnel et uniforme. Ce type de système a été jusqu'à présent réalisé à base de composants optiques classiques comme des lentilles et des miroirs. L'objectif de cette thèse est de proposer une solution plus compacte grâce à l'utilisation des (nano-) technologies d'intégration pour réaliser une émission cohérente, directionnelle et uniforme sur une grande surface à 633 nm en remplaçant les composants optiques volumineux par un circuit intégré photonique. Nous présentons d'abord de manière générale les applications des composants optiques et photoniques dans le domaine automobile, puis la structure plane intégrée que nous visons pour l'éclairage du système holographique. Nous montrons ensuite l'intérêt du développement de circuits photoniques à base de guides de nitrure de silicium pour le fonctionnement dans le domaine du visible, comme requis pour la présente application. Les travaux réalisés sur les guides d'onde en Si_3N_4 pour la propagation de la lumière à 633 nm sont alors détaillés. Dans un premier temps, nous introduisons les méthodes théoriques pour analyser les modes guidés et montrons les résultats de calcul des indices des modes 1D et 2D pour dimensionner un guide rectangulaire monomode. Enfin, nous détaillons l'étude théorique et de simulation pour définir certains composants intégrés du circuit visé, comme le diviseur $1 \times N$ de faisceau et les guides d'onde courbes. Nous présentons alors les travaux de fabrication des guides d'ondes Si_3N_4 encapsulés dans la silice, précédemment conçus, et qui présentent une dimension autour de $250 \text{ nm} \times 300 \text{ nm}$. Nous montrons les principales étapes de fabrication en salle blanche, comprenant le dépôt des diélectriques à l'aide de la PECVD, la lithographie assistée par faisceau d'électron (EBL) et la gravure ionique réactive (RIE). Les résultats de fabrication sont évalués et analysés afin d'optimiser le procédé de fabrication. Finalement, nous présentons le banc de caractérisation des guides d'onde et les résultats des pertes optiques mesurées. Le dernier chapitre est dédié à l'étude du couplage d'un mode photonique guidé à un mode plasmonique dans un système de guides d'onde, qui consiste en une chaîne de nanoparticules métalliques en Au ou en Ag déposée sur le guide d'onde rectangulaire Si_3N_4 . L'état de l'art et l'étude théorique sont d'abord présentés, puis nous montrons les résultats de simulation numérique de l'efficacité de couplage en fonction des tailles des nanoparticules et de la longueur d'onde dans ce système de guides d'onde couplés.

mots clés: dispositifs intégrés photoniques ; guides d'onde plasmonique ; fabrication en salle blanche

Abstract: An auto-embedded 3D holographic system requires the development of a surface lighting integrated device to generate a coherent, directional and uniform lighting beam. Up to now, the realization of this type of system is based on the conventional optical components such as lenses and mirrors. The objective of this thesis is to propose an ultra-compact solution by using the nanotechnologies, in order to realize coherent, directional and uniform light emitting at 633 nm on a large surface in replacing the bulky optical components by a photonic integrated circuit (PIC). In the beginning of the thesis, we present the automotive applications of optics and photonics, and then introduce to the integrated planar structure, which is expected to illuminate the holographic system. We present then our interest of developing silicon nitride waveguides-based PICs, which can be operated in the visible range, as required for the mentioned application. The realized research work on the Si_3N_4 waveguides for the light propagation at 633 nm are then detailed. At first, we introduce the theoretical methods for the analysis of the guided modes and present the calculated indexes of the 1D and 2D modes, which are used to design the single-mode rectangular waveguide. At last, we present exhaustively our theoretical study and simulation work to define some targeted PICs, as the $1 \times N$ beam splitter and the bent waveguides. Then we introduce the fabrication of the predetermined SiO_2 cladded Si_3N_4 waveguide samples, which have a cross-section size about $250 \text{ nm} \times 300 \text{ nm}$. We present main processes of the fabrication in cleanroom, including the deposition of the dielectric layers by using PECVD, the electron beam lithography (EBL) and the reactive ionic etching (RIE). The fabrication of waveguides has been evaluated and analyzed, in order to optimize the fabrication process. Finally, we present the waveguide's characterization set-up and the measurement results of the optical losses. The last chapter of the thesis is dedicated to the study of the coupling effect from a guided photonic mode to a plasmonic mode supported by a guiding structure, which consists of a metallic nanoparticle (Au or Ag) chain deposited on top of the Si_3N_4 rectangular waveguide. The state of the art and the theoretical study are firstly introduced. Then we present the numerical simulation results of the coupling efficiency as a function of nanoparticle's sizes and operation wavelength in this photonic-plasmonic coupled waveguide system.

keywords: photonic integrated device; plasmonic waveguide; cleanroom fabrication